TARGETING THE INTERACTOME OF THE SODIUM IODIDE SYMPORTER TO INCREASE RADIOIODIDE UPTAKE IN DIFFERENTIATED THYROID CANCER





Caitlin E.M. Thornton

A thesis presented to the University of Birmingham
for the degree of Doctor of Philosophy.

Institute of Metabolism and Systems Research
College of Medical and Dental Sciences
March 2021

UNIVERSITY OF
BIRMINGHAM

University of Birmingham Research Archive

e-theses repository

This unpublished thesis/dissertation is copyright of the author and/or third parties. The intellectual property rights of the author or third parties in respect of this work are as defined by The Copyright Designs and Patents Act 1988 or as modified by any successor legislation.

Any use made of information contained in this thesis/dissertation must be in accordance with that legislation and must be properly acknowledged. Further distribution or reproduction in any format is prohibited without the permission of the copyright holder.

Abstract

Currently, the treatment of differentiated thyroid cancer combines surgical resection of the tumour and thyroid with post-surgical radioiodide therapy to ablate remaining cancer cells. Patients may be refractory to radioiodide treatment due to dysregulated expression of the Na^+/I^- symporter (NIS) or its transport to the plasma membrane of thyroid cancer cells. Although some studies have achieved increased expression of NIS, mislocalisation of the protein inside the cell remains common in thyroid tumours. This has led to recent studies exploring the post-translational processing of NIS, which have revealed therapeutic opportunities for targeting NIS-interacting proteins to modulate radioiodide uptake.

This thesis appraised the established NIS interactor valosin-containing protein (VCP), as well as two new binding partners – moesin and annexin A1. Novel strategies for targeting VCP using the inhibitors CB-5083 and CB-5339 resulted in an increase in radioiodide uptake across multiple cellular models. Clotrimazole, which has previously been used as a VCP inhibitor but has limited *in vivo* utility due to its low bioavailability, was chemically modified. Structural analogues of clotrimazole demonstrated moderately improved effects on iodide uptake and improved bioavailability compared to the parent compound. The putative NIS interactors moesin and annexin A1 were shown to bind NIS via NanoBiT technology and to modulate its iodide uptake function, providing two entirely novel potential therapeutic targets in radioiodide refractory differentiated thyroid cancer.

For my Mum and Dad who have always supported me,

and for Pat.

Acknowledgements

Firstly, thank you to Chris McCabe and Vicki Smith for your endless guidance and support, you have made my PhD the most intellectually challenging and fulfilling years of my life. Thank you to the other members of the McCabe lab: Alice Fletcher and Martin Read for sharing your incomparable laboratory and analytical skills, Hannah Nieto for championing my ailing experiments as if they were your own and for all the cups of Harborne tea, and to Kate Brookes and Mohammed Alshahrani for all the fun you both bring to the lab, never a dull day. Thank you to Patricia, you made running eight Westerns a day look like an absolute breeze, even during a pandemic.

I would also like to acknowledge the University of Birmingham and the Medical Research Council for funding this research.

Thank you to Professor Christine Spitzweg and the members of AG Spitzweg who were so welcoming during my time at Klinikum Großhadern, this was an invaluable experience for me. I also thank Bioscientifica UK for contributing funds for my months spent working in Munich.

To my Mum, Dad, Amy, Dom, and Ollie who have supported me over the past few years, thank you for feigning interest in my projects and for invaluable advice from my Dad which has carried me through, including “If at first you don’t succeed, just lower your expectations”. To Nik, you probably did not expect so many cell-related frustrations to come your way when you naively swiped right but thank you for always believing it would work out in the end, you have been my rock. To my Birmingham friends, thank you for always being ready to eliminate all stress by splitting a £20 bottle at The Plough. And finally, to my many IMSR friends, thank you for making our environment a welcoming, sociable, collaborative, and happy place to work. However, given the chance, I would Coup you all.

Table of Contents

1 General Introduction 1
1.1 The Thyroid and Thyroid Hormones 2
1.1.1 Thyroid Anatomy 2
1.1.2 Mechanism of Action of Thyroid Hormone 8
1.1.3 Thyroid Disease States 9
1.2 Thyroid Cancer 11
1.2.1 Classification of Thyroid Cancer 11
1.2.2 Incidence and Demographics of Thyroid Cancers Worldwide 13
1.2.3 Molecular Basis of Thyroid Cancer 15
1.2.4 Diagnosis and Treatment of Thyroid Cancer 28
1.3 The Sodium/Iodide Symporter 35
1.3.1 NIS Function 35
1.3.2 NIS Structure 39
1.3.3 Epigenetic Regulation of NIS 40
1.3.4 Therapeutically Inducing NIS Expression *in vitro* and *in vivo* 42
1.3.5 NIS Trafficking and Dysregulation 44
1.3.6 The Sodium-Iodide Symporter Interactome 45
1.4 Aims and Hypothesis 60
2 Materials and Methods 63
2.1 Cell culture 64
2.1.1 Cancer Cell Line Culture 64
2.1.2 Primary Thyroid Culture 66
2.2 Plasmid Preparation 67
2.2.1 Table of Plasmids 67
2.2.2 Transformation of DNA into *E. coli* 70
2.2.3 Purification of Plasmid DNA 70
2.2.4 Sequencing 71
2.3 Transfection 72
2.3.1 Plasmid DNA Transfection 72
2.3.2 siRNA Transfection 72
2.4 Radioiodide Uptake Assay 73
2.5 Protein Preparation and Western Blotting 75
2.5.1 Protein Isolation 75

2.5.2 Protein Quantification 76
2.5.3 Western Blotting 76
2.6 Immunofluorescence and Imaging 77
2.7 Table of Antibodies 78
2.8 Protein-Protein Interaction Assays 79
2.8.1 Co-Immunoprecipitation 79
2.8.2 Preparing Luciferase-tagged Plasmids 80
2.8.3 NanoBiT 83
2.8.4 Site-directed Mutagenesis 84
2.8.5 Bioluminescence Resonance Energy Transfer (BRET) 86
2.9 *BRAF*-Inducible Cell Systems 87
2.10 Analysis of Data from The Cancer Genome Atlas 88
2.11 Statistics 89
3 The Effect of CB-5083 and CB-5339 on Radioiodide Uptake 90
3.1 Introduction 91
3.1.1 CB-5083 Inhibits VCP *in vitro* and *in vivo* 91
3.2 Materials and Methods 95
3.2.1 NIS-expressing Cell Models 95
3.2.2 Drug Treatments 95
3.2.3 Radioiodide Uptake Analysis 95
3.2.4 Protein Analysis 96
3.2.5 NanoBIT Protein-Protein Interaction Studies 96
3.2.6 Statistical Analysis 96
3.3 Results 97
3.3.1 The VCP Inhibitor CB-5083 Increases Radioiodide Uptake 97
3.3.2 The VCP Inhibitor CB-5339 Modifies Radioiodide Uptake 99
3.3.3 CB-5083 and CB-5339 Disrupt the Interaction Between NIS and VCP 102
3.3.4 Clotrimazole Increases NIS-mediated Iodide Uptake in Thyroid Cells 113
3.3.5 CB-5083 and CB-5339 Disrupt NIS Dimerisation 103
3.4 Discussion 104
3.4.1 VCP Inhibitors CB-5083 and CB-5339 Can Modify Iodide Uptake *in vitro* 104
3.4.2 VCP Inhibitors CB-5083 and CB-5339 Disrupt NIS-Protein Interactions 106
3.5 Concluding Remarks 110
4 Modifications to the Structure of Clotrimazole May Improve its Solubility and Binding to VCP 111
4.1 Introduction 112

4.1.1 Modelling the Binding of Clotrimazole to VCP 112
4.2 Materials and Methods 113
4.2.1 Drug Treatments 116
4.2.2 Radioiodide Uptake Assay 117
4.2.3 Generating Clotrimazole-Derived Compounds 118
4.2.4 Computational Modelling of Clotrimazole Binding to VCP 118
4.2.5 Statistical Analysis 119
4.3 Results 119
4.3.1 Clotrimazole Treatment Does Not Modify Iodide Uptake in L87-NIS Cells 119
4.3.2 Modifications to the Chloro-Substituted Aryl Ring of Clotrimazole Do Not Affect Iodide Uptake 120
4.3.3 Modifications to the Imidazole Ring on Clotrimazole Can Increase Iodide Uptake 124
4.3.4 Characterisation of Compound-17 in Additional Thyroid Cell Lines 130
4.4 Discussion 135
4.4.1 Structural Modifications to Clotrimazole Can Affect its Function as a VCP Inhibitor 135
4.4.2 The Relationship Between the logP Value of Clotrimazole Analogues and Radioiodide Uptake 136
4.4.3 Clotrimazole Analogues May Have Improved Binding to VCP 138
4.5 Concluding Remarks 141
5 Moesin and Annexin A1 Interact with NIS 142
5.1 Introduction 143
5.1.1 Moesin and Annexin A1 in Thyroid Cancer 143
5.2 Materials and Methods 144
5.2.1 Second-Round of Screening Putative NIS Interactors 144
5.2.2 siRNA Transfection 145
5.2.3 Plasmid Preparation 145
5.2.4 Co-Immunoprecipitation 145
5.2.5 Microscopy 146
5.2.6 Bioluminescence Resonance Energy Transfer (BRET) 146
5.2.7 NanoBiT 147
5.3 Results 148
5.3.1 Selection of Further Potential NIS Interactors Relevant to Protein Trafficking and Thyroid Cancer 148
5.3.2 The Effect of Moesin and Annexin A1 on Radioiodide Uptake 151
5.3.3 The Distribution of Moesin and Annexin A1 in Cells 154

5.3.4 Moesin and Annexin A1 Bind to NIS 157
5.3.5 The Putative NIS Binding Site for Moesin 164
5.4 Discussion 167
5.4.1 Moesin and Annexin A1 are Upregulated in Thyroid Cancer 167
5.4.2 Moesin and Annexin A1 Modulate Iodide Uptake 168
5.4.3 NIS Interacts with Moesin and Annexin A1 169
5.4.4 Hypothesis for the Interaction Between NIS and Moesin 173
5.4.5 Hypothesis for the Interaction Between NIS and Annexin A1 174
5.5 Concluding remarks 174
6 Exploring the Regulation of Moesin and Annexin A1 in Thyroid Cancer Cells 176
6.1 Introduction 177
6.1.1 Downstream Targets of the MAPK Pathway in Thyroid Cancer 177
6.1.2 PIK3CA Genomic Alterations in Endocrine Cancers 178
6.1.3 Moesin May be Targeted by Retinoic Acid 179
6.2 Materials and Methods 181
6.2.1 TCGA Gene Expression Analysis in Tumours with Upregulated Moesin and Annexin A1 181
6.2.2 $BRAF^{WT}$ and $BRAF^{V600E}$ Inducible Cell Systems 184
6.2.3 MAPK and PI3K Pathway Inhibitor Treatments 184
6.2.4 Retinoic Acid Treatment 185
6.3 Results 185
6.3.1 mRNA Expression of Moesin and Annexin A1 in Differentiated Thyroid Cancer 185
6.3.2 Moesin and Annexin A1 are Not Modulated by Induction of the MAPK Pathway 188
6.3.3 Moesin and Annexin A1 Is Not Modulated by Inhibition of the MAPK Pathway 189
6.3.4 Moesin is Not Downregulated by Inhibition of the PI3K-Akt-mTOR Pathway ..193
6.3.5 Moesin is Not Regulated by Retinoic Acid in Thyroid Cancer Cell Lines 195
6.4 Discussion 196
6.4.1 Transcriptomic Analysis of Tumour Samples which Express High Levels of *MSN* or *ANXA1* 196
6.4.2 The Regulation of Moesin and Annexin A1 by the MAPK Pathway 197
6.4.3 The Regulation of Moesin by PI3K Signalling 199
6.4.4 The Regulation of Moesin By Retinoic Acid in Thyroid Cancer Cells 200
6.5 Concluding Remarks 200
7 Concluding Thoughts and Future Directions 202

7.1 The Challenge of Radioiodide-Refractory Thyroid Cancer 203
7.2 Investigating the Interaction Between NIS and VCP 203
7.2.1 Targeting the interaction between NIS and VCP with CB-5083 and CB-5339 ... 203
7.2.2 Targeting the Interaction Between NIS and VCP Using Clotrimazole-Derived Compounds 205
7.2.3 Determining the Optimal VCP Inhibitor 206
7.2.4 Determining the Efficacy of VCP Inhibitors Against Thyroid Cancer in vivo 207
7.3 Investigating the Interaction Between NIS and Moesin 210
7.3.1 Future Directions 211
7.4 Investigating the Interaction Between NIS and Annexin A1 214
7.4.1 Future Directions 214
7.5 Concluding Remarks 216
8 Appendix 218
9 References 223

List of Figures

Figure 1.1 ***The structure of the thyroid gland and substructure of thyroid follicular cells.*** *3*
Figure 1.2 ***The hypothalamus pituitary thyroid axis.*** *4*
Figure 1.3 ***The process of thyroid hormone biosynthesis.*** *7*
Figure 1.4 ***A summary of the classification of thyroid cancers.*** *13*
Figure 1.5 ***Gender disparity between males and females diagnosed with differentiated thyroid cancer.*** *14*
Figure 1.6 ***A diagnosis of differentiated thyroid cancer typically presents earlier in females than males.*** *15*
Figure 1.7 ***Molecular signalling pathways that contribute to the tumorigenesis and progression of thyroid cancer.*** *16*
Figure 1.8 ***Anterior and posterior radiological imaging of a female patient with metastatic papillary thyroid cancer using a I^{123} tracer to assess radioiodide avidity of the tumours.*** *31*
Figure 1.9 ***Treatment with MAPK inhibitors may restore NIS expression at the plasma membrane.*** *33*
Figure 1.10 ***The structure of the sodium/iodide symporter protein.*** *38*
Figure 1.11 ***The proposed structure of dimeric NIS.*** *40*
Figure 1.12 ***2-D and 3-D structure of valosin-containing protein (VCP).*** *48*
Figure 1.13 ***The process of endoplasmic reticulum associated degradation*** *50*
Figure 1.14 ***Analysis of VCP expression in human cancers*** *52*
Figure 1.15 ***The structure of the MSN gene encoding Moesin*** *55*
Figure 1.16 ***The structure of the ANXA1 gene encoding Annexin A1.*** *57*
Figure 2.1 ***Plasmid maps of vectors used in this investigation.*** *69*
Figure 2.2 ***The NanoBiT assay measures interaction between tags on two proteins, LgBiT and SmBiT; in the event of protein-protein interaction, these tags may interact to form active luciferase.*** *84*
Figure 2.3 ***Bioluminescence resonance energy transfer requires tagging two proteins with an acceptor fluorophore and donor luciferase.*** *87*
Figure 3.1 ***CB-5083 is a specific and potent inhibitor of VCP inhibitor.*** *92*
Figure 3.2 ***Effect of the VCP inhibitor CB-5083 on radioiodide uptake and protein level of NIS and VCP in TPC1-NIS, 8505C-NIS and L87-NIS after treatment for 24 hours.*** *98*
Figure 3.3 ***Human primary thyrocytes demonstrate a significant increase in radioiodide uptake at a CB-5083 dose of 0.25 µM.*** *99*
Figure 3.4 ***Effect of the VCP inhibitor CB-5339 on radioiodide uptake and NIS and VCP protein levels in TPC1-NIS, 8505C-NIS and L87-NIS cells after treatment for 24 hours.*** *101*
Figure 3.5 ***The VCP inhibitors CB-5083 and CB-5339 disrupt the interaction between NIS and VCP in HeLa cells after treatment with 0.5µm for 24 hours.*** *102*
Figure 3.6 ***The VCP inhibitors CB-5083 and CB-5339 disrupt the interaction between NIS monomers.*** *103*
Figure 4.1 ***VCP structure and the regions targeted by known VCP inhibitors.*** *113*
Figure 4.2 ***Treatment with clotrimazole increases NIS-mediated iodide uptake in TPC1-NIS cells.*** *114*
Figure 4.3 ***L87-NIS cells did not respond to increasing doses of clotrimazole after treatment for 24 hours.*** *120*
Figure 4.4 ***Changes to the clotrimazole structure made during the first round of drug synthesis.*** *121*
Figure 4.5 ***Removal of groups on the chloro-substituted aryl ring of clotrimazole had no effect on radioiodide uptake.*** *123*
Figure 4.6 ***Changes to the clotrimazole structure made during the second round of novel compounds.*** *124*
Figure 4.7 ***In the second iteration of analysing clotrimazole analogues, two compounds significantly increased iodide uptake when co-treated with SAHA in 8505C-NIS cells.*** *126*
Figure 4.8 ***Modelling the binding of clotrimazole, compound-11 and compound-12 to VCP.*** *127*
Figure 4.9 ***Changes to the clotrimazole structure made during the third round of novel compounds.*** *128*
Figure 4.10 ***In the final round of screening clotrimazole analogues, TPC1-NIS cells treated with compound-17 resulted in statistically significant increases in radioiodide uptake.*** *129*
Figure 4.11 ***The binding of compound 17 to the allosteric binding pocket of VCP was modelled by Dr Giovanni Bottegoni.*** *130*
Figure 4.12 ***The effect of compound-17 on four additional cell lines was assessed.*** *132*
Figure 4.13 ***Compound-17 was redeveloped to GB002 based on an overlapping model with the VCP inhibitor UPCDC30245.*** *134*

Figure 5.1 ***Comparison of Moesin (MSN) and Annexin A1 (ANXA1) expression in thyroid cancer vs normal and across multiple known driver mutations in thyroid cancer.*** *149*
Figure 5.2 ***Breakdown of groups that have upregulated MSN and ANXA1 expression by oncogenic driver mutation, compared to normal tissue control.*** *150*
Figure 5.3 ***(A) siRNA knockdown of Moesin and Annexin A1 genes resulted in statistically significant increases in radioiodide uptake in TPC1-NIS and 8505C-NIS cells.*** *152*
Figure 5.4 ***(A) Overexpression of moesin or annexin A1 by exogenous gene transfection did not affect radioiodide uptake on TPC1-NIS and 8505C-NIS cells.*** *153*
Figure 5.5 ***(A) TPC1 cells and (B) HeLa cells transfected with NIS-HA and stained with anti-HA (green), anti moesin (red) and DAPI nuclear stain.*** *155*
Figure 5.6 ***(A) TPC1 cells and (B) HeLa cells were transfected with NIS-HA and stained for anti-HA, anti-annexin A1 and the DAPI nuclear stain.*** *156*
Figure 5.7 ***Co-immunoprecipitation assays in TPC1-NIS and MDA-NIS cells.*** *157*
Figure 5.8 ***BRET ratio of fluorescence signal divided by luminescence background.*** *159*
Figure 5.9 ***Three NanoBiT assay positive controls show significant increases in luminescence against assay specific negative control.*** *161*
Figure 5.10 ***The NanoBiT assay to assess the interaction between (A) NIS and Moesin and (B) NIS and Annexin A1.*** *163*
Figure 5.11 ***The Reverse NanoBiT assay using LgBiT tagged NIS and SmBiT tagged protein of interest.*** *164*
Figure 5.12 ***The amino acid structure of NIS in the plasma membrane reveals a KR motif, in the juxta membrane region of the cytoplasmic C-terminus.*** *T* *165*
Figure 5.13 ***Comparison of the iodide uptake functionality of the NIS vectors used in NanoBiT analysis in HeLa cells.*** *166*
Figure 5.14. ***The influence of NIS C-terminal mutations on the binding of NIS-SmBiT and LgBiT-MSN.*** *167*
Figure 6.1 ***Proteins which are downstream effectors of the MAPK pathway and contribute to thyroid cancer phenotypes can be downregulated in thyroid cells by treatment with MAPK inhibitors.*** *178*
Figure 6.2 ***Treatment with retinoic acid decreases moesin protein level in MCF7 cells.*** *180*
Figure 6.3 ***A flow diagram of RNAseq data obtained from THCA database of the Cancer Genome Atlas..*** *183*
Figure 6.4 ***A comparison of the genes which display enriched expression in samples which also express high levels of (A) Moesin and (B) Annexin A1, in both $BRAF^{WT}$ and $BRAF^{V600E}$ tumour samples.*** *187*
Figure 6.5 ***Moesin and Annexin A1 protein levels are not induced upon MAPK stimulation by induction of $BRAF^{WT}$ or $BRAF^{V600E}$*** *189*
Figure 6.6 ***Treatment of TPC1-NIS (A) and 8505C-NIS cells (B) with increasing doses of selumetinib does not affect protein level of either moesin or annexin A1.*** *190*
Figure 6.7 ***Treatment of TPC1-NIS (A) and 8505C-NIS cells (B) with increasing doses of vemurafenib from 1 to 8μM does not affect protein level of either moesin or annexin A1.*** *191*
Figure 6.8 ***Effect of MAPK inhibition on radioiodide uptake in TPC1-NIS and 8505C-NIS cells.*** *192*
Figure 6.9 ***The PI3K-Akt-mTOR inhibitor alpelisib has no effect on moesin protein levels after treatment with doses between 10 and 40 μM in TPC1-NIS (A) and 8505C-NIS (B) cells..*** *194*
Figure 6.10 ***The PI3K-Akt-mTOR pathway inhibitor alpelisib has no effect on radioiodide uptake in TPC1-NIS and 8505C-NIS cells after treatment for 24 hours at multiple doses.*** *195*
Figure 6.11 ***Treatment with 1 μM retinoic acid over 72 hours does not affect moesin protein level in TPC1 and 8505C cell lines.*** *196*
Figure 7.1 ***The working model of post-translational processing of NIS.*** *217*

List of Tables

Table 1 ***The biochemical definition of thyroid dysfunction.*** *10*

Table 2 ***Mass spectrometry list of NIS and putative interacting proteins including moesin and annexin A1 from MDA-MB-231 cell stably expressing NIS.*** *46*

Table 3. ***Densities at which each cell line was seeded for experiments in 6-well and 24-well plates.*** *66*

Table 4 ***Plasmids used in this investigation.*** *68*

Table 5 ***Primers used to sequence plasmids in this investigation.*** *71*

Table 6 ***siRNAs used for knockdown experiments in this investigation.*** *73*

Table 7 ***Antibodies used in this investigation for analysis by Western blot or microscopy.*** *78*

Table 8 ***PCR primers used to amplify LgBiT and Nanoluc tags for insertion into pcDNA3.1 (+).*** *80*

Table 9 ***PCR primers for amplifying genes of interest prior to insertion into pcDNA3.1 (+) containing LgBiT or Nanoluc tags.*** *81*

Table 10 ***PCR primers for amplifying SmBiT tag directly onto genes of interest.*** *82*

Table 11 ***Sequences of primers used to generate mutation in NIS coding sequence in the C-terminal tail domain immediately adjacent to the membrane.*** *85*

Table 12 ***PCR Thermocycler conditions for generating NIS-SmBiT mutants.*** *85*

Table 13 ***Sequencing primers used to confirm insertion of BRAF into pcDNA5/FRT/TO vector.*** *88*

Table 14 ***The predicted logP values of reported VCP inhibitors.*** *115*

Table 15. ***Transfection combinations for the BRET assay.*** *146*

Table 16 ***Transfection combinations for the NanoBiT assay.*** *147*

Table 17. ***Transfection combinations for the reverse NanoBiT assay.*** *147*

Table 18 ***The doses of MAPK and PI3K inhibitors that were used to assess the effect on moesin and annexin A1 protein level.*** *184*

Table 19 ***Full summary of clotrimazole-derived compounds: compound name, 2-D structure, 3-D structure, chemical formula, molecular weight, logP value as indicator of lipophilicity and number of rotational bonds which may form interactions in allosteric VCP binding pocket.*** *219*

Abbreviations

ANOVA	Analysis of Variance
ANXA1	Annexin A1
ARF4	ADP-Ribosylation Factor 4
ATC	Anaplastic Thyroid Cancer
BRAF	Rapidly Accelerate Fibrosarcoma, type B
BRET	Bioluminescence Resonance Energy Transfer
cDNA	complementary DNA
CHOP	C/EBP homologous protein
CMAP	Broad Institute Connectivity Map
CMV	human Cytomegalovirus
Co-IP	Co-Immunoprecipitation
DMSO	Dimethyl Sulfoxide
DTC	Differentiated Thyroid Cancer
EGF	Epithelial Growth Factor
EGFR	Epithelial Growth Factor Receptor
EMT	Epithelial to Mesenchymal Transition
ER	Endoplasmic Reticulum
ERAD	Endoplasmic-Reticulum Associated degradation
ERK	Extracellular Signal-regulated kinases
ERM	Ezrin-Radixin-Moesin Protein Family
FDA	United States Food and Drug Administration
FGF	Fibroblast Growth Factor
FoxE1	Forkhead Box E1
FTC	Follicular Thyroid Cancer
GFP	Green Fluorescent Protein
HBSS	Hanks Balanced Salt Solution
HDACi	Histone Deacetylase Inhibitor
HT	Hashimoto's Thyroiditis
MAPK	Mitogen Activated Protein Kinase
MCT8	Monocarboxylate Transporter 8
MEK	MAPK/ERK Kinase
miR	Micro-RNA
MSC	Mesenchymal Stem Cell
MSN	Moesin
MTC	Medullary Thyroid Cancer
mTOR	mammalian Target of Rapamycin
MVB	Multivesicular Body
NCT#	National Clinical Trial Number
NICE	National Institute of Health and Clinical Excellence
NIS	Na+/I- Symporter
PAX8	Paired Box Gene 8
PBF	PTTG1- Binding Factor
PBS	Phosphate Buffered Saline
PDE6	Phosphodiesterase 6

PDGFR	Platelet-Derived Growth Factor Receptor
PI3K	Phosphatidyl- inositol-3-kinase
PKC	Protein Kinase C
PPARγ	Peroxisome Proliferator-Activated Receptor Gamma
PTC	Papillary Thyroid Cancer
PTEN	Phosphatase and Tensin homolog
PTTG	Pituitary Tumor-Transforming Gene
RA	Retinoic Acid
RAS	Rat Sarcoma Protein
RET	Rearranged During Transfection
RRTC	Radioiodide Refractory Thyroid Cancer
rT3	reverse T3 hormone
SAHA	Suberoylanilide Hydroxamic Acid
siRNA	Small-interfering-RNA
SLC5A5	Solute Carrier Family 5, Member 5
T3	Tri-iodothyronine
T4	Tetra-iodothyronine/ thyroxine
TBST	Tris Buffered Saline Tween
TCGA	The Cancer Genome Atlas
TERT	Telomerase Reverse Transcription
TG	Thyroglobulin
TH	Thyroid Hormone
THCA	Thyroid Cancer Database
THSR	Thyroid Stimulating Hormone Receptor
TPO	Thyroid Peroxidase
TRE	Thyroid Hormone Response Element
TRH	Thyrotropin Releasing Hormone
TSH	Thyroid Stimulating Hormone
TTF1	Thyroid Transcription Factor 1
VCP	Valosin Containing Protein
VEGF	Vascular Endothelial Growth Factor

1 General Introduction

1.1 The Thyroid and Thyroid Hormones

1.1.1 Thyroid Anatomy

The thyroid is a bi-lobed endocrine organ located anterior to the trachea in the neck (Figure 1A), that functions to synthesise thyroid hormones triiodothyronine (T3) and tetraiodothyronine/thyroxine (T4). T3 and T4 tightly regulate the metabolic rate of somatic cells and exert their effects through the thyroid hormone receptors (THR). The anatomy of the thyroid consists of densely packed spheroid structures called follicles which make up the functional units of the thyroid. Each follicle is comprised of polarised epithelial cells encircling a viscous colloid centre (Figure 1.1B). Deep capillary networks supply oxygen and nutrients to the follicular cells in this highly vascular organ. The central colloid contains the glycoprotein prohormone thyroglobulin, in its pre- and post- iodinated forms. Polarisation of the follicular cells allows for spatial separation of proteins that are relevant to thyroid function including the sodium/iodide symporter (NIS) and pendrin which function as basolateral and apical iodide transporters, respectively (Carrasco, 1993; Royaux et al., 2000; Scott et al., 1999). The thyroid hormone transporter monocarboxylate transport-8 (MCT8) is also found on the basolateral, capillary-facing membrane to transport thyroid hormone out of the follicular cell and into systemic circulation (Friesema et al., 2003). Parafollicular cells lie adjacent to the follicles in the connective tissue matrix and secrete calcitonin which regulates calcium homeostasis.

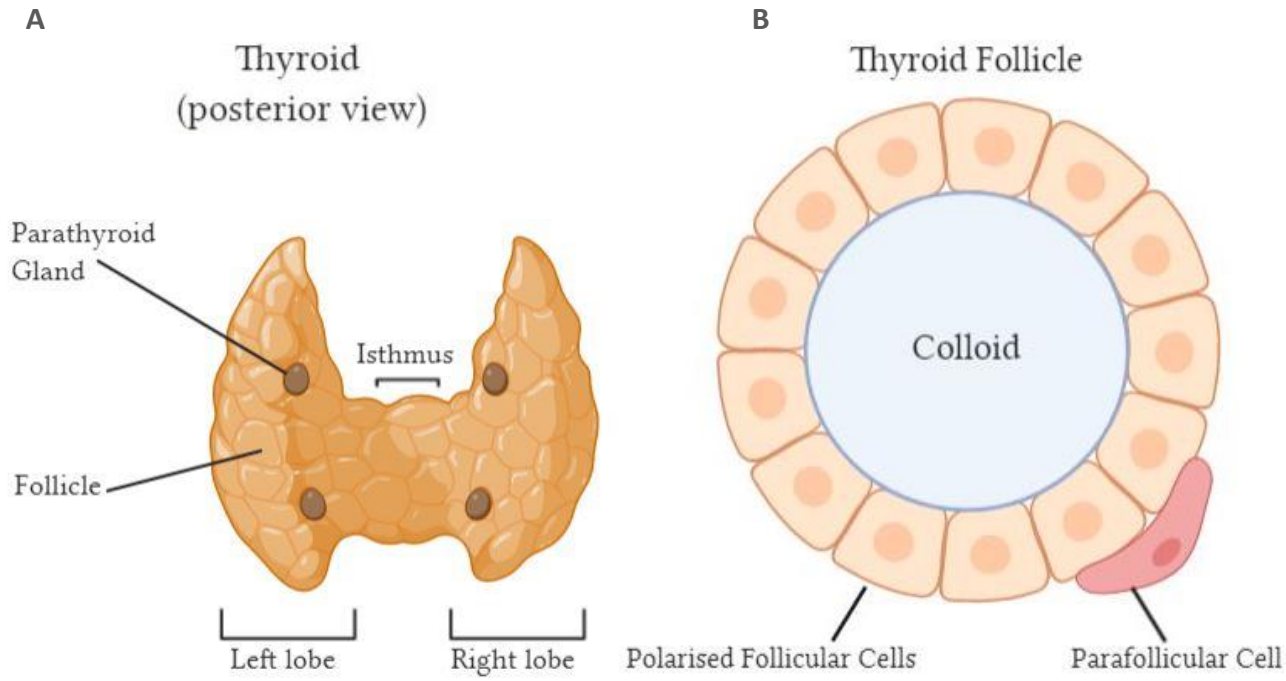


Figure 1.1 ***The structure of the thyroid gland and substructure of thyroid follicular cells****.* ***(A)*** *The posterior view of the thyroid gland displaying the parathyroid glands located behind.*

The production of thyroid hormones is regulated by the hypothalamic-pituitary-thyroid axis (Figure 1.2). Thyroid hormone (TH) synthesis is initiated by release of thyrotropin-releasing hormone (TRH) from the hypothalamus which is first produced as a pro-peptide before undergoing post-translational modifications to form a functional tripeptide. TRH travels through axon terminals in the brain to the median eminence where it enters the capillary circulation supplying the pituitary and acts on the anterior pituitary to stimulate release of prolactin and thyroid stimulating hormone (TSH) (Harris et al., 1978). Mutations within the gene encoding TRH can result in central hypothyroidism in both mice and humans (Collu et al., 1997; Yamada et al., 1997).

TSH travels in the circulatory system to the thyroid where it binds to its cognate TSH receptor (TSHR) triggering an internal signalling cascade (Figure 1.7), which culminates in the upregulation of master gene transcription factors Paired-Box 8 (PAX8), Thyroid Transcription Factor-1 (TTF1) and forkhead box protein E1 (FoxE1) via cAMP-mediated signalling (Carvalho and Dupuy, 2017; Kogai et al., 1997). Collectively, these transcription factors regulate expression of thyroid specific genes including NIS (*SLC5A5*), thyroglobulin (*TG*) and thyroid peroxidase (*TPO*) which subsequently aid thyroid hormone synthesis.

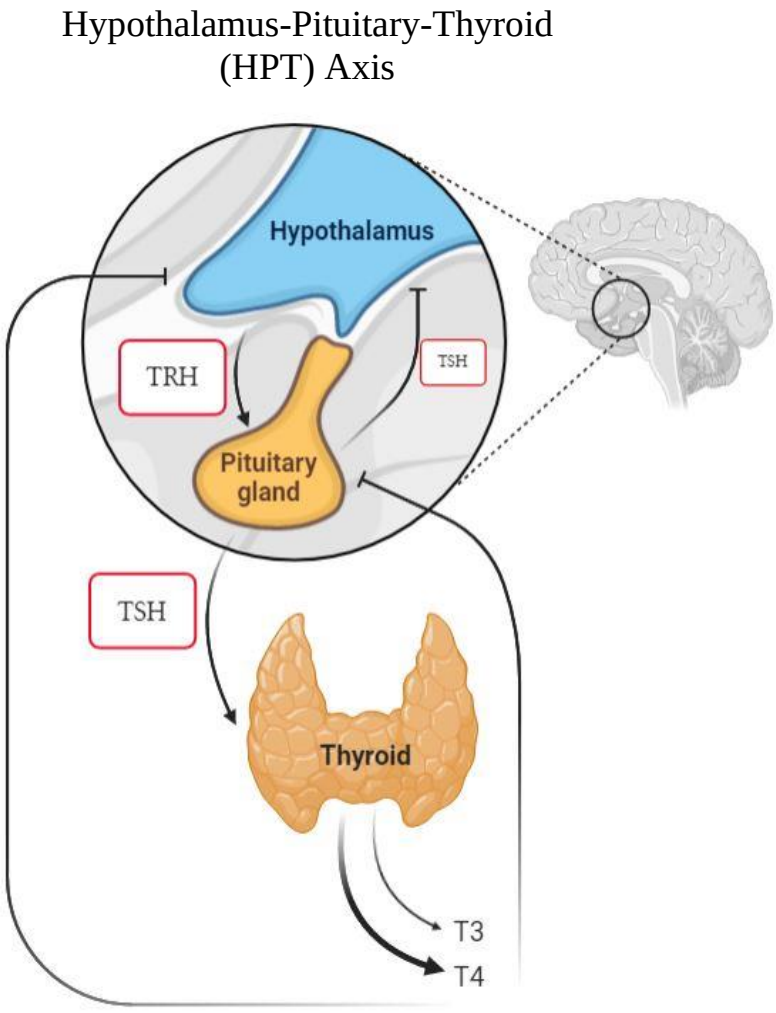


Figure 1.2 ***The hypothalamus pituitary thyroid axis****. This axis regulates the stimulation of thyroid hormone synthesis with positive and negative feedback loops. TRH – thyrotropin releasing hormone; TSH – thyroid stimulating hormone; T3- triiodothyronine; T4- tetraiodothyronine.*

Figure 1.3 depicts the full process of thyroid hormone synthesis beginning with iodide uptake from the blood and resulting in the secretion of hormones T3 and T4. NIS expression in the thyroid is key for uptake of dietary iodide from the circulatory system supplying the thyroid. NIS is synthesised through canonical protein synthesis pathways and trafficked to the capillary-facing basolateral membrane surface adjacent to capillaries where it has access to circulating iodide (Dai et al., 1996). Iodide accumulates in the thyroid at concentrations over twenty times higher than plasma levels. A capillary-to-thyroid Na^+ gradient is maintained by Na^+/K^+ ATPase pumps on the basolateral membrane to enable uptake of scarce iodide ions against the concentration gradient (Carrasco, 1993). Simultaneously, the thyroid hormone precursor protein, thyroglobulin (Tg), is synthesised in the follicular cell and translocated into the colloid of the follicle by exocytosis. Iodide is moved into the colloid at least in part via an apically expressed iodide transporter, pendrin (Royaux et al., 2000; Scott et al., 1999). In the colloid, iodide undergoes organification by TPO from monovalent anionic iodide to diatomic iodine using H_2O_2 generated by the enzyme DUOX2 as a reducing agent. Expression of the membrane-bound-glycoprotein TPO is under the regulation of TSH signalling. During organification, the iodine is simultaneously coupled to specific tyrosyl residues on thyroglobulin in the following reaction: $\mathrm{Tg} + \mathrm{I}^- + \mathrm{H}^+ + \mathrm{H_2O_2} \xrightarrow{\mathrm{TPO}} (\mathrm{Tg} - \mathrm{I}) + 2\mathrm{H_2O}$ where a proton is donated by the carboxylic acid group of tyrosine.

Expression of the membrane-bound-glycoprotein TPO is under the regulation of TSH signalling. Iodide-bound-thyroglobulin is taken back into the follicular cell by non-specific pinocytosis and is hydrolysed into mono/di-iodotyrosine and three different isomers of thyroid hormone: T3, reverse T3 (rT3) and T4. Cleavage of the iodinated thyroglobulin polymer into thyroid hormone molecules is biased towards the less biologically active

hormone T4 in an approximately 80:20 ratio (Mortoglou and Candiloros, 2004). T4 is converted to T3 by de-iodinating enzymes in peripheral tissues, primarily the kidney, liver, and skeletal muscles (Bianco et al., 2002; Lei et al., 2003). The de-iodinating enzymes D1, D2, and D3 are responsible for production of T3 in the blood from T4 and clearance of the metabolically inert rT3. The iodotyrosine compounds are recycled and thyroid hormones are released from the follicular epithelial cells into the capillary circulation by basolateral membrane proteins belonging to the monocarboxylate-transporter family of proteins (Friesema et al., 2003); Figure 1.3).

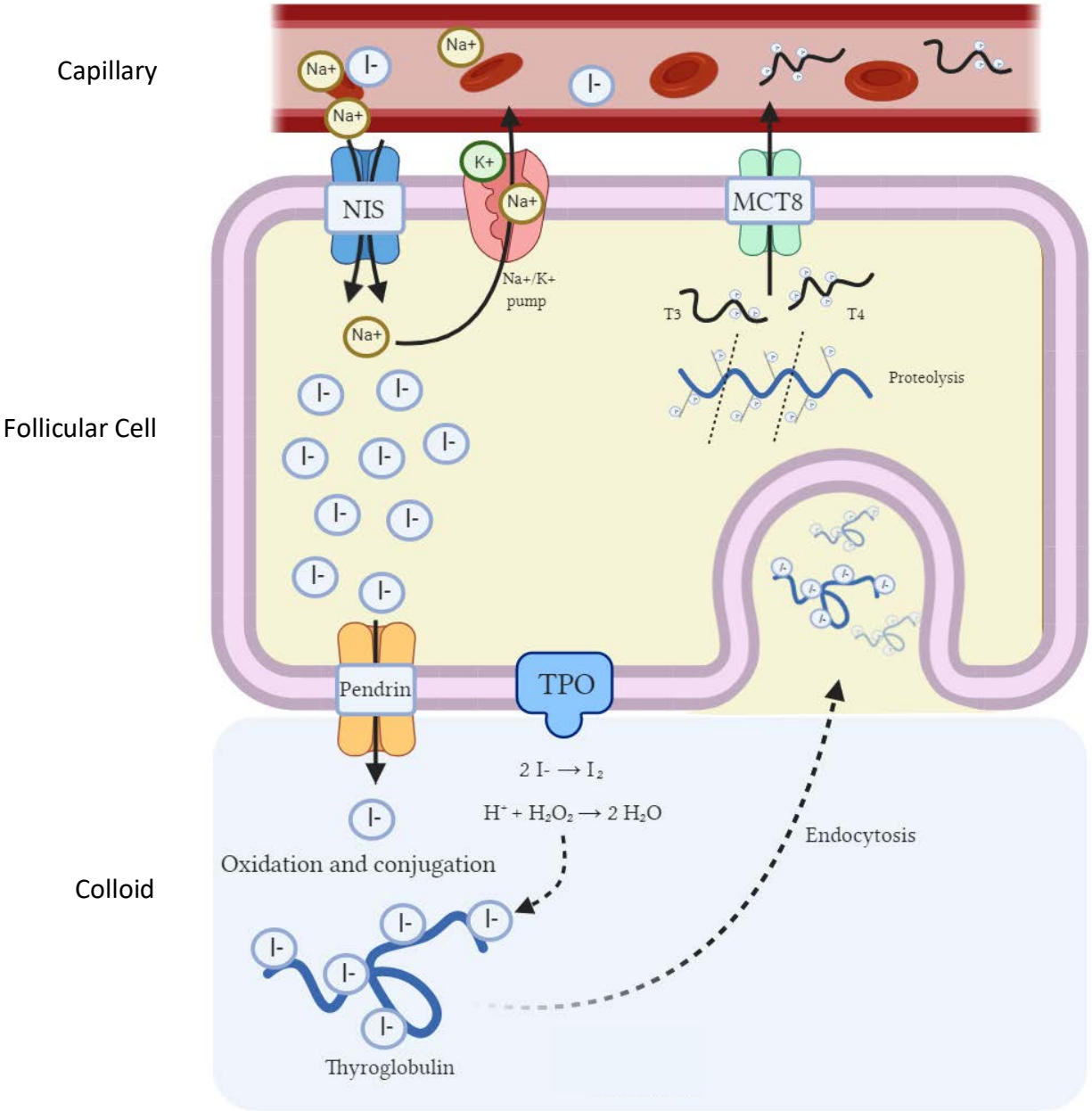


Figure 1.3 ***The process of thyroid hormone biosynthesis****. Iodide is taken into the follicular cells from the circulation by the sodium iodide symporter, and organified in the colloid of the follicle in a reaction in which hydrogen peroxide is reduced and the iodide groups are conjugated to thyroglobulin chains. The Tg-I is taken back into the follicular cell where it is cleaved into thyroid hormones T3 and T4 which are transported into the capillaries via MCT8. Na+ - sodium ions; I- -iodide ions; NIS – Na+/I- symporter; TPO – thyroid peroxidase enzyme; MCT8-monocarboxylate transporter 8; T3 triiodothyronine; T4- tetraiodothyronine; rT3 – reverse triiodothyronine.*

1.1.2 **Mechanism of Action of Thyroid Hormone**

T3 and T4 are poorly soluble and travel in the circulatory system bound to plasma proteins thyroxine-binding globulin, albumin, and transthyretin. TH receptors have a near-15-fold higher binding affinity for T3 than T4 and hence T4 is locally modified to T3 by de-iodinating enzymes in tissues. T3 binds to the TH receptor that mediates changes in expression of genes containing thyroid hormone response elements (TREs). TREs are made up of two hexanucleotide AGGTCA half sites separated by four nucleotides present upstream of the promoter in TH-targeted genes. Thyroid hormone receptors in complex with T3 bind to one or both sites and may also heterodimerise with the retinoic acid receptor to regulate gene expression (Zhang and Lazar, 2000).

One of the primary functions of TH is to increase the basal metabolic rate. T3 can stimulate translocation of Na^+/K^+ ATPase to the membrane and increase its functional activity, raising ATP and oxygen consumption (Lei et al., 2003). To meet these higher demands in oxygen consumption, T3 also mediates mitochondriogenesis and thermogenesis through uncoupling oxidative phosphorylation in the mitochondrial membranes. T3 increases the permeability of the inner membrane to protons resulting in increased oxidation of respiratory cofactors to compensate and maintain ATP synthesis homeostasis which subsequently drives heat production from the TCA cycle (Brand et al., 1992; Kalderon et al., 1995; Kalderon et al., 1992). Whilst this work was evaluated in rodent models, the effects of TH on mitochondrial membrane potential are mimicked in clinical observations for patients with subclinical hypothyroidism and patients with Grave's disease transitioning from hyperthyroidism to a euthyroid state (Chng et al., 2016; Kvetny et al., 2010). Thyroid hormones mobilise triglyceride

lipids from adipocytes and induce degradation via beta-adrenergic stimulated lipolysis (Haluzik et al., 2003; Hellström et al., 1997). TH also has well-documented roles in carbohydrate metabolism: T3 stimulates gluconeogenesis through increases in genes regulating this process (Feng et al., 2000). Despite TH stimulating hepatic glucose secretion through gluconeogenesis, studies have not demonstrated dysregulation of thyroid hormone signalling in patients with type 2 diabetes (Díez et al., 2011; Gopinath et al., 2008).

T3 and T4 can also have acute, non-genomic pathways through interactions with cellular enzymes. Non-genomic roles of thyroid hormone include modulation of calcium Ca^{2+} -ATPase pumps, activation of PI3K and MAPK pathways and acting on the integrin αvβ3 receptor to promote translocation of thyroid hormone receptor β from the cytoplasm to the nucleus (Cao et al., 2009; Galo et al., 1981; Lin et al., 2009). T3 can also interact with integrin on the plasma membrane to induce cell migration and angiogenesis, which may be critical in the progression of malignancy (Liu et al., 2014). Indeed, lower T3 levels have been associated with better outcomes in multiple cancers (Cristofanilli et al., 2005; Nelson et al., 2006). Additionally, the T4 metabolite and thyroid hormone agonist, tetraiodothyroacetic acid is under investigation as an anti-metastatic therapy which functions via disrupting the TH-integrin αvβ3 interaction (Mousa et al., 2018; Schmohl et al., 2019).

1.1.3 **Thyroid Disease States**

Thyroid dysfunction can arise for a variety of reasons. (Table 1) defines the biochemical definition for the different states of thyroid dysfunction. Thyrotoxicosis is a condition of thyroid hormone excess due to any physiological cause, while hyperthyroidism refers to

thyroid hormone excess specifically due to overproduction by the thyroid gland; however, these terms are sometimes used interchangeably in the literature. Hyperthyroidism is characterised by an increase in the basal metabolic rate, cardiovascular symptoms, and sympathetic nervous system symptoms. Typical clinical presentation includes shortness of breath, atrial fibrillation, unexplained weight loss, anxiety, or tremor.

The most common cause of hyperthyroidism is the autoimmune condition Grave's disease. Grave's disease arises due to production of antibodies against the TSH receptor which hyper-stimulate the thyroid gland to secrete above-normal levels of thyroid hormone, as outlined in (Table 1). Grave's disease can also lead to sight-threatening orbitopathy characterised by a variety of ophthalmological symptoms including eyelid retraction, photophobia, oedema and corneal ulceration (Bahn, 2010).

Condition	Thyroid Stimulating Hormone	Thyroid Hormones
Overt Hyperthyroidism	< 0.1mIU/L or undetectable	Elevated T4 or T3
Overt Hypothyroidism	> 4.5 mIU/L	Low T4
Subclinical Hyperthyroidism	TSH< 0.1 mIU/L, clearly low	Normal T4 and T3
	0.1 mIU/L <= TSH < 0.4 mIU/L, low but detectable	Normal T4 and T3
Subclinical Hypothyroidism	4.5 mIU/L < TSH <10 mIU/L, mildly elevated	Normal T4
	TSH >=10 mIU/L, markedly elevated	Normal T4

Table 1-1 ***The biochemical definition of thyroid dysfunction****. Adapted from (Rugge et al., 2015).*

Hypothyroidism can be a result of lack of production of thyroid hormone by the thyroid gland (primary hypothyroidism) or lack of pituitary or hypothalamic hormones resulting in lower stimulated release of thyroid hormones from the thyroid (central hypothyroidism). Primary hypothyroidism is more common and can result from other diseases including Hashimoto's Thyroiditis (HT). Hashimoto's is an autoimmune disease arising from production of antibodies against thyroid proteins such as Tg, TPO, and TSH, leading to diminished thyroid hormone production. The sustained immune response observed during HT can lead to enlargement of the thyroid into goitre. Hypothyroidism typically presents with symptoms including unexplained weight gain, sleep apnoea, changes in motor activity (El-Shafie, 2003) and can be treated using synthetic thyroid hormone analogues, firstly levothyroxine (synthetic T4) which more closely mimics the physiological state of T4 bias but liothyronine (synthetic T3) can be administered in case of levothyroxine intolerance.

1.2 Thyroid Cancer

1.2.1 Classification of Thyroid Cancer

Carcinomas arise from tumour formation from epithelial cell layers and thyroid carcinomas of follicular cell origin can be classified into 2 main groups: well-differentiated and poorly-differentiated. Well-differentiated thyroid cancers (DTC) include papillary carcinomas and follicular carcinomas which comprise 80 % and 5-10 % of all thyroid cancer diagnoses, respectively. Poorly-differentiated thyroid cancers (PDTC) include anaplastic carcinomas which are highly metastatic and invasive and make up 2-5 % of thyroid cancers (Figure 1.4). Medullary thyroid carcinomas (MTC) are derived from parafollicular cells which make up the

remaining 5-10 % of thyroid cancer diagnoses (Figure 1.4). A significant proportion of MTC diagnoses are a result of germline mutations in the RET proto-oncogene while papillary, follicular, and anaplastic carcinogenesis typically arises from somatic mutations. Sub-groups of thyroid cancer display characteristic mutational profiles that can determine response to treatment and overall prognosis, as discussed in section 1.2.3.

Papillary and follicular thyroid cancers have a 5-year survival rate of over 90 %, however these cancers remain a substantial public health problem given the continued rise in incidence of differentiated thyroid cancers over recent years (Ito et al., 2018; Milano, 2018). A retrospective cohort study of 360 anaplastic thyroid cancer patients calculated a dismal 5-year survival of 11 % and a median overall survival of nine months (Xu et al., 2020). This study demonstrated aggressive, advanced cancers have common driver mutations with papillary thyroid cancer including *BRAF* and *RAS* mutations and a higher incidence of mutations in *TERT* promoter, PI3K-Akt-mTOR pathway activating mutations, histone methyltransferase and mismatch excision repair pathways and *TP53* mutations. This is consistent with the theory that anaplastic thyroid cancers arise from differentiated tumours of follicular cell origin after accumulating further mutations that drive evolution to a poorly differentiated, advanced tumour (Landa et al., 2016).

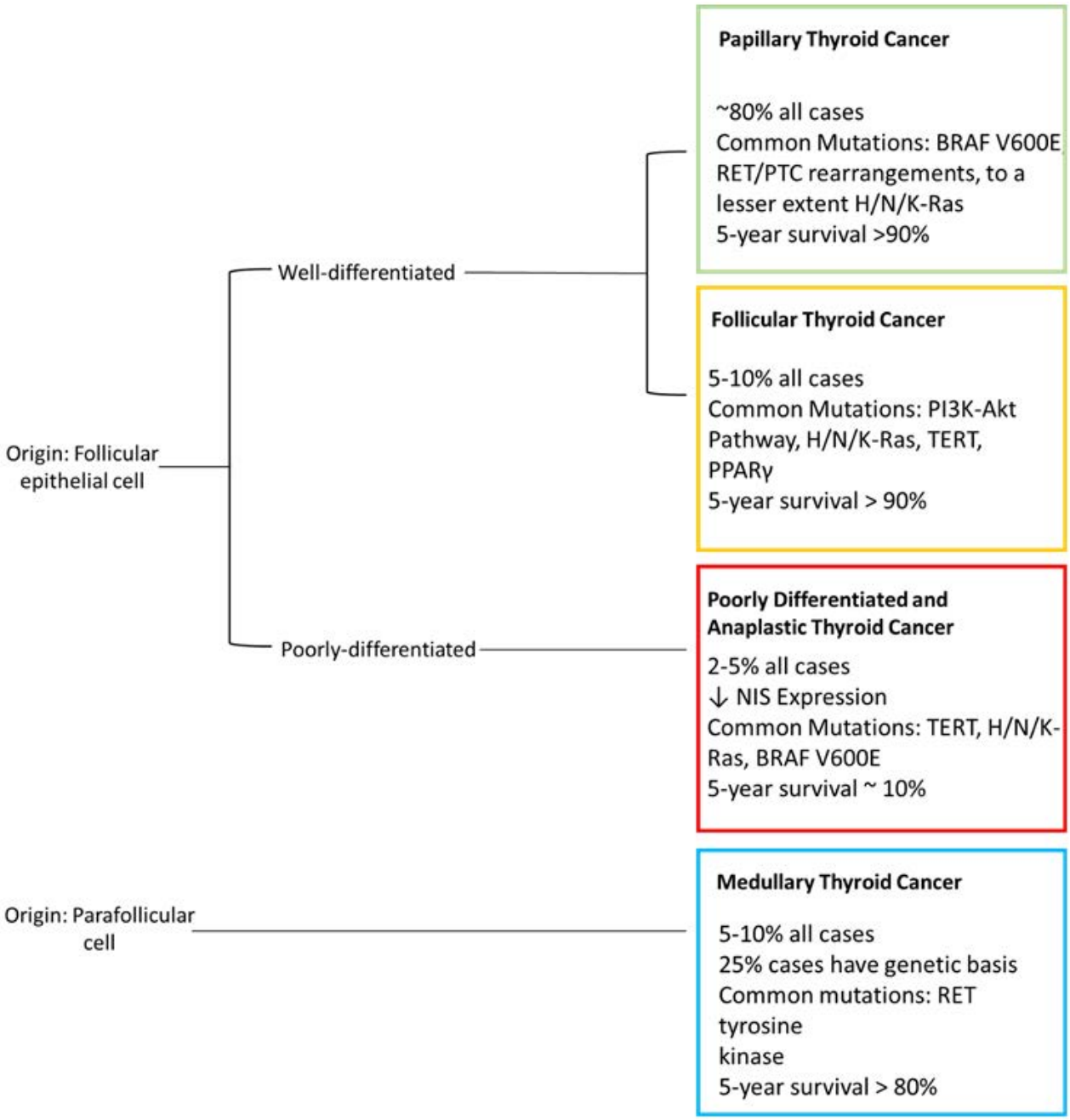


Figure 1.4 ***A summary of the classification of thyroid cancers****. There are four distinct groups of thyroid cancers which display characteristic mutation profiles and 5-year survival prognosis. Data derived from (A et al., 2011; Abdullah et al., 2019; Duan et al., 2019; Landa et al., 2016).*

1.2.2 **Incidence and Demographics of Thyroid Cancers Worldwide**

The global incidence of thyroid cancer has increased over recent years (Berontiene et al., 2017; James et al., 2018; Lim et al., 2017). This increase has partly been driven by

developments in diagnostic imaging techniques and the frequency of scanning both of which can increase the frequency of subclinical findings. However, other factors have been suggested to contribute to rises in thyroid cancer diagnoses, including rising obesity (Kim et al., 2015; Marcello et al., 2014; Zhao et al., 2012).

Exposure to ionising radiation is a known risk factor for papillary thyroid carcinoma, which typically present with RET/PTC rearrangements (Fugazzola et al., 1995; Klugbauer et al., 1995). Nuclear disasters such as the Chernobyl nucelar power plant disaster resulted in accumulation of volatile iodide species in the thyroids of nearby populations and there was significantly increased incidence of thyroid cancer diagnoses for many years after the event (Drozdovitch et al., 2013).

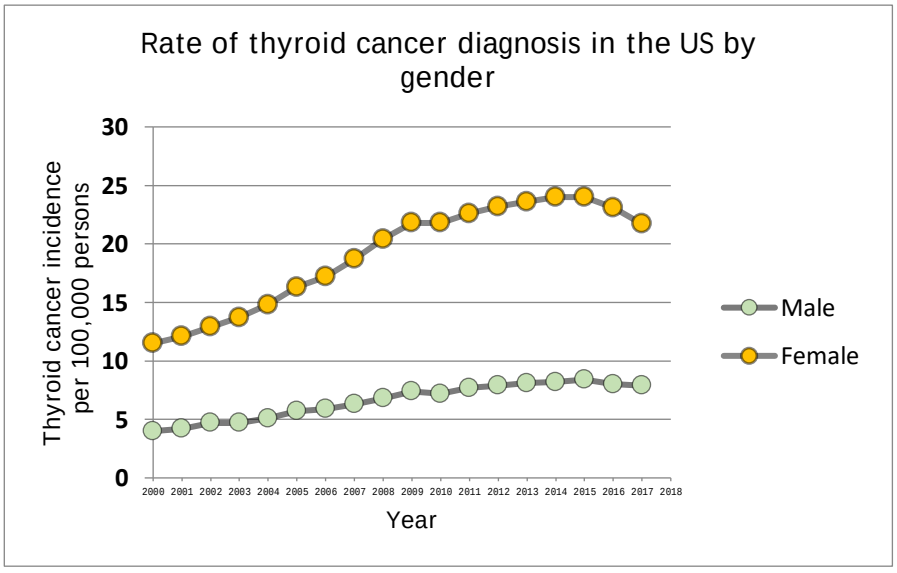


Figure 1.5 ***Gender disparity between males and females diagnosed with differentiated thyroid cancer****. Data downloaded from Surveillance, Epidemiology and End Results (SEER) Program (1969-2018) (www.seer.cancer.gov/popdata), National Cancer Institute, DCCPS, Surveillance Research Program, released December 2019.*

Thyroid cancer has a well-documented bias towards female incidence (Figure 1.5). A randomised study of patients undergoing thyroidectomies and lobectomies observed a 1:2.85 male-to-female ratio for differentiated thyroid cancers overall (Ortega et al., 2004) and 1:3.03 male-to-female ratio for papillary thyroid cancers specifically (Lupi et al., 2007). Interestingly, a gender disparity was not observed in more aggressive, anaplastic carcinomas, nor in patients above the age of 80 years old (Kilfoy et al., 2009; Ortega et al., 2004). The prevalence of thyroid cancer in women peaks between 40 and 49 while men peak at 65 to 69 years of age (Figure 1.6).

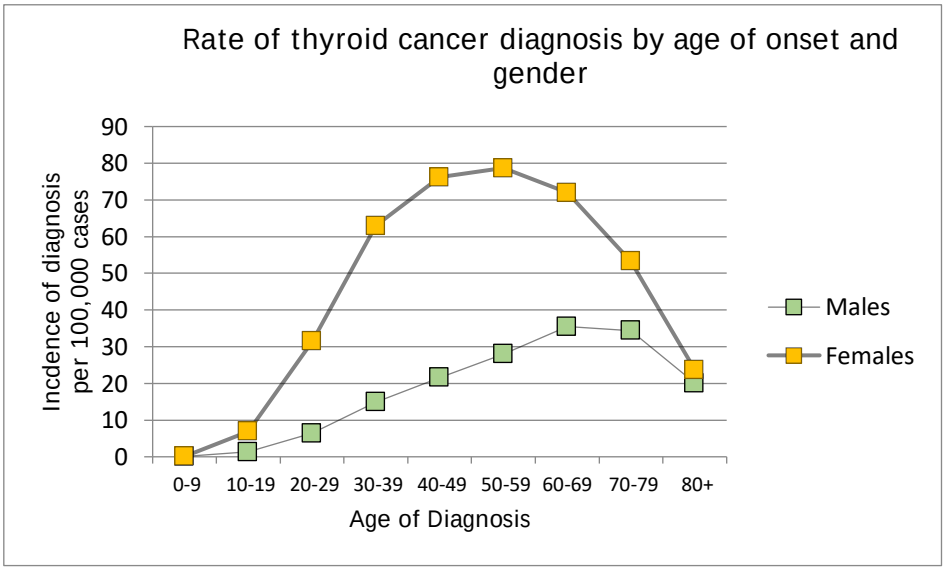


Figure 1.6 ***A diagnosis of differentiated thyroid cancer typically presents earlier in females than males****. Data downloaded from Surveillance, Epidemiology and End Results (SEER) Program (1969-2018) (www.seer.cancer.gov/popdata), National Cancer Institute, DCCPS, Surveillance Research Program, released December 2019.*

1.2.3 **Molecular Basis of Thyroid Cancer**

There are multiple genetic mutations in human cancers which act as gateways to uncontrolled cell growth and tumourigenesis, and thyroid cancer is enriched for specific mutation driver events. This includes activation of the mitogen-activate protein kinase pathway (MAPK) via

mutations in the *BRAF* or *N/H/K-RAS* genes, activation of PI3K-Akt-mTOR pathways either through activating mutations in key pathway proteins or inactivating mutations in the PTEN negative regulator of the pathway. Additionally, mutations in key tumour-suppressor and proto-oncogenes including tyrosine kinase *RET, TERT* and *TP53* can all contribute towards malignancy.

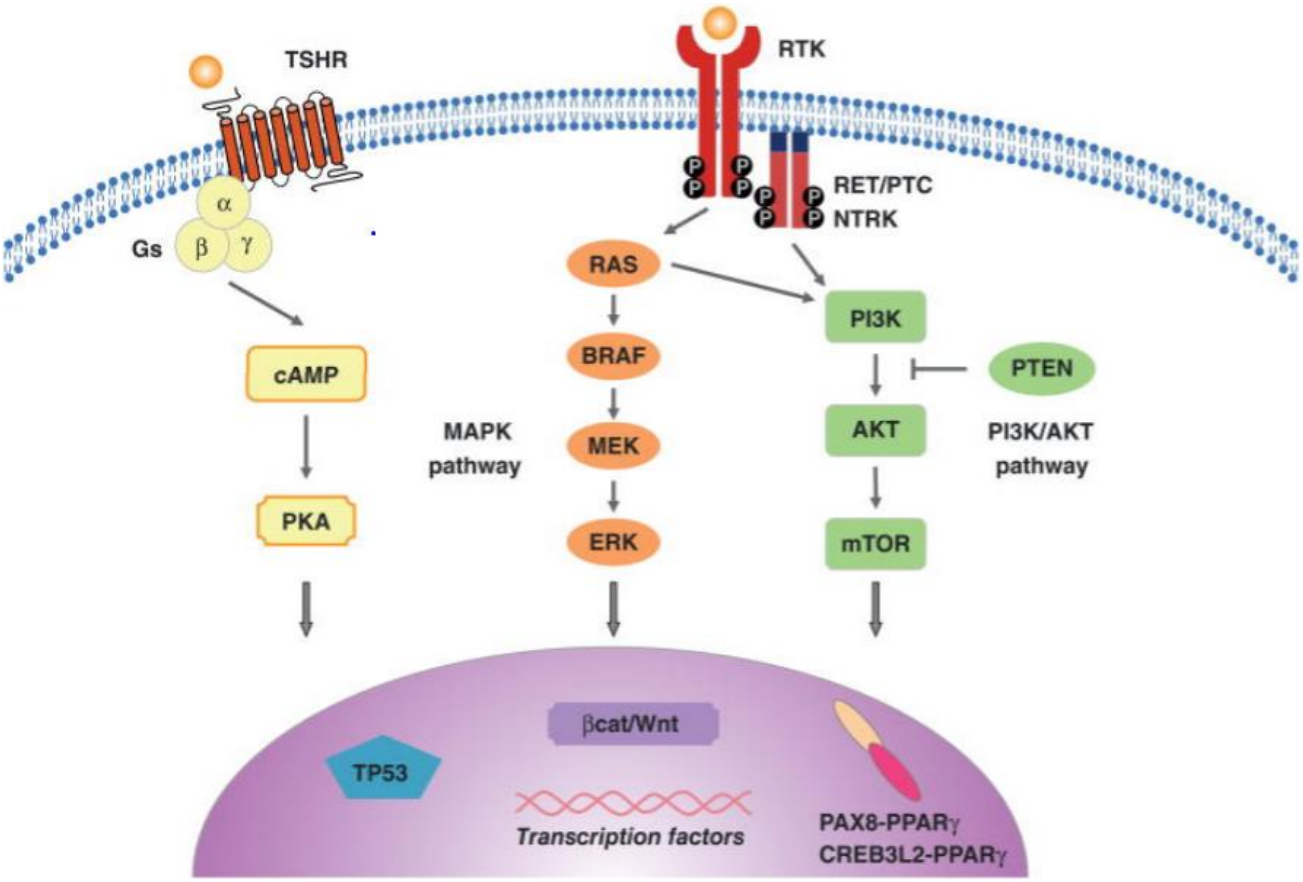


Figure 1.7 ***Molecular signalling pathways that contribute to the tumorigenesis and progression of thyroid cancer.*** *Most thyroid cancers display dysregulation of the MAPK (orange) pathway with additional mutations found in the PI3K (green) pathway, TP53 loss-of-function mutations and PPARγ fusion proteins. TSH dysregulation also contributes to a dedifferentiated phenotype in thyroid cancer. Adapted from Hsiao and Nikiforov, 2014.*

1.2.3.1 BRAF^{V600E} Mutation and BRAF Gene Fusion Events

The gain-of-function BRAF^{V600E} mutation is the most common driver mutation in papillary thyroid cancer. This transverse genetic mutation *BRAF^{T1799A}* resulting in the substitution of a valine for a glutamic acid on the activation loop of the BRAF protein kinase. BRAF^{V600E} monomers are capable of dimerising and activating in the absence of upstream Ras signalling, resulting in a constitutively active signal and high MAPK pathway output (Yao et al., 2015). Independent studies have measured BRAF^{V600E} mutation status in approximately 38 – 45 % of papillary thyroid carcinomas while 47 % of PTC samples in The Cancer Genome Atlas (TCGA) database for PTC samples harbour BRAF^{V600E} mutations (Cerami et al., 2012; Gao et al., 2013; Network, 2014).

BRAF activation results in higher MAPK pathway output (Figure 1.7), which enriches expression of genes that control entry into the cell cycle and proliferation (Brunet et al., 1999; Network, 2014). BRAF activation by gene fusion events have been recorded in a small number of thyroid cancer cases and display increased MAPK transcriptional output. BRAF and non BRAF-fusion driven cancers were typically detected in younger papillary thyroid cancer patients, an observation which is recapitulated in poorly differentiated and anaplastic thyroid cancers (Landa et al., 2016; Network, 2014). *BRAF* fusion events involved chromosomal rearrangements with *LMO7*, *MKRN1*, *FAM114A2* and *AGK* and most fusions conserved the kinase domain of *BRAF* (He et al., 2018; Network, 2014). There is an expansive spectrum of mechanisms behind BRAF activation, which only serves to highlight the importance of this oncogene to thyroid tumourigenesis. Here, the most common activation mutation, BRAF^{V600E}, is discussed.

BRAF mutation status is associated with the aggressiveness of disease. While small studies have suggested the $BRAF^{V600E}$ mutation in papillary thyroid cancer is observed more commonly in males than in females (Nakayama et al., 2007; Xu et al., 2003), this has not been observed in larger patient cohorts such as the TCGA or meta-analyses which report non-statistically significant differences between *BRAF* mutation status and gender (Lee et al., 2007; Lupi et al., 2007; Network, 2014).

Multiple mouse models have been generated to study the pathogenesis of $BRAF^{V600E}$-driven papillary thyroid tumours and to investigate efficacy of new treatments and drug combinations which can form the basis of human clinical trials. *In vivo* models of thyroid-specific expression of $BRAF^{V600E}$ have been generated by coupling the oncogene to promoters of thyroid specific genes such as thyroglobulin. In early animal models, this construct resulted in tumour development, but subsequent tumour dedifferentiation was accompanied by a loss in expression of thyroid specific genes including thyroglobulin which therefore reduced expression of the oncogene construct (Knauf et al., 2005; Rusinek et al., 2015). This negative feedback loop necessitated the development of a new model of thyroglobulin promoter-driven *Cre* recombinase with an oestrogen ligand binding domain fusion to enable tamoxifen-induced oncogene activation of $BRAF^{V600E}$. In 2011, a doxycycline-inducible, thyroid specific $BRAF^{V600E}$ mouse model showed promising results when treated with small molecular MAPK inhibitors targeting MEK or $BRAF^{V600E}$ protein including tumour regression and restoration of radioiodide avidity, discussed in section 1.2.4.4 (Chakravarty et al., 2011).

1.2.3.2 Ras Mutation

Activation of *N-RAS, K-RAS and H-RAS* oncogenes was detected in 49 % of follicular thyroid carcinomas, 28 % of poorly differentiated and 24 % of anaplastic thyroid carcinomas (Landa et al., 2016; Nikiforova et al., 2003). Despite rarely occurring in classical papillary thyroid cancer, 30-45 % of follicular variant papillary thyroid cancers harbour activating *RAS* mutations demonstrating a bias of Ras activation in follicular patterned tumours. Studies of thyroid cancer genotypes have found genetic mutations in *RAS* and *BRAF* to be mutually exclusive (Landa et al., 2016; Network, 2014). This suggests that MAPK activation is the dominant driver in thyroid cancer regardless of the mutational event that is driving constitutive MAPK signalling, although there are distinct differences between carcinomas with *RAS* and *BRAF* mutations. BRAF signals through the MAPK pathway by phosphorylating MEK1/2 while Ras phosphorylates Raf kinases and also binds p110α (Figure 1.7). P110α is the catalytic subunit of PI3K encoded by *PIK3CA*, thereby Ras additionally signals to effectors of the PI3K-Akt-mTOR pathway and resulting in differences in the tumour transcriptomes and behaviours arising from *RAS*-driven and *BRAF*-driven tumours. *RAS* mutations in PTC are more associated with the preservation of iodine related genes including *TG* and *SLC5A5,* and are less likely to have a radioiodide-refractory phenotype than $BRAF^{V600E}$ -driven tumours (Durante et al., 2007). Through transcriptomics analysis it has been shown that *RAS*-driven tumours typically have a lower flux through the MAPK pathway than $BRAF^{V600E}$ tumours (Network, 2014). This variation in transcriptional output may be due to negative feedback mechanisms further down the MAPK pathway which are abrogated by the $BRAF^{V600E}$ mutation but preserved in *RAS* mutant tumours.

Under normal signalling conditions, activation of Ras is dependent on by binding by GTP and subsequent hydrolysis of this nucleotide to GDP inactivates Ras. Ras-activating mutations typically fall in codon Q61 which results in inhibition of the autocatalytic GTPase function and permanently GTP-bound, active Ras. In some tumours, mutation of codon G12 in Ras also results in protein with an increased affinity for GTP and a bias towards the active isoform. *NRAS*^{61} mutations are more common than *KRAS* or *HRAS* in thyroid cancers (Gupta et al., 2013; Lemoine et al., 1989).

Despite *RAS* mutations being the most common oncogenic drivers in human cancer overall, targeted pharmacological inhibition of Ras has been challenging. Currently, an siRNA-based treatment for *KRAS*^{G12D} pancreatic tumours administered by intratumoral injection is under phase II clinical trials as one of the first specific anti-Ras drugs (NCT01676259) and it remains to be seen whether this mechanism of inhibition is effective. This treatment targets the KRAS isoform while *NRAS* and *HRAS* mutations are most frequently found in thyroid cancers; for this to be translated to thyroid cancer treatment, the treatment would require optimisation against these specific isoforms. Treatment of patients with advanced thyroid cancer with the MEK1/2 inhibitor selumetinib demonstrated preferential restoration of iodide uptake in patients with *RAS* mutations over BRAF^{V600E} mutant tumours, indicating MAPK inhibitors may be effective against *RAS*-driven thyroid cancer (Ho et al., 2013), also discussed in section 1.2.4.4.

1.2.3.3 PAX8/PPAR-Gamma Fusion

Paired Box Gene 8, or PAX8, is one of three master transcriptional regulators for thyroid specific genes. In normal thyroid follicular cells, PAX8 is upregulated upon binding of circulatory TSH to the TSH receptor on the outer membranes of the follicular cell, and is

essential in embryonic thyroid development and post-natal thyroid function into adulthood (Mansouri et al., 1998; Marotta et al., 2014). PAX8 works synergistically with the transcription factor TTF1, as despite both proteins being expressed in extrathyroidal tissues they are only co-expressed within the thyroid that where they co-operatively regulate thyroid specific gene expression (Di Palma et al., 2003). *PAX8* knock-out mouse models and *in vitro PAX8* knock-down experiments have been used to study downstream target genes of PAX8. These studies identified genes encoding *TG*, *TPO*, *SLC5A5* and *DUOX2* that are specific to thyroid function (Di Palma et al., 2011; Ohno et al., 1999; Zannini et al., 1992). Interestingly, multiple studies also reported PAX8 to modulate expression of genes involved in phosphatidylinositol-3-kinase and MAPK signalling pathways which are paramount in thyroid tumorigenesis (Di Palma et al., 2011; Ruiz-Llorente et al., 2012).

The peroxisome proliferator-activated receptor gamma (PPARγ) is a ligand-activated nuclear receptor family transcription factor which regulates cellular processes such as differentiation of adipose tissue and insulin sensitivity (Kim and Ahn, 2004; Rosen et al., 1999). PPARγ must heterodimerise with the retinoic X receptor to bind DNA and regulate gene expression (Chandra et al., 2008). In the PAX8/PPARγ rearrangement, the majority of the *PAX8* coding sequence is fused in frame to the coding exons of *PPARγ*. The resulting fusion protein is oncogenic and cells transfected with this protein exhibit increased growth rates and decreased apoptosis which may also accelerate growth (Gregory Powell et al., 2004). The precise mechanism behind the oncogenic properties of the fusion protein are not clear, but the presence of another less frequent *PPARγ* fusion protein in thyroid follicular carcinomas-*CREB3L2/PPARγ*- suggest that the *PPARγ* portion of the protein is necessary for the carcinogenic activity of the fusion protein (Lui et al., 2008). Although the effect of the fusion

protein in patients is not defined, i*n vitro* studies of the function of the fusion protein using xenograft models indicates increased cell growth and decrease apoptosis in cells, but decreased angiogenesis (Reddi et al., 2010). In addition, PPARγ has been reported to have tumour suppressor properties and it has been suggested that PAX8/PPARγ fusion protein is oncogenic simply by abrogating the normal anti-tumour function of wild-type PPARγ (Raman and Koenig, 2014).

The PAX8-PPARγ fusion protein driver is more commonly found in follicular thyroid cancers and is a rare event in papillary thyroid cancer. A study of 88 tumours found 36 % of follicular thyroid carcinomas harboured the *PAX8/PPARγ* chromosomal rearrangement, and that this fusion event was predominantly mutually exclusive to follicular carcinomas with *RAS* mutations (Nikiforova et al., 2003). The presence of *PAX8/PPARγ* rearrangement in follicular carcinomas correlates with increased capsular and vascular invasion (French et al., 2003; Nikiforova et al., 2003).

1.2.3.4 PI3K-Akt-mTOR Pathway

The PI3K-Akt-mTOR pathway also promotes key biological processes including metabolism, growth, proliferation, survival and motility (Osaki et al., 2004). The pathway is tightly regulated by the phosphatase PTEN which dephosphorylates the pathway intermediate PIP3, and prevents downstream signalling (Figure 1.7). A link between the PI3K pathway and thyroid cancer is demonstrated through the increased incidence of goitre and risk of thyroid cancer in patients with Cowden syndrome harbouring germline *PTEN* mutations (Liaw et al., 1997; Nelen et al., 1997). Activation of PI3K signalling has been shown to reduce NIS expression at the transcriptional level and inhibition of PI3K signalling is associated with

increased NIS expression via the upregulation of *PAX8* and post-translational regulation of NIS (Kogai et al., 2008). Inhibition of other components of the PI3K-Akt-mTOR pathway have yielded varied effects on iodide uptake; inhibition of mTOR does not affect radioiodide uptake but inhibition of AKT1/2 increases iodide uptake by decreasing iodide efflux and enhancing iodide affinity to NIS and the rate of iodide transport (Liu et al., 2012).

Phosphatidyl-inositol-3-kinase (PIK3) is an enzyme heterodimer made up of a regulatory p85 and a catalytic p110 subunit and each subunit has multiple variants encoded by different genes. The alpha and beta variants of p110 are expressed ubiquitously while the delta subunit is primarily expressed in cells which function in adaptive immunity. *PIK3CA* encodes the p110α subunit of the PI3K complex. Although *PIK3CA* mutations are not commonly observed in papillary thyroid cancer, they are overrepresented in poorly differentiated and anaplastic thyroid cancers (ATC). Missense mutations in *PIK3CA* were identified in 18 % of anaplastic thyroid cancers and truncating mutations in *PTEN* were identified in 15 % of ATCs (Landa et al., 2016). The same dataset showed *PIK3CA* mutations often co-occur with *BRAF* mutations whereas *PTEN* truncations often co-occur with *NF1* mutations in ATC. Mutations in *PIK3CA* and *PTEN* are rarely seen in papillary thyroid cancers implying a role in progression of papillary carcinoma to less differentiated tumours. This hypothesis is strongly supported by mouse models showing that induction of *PIK3CA* is inadequate for initiating tumour formation, but when co-expressed with the $BRAF^{V600E}$ driver the observations were faster progression and histological features typical of anaplastic tumours compared to $BRAF^{V600E}$ driven tumours alone (Charles et al., 2014). Another mouse model combining $BRAF^{V600E}$ oncogenic driver with loss of one PTEN allele showed 67 % of mice displayed lung metastases compared to just 22 % of $BRAF^{V600E}$ only mice (Shimamura et al., 2018). This supports the activation of the PI3K-

Akt pathway as key to further dedifferentiation and tumour progression. However, as BRAF activation and PTEN haploinsufficiency are rarely observed in human thyroid cancers this limits the physiological relevance of the second model. These mouse models also provide opportunities to investigate drug combinations. For example, melanoma mouse models currently indicate activation of the PI3K pathway promotes resistance to RAF inhibitors suggesting dual inhibition of MAPK and PI3K pathways may be a promising combination in radioiodide refractory or anaplastic thyroid cancer. Despite this combination showing promising synergistic results in mice (ElMokh et al., 2017), a human trial on patients with advanced solid-tumours using MEK inhibitor pimasertib and pan-PI3K inhibitor voxtalisib reported significant toxicities resulting in many cases of dose de-escalation or treatment discontinuation (Schram et al., 2018). Other early-phase trials have also reported toxicities and limited efficacy of dual pathway inhibition compared to single- agent treatments (Bardia et al., 2020; Ramanathan et al., 2020; Shapiro et al., 2020). Further trials into combined MAPK and PI3K inhibition remain ongoing.

1.2.3.5 RET Fusions and RET/PTC Rearrangements

The first genetic mutation associated with thyroid cancer was the *RET*/PTC rearrangement (REarranged during Transfection/Papillary Thyroid Carcinomas) (Nikiforov, 2002). This chromosomal inversion results in coupling RET tyrosine kinase to the 5' portion of different genes, and at least thirteen different fusions have been reported (Nikiforov, 2002; Santoro and Carlomagno, 2013). The rearrangement activates the RET tyrosine kinase in the absence of its normal ligand, the glial cell-derived neurotrophic factor (Pierotti et al., 1992). Receptor tyrosine kinases signal internally through PI3K and MAPK pathways to stimulate cell proliferation. Aberrant activation of *RET* results in higher MAPK output and PI3K-Akt-mTOR

signalling and a similar phenotype to tumours driven by $BRAF^{V600E}$ and *PI3KCA* mutations. PCCL3 cells transfected with RET/PTC have lower *TG*, *TPO* and *TSHR* mRNA, and decreased iodide uptake (Santoro et al., 1993). In tumours driven by a *RET*/PTC rearrangement both Tg and NIS expression in the presence of TSH were decreased, which can be reversed by introduction of a MEK inhibitor to block downstream components of this pathway (Knauf et al., 2003). *In vitro* experiments demonstrated doxycycline-induced expression of *RET*/PTC oncogenes act as a weak tumour initiating event that disrupts normal TSH signalling (Wang et al., 2003). Germline missense mutations in the *RET* gene, the majority being M918T or A883F, are a known cause of Multiple Endocrine Neoplasia Type 2, the group of diseases to which familial medullary thyroid cancer belongs (de Groot et al., 2006). The RET^{M918T} mutation is found in half of sporadic MTC cases (Santoro and Carlomagno, 2013).

1.2.3.6 TERT Promoter Mutations

Reactivation of the telomerase reverse transcription (TERT) enzyme is observed in 90 % of aggressive human cancers (Yuan et al., 2019). The TERT complex uses an RNA template to add six base repeats making up a telomere onto the overhanging 3' end of chromosomal DNA, thus increasing the number of divisions a cell may undergo before replication of the DNA causes loss of coding regions and genomic instability. Mutations in the *TERT* promoter (*TERTp*) region may drive expression of TERT by acting as *de novo* response elements for the ETS family of transcription factors (Bell et al., 2015). The ETS family of transcription factors are a downstream target of the MAPK pathway, and *TERT*p mutations are commonly found in conjunction with MAPK pathway activating mutations in *BRAF* or *RAS*. In gastric cancer, mutations in the proximal promoter region binding sites of transcriptional repressors such as EBF1 may prohibit binding and result in de-repression of TERT and reactivation of expression

(Xing et al., 2020). Mouse models used to study global overexpression of wild-type TERT exhibit tumour formation (Artandi et al., 2002). Despite these models exhibiting lengthened telomeres, the extent to which the oncogenic properties of TERT reactivation stem from telomere maintenance rather than an alternative function of inducing telomerase enzyme activity are still disputed. This is partly because TERT transgenic mice develop neoplasia in mammary tissues where telomeres are not expected to be short enough to induce senescence and thus benefit from telomere elongation (Artandi et al., 2002).

*TERT*p mutations are usually found to be in low frequency and sub-clonal in papillary thyroid cancer- where there is heterogeneous distribution of these mutations throughout some of the tumour cells. However, these mutations are found in a much higher frequency in poorly differentiated thyroid cancers and in anaplastic tumours. In less-differentiated tumours the *TERT*p mutation is found to be clonal i.e., present in all cells of the tumour (Landa et al., 2016). The frequency of *TERT*p mutations also increases with disease stage and frequency: 9 % of papillary thyroid carcinoma, 40 % of poorly differentiated thyroid cancer and 73 % of anaplastic thyroid cancers (Landa et al., 2016). In this study, *TERT* mutation was a strong predictor of development of distant metastases and mortality, with an average survival of 147 days versus 732 days in ATC patients without *TERT*p mutation. *TERT*p mutations frequently co-occur in with TERT copy number alternations in later stage tumours which further amplifies TERT expression (McKelvey et al., 2020). The preference for cells harbouring *TERT*p mutations and copy number variations as cells dedifferentiate indicates reactivation of TERT-mediated limitless replicative potential and avoidance of senescence is key to maintaining the growth and survival of highly aggressive tumours.

Multiple studies indicate that the acquisition of a *TERT*p mutation in a $BRAF^{V600E}$-driven tumour confers an increased risk of recurrence and aggressive tumour characteristics. A retrospective review of 25 well differentiated, locally-advanced thyroid tumours identified twelve samples with co-occurring *TERT* promoter and *BRAF* mutations of which eight patients experienced recurrent disease, with a data-derived recurrence rate of 58.3 % versus 47.4 % ($BRAF^{V600E}$ only) or 50 % (*TERTp* mutation only) (Mady et al., 2020). In addition, four out of the five patients in this cohort who harboured both $BRAF^{V600E}$ and *TERT*p mutation developed distant metastases. This study supported previous findings that patients with PTC who displayed co-existing $BRAF^{V600E}$ and *TERT*p mutations had dismal disease free survival and elevated risk of recurrence compared to patients with either mutation alone (Xing et al., 2014). This indicates that TERT reactivation on a $BRAF^{V600E}$ background could be considered as a discrete genetic profile associated with worse outcomes and may be used prognostically when deciding how aggressively to treat such tumours. The high prevalence of *TERT*p mutations in advanced cancers such as ATC suggests that initial mutations in pathways governing cell proliferation - such as $BRAF^{V600E}$ or *RAS* mutations - are sufficient in initiating tumourigenesis and sustaining early-stage tumour growth, but require additional mutations, such as TERT reactivation, to transform to more aggressive malignant states.

1.2.3.7 Additional Oncogenes Associated with Thyroid Cancer

Thyroid cancers with substantial loss of thyroid specific gene expression, such as *SLC5A5*, are considered more aggressive and difficult to treat with radioiodide. Therefore, changes in gene expression that indirectly affect function of NIS also contribute to the pathogenesis of thyroid cancer. Pituitary-tumor-transforming-gene Binding Factor (PBF) was identified as the first functional interactor of NIS and mediates its internalisation into intracellular vesicles (Smith

et al., 2009). Both PBF and its partner pituitary-tumor-transforming-gene (PTTG) are oncogenic in thyroid cells and have been shown to inhibit iodide uptake *in vitro* (Boelaert et al., 2007; Kim et al., 2006; Stratford et al., 2005). Consequently, patients with elevated *PBF* expression display more aggressive tumour characteristics including higher recurrence, DNA damage and a correlation with positive $BRAF^{V600E}$ mutation status (Read et al., 2017; Stratford et al., 2005). Two other functional interactors of NIS, ARF4 and VCP, as well as the implications for thyroid cancer aggressiveness and the response to treatment will be discussed in Section 1.3.6.

Both the PI3K-Akt-mTOR pathway and the MAPK pathway may be stimulated by TSH (Pomerance et al., 2000; Suh et al., 2003). As such, hormones which stimulate TSH secretion from the pituitary have also been implicated as pro-tumourigenic. This includes human chorionic gonadotrophin produced during pregnancy and TRH in the post-partum period which may account for the strong female bias in thyroid cancer development (Amino et al., 1981; Rahbari et al., 2010; Yoshimura and Hershman, 1995). In addition, TSH and chorionic gonadotrophin share 40 % sequence homology of protein primary structure and can cross-react with the opposite receptor (Kraiem et al., 1994).

1.2.4 **Diagnosis and Treatment of Thyroid Cancer**

Patients who present with suspected thyroid cancer will undergo a fine needle aspiration (FNA) biopsy to confirm diagnosis by histopathology. Blood tests to measure TSH, T3 and T4 levels can be used to indicate a diagnosis of hypo or hyperthyroidism but cannot conclusively diagnose a carcinoma. If the FNA biopsy also proves to be suspicious of cancer, a hemithyroidectomy is generally performed for histological confirmation. A

hemithyroidectomy involves removal of either the right or left thyroid lobe under general anaesthetic and the specimen is examined to confirm or exclude thyroid cancer.

1.2.4.1 Surgical Resection and Radioiodide Ablation Therapy

Upon the diagnosis of thyroid cancer, a complete thyroidectomy is performed to remove the remaining thyroid lobe and carcinoma. Diagnosed individuals who undergo a thyroidectomy are required to take lifelong T4 supplements to maintain systemic thyroid hormone action.

The birth of nuclear medicine began in the 1940s with animal studies and small case-studies describing use of I^{128} and I^{130} to study iodide uptake in the thyroid and to treat thyroid disorders (Keston et al., 1942; Sawin and Becker, 1997). In 1946, two seminal papers were published reporting the use of iodide radioisotopes to treat Grave's disease-associated hyperthyroidism (Chapman and Evans, 1946; Hertz and Roberts, 1946). In the following years, the use of a cyclotron to generate a more stable I^{131} isotope expanded use of this novel therapy to patients with thyroid carcinomas (Seidlin et al., 1948). Currently, the British Thyroid Association guidelines recommend post-operative treatment with I^{131} for patients with tumour >4 cm, with presence of gross extrathyroidal invasion and/or distant metastasis. Injections of recombinant human TSH are administered in the 48 hours prior to radioactive iodine to increase uptake. Radioiodide uptake usually induces ablation of residual thyroid cancer cells and micro-metastatic disease.

1.2.4.2 Radioiodide-Refractory Thyroid Cancer

Up to 15 % of DTC patients and 50 % of metastatic DTC patients are refractory to radioiodide therapy, a complication of thyroid cancer that is associated with poorer outcomes (Sciuto et al., 2009; Worden, 2014; Xing et al., 2013). Using conventional FDG-PET/CT imaging, radioactive iodide uptake can be verified (Figure 1.8). Patients display darker regions where there is overt iodide uptake. In patients without cancer this would typically be seen in the stomach, bladder, salivary gland, and thyroid. Uptake in the thyroid suggests patients are more likely to respond to radioiodide treatment. This imaging modality may also be used to identify local and distant metastases, as demonstrated by red arrows in (Figure 1.8, panel A). Typically, if a patient does not respond to radioiodide therapy, there is no obvious uptake in the lower neck region corresponding to thyroidal uptake (Figure 1.8, panel B). Patients with radioiodide refractory thyroid cancer are considered to have more aggressive disease due to the dedifferentiation of the carcinoma resulting in lack of NIS expression and therefore NIS-mediated iodide uptake.

1.2.4.3 Approved Treatments for Radioiodide Refractory Thyroid Cancer

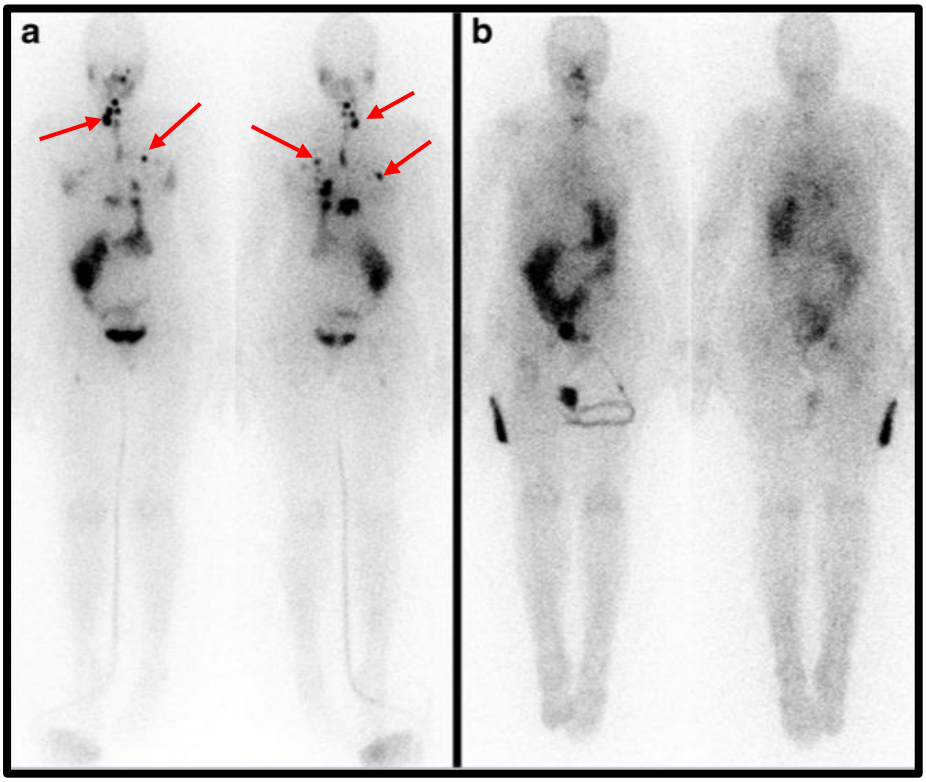


Figure 1.8 ***Anterior and posterior radiological imaging of a female patient with metastatic papillary thyroid cancer using a I^{123} tracer to assess radioiodide avidity of the tumours****. Red arrows in Panel A show examples of radioiodide-avid lesions in the neck and lung area and residual thyroid tissue which were subsequently treated with radioiodide. After disease progression, the same patient in panel B did not display uptake of I^{123} tracer in keeping with radioiodide-refractory disease. Adapted from (Lengana et al., 2019).*

Multiple anti-cancer drugs have undergone, and are currently undergoing, randomised controlled trials to assess their efficacy in a radioiodide refractory thyroid cancer setting. Patients who experience progressive disease after the trifecta of surgical resection, radioiodide therapy and TSH suppression therapy may be offered tyrosine kinases as further treatment. In 2018, the UK's National Institute for Health and Clinical Excellence (NICE) approved the multikinase inhibitors lenvatinib and sorafenib for treating progressive, locally advanced, or metastatic DTC. These decisions were based on data from the SELECT and DECISION trials, respectively (Brose et al., 2014; Schlumberger et al., 2015). These drugs

remain the only post-radioactive iodide treatment options for patients with differentiated thyroid cancer. Lenvatinib inhibits ligand binding to the receptors VEGFR1, 2 and 3, FGF1, 2,3 and 4 and PDGFR alpha receptors for vascular endothelial growth factor (VEGF), fibroblast growth factor (FGF) and platelet-derived growth factor (PDGFR) (Matsui et al., 2008). Sorafenib is also active against the VEGF and PDGFR receptors and also RET and RAF kinases (Wilhelm et al., 2008).

Other treatment strategies are currently under evaluation in randomised controlled trials including targeting PPARγ with bexarotene (NCT00718770) and the PDL-1 receptor with monoclonal antibody therapy pembrolizumab (NCT02688608), but these studies have not yet reported clinical findings. Combinations of multikinase inhibitors that simultaneously target multiple components of the MAPK pathway are described in more detail in section 1.2.4.4.

There are no approved treatment options specifically for anaplastic thyroid cancer in the UK and patients are offered radiotherapy and/or chemotherapy. Vandetanib and cabozantinib are both approved treatments for medullary thyroid cancer and offered to patients on the NHS through NICE technology appraisals 463 and 550, respectively. The outcome of medullary thyroid cancer is not affected by radioiodide treatment as this carcinoma arises from parafollicular cells which neither uptake iodide nor synthesise thyroid hormone.

1.2.4.4 Targeting the MAPK Pathway in Thyroid Cancer

As a result of the prominent role $BRAF^{V600E}$ and *RAS* mutations play in thyroid cancers, inhibition of the MAPK pathway has been an attractive therapeutic target for many years. A doxycycline inducible $BRAF^{V600E}$ mouse model generated by Chakravarty *et al* demonstrated induction of the oncogene resulted in high grade papillary thyroid tumours with features of poorly differentiated cancer (Chakravarty et al., 2011). In this model, both withdrawal of the $BRAF^{V600E}$ induction and inhibition of the protein with small molecular MAPK inhibitors was enough to restore NIS expression on the basolateral membrane of the mouse thyroids (Figure 1.9), and to make the mice susceptible to I^{131} induced DNA damage.

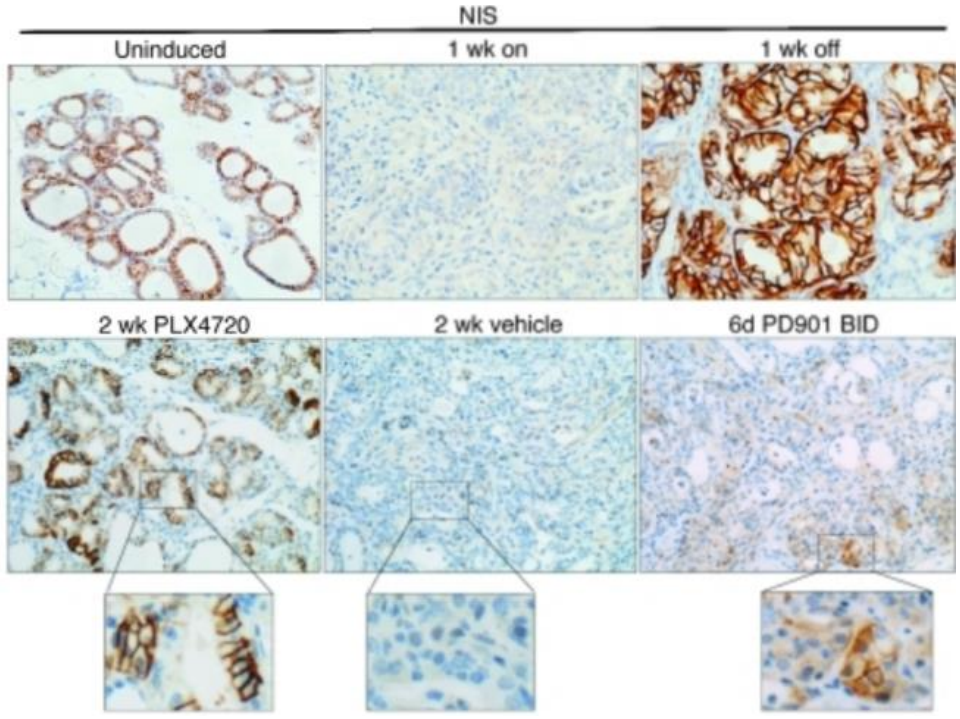


Figure 1.9 ***Treatment with MAPK inhibitors may restore NIS expression at the plasma membrane.*** *Top panel shows restoration of NIS protein (brown) at the plasma membrane of thyroid tissue extracted from dox-inducible $BRAF^{V600E}$ transgenic mice, after doxycycline withdrawal. The lower panel shows similar effect of NIS staining at plasma membrane after treatment with small MAPK inhibitors PLX4720 and PD901. Adapted from Chakravarty et al, 2011.*

These experiments provided preclinical evidence that inhibition of the MAPK pathway may restore radioiodide avidity in humans and paved the way for a randomised clinical trial using the MEK1/2 inhibitor selumetinib on patients with metastatic thyroid cancer NCT00970359). This trial resulted in only four out of nine patients with $BRAF^{V600E}$ driven cancer displaying an increase in iodide uptake whereas all five patients with *NRAS* mutations showed increased I^{131} avidity (Ho et al., 2013). While this contrasted with the murine data, it was proposed that MAPK activation by $BRAF^{V600E}$ was so strong that selumetinib was unable to inhibit the pathway, as compared to *NRAS*-mutant tumours. Additionally, treatment of thyroid carcinomas with MAPK inhibitors was shown to promote activating mutations in other tyrosine kinases, including the human epidermal growth factor receptor 3 (HER3) which signal via PI3K-Akt-mTOR signalling (Montero-Conde et al., 2013). In this mechanism, HER3 activation relieves the MAPK signal blockade and drives resistance to MAPK inhibitors. Further trials with other MAPK inhibitors demonstrated a restoration of iodide uptake at similar rates of success for $BRAF^{V600E}$ driven tumours. Treatment with dabrafenib restored avidity in six out of ten patients (Rothenberg et al., 2015) (NCT01534897). A larger scale study of 51 patients with $BRAF^{V600E}$ -driven PTC showed the specific $BRAF^{V600E}$ inhibitor vemurafenib induced a partial response in 38.5 % of patients who had not received prior treatment with a VEGFR inhibitor (Brose et al., 2016) (NCT01286753). In 2015, seven patients with $BRAF^{V600E}$ anaplastic thyroid cancer were treated with vemurafenib. Of this small cohort, one patient achieved a complete response, another displayed partial response, but four patients developed progressive disease, while data on the final patient were missing (Hyman et al., 2015) (NCT01524978). In the same trial, patients with $BRAF^{V600E}$ mutant cutaneous melanoma responded more positively to vemurafenib, again showing that a common oncogenic driver does not equate to drug response in different cancers.

To enhance the response to MAPK inhibitors and reduce drug resistance which may evolve, a double-agent treatment with the BRAF inhibitor dabrafenib and the MEK1/2 inhibitor trametinib was developed, and demonstrated a robust response in a 2017 trial on sixteen patients with anaplastic thyroid cancer (Subbiah et al., 2018). In 2018, this treatment strategy received approval from the United States Food and Drug Administration (FDA), which marked the first authorisation for MAPK inhibitors in any thyroid cancer setting (NCT02034110). This drug combination is not currently approved by the UK's Medicine and Healthcare Regulatory Agency (MHRA), and therefore is not offered to NHS patients.

Although the last decade has shown significant progress in targeting the molecular pathways of thyroid cancer, and in some cases improving tumoural iodide uptake, it is clear that the complexities of this disease are not yet fully understood. Further investigations into the key requirements for iodide uptake in thyroid tumours and the effect of combinatorial drug approaches on tumour growth will likely underpin future treatment of thyroid cancer.

1.3 The Sodium/Iodide Symporter

1.3.1 **NIS Function**

The sodium-iodide symporter (NIS) is encoded by the *SLC5A5* gene located on the short arm of chromosome 19. The cDNA of the gene was first cloned in 1996 allowing further characterisation of the protein (Dai et al., 1996). NIS is a 618 amino acid membrane protein with 13 transmembrane helices and multiple asparagine residues which undergo N-linked glycosylation (Figure 1.10). The N-terminus of NIS is extracellular and the COOH terminus is cytosolic (Levy et al., 1998). NIS mediates active iodide transport in the thyroid and in some

non-thyroidal tissues including the stomach and salivary glands. In the latter two tissues, the function of the iodide transporter is not fully known but is thought to move iodide from the blood into the gastrointestinal tract to be reabsorbed in the small intestine for iodide-conserving purposes (Nicola et al., 2009).

In addition to transporting iodide, NIS actively transports perchlorate and perrhenate ions (ClO_4^- and ReO_4^-) and other monovalent anions. The ClO_4^- anion is typically used as a competitive inhibitor for iodide ions in *in vitro* radioiodide uptake experiments to control for non-NIS mediated iodide uptake, for example through non-specific halide channels. NIS transports different ions in different stoichiometries. Na^+ and I^- are transported in a 2:1 stoichiometry and Na^+ and ClO_4^- are transported in a 1:1 stoichiometry (Dohan et al., 2007; Eskandari et al., 1997). Binding of the Na^+ and I^- ions are sequential, with the cation binding first to induce a small conformational change that facilitates anion binding (Eskandari et al., 1997).

The first reported mutation in *SLC5A5* resulting in defective iodide transport was T354P which was identified in eight Japanese patients presenting with a variety of symptoms including low iodide uptake in absence of iodide excess, diffuse goitre and apparent or latent hypothyroidism (Matsuda and Kosugi, 1997). Initially, a mutation at G93R was identified as a compound heterozygous germline mutation (G93R/T354P) in a 22-year-old male patient presenting with goitrous hypothyroidism and an iodide-transport defect. G93R and G543E mutations result in minimal iodide transport while the G93E/Q mutant transport Na^+ and perchlorate in a 2:1 stoichiometry as opposed to its' normal electroneutral transport (Kosugi et al., 1998; Paroder-Belenitsky et al., 2011). Further analysis of the G93 residue suggested it

has a role in coordinating the conformational change between the outwardly facing and inwardly facing open cavity and the $K_m(I^-)$ of NIS (Paroder-Belenitsky et al., 2011). In addition, a single allele of wild-type NIS is sufficient to maintain iodide uptake and hence these mutations are only pathogenic in patients who display homozygous or compound heterozygous mutant alleles of *SLC5A5.*

It is the iodide importing function of NIS that is exploited by post-adjuvant radioiodide therapy in DTC patients. As mentioned in section 1.2.4, UK patients with thyroid cancer will typically be offered a full thyroidectomy and suspicious lymph node removal followed by post-surgical radioiodide therapy with beta emitting I^{131} to ablate residual malignant cells and micro-metastatic disease. Papillary thyroid cancer cells are morphologically different from normal follicular epithelial cells and can lose their polarised organisation, leading carcinomas to display a spectrum of avidity for radioiodide uptake (Guo et al., 2014; Ma et al., 2014). Despite this, the success of radioiodide therapy relies on both the expression of NIS, and its trafficking to the basolateral membrane, which will be discussed in section 1.3.5.

Feng et al were the first to propose an alternative non-pump function of NIS when they reported a role for cell migration in cells that overexpress hypoglycosylated, cytoplasmic NIS via activation of RhoA GTPase. In this study, overexpression of NIS in thyroid cells resulted in a pro-migratory phenotype which was dependent on RhoA activation by the Rho-guanine nucleotide exchange factor LARG. Additionally, activation of the PI3K-Akt-mTOR signalling was associated with localisation of NIS in the cytoplasm rather than plasma membrane and this was also shown to be dependent on LARG. Data indicated that the effects of NIS localisation were associated with changes in the glycosylation state of NIS- with PTEN

knockdown resulting in decrease glycosylated NIS. NIS is known to be glycosylated at three sites when performing its canonical pump function (Figure 1.10).

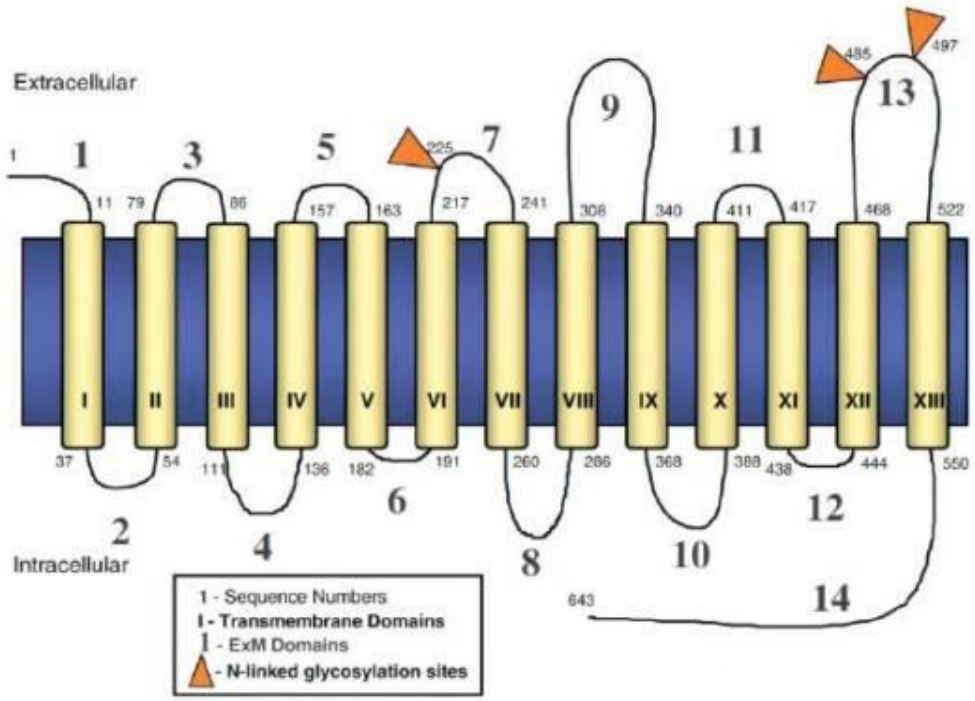


Figure 1.10 ***The structure of the sodium/iodide symporter protein****. 13 transmembrane domains and a C-terminal intracellular tail to which interacting proteins have been shown to bind. N-linked glycosylation sites are situated on the extracellular loops of the protein. Adapted from Hingorani et al 2010.*

Feng *et al* postulated that loss of N-linked glycosylation results in a cytoplasmic NIS-LARG interaction which stabilises the protein and the downstream effects of this interaction include enhanced cell migration (Feng et al., 2018). PTEN knockdown alleviates the negative regulation of the PI3K-Akt-mTOR pathway enabling higher pathway flux, a phenotype also seen in *RAS*-driven thyroid tumours. Thyroid carcinomas more commonly display loss of NIS expression over mislocalisation of NIS to the cytoplasm, however here it was demonstrated that cytoplasmic NIS may generate a pro-tumourigenic cell migratory phenotype in tumours with activated PI3K signalling.

1.3.2 **NIS Structure**

In lieu of a resolved crystal structure of NIS, a 3-D homology model based on the *Vibrio parahaemolyticus* sodium/galactose transporter, vSGLT, has been used as a template to identify key amino acid residues relating to structure and function (Paroder-Belenitsky et al., 2011). Despite having only 27 % sequence homology between NIS and vSGLT, many Na^+ transporter proteins- including both NIS and vSGLT- display the same fold as a way of coordinating Na^+ substrate binding. This shared critical fold is sufficient to provide mechanistic information on NIS and was used to investigate NIS dimerisation (Thompson et al., 2019).

NIS was proposed to dimerise following observation of a high molecular weight band (135 kDa – 180 kDa) on Western blots generated from co-immunoprecipitation experiments. NIS was confirmed to dimerise *in vitro* via the residues Y242, T243 and Q417 (Thompson et al., 2019). Mutation of these residues has a varied effect on the ability of NIS to uptake iodide, and uptake was significantly reduced when two or more of these sites were mutated. The chronology of NIS dimerisation with other post-translational protein modifications such as glycosylation and the functional relevance of dimerisation are not yet understood.

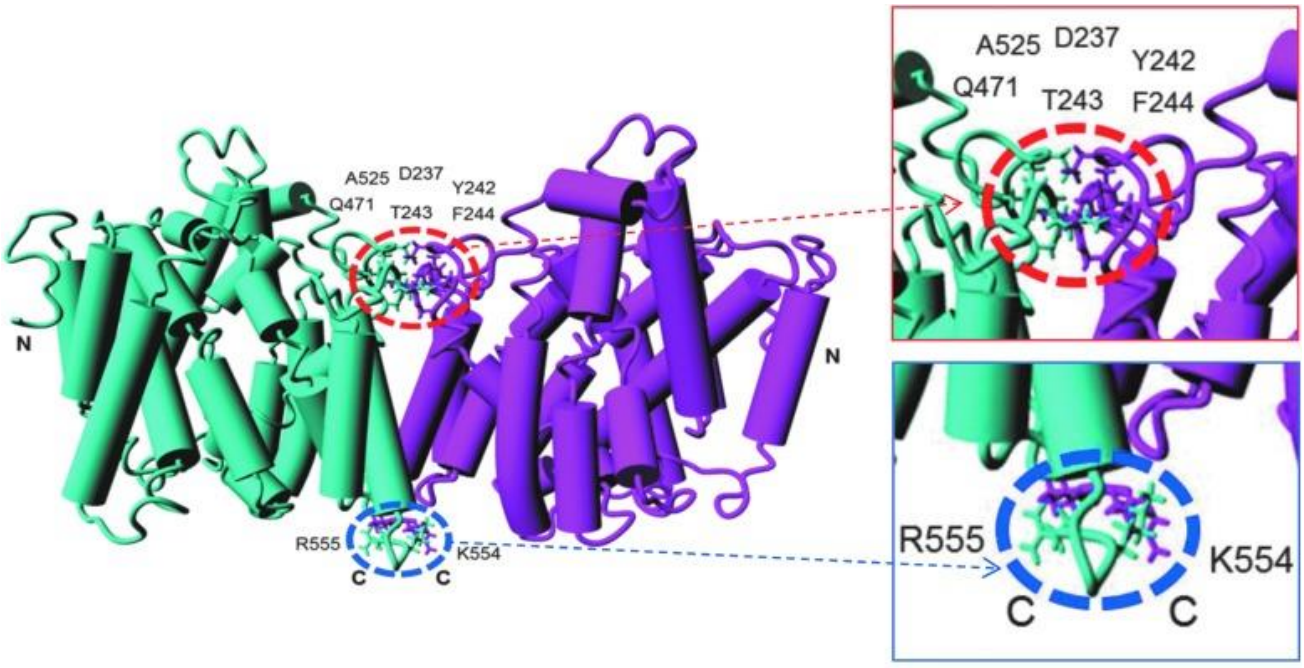


Figure 1.11 ***The proposed structure of dimeric NIS.*** *8 key residues at the interface between two monomers are hypothesised to aid formation of the dimer of which Y242, T243 and Q417 were shown to be critical for dimerisation. Adapted from Thompson et al, 2019.*

NIS has been reported to have four key phosphorylation sites which affect functionality. Phosphorylation at Thr-577 was shown to be important in protein stability, pSer-43 and pSer-581 affected the velocity of iodide transport, and pThr-49 affected the conformation of NIS at the plasma membrane (Vadysirisack et al., 2007a). The kinases and phosphatases that regulate these phosphorylation events have not been identified, nor it is known how phosphorylation at these sites might be aberrantly regulated in cancer or whether this may affect radioiodide uptake.

1.3.3 **Epigenetic Regulation of NIS**

SLC5A5 expression is largely contained to the thyroid, stomach, and salivary gland tissues. However, certain non-thyroidal tumours have been shown to have elevated intracellular NIS protein including breast and prostate cancers as well as some metastases originating from

these primary cancers (Renier et al., 2010; Wapnir et al., 2003). This has led to research into non-canonical, tumour promoting properties of NIS which may function independently of its iodide pump role. It has been proposed that mislocalisation of NIS to the cytoplasm allows interactions with different proteins and results in non-pump functions of NIS as discussed in section 1.3.1 (Feng et al., 2018).

As part of the hypothalamus-pituitary-thyroid axis TSH regulates the expression of NIS on an mRNA and protein level (Figure 1.2). The addition of TSH to media of thyroid cells stimulates an increase in NIS mRNA expression from 3 hours post-addition, peaking at 24 hours and resulting in an accompanied increase in iodide uptake (Kogai et al., 1997). Activated TSH receptors stimulate iodide uptake via cyclic-AMP pathways which modulate PKA (Figure 1.7), although this cannot be recapitulated by exogenously increasing cAMP with the potent adenylyl cyclase activator forskolin, indicating that TSH-induced iodide organification is more complex than just cAMP signalling (Totsuka et al., 1983).

NIS is expressed in lactating breast tissue to accumulate iodide in the milk for thyroid hormone synthesis in newborns. However, NIS expression in breast cancers is TSH-independent (Tazebay et al., 2000). Notably, increased cytoplasmic NIS in breast cancer is associated with higher malignancy in cell lines and poorer patient prognosis (Chekhun et al., 2017; Lukianova et al., 2016). NIS has an oestrogen-response element in its upstream promoter region which is a possible explanation for above-normal levels of NIS expression in oestrogen-driven breast cancer.

Micro-RNAs (miRNAs) are non-coding RNA oligomers which bind to the 3' untranslated region of mRNA and have been shown to both promote degradation and prevent translation of mRNA. Synthesis of micro-RNAs is mediated by the DICER endoribonuclease complex. Mutations in *DICER* underpin DICER1 syndrome, characterised by a higher lifetime risk of endocrine cancers and benign tumours. This substantiates the association between RNA processing and thyroid tumourigenesis and has prompted studies into how miRNAs affect the characteristics of thyroid malignancy. The micro-RNA profile of a cancer cell often diverges from its non-malignant counterpart and up or down regulation of specific miRNAs can lead to dysregulation of *SLC5A5* expression and a reduction in iodide uptake. miR-146b-3p, miR-146b-5p and miR-339-5b have all been demonstrated to bind to NIS mRNA and reduce iodide uptake via impaired translation (Lakshmanan et al., 2015; Riesco-Eizaguirre et al., 2015).

Expression of the *SLC5A5* gene is also known to be suppressed by the MAPK pathway via a two-factor mechanism involving both promoter methylation and histone deacetylation (Choi et al., 2014; Zhang et al., 2014). Inhibition of the MAPK pathway temporarily relieves *SLC5A5* silencing and restores responsiveness to radioiodide in mouse and human studies (Brose et al., 2014; Chakravarty et al., 2011). As mentioned in section 1.2.4.4, efficacy of MEK and BRAF inhibitors are being explored as a therapeutic strategy for RR-DTC.

1.3.4 **Therapeutically Inducing NIS Expression *in vitro* and *in vivo***

The clinical trials of MAPK inhibitors described in section 1.2.4.4 showed restoration of iodide uptake in primary and metastatic lesions in some patients. Globally, further trials have sought to target NIS expression directly to improve radioiodide uptake. Epigenetic silencing of the

SLC5A5 gene is seen ubiquitously across advanced thyroid cancer and histone deacetylation of the *SLC5A5* promoter can be driven by $BRAF^{V600E}$ (Zhang et al., 2014). Histone deacetylase inhibitors (HDACi) have been studied to reintroduce NIS expression in thyroid cells. The HDACi suberoylanilide hydroxamic acid (SAHA), works well *in vitro* to increase expression of *SLC5A5* (McCabe Group, unpublished data (Wächter et al., 2018; Zhang et al., 2014). In 2008, 19 differentiated and medullary thyroid cancer patients with radioiodide refractory disease were treated with SAHA, but this trial did not demonstrate any decrease in tumour growth in response to this treatment (Woyach et al., 2009); NCT00134043). However, this study was not designed to test the avidity of radioiodide after treatment, and only three patients in the cohort had post-treatment radioiodide scans of which one patient displayed increase uptake. Given the strong response of radioiodide uptake after treatment with SAHA *in vitro*, clinical trials specifically testing the response to radioiodide therapy after pre-treatment with SAHA may offer better results in thyroid cancer patients than utilising SAHA to reduce tumour growth.

The specific cause and effect of NIS expression and measurable iodide uptake has been used by the Spitzweg group to induce exogenous NIS expression in non-thyroidal tumours. This system involves delivering the NIS-encoding *SLC5A5* gene to tumour sites in mice via polyplexes or NIS-expressing mesenchymal stem cells (MSCs) (Urnauer et al., 2019) . The polyplex system uses EGFR-targeting peptides on the surface of the complex to deliver the genetic material specifically to tumour cells; NIS-expressing MSCs take advantage of the nature of stem cells to home in on tumour sites and accumulate in the tumour microenvironment, which may be enhanced by external beam radiation therapy or regional hyperthermia (Knoop et al., 2013; Schug et al., 2018; Tutter et al., 2020). Radioiodide can then

be administered and uptake in the tumour region measured using I^{123} scintigraphy. This system may also be used to image tumours and metastatic lesions. This strategy offers the therapeutic potential to enable thyroid-specific iodide uptake to non-thyroidal tumours and expand the use of radioiodide across multiple cancers.

1.3.5 **NIS Trafficking and Dysregulation**

Protein trafficking describes the many processes by which newly synthesised proteins are delivered to the correct membrane or subcellular compartment and recycled back into the cytoplasm for degradation to be turned over. Disruption in protein trafficking can result in protein mislocalisation and disturb normal cellular function. In cancer, protein trafficking is often perturbed and can contribute to malignant characteristics including metastasis and invasion (Tzeng and Wang, 2016; Yarwood et al., 2020).

In vitro and *in vivo* studies have so far sought to increase NIS expression in thyroid cancer cells. However, increases in NIS expression are not consistently accompanied by a rise in NIS-mediated iodide uptake (Vadysirisack et al., 2007b). This implies that post-translational processing of NIS is dysregulated in thyroid cancer such that inducing NIS expression does not correlate with restoration of iodide avidity. Disruption to NIS trafficking has been shown to occur in differentiated thyroid cancer and negatively affects radioiodide uptake (Fletcher et al., 2020).

One of the first studies looking into NIS trafficking between the ER and Golgi network to the plasma membrane identified AP-B1, a subunit of the clathrin adaptor protein γ-adaptin/AP1, as a key determinant of targeted NIS trafficking to the basolateral membrane (Martin et al.,

2019). siRNA knockdown of both subunits of the γ-adaptin/AP1 protein, AP-1A and AP-1B showed severe mis-sorting of NIS to apical membrane in MDCK polarised cell models although NIS retained iodide uptake capability (Koumarianou et al., 2014). Computer simulations have also indicated that AP-1B recognises a conserved mono-leucine based sorting signal in the intracellular C-terminal tail of NIS. In these experiments, truncation of the NIS C-terminus from the region proximal to the thirteenth transmembrane domain, which covers this conserved mono-leucine sorting signal, and resulted in protein that was retained intracellularly in the ER (Martin et al., 2019).

1.3.6 The Sodium-Iodide Symporter Interactome

In a recent investigation into post translational processing and trafficking of NIS, previously unknown proteins interactors of NIS were identified using co-immunoprecipitation and tandem mass spectrometry (Fletcher et al., 2020). A shortlist of proteins was generated by comparing the number of peptides bound to NIS, number of experimental repeats in which these peptides were detected, and described roles of the peptides in post-translational protein processing. ADP-Ribosylation Factor 4 (ARF4) and valosin-containing protein (VCP) were studied from this shortlist and their role in NIS trafficking was further explored (Fletcher *et al* 2020). ARF4 was demonstrated to positively modulate NIS trafficking to the plasma membrane while VCP was shown to mediate degradation of NIS by ER-associated degradation as further discussed in Chapter 3. The original data from the mass spectrometry experiments identified moesin and annexin A1 as putative NIS interactors in the plasma membrane fraction of the cell lysate which is further discussed in Chapter 5 (Fletcher, 2018); Table 1-2).

Entrez Gene ID	Protein	Whole Cell/ Plasma Membrane Fraction	Average Scores	Number of Peptides
NIS_HUMAN	Na^+/I^- Symporter	Both	284.6	32
ARF4_HUMAN	ADP-ribosylation Factor 4	Plasma Membrane Only	121.9	13
VCP_HUMAN	Valosin Containing Protein/p97	Whole Cell Only	161.0	12
MSN_HUMAN	Moesin	Plasma Membrane Only	76.3	3
ANXA1_HUMAN	Annexin A1	Plasma Membrane Only	157.6	7

Table 1-2 ***Mass spectrometry list of NIS and putative interacting proteins including moesin and annexin A1 from MDA-MB-231 cell stably expressing NIS****. VCP and ARF4 were validated as NIS interacting proteins by Fletcher et al 2020. The third column indicates whether a peptide was identified in the membrane fraction of cell lysates, whole cell lysate or both. The fourth column indicates average Mascot score,a predictor of the significance of the predicted peptide binding, the score threshold for validation is >70 and higher scores correlate with lower chance of random binding. The fifth column indicates number of peptides matched to the protein which bound to NIS across three biological experimental repeats.*

1.3.6.1 ARF4

Through multiple *in vitro* assays, a small GTPase ARF4 was shown to bind to NIS and modulate its intracellular movement (Fletcher et al., 2020). This demonstrated the first evidence of direct interactors of NIS since identification of PTTG1-IP Binding Factor (Smith et al., 2012; Smith et al., 2009) . Some differentiated thyroid cancers display downregulation of ARF4, a phenotype that corresponds to a reduction in iodide uptake *in vitro*. In addition, vesicles on which NIS was observed to colocalise with ARF4 moved faster than vesicles containing NIS but not ARF4 (Fletcher et al., 2020). These data indicate that ARF4 is a positive regulator of NIS trafficking to the plasma membrane. However, there are currently no pharmacological agents to enhance this interaction to improve trafficking of NIS to the plasma membrane. As with binding clathrin adaptor proteins, the c-terminal tail of NIS was shown to be important again in binding ARF4 via a conserved four-nucleotide VAPK motif (Fletcher et al., 2020). This

demonstrates that the C-terminal tail of NIS contains amino acids binding sites for multiple protein interactors which facilitate the movement of NIS around the cell.

1.3.6.2 VCP

1.3.6.2.1 VCP Structure and Function

In the aforementioned study on novel NIS interacting proteins, VCP was also demonstrated to bind to NIS and mediates is degradation (Fletcher et al., 2020). Valosin containing protein (VCP), also known as p97, is a multimeric protein complex that functions in multiple cell systems including protein turnover, autophagy, and DNA damage repair (Bodnar and Rapoport, 2017a; Ju et al., 2009; Wang et al., 2004). This investigation specifically focusses on the role of VCP in endoplasmic reticulum-associated protein degradation (ERAD), a quality control process that removes aberrantly folded proteins from the secretory system and diverts them towards proteasomal degradation.

Monomers of VCP are made up of an N domain, D1 and D2 ATPase domains and a flexible C-terminal tail (Figure 1.12A). Six monomers are arranged to form a central pore through which proteins are translocated and unfolded from the tertiary protein structure (Figure 1.12B). ATP hydrolysis at the D1 domain regulates cofactor binding and oligomerisation, while the D2 domain contributes most of the ATP hydrolysis to drive enzyme activity (Chia et al., 2012; Song et al., 2003). Other proteins, such as Ufd1 and Npl4, act as cofactors to facilitate VCP function. Cofactors typically bind to the N domain of VCP, and a 20 amino acid conserved VCP-interacting motif has been identified in known cofactors gp78, SVIP and ANKZF1 (Hänzelmann and Schindelin, 2011). Cofactors are thought to share common binding regions on the N-

terminus and in the linker between N and D1 domains of VCP monomers, possibly to preclude binding of multiple cofactors with competing functions and instead favour sequential binding to regulate the sequence of events required for VCP to facilitate protein degradation. The Ufd1/Npl4 cofactor has been shown as essential for eukaryotic viability; yeast models harbouring transgenic temperature sensitive *Ufd1* alleles exhibited genome instability upon thermally induced breakdown of UFD1 protein (Nie et al., 2012).

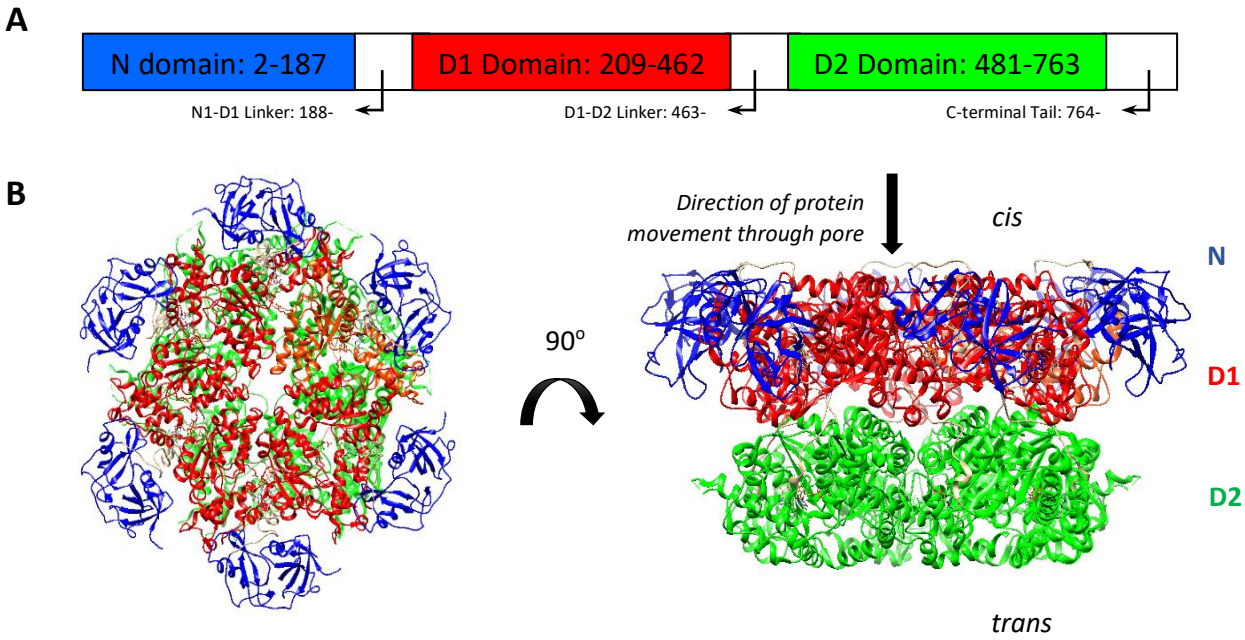


Figure 1.12 ***2-D and 3-D structure of valosin-containing protein (VCP).*** *(**A**) The structure of the VCP protein, made up of 806 amino acids. VCP is split into three domains: N,D1 and D2 separated by short linker regions. (**B**) 2.3Å resolution Cryo-EM structure of VCP from Banerjee et al 2016. This structure was downloaded from the protein data bank entry 5FTK and the N, D1, D2 domains were colour coded using UCSF Chimera program; N domains sit planar to D1 ATPase domain when D1 is bound to ADP. D2 domain sits beneath D1 domain. Proteins move through the central pore of the VCP complex from the* cis *to* trans *side.*

3-D electron microscopy structures of VCP in complex with Ufd1/Npl4 (UN) cofactors indicated that the UN heterodimer binds to the N domain directly on top of the D1 domain when there is no bound adenosine nucleotide. Upon nucleotide binding, the range of

positioning of the N domain and UN cofactor becomes highly dynamic and the N domains move from being planar with the D1 domains to an upwards conformation (Bebeacua et al., 2012). This study provides mechanistic information about the interaction between VCP and its cofactor the UN complex, and suggested that the role of the cofactors is to aid recruitment of substrates to VCP for ERAD, which then interact directly with VCP for unfolding.

Proteostasis is essential in balancing a cell's protein load with its capacity for correct protein folding by the endoplasmic reticulum (ER). After translation, plasma membrane bound proteins are translocated to the ER to undergo chaperone-mediated folding and N-linked glycosylation. Misfolded proteins may be either extracted from the ER and diverted towards the ERAD pathway or remain in the ER for correct refolding.

During ERAD, the N-glycan branches of misfolded proteins are trimmed to leave an α-1,6-linked mannose residue which is recognised by the carbohydrate binding protein lectin (Ferris et al., 2014). Now tagged as a misfolded protein, the polypeptide inserts into an ER membrane pore protein, first identified in yeast as the Hrd1 RING finger ligase and subsequently in humans as gp78 (Carvalho et al., 2010; Gardner et al., 2000; Wu and Rapoport, 2018). The polypeptide is exported from the ER lumen to the cytosol where ubiquitin groups are added by ubiquitin ligases. Ubiquitination prevents translocated proteins returning to the ER and enables cofactors of VCP, the Ufd1/Npl4 complex, to recognise the protein as an ERAD substrate. On the *cis* side of VCP, the peptide chain remains attached to the UN cofactor and this is trimmed by the deubiquitinating enzyme Otu1 (Kim et al., 2014). Some ubiquitin moieties may remain attached and move through the VCP pore, during which they are likely to unfold and refold on the *trans* side, suggesting that the central pore can accommodate at least two polypeptides at once (Wu and Rapoport, 2018). The ATP hydrolysis cycle by the D1

domain regulates cofactor positioning via conformational changes and may also facilitate oligomerisation into a functional VCP hexamer. ATP hydrolysis by the D2 domain exerts a ratcheting mechanical force required to move the polypeptide through the central pore from the *cis* to the *trans* side, simultaneously unfolding the protein (Blythe et al., 2017; Bodnar and Rapoport, 2017b). Whether the protein can be directly degraded by the proteasome or requires shuttling factors to move between VCP and the proteasome is not understood, but after the peptide is released from VCP it becomes degraded by the 26S proteasome (Figure 1.13).

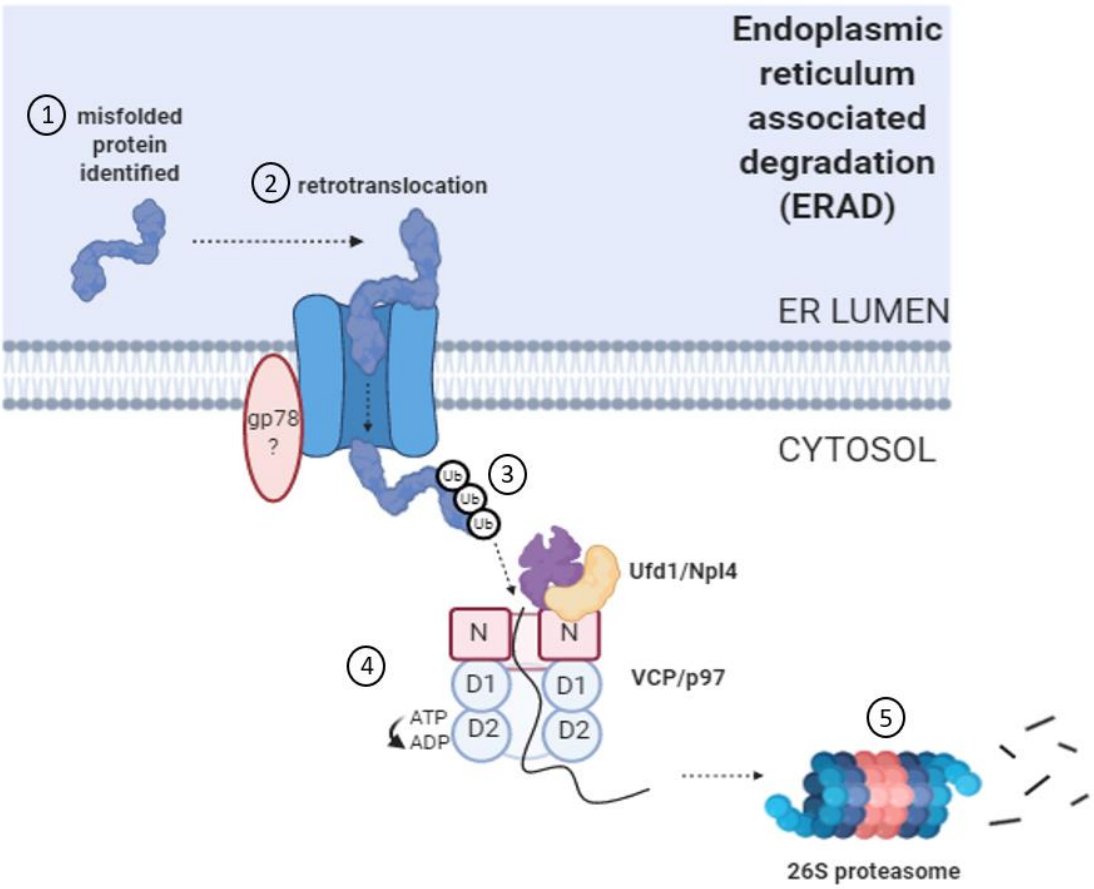
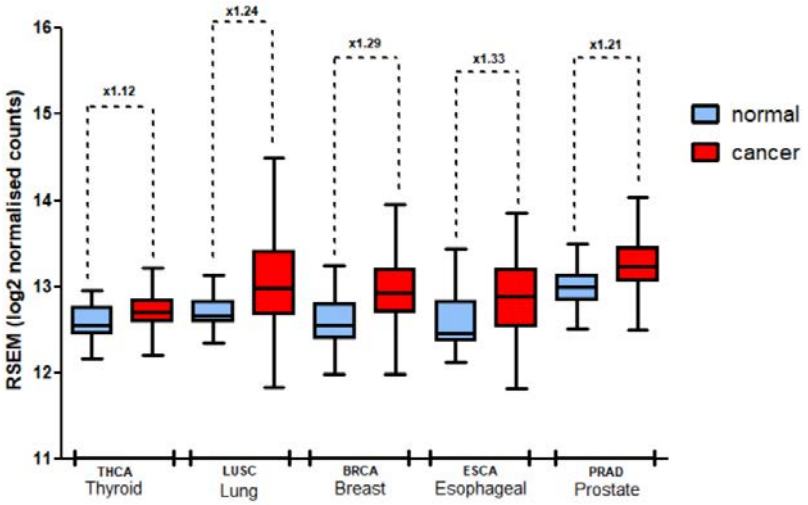


Figure 1.13 ***The process of endoplasmic reticulum associated degradation*** *begins with (**1**) identification of misfolded proteins in the ER which (**2**) exit the ER through a trans-membrane pore protein, (gp78 has been proposed to function as the channel for retro-translocation based on homology to yeast pore protein Hrd1). After exit from the ER, (**3**) ubiquitin groups are added to the misfolded protein and (**4**) the protein is fed through the VCP/P97-UN channel where the secondary structures are unfolded. The ubiquitin groups are removed on the trans side by ubiquitin ligases and (**5**) the protein is degraded by the 26S proteasome.*

1.3.6.2.2 VCP in Human Cancers

Although protein synthesis and degradation pathways are not inherently oncogenic, high levels of cell turnover in cancers cause dependencies on these pathways to sustain tumour growth. Consequently, tumour growth can be vulnerable to disruptions in these pathways and targeting this dependency has been explored through the use of proteasomal inhibitors as anti-cancer agents (Goy et al., 2005; Richardson et al., 2003). Bortezomib has been approved by the MHRA for use in multiple myeloma and mantle cell lymphoma but trials have shown a lack of therapeutic effect in solid tumours (Huang et al., 2014). Tumour reliance on protein homeostasis pathways is evidenced through the dysregulation of key proteins such as ubiquitin ligases and the proteasome (Chen et al., 2017; Qi and Ronai, 2015). Analysis of multiple human cancers shows a moderate upregulation of VCP gene expression (Figure 1.14A). In patients with thyroid cancer, VCP overexpression was associated with poorer survival, and this decrease in survival based on VCP overexpression was significantly more pronounced in patients who received I^{131} treatment (Figure 1.14B).

A



B

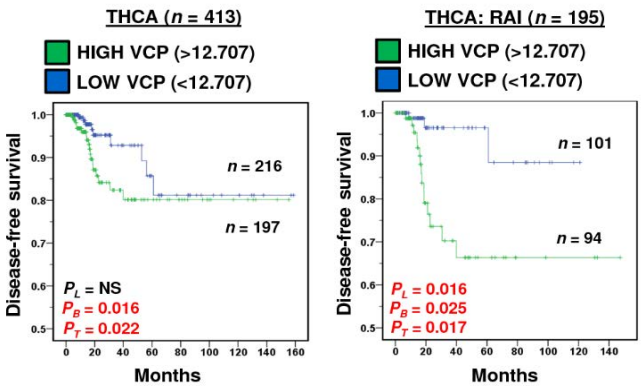


Figure 1.14 ***Analysis of VCP expression in human cancers*** *(**A**) The VCP gene is overexpressed in multiple human cancers compared to matched normal controls, fold change in VCP expression in above plots. Cancer vs Normal n values: THCA Thyroid Carcinoma, 509 vs 59; LUSC lung squamous cell carcinoma, 501 vs 51; BRCA Breast invasive carcinoma, 1100 vs 112; ESCA esophagael carcinoma 185 vs 11; PRAD prostate adenocarcinoma, 498 vs 52. (**B**) VCP overexpression is associated with significant decrease in disease-free survival across papillary thyroid cancer dataset THCA; this is more pronounced in patients who received I^{131} treatment for thyroid cancer. High and low VCP expression defined as upper and lower quartile of mRNA expression, respectively. Adapted from Fletcher et al 2020.*

Fletcher *et al* demonstrated that VCP directly interacts with the sodium/iodide symporter (NIS) by mass spectrometry, co-immunoprecipitation, and proximity ligation assays, and that the overexpression of VCP reduced the proportion of NIS at the plasma membrane of cells.

The authors proposed that VCP mediates degradation of NIS through ERAD, resulting in decreased iodide uptake. These data presented a mechanistic link between the decreased survival in patients who received radioiodide treatment and patients who had concomitant upregulation of VCP expression displayed in Figure 1.14B. Radioiodide avidity of cells was increased *in vitro* through silencing of VCP by siRNA and by pharmacologically inhibiting VCP function (Fletcher et al., 2020). Based on these data, this investigation builds on the hypothesis that increases in radioiodide uptake in thyroid cancer cells may be achieved by treatment with VCP inhibitors.

Fletcher *et al* utilised the E375Q E575Q (QQ) ATPase-deficient mutant of VCP to demonstrate that the NIS interacts with VCP independently of the VCP ATPase capacity (Rumpf et al., 2011). In contradiction of this, clotrimazole and CB-5083 were described to directly inhibit the ATPase function of VCP *in vitro* (Anderson et al., 2015; Fletcher et al., 2020; Segura-Cabrera et al., 2017). It therefore remains unclear whether the interaction between NIS and VCP is part of the canonical ERAD function of VCP, which is reliant upon on ATP hydrolysis, or whether NIS interacts with VCP via other pathways, such as autophagy, regardless of ATPase capacity. The use of VCP inhibition as a therapeutic strategy for restoring radioiodide avidity in thyroid cancer cells will be discussed in depth in Chapters 3 and 4.

1.3.6.3 Moesin

1.3.6.3.1 Moesin Structure and Function

Moesin is a 68 kDa member of the ezrin-moesin-radixin (ERM) family of membrane-interacting proteins encoded by the *MSN* gene. ERM proteins contain a conserved amino-terminal FERM domain which interacts with integral plasma membrane proteins, an extended alpha helical domain and a c-terminal domain that interacts with F-actin (Figure 1.15A). The helical domain acts as a hinge to allow the c-terminus and FERM domain to interact in the inactive state. Moesin is activated by phosphorylation of Tyr-558 which temporarily stabilises the open, active conformation of the protein (Huang et al., 1999; Nakamura et al., 1996). This post-translational modification is dependent on rho-associated kinase (Hébert et al., 2008; Oshiro et al., 1998). Once activated, moesin binds to actin via its FERM domain and thereby links the cytoskeleton with integral plasma membrane proteins. Moesin and closely related family proteins ezrin and radixin were observed to bind CD44 and CD43 membrane proteins via positively charged amino acids clustered in the juxta-membrane region of these proteins-defined by the thirty amino acids in the cytoplasmic C-terminus immediately beneath the final transmembrane domain (Yonemura et al., 1998). Site-directed mutagenesis of the tri-basic motifs present in these proteins markedly reduced moesin binding by GST-pull-down assay (Brown et al., 2006). ERM proteins have also been demonstrated to interact with glycoproteins in leukocytes and the adhesion regulator L-selectin. Mutation of either R357 or K362 codons in the juxta-membrane region of L-selectin results in decreased moesin binding (Ivetic and Ridley, 2004).

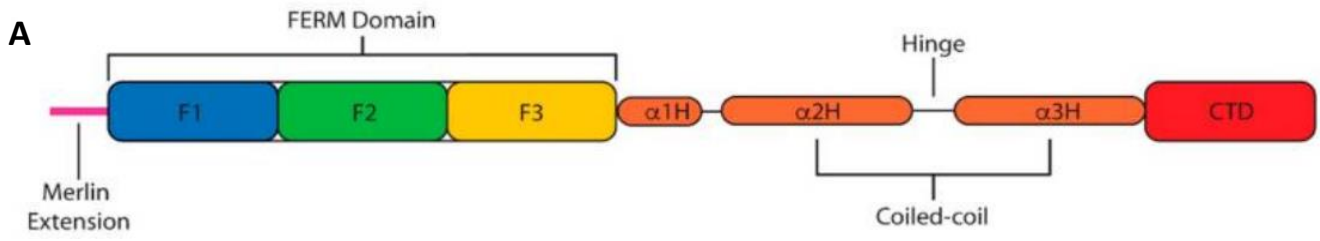


Figure 1.15 ***The structure of the MSN gene encoding Moesin*** *(**A**) Moesin, ezrin and radixin genes share a common structure of an N-terminal FERM domain with three modules F1, F2 and F3 that form a clover shape in the tertiary protein structure; an extended alpha helical domain and a C-terminal, membrane-interacting domain. Adapted from Michie et al 2019.*

Multiple studies have positioned moesin as a bridge between the formation of clathrin-coated vesicles and the cell cytoskeleton remodelling that facilitates endocytosis (Barroso-González et al., 2009; Nomachi et al., 2013). Barroso-Gonzales *et al* described the co-distribution of moesin with components of clathrin coated-structures in the membrane and demonstrated that an interaction between the N-terminal domain of moesin and phosphatidylinositol-4,5-bisphosphate was essential for internalisation of clathrin-coated vesicles. In T-cells, moesin was shown to regulate internalisation of S1PR1, a G-protein coupled receptor for sphingosine-1-phosphate which acts as a key mediator for lymphocyte behaviour (Cyster and Schwab, 2012; Nomachi et al., 2013). Nomachi *et al* reported that moesin-deficient cells did not internalise S1PR1 when stimulated with the cognate ligand, and utilisation of clathrin inhibitor pitstop-2 abrogated S1PR1 internalisation, demonstrating that internalisation was dependent on moesin and mediated by clathrin-dependent endocytosis. In contrast, moesin was copurified with early endosomes after fractionation of BHK renal cells, and siRNA knockdown of moesin did not affect clathrin-mediated internalisation of the transferrin receptor (Muriel et al., 2016). These data suggest that moesin may not have an exclusive role in clathrin-

mediated endocytosis but may bind specifically to client proteins and facilitate their internalisation via multiple mechanisms.

1.3.6.3.2 Moesin in Human Cancers

Upregulation of moesin has been noted in squamous cell carcinomas, breast cancer, and glioblastoma (Wang et al., 2017). In glioma, moesin upregulation arises from decreased miR-200c, which normally targets moesin for degradation, and moesin has been shown to act in an oncogenic fashion by increasing cell proliferation and promoting metastasis (Alam et al., 2017; Zhu et al., 2013). The underlying mechanism by which moesin overexpression confers these characteristics is not known.

1.3.6.4 Annexin A1

1.3.6.4.1 Annexin A1 Structure and Function

Annexin A1, encoded by the *ANXA1* gene, is one of twelve calcium-dependent phospholipid binding annexins. Annexin A1 has a C-terminal protein core that is conserved across annexin proteins and contains four calcium ion binding sites, and a protein-specific N-terminal region (Figure 1.16). The third annexin domain repeat contains a nonapeptide sequence called antiflammin-2 which exerts anti-inflammatory effects when isolated and introduced exogenously to cells (Miele et al., 1988).

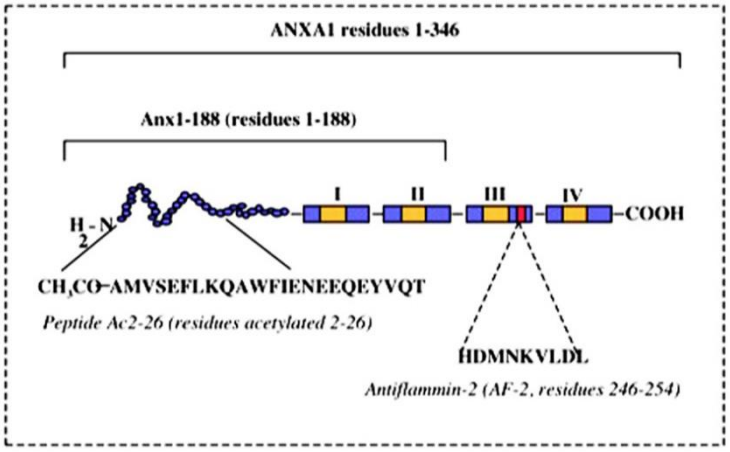


Figure 1.16 ***The structure of the ANXA1 gene encoding Annexin A1****. Four homologous repeats towards the C-terminal end are comprised of five alpha-helices which form a core region with multiple calcium binding sites in the tertiary protein structure. In the third repeat, labeled III, a 9 amino acid sequence called antiflammin-2 is a nonpeptide which when isolated also exerts anti-inflammatory effects. Peptide Ac 2-26 isolated from the N-terminal region can reproduce the anti-inflammatory effects of endogneous Annexin A1. Image adapted from Gavins and Hickey, 2012.*

When Ca^{2+} binds to annexin proteins it induces a conformational change, which enables the protein to bind to negatively charged phospholipids including phosphatidylserine, phosphatidic acid and phosphatidylinositol-4,5-bisphosphate. Upon calcium entry into the cell from the extracellular milieu or intracellular stores, annexin A1 rapidly re-localises to membranes where it can function in many roles which utilise its membrane binding properties. Phosphorylation of serine-27 by Protein Kinase C is necessary for annexin A1-membrane localisation but recruitment of annexin A1 to specific membranes is determined by the availability of the negatively-charged phospholipids to which the protein binds (D'Acunto et al., 2014); (Rentero et al., 2018).

The canonical function of annexin A1 is to mediate the anti-inflammatory effects of glucocorticoids. Annexin A1 inhibits phospholipase A2 subsequently blocking the release of arachidonic acid and preventing synthesis of pro-inflammatory eicosanoids including

prostaglandin (Hannon et al., 2003; Kim et al., 1994; Solito et al., 1998). Glucocorticoids positively regulate the expression of *ANXA1* and induce secretion of annexin A1 into the extracellular region where it binds to its cognate G-protein coupled receptor FPR2, and induces an anti-inflammatory intracellular signalling cascade. Given the absence of a signalling peptide in the primary sequence of annexin A1, it is inferred that the protein is secreted via a different process that the ER-Golgi secretory pathway to exert paracrine effects (Christmas et al., 1991). While externalised annexin A1 has well-characterised anti-inflammatory functions, the full-length cytoplasmic protein has been implicated in an array of intracellular functions including vesicle trafficking and autophagy. The main role for annexin A1 in vesicle trafficking focusses on tethering the ER and endosome membranes, and regulating protein trafficking between the plasma membrane and lysosome or recycling endosomes via multivesicular bodies (MVB) (Eden et al., 2016). Histological examination has shown annexin A1 localises to endosome membranes and data suggest annexin A1 can act as a tether at membrane contract sites between ER and endosomes containing epithelial growth factor receptor (EGFR), and facilitate inward vesiculation of these endosomes to form multivesicular bodies (Diakonova et al., 1997; White et al., 2006). Knockdown of annexin A1 resulted in a reduced number of organelles with membrane contact sites between EGFR-containing multivesicular bodies and the ER (Eden et al., 2016). Interestingly, there was no change in the quantity of membrane contact sites between non-EGFR containing MVBs and the ER, suggesting annexin A1 may be involved in recycling specific proteins including EGFR. Other members of the annexin family also have described roles in pre-endocytic plasma membrane curvature and budding of clathrin-coated vesicles, but annexin A1 has not been implicated specifically in these processes (Boye et al., 2017; Drücker et al., 2013; Lin et al., 1992). Annexin A1 has been shown to be upregulated more than three-fold upon starvation-

induced autophagy, and knockdown of *ANXA1* expression reduces autophagic degradation (Kang et al., 2011). The authors of this study opined that the previously described role of annexin A1 in MVB dynamics may assist formation of autophagosomes prior to lysosomal degradation.

In 2003, Hannon *et al* published the first *ANXA1*$^{-/-}$ mouse model (Hannon et al., 2003). In this model, tissues displayed a compensatory up or down regulation of other annexin family members implying a functional redundancy between the proteins which have highly conserved C-terminal domain and membrane binding properties. Defects in the secretory pathway resulted in an inability to secrete insulin from pancreatic beta-cells upon glucose stimulation. *ANXA1*$^{-/-}$ mice also showed protection against influenza virus via reduced viral uptake and trafficking of the internalised virus to the late endosome. Annexin A1- deficient mice displayed significantly increased tumour growth compared to wild-type mice, for carcinogen-induced breast tumours (Ang et al., 2009). Comparatively, orthotopic breast and lung cancer models displayed significantly slower tumour growth, metastasis, and vascularisation in the absence of annexin A1 and proposed novel pro-angiogenic functions of annexin A1 (Bist et al., 2011; Yi and Schnitzer, 2009). The disparate results of these *in vivo* studies support the notion that the role of annexin A1 in cancer is dependent on tumour cell origin and stage of disease.

1.3.6.4.2 Annexin A1 in Human Cancers

Despite annexin A1 conferring anti-inflammatory effects and large efforts being made to replicate its function in settings of inflammatory disease, *ANXA1* overexpression has been

determined to be detrimental in many cancers (Bai et al., 2004; Duncan et al., 2008; Liu et al., 2011; Rondepierre et al., 2009). In models of hepatocellular carcinoma, upregulation of *ANXA1* preceded tumour nodule development and correlated with both severity of disease and tumour stage (de Coupade et al., 2000). Downregulation of annexin A1 protein has been observed *in vitro* via treatment with anti-inflammatory indomethacin in HCT116 cells, the NFκB inhibitor eurycomanone in A549 cells, and the p38 MAPK inhibitor SB203580 in colorectal BCS-TC2 cells (Lecona et al., 2008; Wang et al., 2006; Wong et al., 2012). These drugs do not exclusively affect annexin A1 protein level and a specific annexin A1 inhibitor has not yet been developed.

Interestingly, multiple cancers typically display downregulation of annexin A1 in correlation with tumour severity, and indicate that downregulation of annexin A1 may serve as an early indicator of tumour progression. This highlights the complexity of annexin A1's function in cancer pathways, suggesting it may have a tissue-specific role as either tumour-suppressor or oncogene. Annexin A1 was reported to be downregulated in head and neck squamous cell carcinoma resulting in increased EGFR phosphorylation, and signalling of downstream PI3K-Akt-mTOR signalling (Raulf et al., 2018). This study adds to the data implicating annexin A1 as a regulator of EGFR signalling through facilitating lysosomal degradation of the internalised active receptor and curtailing the signalling cascade.

1.4 Aims and Hypothesis

Recent developments in understanding the regulation of NIS at the transcriptional, translation and post-translational levels have led to *in vitro* improvements in radioiodide uptake. Differentiated thyroid cancers can be uniquely treated by radioiodide ablation

therapy, the success of which hinges on adequate NIS expression and function. Current treatment strategies to re-differentiate thyroid tumours and induce iodide uptake capabilities do not address the post-translational processing of NIS. As such, the dysregulation of proteins involved in NIS trafficking to the membrane may hinder the efficacy of treatments that successfully increase *SLC5A5* expression. Optimising radioiodide uptake in tumours would not only improve the efficacy of treatment but may reduce the number of patients who go on to receive tyrosine kinase inhibitors. Despite numerous ongoing trials, tyrosine kinase inhibitors have adverse side effects and are therefore unsuitable for long term treatment for patients who have persistent disease after radioiodide therapy.

New proteins implicated in NIS synthesis and processing may present novel therapeutic targets that may be pharmacologically modulated to improve the quantity of functional, plasma membrane bound NIS in thyroid cancer cells prior to administering radioiodide therapy. The understanding of VCP-mediated NIS degradation has thus led to a breakthrough in identifying drug treatments that may enhance radioiodide uptake. Despite multiple compounds with anti-VCP activity reported in the literature, achieving meaningful VCP inhibition *in vivo* has made slow progress. This is a result of both tolerability of the compounds *in vivo* and reduced efficacy due to physical properties such as bioavailability. As a widely studied protein that is reported to be dysregulated in malignancy, VCP is an attractive anti-cancer target and the experiments of this thesis sought to improve VCP inhibition in the specific setting of differentiated thyroid cancer through multiple pharmaceutical approaches. It was hypothesised that specific VCP inhibitors, which have recently been developed, may elicit increased NIS-mediated iodide uptake as previously observed with repurposed allosteric inhibitors of VCP, such as clotrimazole. It was also hypothesised that the VCP inhibitor activity

of clotrimazole may be enhanced by structural modifications which may also modulate the chemical characteristics of this drug, such as logP value, to improve bioavailability of the compound *in vivo*.

Further, this PhD sought to identify additional components of the NIS protein interactome that contribute to NIS trafficking, and determine whether these proteins may be appropriate molecular targets for pharmaceuticals to improve NIS-mediated iodide uptake. It was hypothesised that additional analysis of putative NIS interactors previously identified by mass spectrometry may identify further NIS-interacting proteins and enhance understanding of post-translational processing of NIS in thyroid cancer.

The primary aims were to:

- Assess the efficacy of specific VCP inhibitors in the context of inducing radioiodide uptake in thyroid cancer cells.
- Modify the biochemical profile of the known VCP inhibitor clotrimazole to improve potency for increasing iodide uptake *in vitro*.
- Investigate further NIS interactors which may have roles in post-translational processing of NIS and may act as therapeutic targets for improving NIS-mediated iodide uptake.

2 Materials and Methods

2.1 Cell culture

2.1.1 Cancer Cell Line Culture

Cells were cultured in RPMI (Gibco) or DMEM (Sigma) cell culture medium supplemented with 10 % foetal bovine serum (Gibco), penicillin-streptomycin (Gibco) and L-glutamine (Gibco; added to RPMI only). Cells were grown in 75 cm^2 flasks and seeded in cell culture plates which were incubated at 37^oC with 5 % CO_2 in a humidified environment.

TPC1 and 8505C cells were kindly donated by Dr Rebecca Schweppe. TPC1 cells are derived from an adult female papillary thyroid tumour and are characterised by *RET-CCDC6* fusion, *TERT* promoter mutation C228T, and mutations in *CDKN2A* and *STAG2* (Landa et al., 2019). 8505C cells are derived from the anaplastic thyroid tumour of a 78-year-old female. 8505C cells are homozygous for the $BRAF^{V600E}$ mutation, and harbour mutations in *NF2, TP53*, and the *TERT* promoter region (Landa et al., 2019). HeLa cells were obtained from the European Centre for Authenticated Cell Cultures. HeLa cells were the first human cell line to be continually grown in culture and derive from the endocervical adenocarcinoma of a 30-year-old female patient. The tumour from which HeLa cells were extracted was driven by human papilloma virus type 18 which underpins the propagation of this cell line in culture. HeLa cells do not have reported oncogenic driver mutations although it is possible these may be acquired during extended periods of cell culture. HeLa cells are the most common contributor to cell line contamination and therefore were cultured, split, and seeded in separate incubators to non-HeLa cell lines. N-thy-ORI3.1 cells are derived from the thyroid of a healthy female patient, and were used briefly in this investigation and were thankfully received from Dr Vicki Smith. L87-NIS cells were kindly donated by Professor Christine Spitzweg (Ludwig-

Maximilians University, Munich) with thanks to Nathalie Schwenk. L87 mesenchymal stem cells are derived from the bone marrow of a haematologically normal 70-year-old male patient. In these cells, NIS is driven by the CMV promoter. Both N-thy-ORI 3.1 and L87-NIS cells were originally immortalised using SV40 virus for continuous cell culture.

HeLa and U2OS host cell lines for the Flp-In™ T-Rex™ inducible cell systems (Invitrogen) were received from Professor Grant Stewart (University of Birmingham, UK). These cells had previously been transformed with the pFRT/lacZeo vector and were characterised as having a single FRT recombination site stably integrated into the genome. The development of these cell lines to produce tetracycline inducible BRAF systems is described in Section 2.9.

TPC1 and 8505C cells stably transfected with NIS and YFP constructs were kindly provided by Dr Martin Read and Kate Brookes. NIS expression in these cell lines was maintained by cell culture in media supplemented with 500 µg/ml geneticin (Gibco). Cells were tested for mycoplasma bacterium (Jena Bioscience) every six months against positive and negative controls, with consistently negative results.

At 80-90 % confluency cells were split and seeded. Seeding densities are displayed in (Table 2-1). Media was aspirated from 75 cm^2 flasks and cells were washed with 5 ml sterile PBS. 1 ml 0.25 % trypsin was added, and flasks were incubated for three to five minutes at 37^oC to complete detachment from the flask base. Cells were resuspended in 9 ml RPMI or DMEM media, and 10 µl cell suspension was transferred to cytometer and counted under a 10x objective. An average of four squares was used to calculate number of cells per ml, and subsequently the correct number of cells to seed into 6-well or 24-well plates. Radioiodide

uptake assays performed at Ludwig-Maximilians University, Munich employed 12-well plates and the specific densities and volumes used in this experiment are described in section 2.4. Specific seeding densities depended on the cell lines and the length of time between seeding and harvesting, and are outlined in (Table 2-1).

Plate	6-well plate			24-well plate		
Volume	2 ml			500 µl		
	72 hour siRNA knockdown	48 hour transfection	24 hour drug treatment	72 hour siRNA knockdown	48 hour transfection	24 hour drug treatment
TPC1	-	7.5×10^4	1.5×10^5	-	-	-
8505C	-	1.0×10^5	1.5×10^5	-	-	-
TPC1-NIS	3×10^5	-	2.5×10^5	8×10^4	-	7.5×10^4
8505C-NIS	3×10^5	-	2.5×10^5	8×10^4	-	7.5×10^4
L87-NIS	-	-	2.5×10^5	-	-	7.5×10^4
HeLa	-	3.5×10^5	-	-	8.75×10^4	-

Table 2-1. ***Densities at which each cell line was seeded for experiments in 6-well and 24-well plates.*** *Experiments involving longer incubation between seeding and harvesting required lower numbers of seeded cells to be 90-100 % confluent at the final experimental timepoint.*

2.1.2 Primary Thyroid Culture

Primary thyroid samples were collected from the Queen Elizabeth Hospital Birmingham via the Human Biomaterials Resource Centre (Project Number 17-291) with informed patient consent and local ethics approval. The thyroid tissue was cut into small pieces and digested in HBSS and 0.2 % Type II collagenase (Worthington) for 12-16 hours with end-over-end

rotation. After incubation, the sample was sieved to remove undigested pieces of extracellular matrix or surgical clips, then collected in a 50 ml Falcon tube with HBSS. The sample was centrifuged at 300 g for three minutes and resuspended in HBSS six times to remove erythrocytes and thyroglobulin aggregates from the cell pellet. 0.1 ml cells were resuspended in 50 ml Coon's modified Ham's F12A media (Biochrom F0855) supplemented with 4 % FBS, pen-strep, L-glutamine (as above), 2 mg/ml insulin (Sigma I6634) and 300 mU/ml TSH (Sigma T8931) and plated 500 µl per well of a 24-well plate. Two to three days after plating, medium was removed and replaced with Coon's media without FBS, supplemented with insulin and TSH, as above. The plate remained incubated in 37^{o}C with 5 % CO_2 and adequate humidity for five to six further days before performing drug treatment and subsequent radioiodide uptake assay. 12 wells per sample were separated to measure TSH responsivity. In these wells, media was changed to serum-free and TSH-free three days after plating, TSH was re-introduced five days later at doses of 0 mU/L, 300 mU/L, 1 U/L and 10 U/L. Experimental wells were cultured in 300 mU/l TSH as described in (Eggo et al., 1996). Cultures that responded to 300 mU/L in the TSH dose response curve were taken forward for analysis.

2.2 Plasmid Preparation

2.2.1 Table of Plasmids

Mammalian expression vectors used to generate the data in this thesis are described in detail in Table 2-2 and the vector maps are displayed in Figure 2.1. All plasmids contain either an ampicillin or kanamycin resistance cassette for selecting transformed bacteria. All plasmids are driven by the human cytomegalovirus promoter. Plasmids were used for transient transfection of cells and compared to transfection with an empty expression vector control.

Moesin and annexin A1 full length coding sequences were received in pCMV3 vectors (Sino Biological: moesin HG-13866-UT and annexin A1- HG-12113-UT) and inserted into the pcDNA3.1 (+) vector. Lyophilised moesin and annexin A1 plasmids were resuspended in 100 µl nuclease-free water. Moesin and annexin A1 coding sequences were digested with *XbaI* and *KpnI* restriction enzymes (Promega), in 10x multi-CORE buffer (Promega) and H_2O then run on a 2 % agarose gel at 140 V for thirty minutes. Bands corresponding to moesin and annexin A1 coding sequence and linearised pcDNA3.1 vector were excised and purified using Qiaquick Gel Purification Kit (Qiagen). Digested pcDNA3.1 was ligated to both moesin and annexin A1 cDNA using T4 DNA Ligase (NEB) in a T4 DNA Ligase buffer (NEB) and nuclease-free water for one hour at room temperature.

Plasmid Name	Insert	Expression Vector	Resistance Marker
VO	No insert	pcDNA3.1 (+)	Ampicillin
NIS-HA	NIS cds with c-terminal HA tag	pcDNA3.1 (+)	Ampicillin
NIS-GFP	NIS cds with c-terminal GFP tag	peGFP	Ampicillin
MSN	Moesin cds	pCMV3	Ampicillin
ANXA1	Annexin A1 cds	pCMV3	Ampicillin
VCP	VCP cds	PcDNA3.1 (+)	Ampicillin
LgBiT	LgBiT tag for N-or C- terminal tagging	pBIT1.1-N/C-[TK/LgBiT]	Kanamycin
SmBiT	SmBiT tag for N-or C- terminal tagging	pBIT2.1-N/C-[TK/SmBiT]	Kanamycin
Nanoluc	Nanoluc luciferase	PcDNA3.1 (+)	Ampicillin
Tet-inducible expression vector	$BRAF^{WT}$ and $BRAF^{V600E}$	PcDNA5/FRT/TO	Ampicillin
T-Rex™ Flp In™ recombinase	None	pOG44	Ampicillin

Table 2-2 ***Plasmids used in this investigation,*** *including gene of interest, vector backbone and nature of the resistance marker. Cds = coding sequence.*

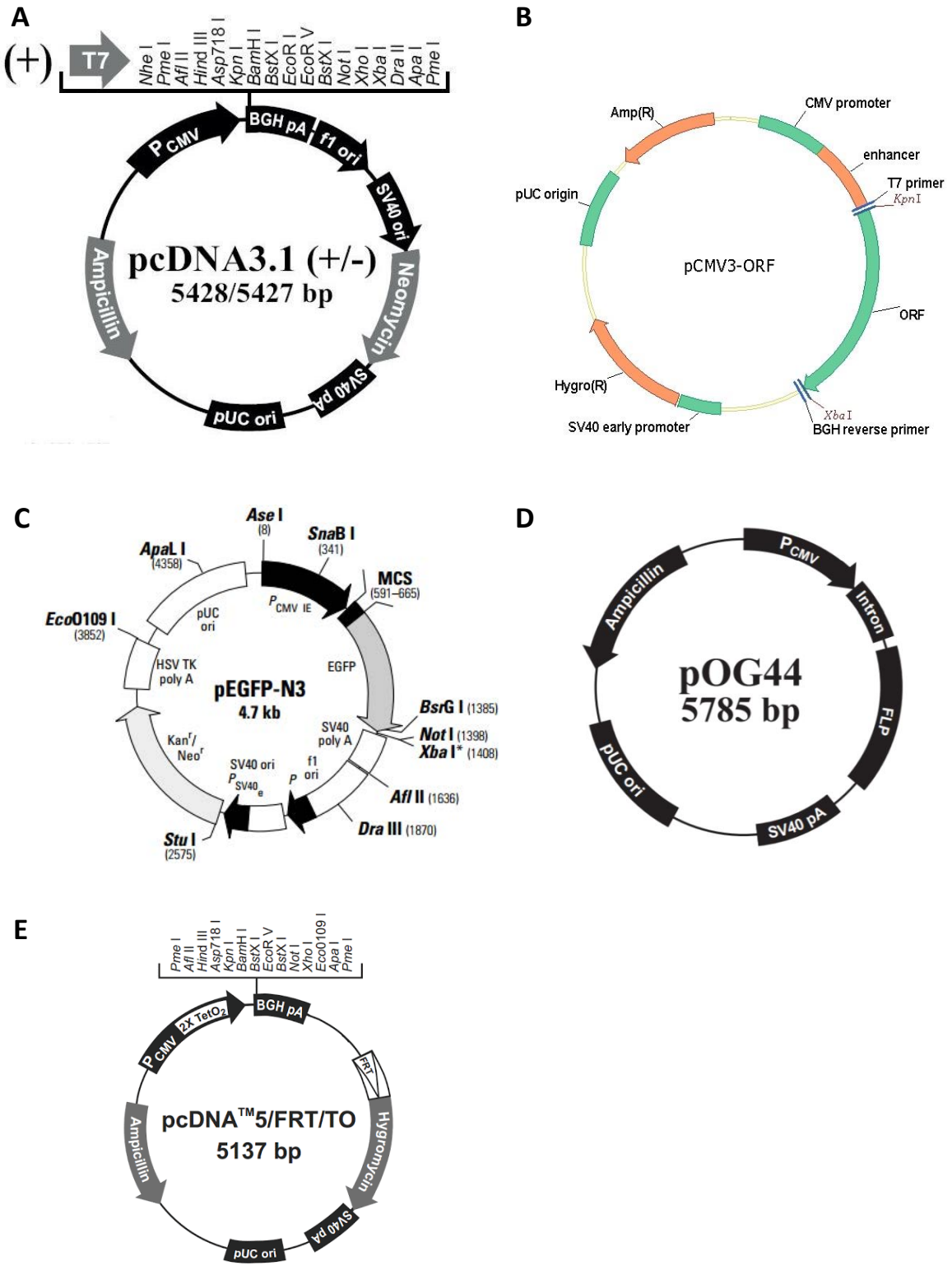


Figure 2.1 ***Plasmid maps of vectors used in this investigation****. (**A**) pcDNA3.1 (+) vector was the primary vector used in transformations containing the genes-of-interest NIS, MSN, ANXA1 and VCP with associated tags; (**B**) The pCMV3 vector was purchased from Sino Biological containing the MSN and ANXA1 open reading frames which were transferred to pcDNA3,.1 (+). (**C**) The pEGFP-N3 vector contained the NIS open reading frame for use in imaging and protein-protein interaction studies. (**D**) and (**E**) were co-transfected into HeLa and U2OS cells with a single recombination site stably transfected into the genome to generate Flp-In™ T-REx™ Tet-inducible BRAF cell systems, where (**E**) contained $BRAF^{WT}$ and $BRAF^{V600E}$ inserts.*

2.2.2 Transformation of DNA into *E. coli*

Plasmids were transformed into the DH5α strain of *E. coli*. 10 ng DNA were mixed with cells and incubated on ice for thirty minutes before being shocked at 42°C for forty-five seconds. 250 µl SOC media was added (2 % tryptone, 0.5 % yeast extract, 10 mM NaCl, 2.5 mM KCl, 10 mM $MgCl_2$, 10 mM $MgSO_4$ and 20 mM glucose; Sigma) and samples were shaken horizontally at 37°C for one hour before being centrifuged at 13000 rpm and resuspended in 50 µl SOC media and plated on antibiotic plates and incubated for 16 hours. Ampicillin plates were made from LB-agar and 100 µg/ml carbenicillin or 50 µg/ml kanamycin.

2.2.3 Purification of Plasmid DNA

Colonies were picked from antibiotic-LB-Agar plates after 16 hours of incubation at 37°C. Colonies were resuspended in 10 ml LB bacterial broth and incubated for 8 hours at 37°C with shaking at 225 rpm. Next, the culture was processed via miniprep or maxiprep purifications. Minipreps were performed using Wizard SV Plus Miniprep System (Promega) following the manufacturer's instructions with the addition of 96 % ethanol in an equal volume to supernatant after precipitation of proteins and chromosomal DNA to maximise binding of plasmid DNA to the column and increasing DNA concentration in the final elution. Where large volumes of plasmid were required, the 10 ml starter culture was transferred to 150 ml LB broth for overnight shaking incubation at 225 rpm and 37°C. The following morning the culture was processed using the GenElute HP Plasmid DNA Maxiprep kit (Sigma) following the manufacturer's instructions. DNA concentration was quantified using a NanoDrop 1000 spectrophotometer (Thermo Fisher) and the 260 nm/280 nm ratio was used as an indicator

of purity. Only DNA preparations with a concentration above 500 ng/µl and a 260/280 nm ratio of 2.1 or above were used for downstream transfections.

2.2.4 Sequencing

Once purified, 500 ng DNA in 5 µl H_2O were sent for Sanger sequencing, performed by Source Bioscience, UK. Sequencing primers used in this thesis are documented below (Table 2-3). CMV_Forward and BGH_Reverse primers were supplied by Source Bioscience. All other primers were designed using Primer3 software and ordered from Sigma-Aldrich as 0.05 µM desalted oligomers. Data was received as .abi chromatogram files and analysed using Chromas software version 2.6.6.

Primer	Sequence (5' → 3')	Target Gene(s)
CMV_Forward	CAACGCGACTTTCCAAAATG	VO, VO-LgBiT, VO-SmBiT, MSN WT, VCP WT, NIS WT
BGH_Reverse	TAGAGGGCACAGTCGAGG	VO, VO-LgBiT, VO-SmBiT, MSN WT, VCP WT, NIS WT and ANXA1 WT.
VCP_Forward	TTGCCCAGACCCTTCAGC	VCP WT, VCP- SmBiT, VCP-LgBiT
NIS_Forward	TGGCTTCTTGCCCACCAATG	NIS-HA, NIS-SmBiT, NIS-LgBiT, NIS-SmBiT k554a AND R555A mutants
MSN_Forward	GAAGGCCCTCACTTCGGAGC	MSN WT, MSN- SmBiT, MSN-LgBiT
ANXA1_Forward	TGAAAGGTGGTGGAACTCGCCA	ANXA1 WT, ANXA1-SmBiT, ANXA1-LgBiT

Table 2-3 ***Primers used to sequence plasmids in this investigation****, supplied by Source Bioscience UK or Merck Life Science.*

2.3 Transfection

2.3.1 Plasmid DNA Transfection

Cells were transfected with 0.25 µg and 1 µg DNA in 24-well plates and 6-well cell culture plates, respectively. DNA was added to serum-free media Opti-MEM (Gibco) and incubated at room temperature for five minutes. Lipofectamine reagent TransIT-LT1 (Mirus) was added at a 3:1 ratio of TransIT-LT1 (µl) to DNA (µg), and incubated at room temperature for thirty minutes to facilitate formation of DNA-lipofectamine complexes. 25 µl and 100 µl were added dropwise to 24-well plates and 6-well cell culture plates, respectively incubated at 37^{o}C for 48 hours.

2.3.2 siRNA Transfection

small-interfering-RNAs were used in this investigation to assess the downstream effect of mRNA knockdown of target genes (Table 2-4). All siRNAs were received as lyophilised powder and resuspended in 50 µl nuclease-free water for 100 µM stock and rocked for thirty minutes before long term storage at -20^{o}C. Opti-MEM serum free medium and lipofectamine RNAiMAX (Thermo Fisher) were mixed at a ratio of 12 µl lipofectamine per 1 ml OptiMEM, and incubated at room temperature for five minutes. siRNA was added for a final concentration of 0.2 µM and incubated at room temperature for twenty minutes. Media was removed from plated cells and replace with optiMEM, RNAiMAX and siRNA solution: 1 ml per well for 6-well plates and 250 µl per well for 24-well plates. Plates were incubated for five hours at 37^{o}C before siRNA solution was replaced with standard cell culture medium. Assays were performed 72 hours after transfection to ensure adequate knockdown of the gene-of-

interest and removal of translated protein by normal protein turnover. Protein was harvested simultaneously to each assay and Western blot analysis used to confirm knockdown.

Target Transcript	Source	Number of Target Sequences
Non-targeting control	Dharmacon ON-TARGET SMARTpool, D-001810-10-05	4
VCP	Sigma-Aldrich MISSION #1 Hs-02_00118726, #2 Hs01_00118728 #3 Hs02_0034009, pooled	3
Moesin	Dharmacon ON-TARGET SMARTpool, L-011732-00-0005	4
Annexin A1	Dharmacon ON-TARGET SMARTpool, L-011161-00-0005	4

Table 2-4 ***siRNAs used for knockdown experiments in this investigation****, targeting a minimum of 3 regions in each mRNA transcript.*

2.4 Radioiodide Uptake Assay

Experiments performed at the University of Birmingham

Where cells were to be transfected, cells were seeded at a density of 5 x 10^4 cells per well, transfected 24 hours after seeding and radioiodide uptake analysis was performed 48 hours after transfection. Alternatively, where cells were to undergo drug treatments, cells were seeded at 7.5 x 10^4 cells per well, and drug treatments were performed 24 hours after seeding and radioiodide uptake analysis was performed 24 hours after treatment.

100 µM sodium perchlorate ($NaClO_4$), a strong competitive inhibitor of NIS-mediated iodide uptake, was added to two wells per condition for one hour and incubated at 37°C. I^{125} (Hartmann Analytic) was diluted in sodium iodide to 1.2 x 10^5 counts per minute in 5 µl

solution, 5 µl was added per well and plates were incubated at 37°C a further hour. After this, media was aspirated, and cells were washed with cold Hanks Balanced Salt Solution to halt uptake and remove remaining I^{125} in solution. Cells were lysed with 2 % SDS solution and lysates were transferred to measuring tubes. Counts per minute were quantified using a Berthold Gamma Counter LB2111. Lysates were transferred to microcentrifuge tubes and protein concentration of the samples was analysed via BCA colorimetric assay. Counts per minute were normalise to protein concentration to calculate iodide uptake values. Uptake measured in wells treated with $NaClO_4$ were subtracted from untreated wells to analyse specific NIS-mediated iodide uptake only.

Experiments performed at Klinikum Großhadern, Munich, Germany

Cells were seeded into 12-well plates at a density of 1.5 x 10^5 cells per well for both radioiodide and MTT assay and both plates were identically treated with clotrimazole 24 hours after seeding. On day three, 1 x 10^5 counts per minute of I^{125} solution (10 mM NaI, HBSS, HEPES buffer adjusted to pH 7.3 with KOH) was added to wells of radioiodide plates and incubated at 37°C for forty-five minutes. At the same time as iodide addition, $NaClO_4$ was added to one well per condition to a final concentration of 100 µM. After incubation, media was aspirated, and wells were washed with HBSS/HEPES solution. NaOH was used to lyse cells and plates were shaken at room temperature for fifteen minutes to complete lysis. Lysates were measure on a Berthold Gamma Counter.

At the same time as iodide addition, MTT reagent was added to the second plate and incubated at 37°C for two hours. Media was aspirated under fume hood and DMSO/isopropanol solution was added to wells to dissolve the formazan dye produced only

by living cells. 120 µl solution was transferred to a 96-well plate and measured at 620 nm on Tecan plate reader. The final iodide uptake analysis data was plotted as count per minute iodide uptake over absorbance at 620 nm.

2.5 Protein Preparation and Western Blotting

2.5.1 Protein Isolation

Cells were seeded at a density of 1 x 10^5 cells per well in 6-well plates and transfected with 2 µg DNA 24 hours after seeding. On day 4, media was removed, and cells were washed with 1 ml PBS, then lysed using 120 µl RIPA buffer (TRIS, NaCl, Igepal (Sigma), Sodium deoxycholate, 100 mM EDTA) containing 60 µl protease inhibitor per 1ml RIPA (Sigma). Protease inhibitor cocktail contains aprotinin, bestatin, leupeptin and pepstatin in DMSO to inhibit serine, cysteine, and acid proteases. Where phosphorylated proteins were to be studied downstream, two phosphatase inhibitors were added containing sodium orthovanadate, sodium molybdate, sodium tartrate, cantharidin, p-bromolevamisole oxalate and calyculin A in DMSO (Sigma). This combination inhibits protein phosphatase 1 and 2A, alkaline phosphatase, acid phosphatase, tyrosine phosphatases and serine/threonine phosphatases to preserve target phosphate sites such as phospho-ERK1/2 and phospho-Akt.

To facilitate cell lysis, plates were incubated at -20^{o}C for thirty minutes then thawed on ice. Lysates were collected by scraping and transferred to labelled microcentrifuge tubes then vortexed and centrifuged at 13,000 g for twenty minutes at 4^{o}C. The supernatant containing cell proteins was collected for quantification and the pellet of cell debris was discarded.

2.5.2 Protein Quantification

Protein concentration was analysed using the colorimetric BCA assay (Peirce 23225). 4 µl protein sample was loaded per well of a 96-well plate and 80 µl BCA reagent added per well before incubating for thirty minutes at 37°C. BCA reagent was made up prior to addition by 20 µl Pierce BCA reagent B for every 1 ml Pierce BCA reagent A. Absorbance was measure at 560 nm using a Molecular Devices SpectraMAX ABS plus microplate reader and SoftMAX Pro software. Absorbance values for protein samples were analysed against a standard curve measured concurrently using standards of BSA in RIPA buffer in the range of 0 mg/ml to 5 mg/ml. Protein quantification of the samples was determined by equation of the line of regression of the BSA protein standard curve.

2.5.3 Western Blotting

30 µg protein samples were prepared in 5x loading buffer (0.25 M tris solution in H_2O, 57 % w/v glycerol, 10 % SDS, bromophenol blue and 12.5 % beta-mercaptoethanol) and denatured at 37°C for thirty minutes. Where NIS protein was to be probed downstream, 10 % polyacrylamide gels without stacking were prepared (10 % protogel polyacrylamide (geneflow), 25 % 1.5 M tris solution pH 8.8, 0.1 % sodium dodecyl sulfate (SDS), 0.1 % ammonium persulfate and 0.01 % tetramethyethylenediamine (TEMED) in H_2O). Where downstream membrane probing did not include NIS protein, stacking gel was also prepared (16.6 % protogel polyacrylamide, 25 % 0.8 M tris solution pH 6.8, 0.02 % w/v SDS, 0.02 % w/v ammonium persulfate and 0.2 % TEMED in H_2O). Once set, samples were loaded into gels with running buffer (0.3 % w/v Tris, 1.44 % w/v/ glycine and 0.1 % w/v SDS in H_2O) and run at 70 V for thirty minutes if stacking gel was present, then increasing by 10 V every ten minutes

such that the current did not exceed 25 mA per gel; the average gel running time was seventy-five minutes.

Amersham Hybond 0.45 µm PVDF membranes (GE Healthcare) were activated by shaking in 100 % methanol for thirty seconds and transfer sandwiches were made with two sponges, filter paper, activated membrane and gel, then transferred at 360 mA for seventy-five minutes in transfer buffer (20 % methanol, 0.3 % w/v tris, 1.44 % w/v glycine in H_2O). Membranes were blocked in 5 % milk in TBS-T for two hours then incubated at 4^oC with gentle rocking in TBST- milk solutions of primary antibody overnight (Table 2-5). The following day, membranes were washed with TBS-T (72 % H_2O, 0.2 mM TRIS pH 7.6, 1 % w/v NaCl, 0.03 % Tween 80), for seven minutes repeated four times then incubated with secondary HRP-conjugated antibodies in TBS-T at room temperature for one hour. Membranes for co-immunoprecipitation were incubated with protein-G-HRP conjugated secondary antibodies (Bio-Rad) to prevent cross reaction with heavy and light change IgG at 75 kDa and 25 kDa, respectively. Four washes were repeated, and the membranes were developed using Pierce ECL plus (Thermo Fisher) and x-ray film (Scientific Laboratory Supplies) using an EcoMAX X-ray processor. Validation of protein loading was performed using β-actin as a housekeeping protein using FIJI software (Schindelin et al., 2012).

2.6 Immunofluorescence and Imaging

TPC1 and HeLa cells were seeded at a density of 7.5 x 10^4 cells per well onto sterilised coverslips in 6-well plates and transfected 24 hours later with relevant tagged or untagged plasmids. On day four, cells were washed with PBS, fixed with a PFA-based fixing solution

(0.2% PFA, 0.1M phosphate buffer, 2% glucose and 0.02% sodium azide) for twenty minutes at room temperature. Cells were permeabilised with ice-cold methanol for ten minutes on ice to allow antibodies access to intracellular epitopes, then methanol was replaced with 10 % new-born calf serum in PBS (NCS; Thermo Fisher) before blocking for thirty minutes at room temperature. Primary antibody was prepared in 1 % Bovine Serum Albumin (BSA) in PBS at concentrations described in (Table 2-5), and coverslips were incubated for one- hour face down. Coverslips were transferred to 6-well plates and washed with PBS three times before incubation with 1:250 secondary antibody in 1 % BSA and 1 % NCS in PBS solution for one hour, face down and in low light. Coverslips were mounted using fluorescent mounting medium (Agilent) before imaging after 24 hours on a confocal (Zeiss LSM780) microscope. For imaging using 100x objective, Immersol^{TM} immersion oil was used for optimal imaging (Zeiss).

2.7 Table of Antibodies

Antibody	Manufacturer	Code	Species reactivity	Dilution for Western blot	Dilution for Imaging
NIS	Proteintech	24324-1-AP	Rabbit	1:1000	1:700
MSN	Proteintech	26053-1-AP	Rabbit	1:10000	1:100
ANXA1	Proteintech	21990-1-AP	Rabbit	1:10000	1:100
VCP	Proteintech	10736-1-AP	Rabbit	1:1000	1:250
Beta-Actin	Sigma	A5316	Mouse	1:10000	1:1000
HA	Biolegend	16B12	Rabbit	1:1000	1:200
Myc	Cell Signalling	9B11	Mouse	1:1000	N/A
pERK1/2 (Thr202/Tyr204)	Cell Signalling	9101	Rabbit	1:1000	N/A
ERK1/2	Cell Signalling	9102	Rabbit	1:1000	N/A
pAkt (Ser473)	Cell Signalling	4060	Rabbit	1:1000	N/A
AKT	Cell Signalling	4691	Rabbit	1:1000	N/A

Table 2-5 ***Antibodies used in this investigation for analysis by Western blot or microscopy.***

2.8 Protein-Protein Interaction Assays

2.8.1 Co-Immunoprecipitation

TPC1-NIS cells were used to analyse NIS interactors by co-immunoprecipitation. The NIS antibody was used to pull back NIS protein and bound interactors, and an anti-HA antibody was used as an isotype control. Cells were expanded into three 75 cm^2 cell culture flasks. At 90-100 % confluency media was removed, cells were washed in PBS and lysed in high salt lysis buffer (50 mM Tris pH7.4, 1 % Igepal, 0.4 M NaCl in H_2O, protease inhibitor). Flasks were agitated at 4°C for thirty minutes then frozen for one hour. Cell lysates were collected by scraping, vortexed and incubated at 4°C with end-over-end rotation. Lysates were centrifuged at 13,000 g for twenty minutes in a pre-chilled centrifuge and the pellet of cell debris was discarded. 100 µl supernatant was removed and used subsequently as a non-antibody control. 10 µl NIS or HA antibodies were added to two of the samples, one sample was processed without addition of a primary antibody. Sampled were incubated at 4°C with end-over-end rotation for 16 hours. Next, 110 µl per sample protein G Seraphose beads (GE Healthcare 17-0618-01) were prepared by centrifuging at 4,000 g for one minute to enable removal of the ethanol suspension fluid. The bead pellet was washed in 500 µl high salt lysis buffer and spun at 4,000 g for one minute, this was repeated three times. Once cleaned, the beads were resuspended in 400 µl high salt lysis buffer and 100 µl of bead solution was added to each of the three lysates and incubated at 4°C with end-over-end rotation for two hours. Samples were centrifuged at 4,000 g for one minute and beads were washed in high salt lysis buffer as during preparation. After washing, 50 µl laemelli buffer (BioRad) + 2.5 µl beta-mercaptoethanol was added per sample and incubated at 37°C for thirty minutes to cleave proteins from the beads. Samples were centrifuged at 4,000 g for one minute and the

supernatant was collected for protein analysis by Western blot. Samples were run on 10 % acrylamide gels alongside lysate controls samples collected previously and analysed by Western blot as described in section 2.5.3. During Western blot development, protein-G HRP-conjugated secondary antibody (Bio-Rad) replaced anti-rabbit secondary antibodies to prevent cross reaction of the secondary antibody with the IgG antibodies present in the lysate samples.

2.8.2 Preparing Luciferase-tagged Plasmids

LgBiT and SmBiT vectors from NanoBiT PPI Starter System (N2014) were kindly provided by Dr Caroline Gorvin (University of Birmingham, UK). The nanoluc plasmid was kindly donated by Dr Davide Calebiro (University of Birmingham, UK). LgBiT and nanoluc tags were amplified by Q5 DNA Polymerase PCR (NEB) with the primers below (Table 2-6). PCR products were purified on 1 % agarose gel and bands were extracted using Gel Extraction kit (Qiagen) then digested with *XbaI/ApaI* (Promega) for C-terminal tagging or *HindIII/KpnI* (Promega) for N-terminal tagging. pCDNA3.1 (+) was linearised with *XbaI/ApaI* or *HindIII/KpnI* and tags and vector were ligated. All ligations were performed using T4 DNA ligase (Thermo Fisher) overnight at 16°C.

Amplicon	Forward Primer (5' → 3')	Reverse Primer (5' → 3')
LgBiT (N)	GCCAAGCTTACCATGGTCTTCACACTCGAA	GGCGGTACCACTGTTGATGGTTACTCG
LgBiT (C)	GCCTCTAGAGTCTTCACACTCGAAGAT	GGCGGCGGGCCCTTAGCTGTTGATGGTTAC
Nanoluc (N)	GCCAAGCTTACCATGGTCTTCACACTCGAA	GGCGGTACCCGCCAGAATGCGTTAGCA
Nanoluc (C)	GCCTCTAGAGTCTTCACACTCGAAGAT	GGCGGGCCCTTACGCCAGAATGCGTTC

Table 2-6 ***PCR primers used to amplify LgBiT and Nanoluc tags for insertion into pcDNA3.1 (+).*** *Row 1 and 3 prepared the tags for addition to N-termini of genes of interest and primer pairs contain restriction sites for HindIII and KpnI enzymes. Row 2 and 4 prepared tags for addition to C-termini of genes of interest and primer pairs contain restriction sites for XbaI/ApaI enzymes.*

The coding sequences for NIS, VCP, ANXA1 and MSN were amplified by PCR using the primers below, and digested with *KpnI/XbaI*. Primers were designed to remove the start codon for N-terminally tagged vectors, and to remove the stop codon for C-terminally tagged vectors (Table 2-7). Vector containing LgBiT or nanoluc tags were linearised with *KpnI/XbaI*, purified on a 1 % agarose gel and ligated as described above. VCP, MSN and ANXA1 were tagged individually on N- and C-termini but NIS was tagged only on C-terminus as N-terminal tags are known to abolish normal NIS function.

Amplicon	Forward Primer (5' → 3')	Reverse Primer (5' → 3')
NIS (C)	GCCGGTACCACCATGGAGGCCGTGGAGACC	GCCGCCTCTAGAGAGGTTTGTCTCCTGCTG
VCP (C)	GCCGGTACCACCATGGCTTCTGGAGCCGAT	GCCGCCTCTAGAGAGCCATACAGGTCATCATC
VCP (N)	GCGGTACCGCTTCTGGAGCCGATTCA	GCCGCCTCTAGATTAGCCATACAGGTCATC
MSN (C)	GCCGGTACCACCATGCCCAAAACGATCAGT	GCCGCCTCTAGAGACATAGACTCAAATTCGTC
MSN (N)	GCGGTACCCCCAAAACGATCAGTGTG	GCCGCCTCTAGATTACATAGACTCAAATTC
ANXA1 (C)	GCCGGTACCACCATGGCAATGGTATCAGAA	GCCGCCTCTAGAGAGTTTCCTCCACAAAGAGC
ANXA1 (N)	GCGGTACCGCAATGGTATCAGAATTC	GCCGCCTCTAGATTAGTTTCCTCCACAAAG

Table 2-7 ***PCR primers for amplifying genes of interest prior to insertion into pcDNA3.1 (+) containing LgBiT or Nanoluc tags.*** *Primers for C-terminal tagging omit the stop codon of the gene of interest and primers for N-terminal tagging omit the start codon of gene of interest. All primer pairs contain restriction sites for KpnI and XbaI enzymes.*

NIS, VCP, ANXA1 and MSN were amplified by the primers below for addition of SmBiT tags directly through PCR (Table 2-8). Amplicons were purified on 1 % agarose gels and extracted as described above, then digested with *KpnI/XbaI*. Empty pcDNA3.1 (+) was linearised with *KpnI/XbaI* and tags and vector were ligated overnight.

Vector	Forward Primer (5' → 3')	Reverse Primer (5' → 3')
NIS-SmBiT (C)	GCCGGTACCACCATGGAGGCCGTGGAGACC	GCCTCTAGATTACAGAATCTCCTCGAACAGCCGGTAGCCGGTCACGAGGTTTGTCTCCTGCTG
VCP-SmBiT(C)	GCCGGTACCACCATGGCTCTGGAGGCGAT	GCCTCTAGATTACAGAATCTCCTCGAACAGCCGGTAGCCGGTCACGCCATACAGGTCATCATC
SmBiT-VCP (N)	GCCGGTACCACCATGGTGACCGGCTACCGGCTGTTCGAGGAGATTCTGGCCGCTTCTGGAGCCGATTCA	GCCGCCGCCGCCGCCTCTAGATTAGCCATACAGGTCATC
MSN-SmBiT (C)	GCCGGTACCACCATGCCCAAAACGATCAGT	GCCTCTAGATTACAGAATCTCCTCGAACAGCCGGTAGCCGGTCACCATAGACTCAAATTCGTC
SmBiT-MSN (N)	GCCGGTACCACCATGGTGACCGGCTACCGGCTGTTCGAGGAGATTCTGGCCATGCCCAAAACGATCAGT	GCCGCCGCCGCCGCCTCTAGATTACATAGACTCAAATTC
ANXA1-SmBiT (C)	GCCGGTACCACCATGGCAATGGTATCAGAA	GCCTCTAGATTACAGAATCTCCTCGAACAGCCGGTAGCCGGTCACGTTTCCTCCACAAAGAGC
SmBiT-ANXA1 (N)	GCCGGTACCACCATGGTGACCGGCTACCGGCTGTTCGAGGAGATTCTGGCCATGGCAATGGTATCAGAA	GCCGCCGCCGCCGCCTCTAGATTAGTTTCCTCCACAAAG

Table 2-8 ***PCR primers for amplifying SmBiT tag directly onto genes of interest****. All primer pairs contain restriction sites for XbaI and KpnI for insertion into empty pcDNA3.1 (+).*

All ligation products were transformed into DH5 alpha competent *E. coli* as described in section 2.2.1. DNA was purified by miniprep as described in section 2.2.3. Correct plasmids were confirmed by Sanger sequencing services provided by Source Bioscience, UK.

2.8.3 NanoBiT

The Promega NanoBiT assay is a split-luciferase assay requiring LgBiT and SmBiT tags on the proteins of interest. In the event of protein-protein interaction in a kinetically favourable conformation, these tags will interact to form active luciferase and oxidise Nano-Glo reagent, producing a measurable luminescence signal Figure 2.2.

HeLa cells were seeded into 6-well plates at a density of 3.5 x 10^5 in a 6-well plate. After 24 hours cells were transfected with both LgBiT and SmBiT tagged vectors. On day three, cells were detached with trypsin and resuspended in phenol-red-free DMEM (Gibco) and 100 µl was transferred in duplicates to a white 96-well flat-bottom plate (Corning). Where drug treatments were required, drugs were added five hours after reseeding to allow for cell attachment to the plate substratum. 24 hours after reseeding or drug treatment, Nano-Glo Live Cell Substrate dilution buffer (Promega) was equilibrated to room temperature and prepared 19 volumes to 1 volume Nano-Glo live cell substrate (Promega). 25 µl of solution were added per well and distributed by orbital shaking for two minutes. Luminescence was measured every two minutes for twenty cycles at 37^{o}C using a PHERAstar plate reader. During analysis, luminescence values for each cycle were transformed using the equation $\log_{10}$(luminescence) to reduce the variation between experimental repeats arising from differences in passage, transfection efficiency and cell confluency. Typically, luminescence emission increases for the first ten cycles then plateaus or reduces, therefore a single measurement was taken at cycle ten, twenty minutes after addition of luminescent substrate. The cycle ten values for three to five experimental repeats were taken forward for statistical analysis.

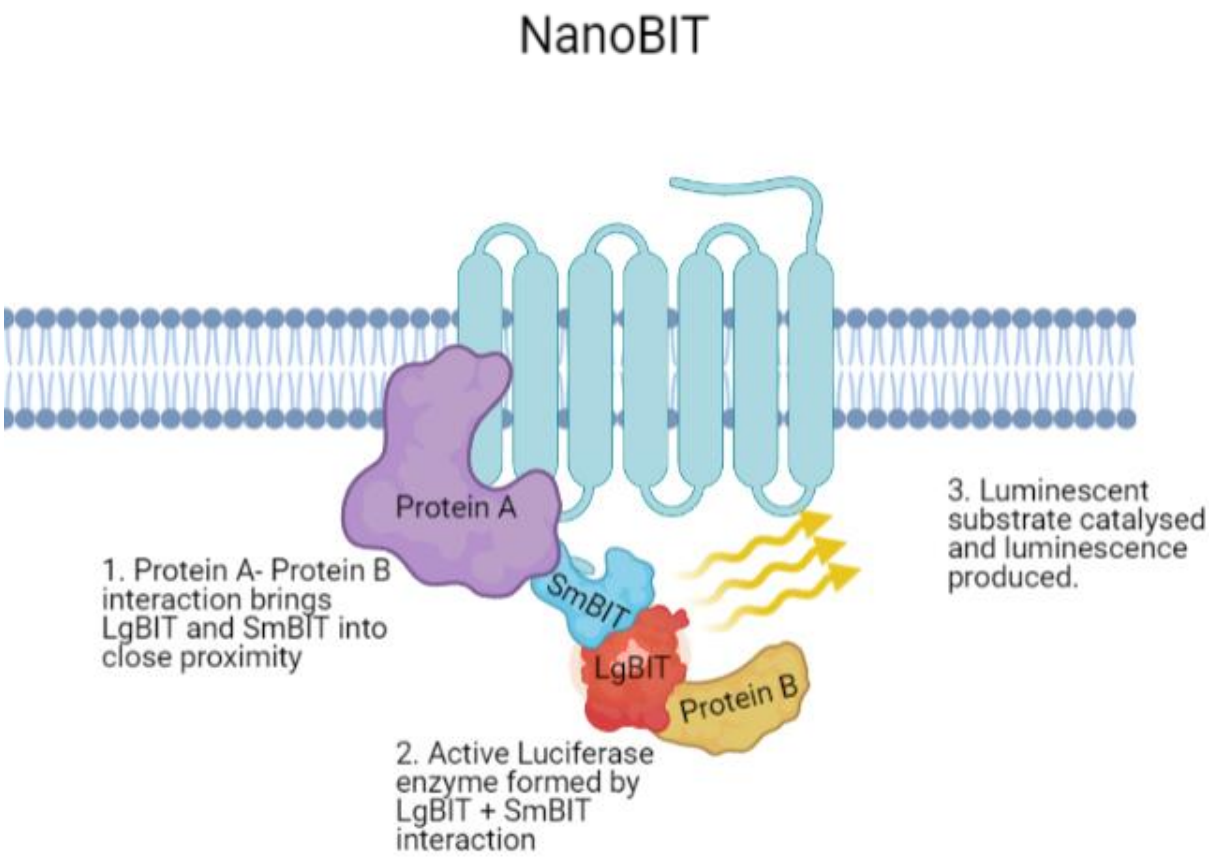


Figure 2.2 ***The NanoBiT assay measures interaction between tags on two proteins, LgBiT and SmBiT; in the event of protein-protein interaction, these tags may interact to form active luciferase.*** *When luciferin substrate is added the enzyme oxidises the substrate and luminescence is detected as a byproduct. In the absence of interaction between the two tagged proteins, full luciferase is not formed and luminescence above negative control is not apparent.*

2.8.4 Site-directed Mutagenesis

Site directed mutagenesis of the NIS-SmBiT vector to modify putative moesin binding sites K554 and R555 was performed using the Agilent QuikChange XL site directed mutagenesis kit (Thermo Fisher) and the primers documented in (Table 2-9).

Target Mutation	Forward Primer (5' → 3')	Reverse Primer (5' → 3')
NIS-SmBiT K554A	CAGGGTGCTGCGCGCGGTGG GGCCTGTC	GACAGGCCCCACCGCGCGCAG CACCCTG
NIS-SmBiT R555A	GCCAGGGTGCTGGCCTTGGT GGGGCC	GGCCCCACCAAGGCCAGCACC CTGGC
NIS-SmBiT K554A/R555A	GGGCCAGGGTGCTGGCCGCG GTGGGGCCTGTCA	TGACAGGCCCCACCGCGGCCA GCACCCTGGCCC

Table 2-9 ***Sequences of primers used to generate mutation in NIS coding sequence in the C-terminal tail domain immediately adjacent to the membrane.***

10 ng of the NIS-SmBiT template were added to 2.5 µl 10x reaction buffer, 1.5 µl Quick Solution, 125 ng each primer, 0.5 µl dNTPs and made up to 24.5 µl final volume with nuclease-free H_2O. 0.5 µl Turbo DNA Polymerase 2.5 U/µl was added, the reaction was mixed and collected in the bottom of the tube by pulse spinning before transferring to a thermocycler set at conditions outlined in Table 2-10.

Cycles	Temperature	Time
1	95°C	60s
18	95°C	50s
	60°C	50s
	68°C	8 minutes 30 seconds (1 minute per kB length)
1	68°C	7 minutes

Table 2-10 ***PCR Thermocycler conditions for generating NIS-SmBiT mutants****. Where required, PCR products were held at 4°C until ready for progressing to DpnI digestion.*

The PCR solution was digested with *DpnI* at 37°C for one hour to cleave methylated template DNA and leave only mutated DNA. XL-10 Gold chemically competent *E. coli* cells were prepared by mixing 50 µl cells with 2 µl beta-mercaptoethanol and incubating on ice for ten minutes. 2 µl digested PCR product was added, mixed by swirling and incubated on ice for thirty minutes. The bacteria were heat shocked at 42°C for thirty seconds and transferred to

ice for two minutes. 500 µl LB broth was added, and the cells were shaken at 225 rpm for one hour. The suspension was poured onto LB-Agar plates containing 100 µg/ml ampicillin and left for five minutes to air dry. Plates were inverted and incubated at 37°C for 16 hours. The following day, two colonies were picked and prepared according to protocol outlined in section 2.2.3. Mutations were confirmed by Sanger sequencing (Source Bioscience, Nottingham UK).

2.8.5 Bioluminescence Resonance Energy Transfer (BRET)

The bioluminescence resonance energy transfer (BRET) assay involves both GFP and luciferase fusion proteins of interest. Excitation of luciferase results in a transfer of energy which excites GFP fluorophores in the immediate vicinity Figure 2.3. Nanoluc luciferase was kindly provided by Dr Davide Calebiro with thanks to Emma Tripp. Nanoluc tags were added to the C-terminus of NIS and both the C- and N- termini of *VCP*, *MSN* and *ANXA1* by PCR amplification. Digestion and ligation were as described in section 2.8.2.

HeLa cells were seeded at a density of 3.5 x 10^5 cells per well and transfected with 1 µg DNA per well. After 24 hours, cells were reseeded after into white 96-well plates as described in section 2.8.3. 24 hours after transfection, NanoGlo reagent (Promega) was prepared from Nano-Glo luciferase assay substrate and Nano-Glo buffer in a 1:50 ratio. The solution was added in a 1:1 ratio of media to reagent per well and distributed by orbital shaking for three minutes to complete lysis. Plates were inserted into PHERAstar luminescent plate reader, preheated to 37°C. A measurement was taken six minutes after adding reagent at both 460 nm and 535 nm wavelengths to measure luciferase and fluorescence, respectively.

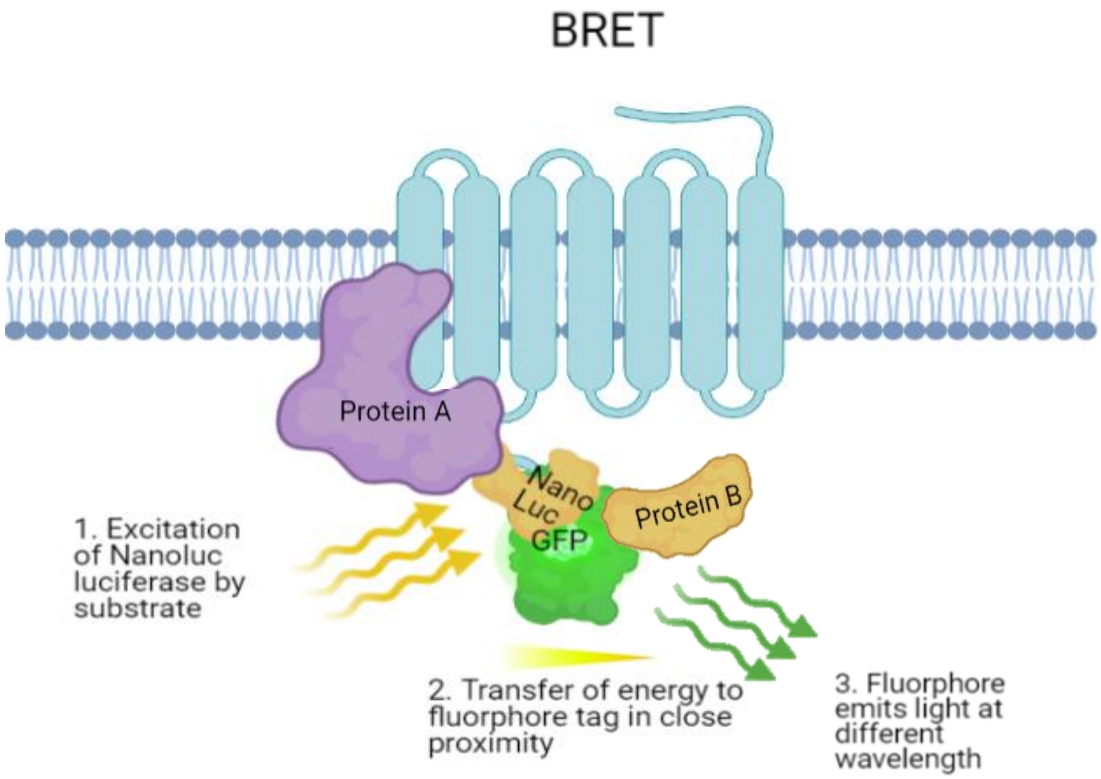


Figure 2.3 ***Bioluminescence resonance energy transfer requires tagging two proteins with an acceptor fluorophore and donor luciferase****. In the event of these proteins interacting, the luciferase substrate will be oxidised and luminescence produced as a by product (1). This results in a transfer of energy to the fluorophore (2) which emits at wavelength 485nm (3). In the absence of interaction between the tagged proteins,the fluorophore tag is not excited resulting in lower detection at 485nm.*

2.9 *BRAF*-Inducible Cell Systems

The Invitrogen Flp-In™ T-Rex™ system was employed to generate cells with conditional BRAF expression. Plasmids containing *Myc-BRAF^{WT}* and *Myc-BRAF^{T1799A}* were kindly received from Dr Vicki Smith and amplified by PCR to add *AflII* and *HindIII* restriction sites. PCR products were digested and ligated into pcDNA5/FRT/TO by addition of T4 DNA ligase (Thermo Fisher) and incubation overnight at 16°C. Insertion of *BRAF* into pcDNA5/FRT/TO was confirmed by Sanger sequencing using custom primers (Source Bioscience, Nottingham, UK; Table 2-11). HeLa and U2OS cells with FRT recombination sites stably integrated into the genome were

kindly received from Professor Grant Stewart. T-REx^{TM} cells were grown to confluency in a 75 cm^2 flask in DMEM media supplemented with 10 % FBS, 1 % penicillin-streptomycin, 5 µg/ml blasticidin and 5 µg/ml zeocin. At 80 % confluency, these cells were transfected with BRAF^{WT} and BRAF^{T1799A} plasmids and selected for in 5 µg/ml blasticidin and 400 µg/ml hygromycin B. Once confluent, induction of the proteins BRAF^{WT} and BRAF^{V600E} was achieved by addition of 1 µg/ml tetracycline to the cell culture medium. Protein was harvested after 24 hours of incubation with tetracycline to assess the effect of BRAF signalling on moesin and annexin A1 protein level. Anti-Myc tag antibody (Cell Signalling, Mouse) was used during Western blot analysis.

Amplicon	Forward Primer (5' → 3')	Reverse Primer (5' → 3')
BRAF^{WT} and BRAF^{V600E}	GCCCTTAAGACCATGGAGCAGAAGCTGAT	GCCAAGCTTCAGTGGACAGGAAACGCAC

Table 2-11 ***Sequencing primers used to confirm insertion of BRAF into pcDNA5/FRT/TO vector****.*

2.10 Analysis of Data from The Cancer Genome Atlas

The cancer genome atlas (TCGA; https://portal.gdc.cancer.gov/) collates data from 67 distinct primary tumour sites and has reported genetic data on over 23,500 genes and 3.4 million mutations. The collaboration between the National Cancer Institute (Bethesda, Maryland, US) and the National Human Research Genome Institute (Bethesda, Maryland, US) provides gene expression profiling, mutational analysis, copy number alterations and DNA methylation profiling, among other data, for multiple cancer types and matched normal controls. Within the TCGA, the THCA database contains data from 501 papillary thyroid cancer samples and 59 matched normal controls. THCA data was accessed via GDAC Firehose

(https://gdac.broadinstitute.org/) (Broad Institute, Massachusetts, US). For mRNA analysis, the file illuminahiseq_rnaseqv2-RSEM_genes_normalized (MD5) was downloaded, consisting of normalised illumina sequencing reads for 20533 genes distinguished by the unique genetic identifier ENTREZ ID. Values were transformed using $\log_2$(normalised counts + 1) to reduce data skew and enable appropriate statistical tests to be applied. The $\log_2$ expression values for *MSN* and *ANXA1* genes were extracted alongside correlating sample ID. Further genomic and clinical data relating to each sample ID, such as mutation status of oncogenes, were downloaded from (https://www.cbioportal.org/). cbioportal is a public site for accessing TCGA data, developed at the Centre for Molecular Biology at Memorial Sloan Kettering Cancer Centre and maintained by multiple international institutes (Cerami et al., 2012; Gao et al., 2013). Mutation data were mapped to sample IDs to enable comparison of *MSN* and *ANXA1* expression between different mutational drivers which was carried out using GraphPad PRISM.

2.11 Statistics

Statistical analysis was completed using PRISM GraphPad Software. All statistical analysis was completed on datasets with at least three biological replicates and significance was assessed at $p < 0.05$. For normally distributed datasets with two variables, a paired, two-tailed t-test was used, and for three or more variables a one-way analysis of variance (ANOVA) was used to assess significance. For non-normally distributed datasets with two variables the Mann-Whitney test was applied, and for three or more variables a Kruskal-Wallis test was used to assess significance.

3 The Effect of CB-5083 and CB-5339 on Radioiodide Uptake

3.1 Introduction

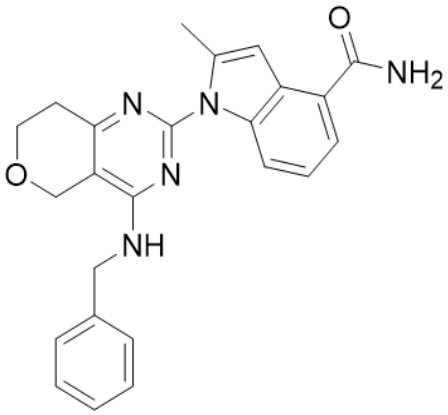
3.1.1 CB-5083 Inhibits VCP *in vitro* and *in vivo*

In the search for therapeutically viable VCP inhibitors, Anderson *et al* presented the first evidence of VCP inhibition within mouse xenograft models via the compound CB-5083 (Anderson et al., 2015). CB-5083 was derived from the earlier VCP inhibitor ML240 and bears structural resemblance to the first identified VCP inhibitor DBeQ yet has an improved bioavailability (Zhou et al., 2015). *In vitro* data characterised CB-5083 as a potent VCP inhibitor with an IC_{50} of 11 nM. CB-5083 functions by inhibiting the ATPase activity of the D2 domain to abrogate VCP function and induce extensive cell death. The cytotoxic effects of CB-5083 are mediated through upregulation of C/EBP homologous protein (CHOP), a pro-apoptotic transcription factor. Studies on 350 cancer cell lines showed that higher sensitivity to CB-5083 was observable in cell lines driven by MAPK-activating mutations in *KRAS* of *RAF* genes, compared to cell lines with low levels of phosphorylated ERK (Anderson et al., 2015) . When assessed against a panel of 358 ATPase-utilising enzymes and kinases, CB-5083 showed high specificity to VCP. The protein with the second-most altered ATPase activity after 10 µM treatment with CB-5083 was DNA-dependent Protein Kinase, which displayed a 29.6-fold lower affinity to CB-5083 than displayed by VCP (Anderson et al., 2015).

Multiple myeloma, colorectal and non-small cell lung cancer cell lines were used to establish xenograft models for testing CB-5083 *in vivo* (Figure 3.1B). 50 % of mice had complete tumour regression in the AMO-1 multiple myeloma cell line after 12 days of treatment with CB-5083. The colorectal cell line HCT116 displayed 78 % inhibition of tumour growth compared to vehicle control, but tumour growth inhibition was abrogated in tumours harboring the

VCP^{T688A} mutation that confers resistance to CB-5083. Comparatively, proteasomal inhibitors displayed no inhibition in HCT116 models, and 50 % and 37 % tumour growth inhibition in A459 cells with carfilzomib and bortezomib, respectively. These studies suggest VCP inhibition may yield higher levels of apoptosis and tumour growth delay than current FDA-approved proteasome inhibitors.

A



B

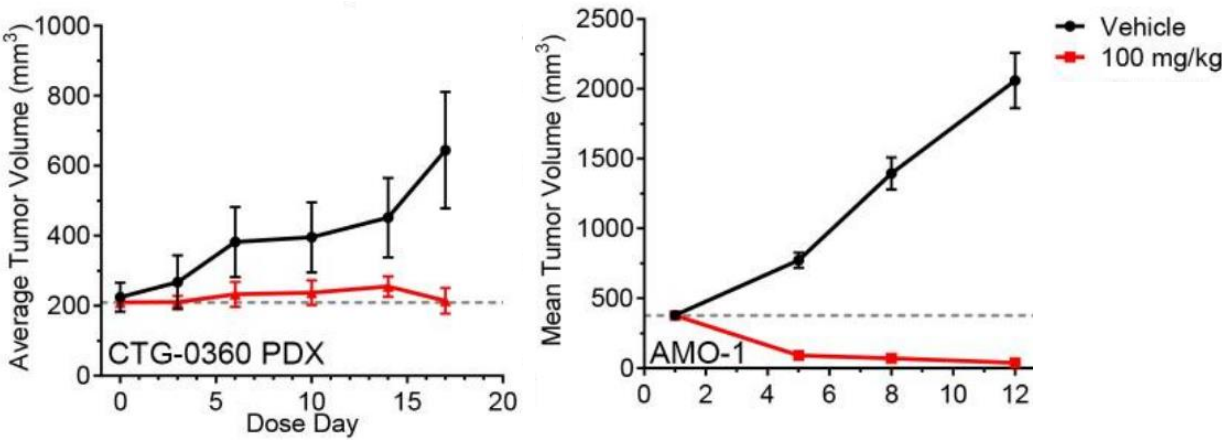


Figure 3.1 ***CB-5083 is a specific and potent inhibitor of VCP inhibitor.*** *(**A**) The 2D structure of CB-5083, which is related to DBeQ and ML240. (**B**) CB-5083 reduced tumour growth rate in mice xenograft models from multiple cell lines. CTG-0360 is a patient derived xenograft of colorectal adenocarcinoma origin, and demonstrated a sustained inhibition of tumour growth in CB-5083 treated mice. The AMO1 model, derived from multiple myeloma, exhibited complete tumour regression after twelve days of treatment. Mice were treated with 100mg/kg once daily via oral gavage in cycles of four days on and three days off. Adapted from Anderson et al 2015.*

Subsequently, these xenograft data led to phase I clinical trials in patients with solid tumours or multiple myeloma (NCT02243917). However, unexpected ocular dysfunction arising from the cross reaction of CB-5083 with phosphodiesterase 6 led to the early termination of the trial. To reduce this cross-reaction, CB-5083 was redeveloped into the second-generation inhibitor CB-5339, which entered clinical trials for haematological malignancies and solid tumours in July 2020 (NCT04372641).

CB-5083 was modelled to bind to the D1 - D2 linker region in VCP as well as at a previously characterised binding site in the ATPase active site of D2 domain (Anderson et al., 2015; Bastola et al., 2017). The binding pocket in the D1 - D2 linker region utilised by CB-5083 is similar to that occupied by both UPCDC30245 and clotrimazole, but these compounds are reported to interact with different residues of VCP within the pocket. The extent to which these VCP inhibitors exploit the same binding site via different residues, or distinct but proximal allosteric binding sites is unclear. Mutations at residues 470, 472, 473 and 474 in the D1 - D2 linker region confer enhanced ATPase activity of VCP and resistance to CB-5083, and VCP^{E470X} has been most commonly used to study the mechanism underlying resistance (Bastola et al., 2017). CB-5083 resistance may arise due to the lower affinity of CB-5083 for VCP^{E470x}, or by increased ATPase activity of the mutant which demands a higher dose of CB-5083 for functional inhibition. Despite giving mechanistic insight into the binding of CB-5083 to VCP, mutations at VCP codon 470 are not observed clinically in any cancers within the TCGA database. However, it does suggest that resistance may be selected for over a relatively short duration of treatment through mutations in the key linker region and the use of VCP inhibitors in cancer may advance selection of resistance-conferring mutations in *VCP*. Patients who respond poorly or have a short-lived response to CB-5083, or the related CB-5339, should be

monitored in clinical trials for these mutations to determine whether these drugs exert a strong enough selective pressure to encourage development of resistance mutations in *VCP*. Modelling of CB-5083 binding to VCP supports the previous characterisation of the drug as both a competitive VCP inhibitor via binding to the D2 ATPase active site, and an allosteric inhibitor by binding to the D1 - D2 linker region. This allosteric inhibition, as with the VCP inhibitor NMS-873, prevents the full conformational changes between the D1 and D2 domains of VCP that is required for movement of the polypeptide through the central pore (Anderson et al., 2015; Segura-Cabrera et al., 2017).

CB-5083 was positioned as a long-term therapy for patients with solid tumours and haematological malignancies with the aim of reducing tumour growth. This approach is supported by the drugs ability to inhibit or regress tumour growth *in vivo* after multiple treatment cycles (Anderson et al., 2015). In these experiments targeting VCP disrupts the delicate balance of protein turnover in cancer cells that is necessary for sustained tumour growth, however in the thyroid cancer setting VCP is targeted to specifically reduce ER-associated degradation of NIS. This function of CB-5083 in modulating iodide uptake in thyroid cells was not considered in the initial development of the compound. Based on data that supports CB-5083 and CB-5339 as strong and potent VCP inhibitors across multiple cancer cell lines and tumour xenograft models, the application of these compounds to modify iodide uptake by inhibiting VCP-mediated NIS degradation was analysed. Given that these compounds are the only compounds which have proceeded to human clinical trials for the specific aim of targeting VCP, they represent the most translational putative strategy for targeting VCP in thyroid cancer. Additionally, CB-5083 and CB-5339 have overcome physical

properties of other reported VCP inhibitors such as clotrimazole, including poor bioavailability, which limits the administration of these compounds orally.

3.2 Materials and Methods

3.2.1 NIS-expressing Cell Models

For the following experiments, TPC1-NIS and 8505C-NIS cells were employed as thyroid cancer derived cell lines. L87-NIS cells represent a third cell line derived from mesenchymal stem cells, which have been engineered to stably express a CMV-driven NIS construct. Despite L87 cells being of non-thyroidal origin, they present a useful additional model to assess cell-specific effects conferred by VCP inhibitors.

3.2.2 Drug Treatments

CB-5083 was obtained from Cayman Chemical (19311) and CB-5339 was kindly provided by Cleave Therapeutics. Both compounds were resuspended in DMSO to a stock concentration of 10 mM. On the day of treatment, stocks were diluted in RPMI cell culture medium to a working solution of 10 µM and cells were treated at doses 0.05, 0.1, 0.25, 0.5 and 1.0 µM. The DMSO vehicle control was equalised across all doses.

3.2.3 Radioiodide Uptake Analysis

Each condition had six replicates of which two were treated with sodium perchlorate for one hour prior to addition of radioiodide. $1 \times 10^5 – 1.2 \times 10^5$ counts per minute I^{125} were added to each well and incubated at 37°C for one hour. Cells were washed in cold HBSS and lysed with 2 % SDS buffer. Activity of the lysates was measured using a gamma counter and protein quantification of the lysates was performed by BCA assay. The full radioiodide uptake assay

protocol is described in Section 2.4. Statistical analysis was completed on a minimum of n = 3 independent experiments.

3.2.4 Protein Analysis

Protein was harvested in cells using RIPA buffer. Protein quantification was performed by BCA assay. Samples were analysed by Western blot, as describe in Section 2.5.3. Membranes were incubated with antibody solution at 4°C overnight before being developed using chemiluminescent substrate and x-ray film. Antibodies used in this investigation were NIS, VCP and β-actin, the details of which can be found in (Table 2-5). Band densitometry analysis was performed using ImageJ FIJI plug-in where NIS expression was normalised to the β-actin loading control.

3.2.5 NanoBIT Protein-Protein Interaction Studies

NIS- LgBiT, NIS-SmBiT, VCP-LgBiT and NanoBiT control plasmids were used in these experiments, as described in Section 2.8.2. HeLa cells were prepared for NanoBIT as described in Section 2.8.3. Luminescence was measured on a PHERAstar plate reader, preheated to 37°C, at 120 s intervals for 20 cycles.

3.2.6 Statistical Analysis

Radioiodide uptake assays measuring CB-5083 and CB-5339 dose responses in TPC1-NIS, 8505C-NIS and L87-NIS cells were analysed by ANOVA with Dunnett's post-test using the DMSO- treated condition as the comparative control. Western blot band densitometry which quantified NIS protein level, normalised to the β-Actin control, was analysed using a paired, two-tailed t-test on a minimum of three biological repeats.

For assessing the significance of NanoBiT assay data, the luminescence value at cycle ten was log_{10} transformed to reduce the effect of inter-repeat variability, and analysed against the DMSO treated control by one-way ANOVA and Dunnett's post-test analysis.

3.3 Results

3.3.1 The VCP Inhibitor CB-5083 Increases Radioiodide Uptake

Although the efficacy of CB-5083 has been tested on a panel of 350 cancer cell lines, this did not include thyroid cancer cell lines and the effect of VCP inhibition on NIS function was not surveyed (Cleave Therapeutics, Personal Communication). TPC1-NIS and L87-NIS cell lines demonstrated a statistically significant increase in iodide uptake with 0.25 µM and 0.5 µM of CB-5083 at 24 hours (Figure 3.2A). NIS protein showed an increasing trend between 0.25 µM and 0.5 µM in both TPC1-NIS and L87-NIS cell lines (Figure 3.2C). Interestingly, 8505C-NIS cells displayed a strong decrease in iodide uptake in contrast to the significantly increased protein levels at the same doses (Figure 3.2). Densitometry analysis of NIS and VCP expression was performed against all doses of CB-5083 and demonstrated the drug does not affect VCP at the protein level (data not shown). Increased NIS protein levels are observed at both 75 kDa which represents fully glycosylated NIS monomers, and 60 kDa which represents hypoglycosylated NIS.

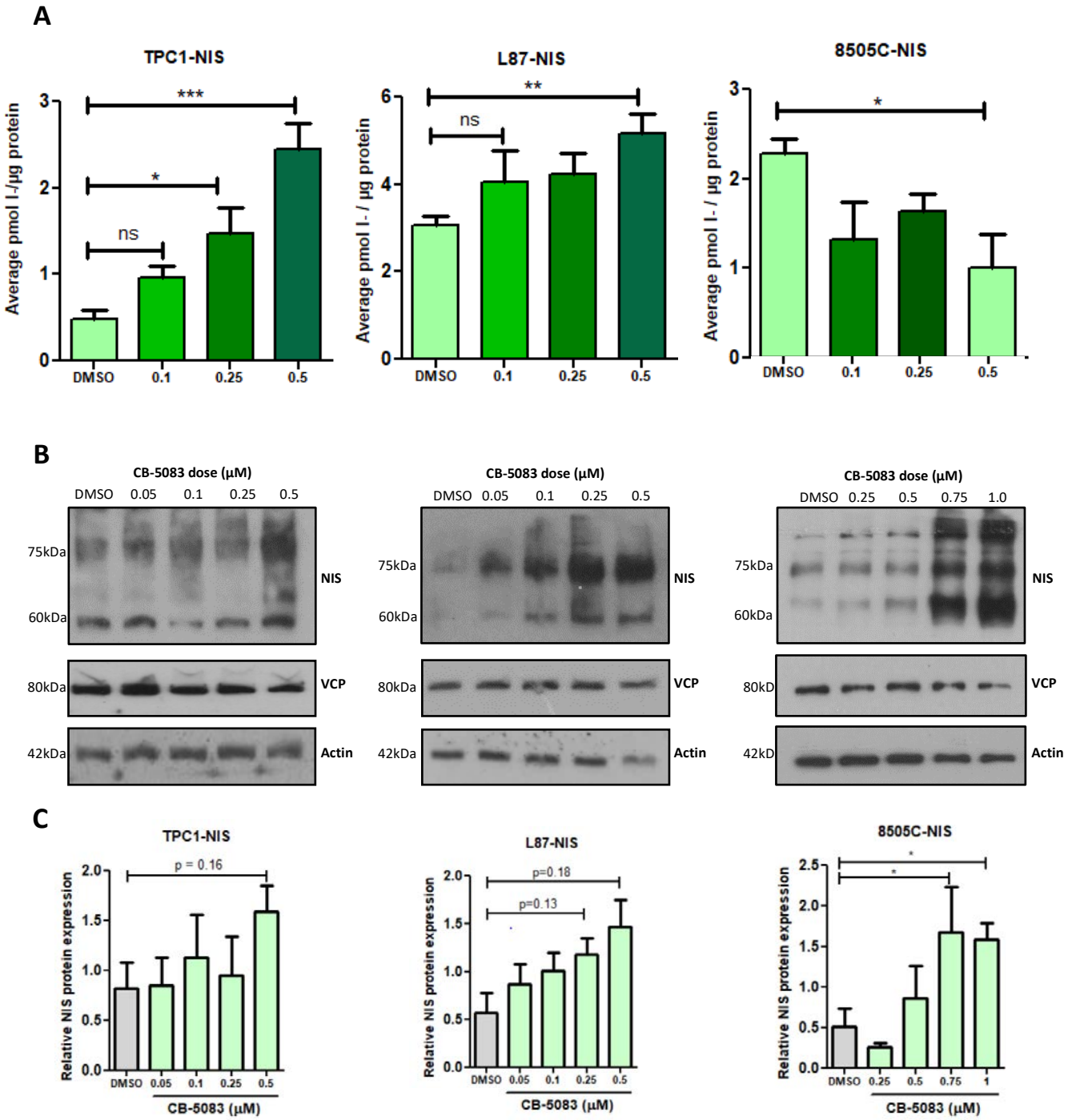


Figure 3.2 ***Effect of the VCP inhibitor CB-5083 on radioiodide uptake and protein level of NIS and VCP in TPC1-NIS, 8505C-NIS and L87-NIS after treatment for 24 hours.*** *(**A**) CB-5083 increases NIS-mediated iodide uptake in TPC1-NIS and L87-NIS cells as analysed by one way ANOVA. (**B**) NIS protein level increases across all cell lines after treatment with CB-5083 for 24 hours. (**C**) Densitometry analysis performed by normalising NIS protein level to β-Actin showed a consistent increase in NIS protein across all measured cell lines. Densitometry analysis on VCP protein level showed no change with increasing doses of CB-5083, data not shown. * = P < 0.05; ** = p < 0.01; *** = p < 0.001; ns= non-significant.*

Human primary thyrocytes were tested at the single dose of 0.25 µM due to the relatively small number of cells harvested from each sample. Despite these samples being obtained from benign multinodular goitre rather than thyroid carcinomas, and therefore less likely to overexpress *VCP*, these cells were responsive to CB-5083 resulting in an approximate 50 % increase in uptake (Figure 3.3).

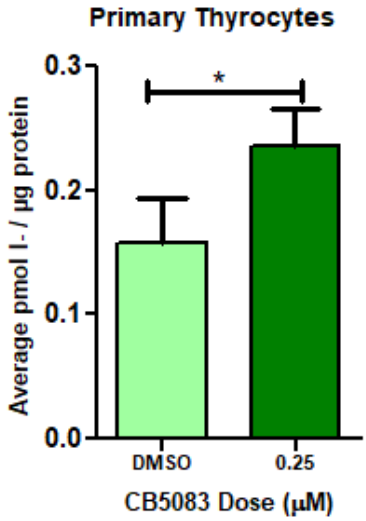


Figure 3.3 ***Human primary thyrocytes demonstrate a significant increase in radioiodide uptake at a CB-5083 dose of 0.25 µM.*** *Data were derived from five discrete multinodular goitre samples. Protein expression data from human primary tissue were unavailable due to the size of received samples. Statistical analysis was performed by paired, two-tailed t-test. * = p < 0.05.*

3.3.2 The VCP Inhibitor CB-5339 Modifies Radioiodide Uptake

CB-5339 is a second generation VCP inhibitor developed from CB-5083, with an IC_{50} of 9 nM. Currently, the structure of CB-5339 and the tumour response observed in mouse xenograft models after treatment with the compound are unpublished. However, the drug has recently moved into phase I clinical trials in multiple cancer settings suggesting encouraging pre-clinical data. The efficacy of CB-5339 in improving NIS-mediated iodide uptake and NIS protein levels was assessed by radioiodide uptake and Western blot.

Contrary to the substantial increase in iodide uptake measured in TPC1-NIS cells after treatment with CB-5083, these cells did not display robust changes in either I^{125} uptake or NIS protein expression after treatment with CB-5339 (Figure 3.4A). CB-5339 induced a ~2.5-fold increase in NIS-mediated iodide uptake in the L87-NIS cell lines at 0.25 µM and 0.5 µM and 8505C-NIS exhibited a downward trend in iodide uptake consistent with CB-5083 treatment (Figure 3.4A). In a similar response to CB-5083, L87-NIS and 8505C-NIS cells displayed an induction of NIS protein after treatment with 0.5 µM CB-5339 (Figure 3.4B), confirmed by densitometry analysis on NIS protein. Densitometry analysis demonstrated VCP protein expression was not significantly changed by CB-5339. Again, treatment with CB-5339 was associated with an increase in both fully glycosylated and hypoglycosylated forms of NIS protein, measured at 75 kDa and 60 kDa, respectively.

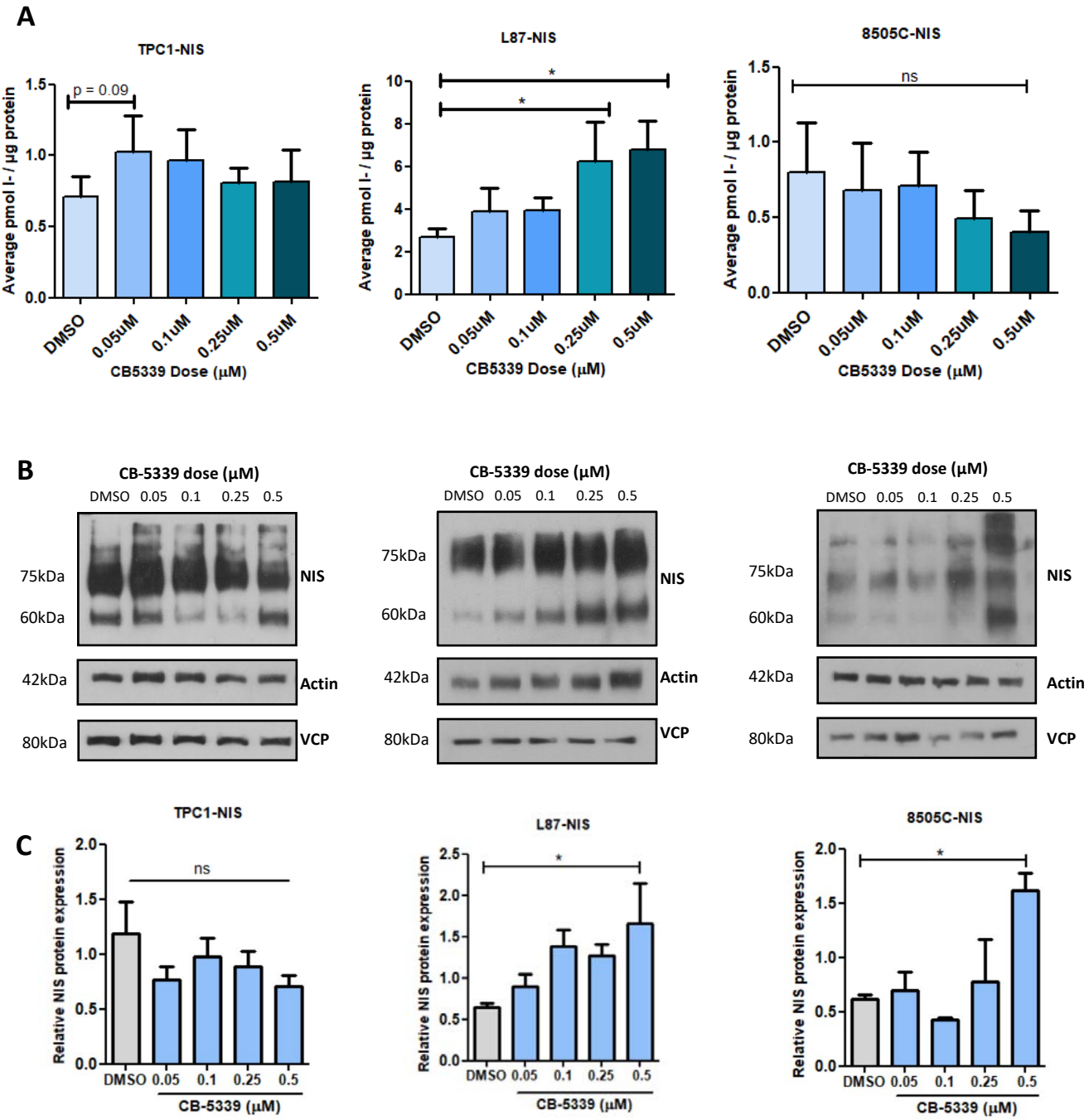


Figure 3.4 ***Effect of the VCP inhibitor CB-5339 on radioiodide uptake and NIS and VCP protein levels in TPC1-NIS, 8505C-NIS and L87-NIS cells after treatment for 24 hours.*** *(**A**) CB-5339 increases NIS-mediated iodide uptake in L87-NIS cells as analysed by one way ANOVA. (**B**) NIS protein level increases across after treatment with CB-5339 for 24 hours in 8505C-NIS and L87-NIS cells. (**C**) Densitometry analysis performed by normalising NIS protein level to Actin housekeeping gene showed a significant increase in NIS protein in L87 and 8505C-NIS cell lines, as analysed by one-way ANOVA after n = 3 to n = 6 experimental repeats. Densitometry analysis on VCP protein level showed no change with increasing doses of CB-5339, data not shown. * = P < 0.05; ns= non-significant.*

3.3.3 CB-5083 and CB-5339 Disrupt the Interaction Between NIS and VCP

To examine whether CB-5083 and CB-5339 altered the affinity of the NIS-VCP binding, protein-protein interaction experiments were performed using NanoBIT technology. Previously, it has been shown that the NIS and VCP interaction may still occur in the presence of the VCP inhibitors clotrimazole and ebastine; NanoBiT provides an alternative and sensitive approach to measure these protein interactions in the presence of the new class of VCP inhibitors. CB-5083 and CB-5339 significantly disrupted the physical interaction between NIS and VCP (Figure 3.5). These data substantiate the hypothesis that VCP inhibitors result in elevated NIS protein by preventing reducing diversion of NIS towards VCP-mediated ERAD. Treatment with 0.5 µM CB-5083 reduced luminescence emitted by 1.52-fold whereas treatment with the same dose of CB-5339 caused a 2.4-fold reduction. This may partially reflect the lower IC_{50} of CB-5339 at 9 nM, compared to 11 nM for CB-5083.

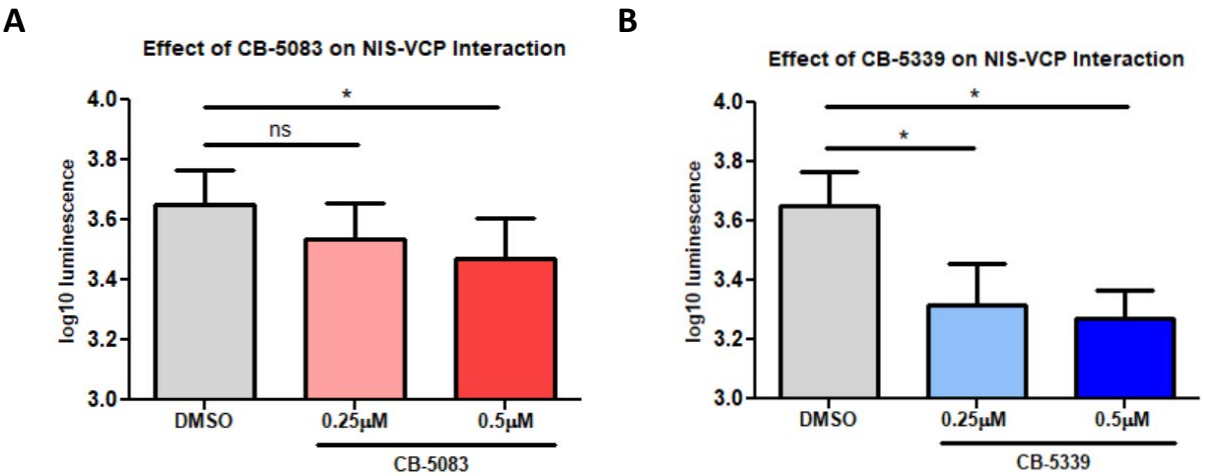


Figure 3.5 ***The VCP inhibitors CB-5083 and CB-5339 disrupt the interaction between NIS and VCP in HeLa cells after treatment with 0.5µm for 24 hours****; analysed by one-way ANOVA. * = p < 0.05; ns = non-significant. CB-5083 dose response n=5; CB-5339 dose response n=3 experimental repeats.*

3.3.4 CB-5083 and CB-5339 Disrupt NIS Dimerisation

NIS has been previously reported to dimerise, however the impact of dimerisation on function is not known, and whether VCP binds monomeric or dimeric NIS is not clear (Thompson et al., 2019). Therefore, the effect of the VCP inhibitors CB-5083 and CB-5339 on NIS dimerisation was assessed by NanoBiT. CB-5083 and CB-5339 significantly disrupted NIS dimerisation (Figure 3.6). Treatment with 0.5 µM CB-5083 resulted in a 1.95-fold decrease in luminescence, whereas treatment with CB-5339 resulted in a 3-fold reduction in luminescence, again positioning CB-5339 as the more effective of the two compounds.

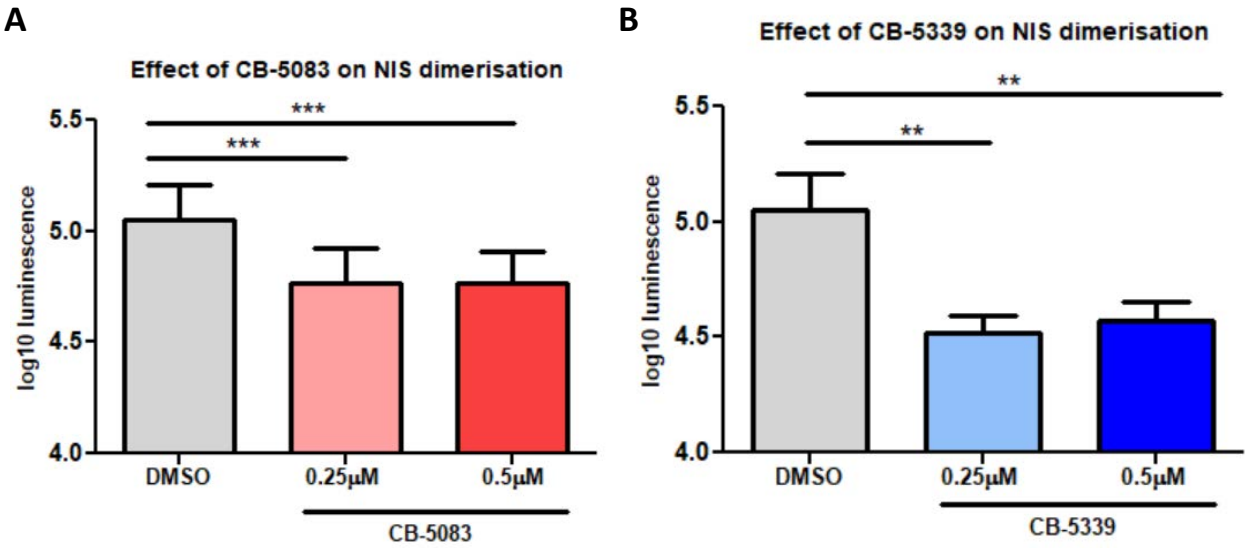


Figure 3.6 ***The VCP inhibitors CB-5083 and CB-5339 disrupt the interaction between NIS monomers.*** *Treatment of HeLa cells with 0.25 µM and 0.5 µM for 24 hours resulted in reduced luminescence emitted by the NIS-SmBiT and VCP-LgBiT interaction, as analysed by one-way ANOVA. *** = p < 0.001; ** = p< 0.01. CB-5083 dose response n=5; CB-5339 dose response n=3 experimental repeats.*

3.4 Discussion

3.4.1 VCP Inhibitors CB-5083 and CB-5339 Can Modify Iodide Uptake *in vitro*

Despite CB-5083 exerting a strong inductive effect on radioiodide uptake in TPC1-NIS, L87-NIS cells, and human primary thyrocytes, there were inconsistencies between treatment with CB-5339 in the TPC1 NIS cell line which questioned the efficacy of using this compound in a thyroid cancer setting. TPC1-NIS constitutes a papillary thyroid cancer cell model, given that 80% of all thyroid carcinomas are of papillary origin, the response of TPC1 cells to compound *in vitro* is of paramount interest. Although the second-generation VCP inhibitor CB-5339 showed a positive response in L87-NIS cells that was consistent with CB-5083 treatment, the drug did not elicit the same effects as the related compound CB-5083 in TPC1-NIS cells. The reasons for this are unknown as structural changes between CB-5083 and CB-5339 are minimal (Cleave Therapeutics; personal communication), and data in Figure 3.5 suggest that both CB-5083 and CB-5339 interrupt the interaction between NIS and VCP in HeLa cells. The response of L87-NIS cells to CB-5083 and CB-5339 was consistently optimistic and iodide uptake increased by 1.7x and 2.6x at 0.5µM each compound, respectively. Although this indicates that targeting VCP may result in high radioiodide uptake, it must be considered that L87 mesenchymal stem cells are not a physiological representation of thyroid epithelial cells and remain solely an *in vitro* tool for observing changes in iodide uptake.

From the data presented, CB-5083 remains the stronger compound to improve radioiodide uptake via VCP inhibition, given its efficacy across three cell lines tested compared to CB-5339 which showed a positive effect on L87-NIS cells only. The discrepancy in the effect of CB-5339 compared to CB-5083 demands further investigation using a broader range of cancer cell lines

and employing human and mouse thyrocytes for appraisal in more physiological cell models. In this investigation, access to human and murine primary thyroid material for testing CB-5339 was prevented by the COVID-19 pandemic and data will be collected in coming months.

Notably, a significant decrease in iodide uptake was observed after treatment with both CB-5083 and CB-5339 in 8505C-NIS cells, which is paradoxical to the elevated NIS protein levels observed at the same doses. This cell-specific response may result from variations in post-translational processing of NIS between cell lines resulting in variable timeframes for NIS to reach the plasma membrane and confer changes in radioiodide uptake capacity. Alternatively, the lack of effect of CB-5083 in 8505C-NIS cells may be artefactual and a result of specific mutations within the monoclonal cell population. 8505C-NIS cells and TPC1-NIS have different genetic drivers: TPC1 cells harbour a *RET/PTC* rearrangement while 8505C cells are homozygous for the $BRAF^{V600E}$ mutation. If the lack of response to CB-5083 and CB-5339 is a product of dysregulated protein trafficking resulting from a $BRAF^{V600E}$ mutation, the future application of these inhibitors in the ~45% patients with $BRAF^{V600E}$-driven papillary thyroid cancer may be limited. Mislocalisation of NIS protein has been previously observed in studies of $BRAF^{V600E}$ driven tumours and may reflect dysregulation in other aspects of post-translational NIS processing (Choi et al., 2014). It should be investigated whether CB-5083 is effective in other cell lines which harbour this mutation, such as BCPAP cells. Within this investigation, these experiments were hindered by the lack of availability of BCPAP cells which stably express NIS.

Treatment with both CB-5083 and CB-5339 induced NIS protein in L87-NIS and 8505C-NIS cells, and in TPC1-NIS cells after treatment with CB-5083 only. Interestingly, the increase in

NIS protein was observed at both 75 kDa and 60 kDa which is thought to correspond to fully glycosylated and hypoglycosylated protein. Hypoglycosylated protein is classically considered *do novo* translated NIS mRNA, most likely representing protein in the ER lumen that has not yet become fully glycosylated, and could putatively accumulate when VCP is inhibited from extracting NIS protein from the ER. Evaluating the mRNA expression level of *SLC5A5* after treatment with CB-5083 and CB-5339 by quantitative PCR could discern whether CB-5083 and CB-5339 also act, at least partially, at the transcriptional level, and therefore whether the protein band at 60 kDa represents *de novo* NIS transcripts.

3.4.2 VCP Inhibitors CB-5083 and CB-5339 Disrupt NIS-Protein Interactions

Proximity ligation assay evidence previously suggested that NIS and VCP may still physically interact in the presence of the VCP inhibitor clotrimazole (Fletcher et al., 2020). The mechanism behind how targeting VCP may increase NIS-mediated iodide uptake is unclear if the interaction between NIS and VCP persists in the presence of an inhibitor. During this investigation, a novel method of measuring the NIS-VCP interaction by NanoBiT was employed. Data demonstrating an interaction between individual NIS monomers, as a result of NIS dimerisation, were used as positive controls in experiments described in Chapter 5, and showed a partial disruption to the NIS-VCP interaction in response to treatment with CB-5083 and CB-5339 (Figure 3.5Figure 3.6).

Interestingly, CB-5083 and CB-5339 also disrupted the NIS-NIS dimer interaction (Figure 3.6). Overexpression of VCP has been associated with loss of the higher molecular weight NIS band on Western blot, which was predicted to be the NIS dimer, and this was rationalised by the

hypothesis that VCP preferentially degrades the NIS dimer during ERAD (Fletcher, 2018). If this were this case, it would have been expected that treatment with VCP inhibitors would result in the increased NIS dimerisation that would be reflected by increased luminescence after treatment with CB-5083 or CB-5339, but instead the opposite was observed (Figure 3.6). Alternatively, the higher molecular weight band on Western blots may represent poly-ubiquitinated NIS prior to degradation, and the disulfide bridges that facilitate dimerisation of NIS may be fully reduced by loading buffer, so as only to present on a Western blot as monomeric NIS at 75 kDa-100 kDa. As the functional relevance of NIS dimerisation is not known, the effect of the disruption by CB-5083 and CB-5339 is also unclear. The data indicate that disrupting the degradation of NIS by treatment with VCP inhibitors results in fewer NIS dimers. Treatment with CB-5083 and CB-5339 at the same doses correlates with increased iodide uptake, thus implying that monomeric NIS is the optimal conformation for iodide uptake. This is consistent with observations that mutations in NIS which preclude dimerisation do not have a negative effect on the ion transport activity of the symporter (Thompson et al., 2019).

The function of NIS dimerisation may be explored by comparison to other members of solute carrier family 5 protein family. The choline transporter encoded by *SLC5A7* dimerises at the cell surface, and disruption of this dimerisation affects transport activity (Okuda et al., 2012). Dimerisation of other sodium- coupled neurotransmitter transporters is also reported to facilitate interaction with COPII vesicle machinery for trafficking to the membrane (Sitte et al., 2004). Comparatively, dimerisation of the sodium-glucose cotransporter, encoded by *SLC5A1,* is necessary for protein stability (Sasseville et al., 2016). Reported functions of dimerisation in NIS and related proteins all favour the hypothesis that disruption of NIS dimers could negatively affect NIS processing and function, whether it is through trafficking to the

membrane, protein stability, or iodide uptake capacity. Therefore, it must be considered how CB-5083 and CB-5339 may positively modulate iodide uptake while concurrently disrupting dimerisation. Previous analysis of protein samples indicated that 77.9 % of NIS exists as a dimer, 20.9 % of NIS exists as a tetramer and only 1.8 % of NIS exists as a monomer (Huc-Brandt et al., 2011). Considering this, NanoBIT technology is unlikely to differentiate between dimers and tetramers. It therefore follows that the disruption to the NIS-SmBiT and NIS-LgBiT interaction by VCP inhibitors similarly does not differentiate between the two oligomeric states. It should be considered instead whether CB-5083 and CB-5339 disrupt tetramers of NIS, which results in more dimers that may traffic to the plasma membrane more effectively and result in the increases in iodide uptake observed in Figure 3.2 and Figure 3.4.

The published characterisation of CB-5083 showed a 29.6-fold higher affinity to VCP than the closest measured protein, DNA-dependent protein kinase. However, not all possible protein binding partners were assessed leading to the unexpected cross-reaction with PDE6 during clinical trials (Cleave Therapeutics; personal communication, 2021). The redevelopment of this compound to CB-5339 specifically screened out PDE6 cross-reaction and result in a more specific VCP inhibitor than CB-5083 (Cleave Therapeutics; Personal Communication). This specificity is also reflected in the lower IC_{50} value of CB-5339 than CB-5083- which are 9 nM and 11 nM, respectively- which may enable a larger inhibitory effect on VCP to be exerted by CB-5339 (Anderson et al., 2015). Together, these data substantiate the hypothesis that VCP inhibitors result in elevated NIS protein by preventing reducing the diversion of NIS towards VCP-mediated ERAD.

The NIS-VCP interaction was reduced by both CB-5083 and CB-5339 (Figure 3.5). This suggests that the increase in NIS protein that is observed after treatment with VCP inhibitors is a result of reduced interactions between NIS and VCP leading to less NIS protein being degraded by ERAD. However, the interaction between NIS and VCP was not completely prohibited in the presence of VCP inhibitors. Treatment with CB-5339 at 0.5 µM resulted in the largest percentage reduction in NIS - VCP interactions of 58.1 %, compared to DMSO treated wells. This may also explain why interactions between NIS and VCP in the presence of a VCP inhibitor were still identified by proximity ligation assays (Fletcher et al., 2020). The notion that NIS and VCP can still interact in the presence of VCP inhibitors, albeit in a significantly reduced capacity, implies that VCP activity is not completely inhibited by CB-5083 or CB-5339. As inhibition of VCP over time is associated with CHOP-mediated apoptosis, the incomplete inhibition may enable an optimal balance of reducing degradation of NIS by ERAD without affecting cell viability. Furthermore, combination of VCP knockdown by siRNA and treatment with CB-5083 resulted in complete cell death in TPC1-NIS cells (data not shown), and doses of CB-5083 or CB-5339 above 1.0 µM resulted in extensive cell death. This implies that complete inhibition of the intracellular pool of VCP through multiple approaches is highly toxic, and while this is the desired outcome for inhibiting tumour growth, high levels of cell death are disadvantageous for maximising iodide uptake. While targeting VCP can produce increases in iodide uptake, it may be that additional increases to iodide uptake can only be achieved by simultaneously targeting other components of the NIS interactome to avoid counterproductively compromising cell viability.

3.5 Concluding Remarks

Data in this chapter have tested the previous findings that targeting VCP in thyroid cancer may result in a significant increase in radioiodide uptake. Treatment with CB-5083 provided moderate support of these findings as increased radioiodide uptake was observed in TPC1-NIS, primary thyroid cells, and the non-thyroidal L87-NIS cell model. However, the second thyroid cell model, 8505C-NIS cells, demonstrated a reduction in iodide uptake after treatment with CB-5083 and CB-5339 which necessitates further investigation into whether the 8505C genotype may confer an inadequate response. Treatment with CB-5339 failed to recapitulate the positive effects on radioiodide uptake in the TPC1-NIS cell line and its usefulness in inducing radioiodide uptake in thyroid cancer generally remains under investigation. Currently, CB-5339 is the only VCP inhibitor being explored in clinical trials as an anti-cancer therapy and these trials are focussed on reducing tumour growth. If CB-5339 can induce a robust increase in thyroidal iodide uptake in wild-type and thyroid cancer mouse models, it will remain an exciting strategy for optimising radioiodide therapy. The dosage and adverse events data derived from the CB-5339 trials will be of interest to thyroid cancer researchers. Nevertheless, treatment strategies for targeting VCP to induce apoptosis in tumours, and those to optimise plasma membrane NIS expression remain distinct therapeutic approaches.

4 Modifications to the Structure of Clotrimazole May Improve Radioiodide Uptake

4.1 Introduction

4.1.1 Modelling the Binding of Clotrimazole to VCP

The development of the early VCP inhibitors DBeQ, NMS-873, and Eeyarestatin-1 established a rationale for targeting VCP in cancer (Chou et al., 2011; Magnaghi et al., 2013; Wang et al., 2008), Figure 4.1). In tandem to the pre-clinical investigations of the specific VCP inhibitors CB-5083 and CB-5339, alternative VCP inhibitors were sought via a drug repurposing strategy. Drug repurposing refers to the identification of new uses for existing drugs which are currently, or have previously been, approved for specific indications. As the safety and pharmacokinetic profiles of these compounds have been established, drug repurposing is more cost-effective than novel drug synthesis, and reduces the timeframe of drug development. Segura-Cabrera *et al* employed an *in-silico* based blind docking model to analyse a library of FDA-approved compounds and identify hits which may also function as allosteric VCP inhibitors (Segura-Cabrera et al., 2017). This modelling was based on the predicted binding of the inhibitor NMS-873 to VCP via the residues Lys-615 and Asn-616, which oriented towards the D1 - D2 interdomain linker (Figure 4.1). This binding region is also shared by the VCP inhibitor UPCDC30245, for which there is a resolved cryo-EM structure of the drug in complex with VCP (Banerjee et al., 2016). Initially, clotrimazole was proposed to serve as a VCP inhibitor based on predicted similarities in the way clotrimazole may bind to VCP, as compared to NMS-873 (Segura-Cabrera et al., 2017). Segura-Cabrera *et al* supported this hypothesis using data from the Broad Institute Connectivity Map (CMAP) which indicated that treatment of 293T cells with clotrimazole elicits an ER stress response that is comparable to the known VCP inhibitor Eeyarestatin-1. When evaluated in *in vitro* assays, clotrimazole perturbed VCP-mediated degradation of polyubiquitinated substrates and affected the

ATPase activity of both the D1 and D2 domains. Collectively, these data portray clotrimazole as a potential allosteric inhibitor of VCP.

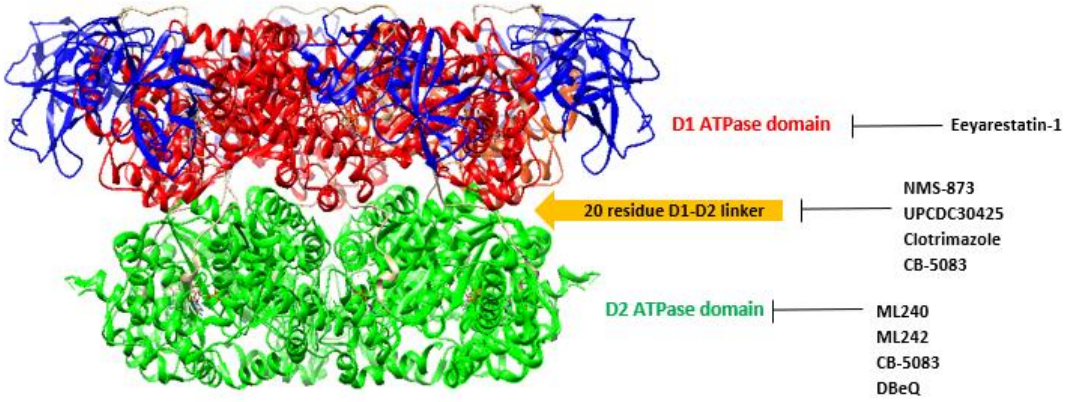


Figure 4.1 ***VCP structure and the regions targeted by known VCP inhibitors.*** *The most targeted regions are the D1 to D2 20 residue linker region which prevents conformational changes required for VCP function and the D2 domain which exerts the majority of the ATPase activity for enzyme function.*

4.1.2 Clotrimazole Increases NIS-mediated Iodide Uptake in Thyroid Cells

VCP is a functional interactor of the key thyroid protein the sodium/iodide symporter, and targeting VCP *in vitro* can increase NIS-mediated radioiodide uptake (Fletcher et al., 2020). Clotrimazole and ebastine were both identified as potential VCP inhibitors through the drug repurposing studies by Segura-Cabrera *et al*, and treatment of TPC1-NIS cells with these compounds resulted in significantly higher levels of membrane bound NIS (Fletcher et al., 2020; Segura-Cabrera et al., 2017). Treatment with clotrimazole for only 24 hours resulted in an at least two-fold increase in iodide uptake (Figure 4.2). This work was recapitulated in MDAMB-231-NIS breast cells, and both mouse and human primary thyroid cells (Fletcher et al., 2020).

Clotrimazole is currently approved by the FDA for use as an anti-fungal medication. It is active against the *Candida* genus and exerts its antimycotic effects by inhibiting the biosynthesis of ergosterol, thereby stalling growth (Crowley and Gallagher, 2014). Despite both clotrimazole and ebastine showing promise in thyroid cancer systems, ebastine has high levels of conversion to its metabolite carebastine and requires a higher dose to impact radioiodide uptake than clotrimazole, and therefore clotrimazole was selected for ongoing studies. However, just like ebastine, clotrimazole is poorly water-soluble, with a relatively high partition coefficient (logP), which limits its use in internal *in vivo* applications.

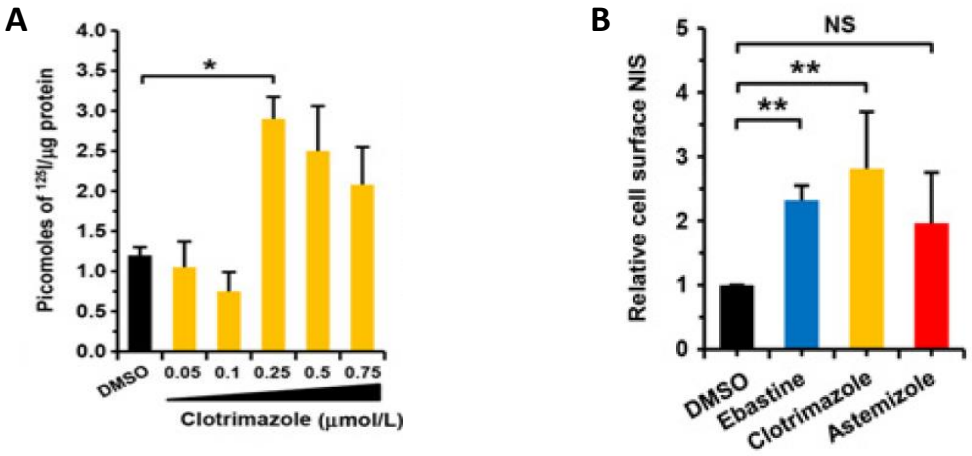


Figure 4.2 ***Treatment with clotrimazole increases NIS-mediated iodide uptake in TPC1-NIS cells.*** *(**A**) 24 hour treatment with clotrimazole increases radioiodide uptake in a dose dependent manner with an optimal dose of 0.25 µM and treatment for 24 hours. (**B**) 24 hour treatment with 0.25 µM clotrimazole and 0.5 µM ebastine increased the proportion of membrane bound NIS resulting in the observed increases in NIS-mediated iodide uptake. Adapted from Fletcher et al 2020.*

LogP is a measurement of the solubility of a compound in hydrophobic and hydrophilic solvents. As logP is a measure of lipophilicity, it can provide information on how effectively compounds cross lipid membranes. The logP values of known VCP inhibitors are shown in (Table 4-1). For orally delivered drugs to achieve over 80 % bioavailability the optimal value is

below three, with Table 4-1 indicating that a breadth of VCP inhibitors display poor bioavailability.

Drug	Predicted logP
Clotrimazole	5
Ebastine	7.2
Astemizole	6
CB-5083	3.1
CB-5339	Not Available
NMS-873	4.9
Eeyarestatin-1	4.2
UPCDC30245	4.7
DBeQ	5.3
ML240	4.5

Table 4-1 ***The predicted logP values of reported VCP inhibitors****. Values were calculated using PubChem XLogP3 3.0 software (PubChem release 2019.06.18). logP values between zero and three are optimal for high bioavailability of orally delivered drugs. Of the reported VCP inhibitors, only CB-5083's logP value resides close to this optimal range. Data for CB-5339 are unavailable as the structure of the compound has not been reported by Cleave Therapeutics.*

In 2019, an exploratory *in vivo* study delivered clotrimazole via oral gavage to wild-type mice with the aim of measuring changes in thyroidal iodide uptake. After normalisation of thyroidal iodide uptake to stomach uptake in both the pre- and post- treatment imaging, there was no observable difference in uptake of the technetium-99 tracer after treatment with clotrimazole for 24 hours (McCabe group, unpublished data). This study utilised wild-type mice which may not display overexpression of VCP, although thyrocytes from wild-type mice were responsive to clotrimazole *in vitro* (Fletcher et al., 2020). The absence of an effect of clotrimazole on *in vivo* thyroidal iodide uptake was conceivably due to poor drug bioavailability and sub-optimal accumulation in the thyroid to a threshold necessary to induce a measurable biological effect.

Using the *in-silico* modelling of clotrimazole and the resolved structure of UPCDC30245 in the allosteric binding pocket of VCP, it was predicted that structural modifications to clotrimazole may improve binding to VCP and be associated with improved bioavailability. As UPCDC30245 has not progressed in development as a VCP inhibitor, it has limited clinical utility. We hypothesised that the redevelopment of clotrimazole, an FDA- approved and well tolerated compound, into a more effective VCP inhibitor that exploits interactions identified in now-defunct VCP inhibitors may enable a more potent VCP inhibitor to be generated.

4.2 Materials and Methods

4.2.1 Drug Treatments

Clotrimazole was obtained from Alfa Aesar (J63895), and resuspended in DMSO to form a 10 mM stock solution that was stored at -20^{o}C. Clotrimazole-derived compounds were received in 10 mM stock solutions from Dr Holly Adcock (University of Birmingham, UK), described further in Section 4.2.3. Three iterations of compounds were tested as single agent treatments and alongside treatment with SAHA deacetylase for 24 hours to maximise NIS transcription. On the day of treatment, stock solutions were diluted in RPMI to 10 µM working solutions and cells were treated with 2.5 µM SAHA or DMSO control. After 12 hours cells were treated with 0.25 µM clotrimazole-derived compounds for a further 12 hours before analysis by radioiodide uptake assay, as described in Section 2.4.The DMSO vehicle control was equalised across all doses.

4.2.2 Radioiodide Uptake Assay

Radioiodide uptake assay data presented in this chapter presents was collected at both the University of Birmingham and Ludwig Maximilians-University in Germany. Both experimental protocols are outlined in Section 2.4 and, in brief, below.

Experiments performed at University of Birmingham

Two wells of six replicates were treated with sodium perchlorate for one hour prior to addition of 1 x 10^5 – 1.2 x 10^5 counts per minute radioiodide. After one hour incubation at 37°C, cells were washed with cold HBSS and lysed with 2 % SDS buffer. Counts per minutes were measured on a Berthold gamma counter as described in Section 2.4. Protein quantification of the lysates was performed by BCA assay as described in Section 2.5.2.

Experiments performed at Klinikum Großhadern, Munich, Germany.

Radioiodide and MTT assay and plates were identically seeded with four technical replicates per condition, and treated with clotrimazole at multiple doses. 1 x 10^5 counts per minute of I^{125} solution (10 mM NaI, HBSS, HEPES buffer adjusted to pH 7.3 with KOH) were added to radioiodide plates and simultaneously $NaClO_4$ was added to one well per condition to a final concentration of 100 µM. Plates were incubated at 37°C for 45 minutes then media was aspirated, and wells were washed with HBSS/HEPES solution. Cells were lysed with NaOH and samples were transferred to glass tubes for measuring counts on a Berthold Gamma Counter. Counts were normalised using MTT cell survival assay on corresponding plates, as described in Section 2.4.

4.2.3 Generating Clotrimazole-Derived Compounds

Modified clotrimazole compounds were synthesised by Dr Holly Adcock and Eleanor Garrett in the lab of Dr Liam Cox (School of Chemistry, University of Birmingham, UK). The synthetic strategy was based on the generation of analogues of clotrimazole, in order to establish which structures of the compound were pharmacologically active, and to investigate the relationship between structure and activity. The synthesis involved alkylation of an imidazole, or related heterocycles with functionalised triaryl and subsequently benzyl substituents. The analogues were designed to improve the physiochemical properties, as compared to clotrimazole, particularly the logP value in order to increase the aqueous solubility. Analogues were supplied in 10 mM DMSO solutions and stored at -20^{o}C. The 2-D and 3-D structures, molecular weight and logP values of all twenty compounds are displayed in Table 8-1 in the Appendix.

4.2.4 Computational Modelling of Clotrimazole Binding to VCP

The predicted binding of clotrimazole to an allosteric binding site on VCP was modelled by Dr Giovanni Bottegoni (University of Birmingham, UK). This modelling was performed using the UCSF Chimera Program using the 3D-coordinates from the cryo-EM resolved structure of VCP in complex with allosteric VCP inhibitor UPCDC30245 which was accessed via the protein data bank (Banerjee et al., 2016; Pettersen et al., 2004); PDB: 5FTJ). This model was optimised by comparison to structural analysis of other compounds in complex with VCP, which supported the confirmation of the isopropyl-piperazine chain of UPCDC30245 within the VCP binding pocket (Alverez et al., 2015). The optimised model acted as a template for the binding conformation of clotrimazole in the allosteric site of VCP. Comparison of clotrimazole and

UPCDC30245 structures showed a common basic nitrogen atom that was modelled to form hydrogen bonds with Glu-498 in the binding region within the D1-D2 linker of VCP. In UPDC30245 this nitro group is part of a piperidin-4-amino nitrogen and in clotrimazole it is part of the imidazole ringed structure.

4.2.5 Statistical Analysis

Clotrimazole-derived compounds were considered discrete groups and analysed using paired, two-tailed t-test between clotrimazole and the clotrimazole-derived compound. For groups which were co-treated with SAHA, these conditions were analysed using one way ANOVA between treatment with SAHA only, SAHA plus clotrimazole, and SAHA plus the clotrimazole analogue. Tukey's post-hoc multiple comparison test was applied to assess significance at $p < 0.05$.

4.3 Results

4.3.1 Clotrimazole Treatment Does Not Modify Iodide Uptake in L87-NIS Cells

Fletcher *et al* demonstrated an increase in iodide uptake in stable NIS-expressing thyroid (TPC1) and breast cells (MDA-MB-231) after treatment with the VCP inhibitors clotrimazole, astemizole and ebastine (Fletcher et al., 2020). In other studies, the iodide uptake function of NIS has been exploited in xenograft and orthotopic murine tumour models whereby exogenous NIS is delivered to the tumour site to enable tumour ablation by radioiodide therapy (Tutter et al., 2020; Urnauer et al., 2019). In this system , NIS is delivered by an injection of L87-NIS mesenchymal stem cells which accumulate at the tumour site by virtue of the tumour honing behaviour of stem cells (Tutter et al., 2020). VCP inhibitors which had

been shown to improve iodide uptake in NIS-expressing endocrine cells were assessed for their effect in L87-NIS mesenchymal stem cells.

L87-NIS cells showed no response to clotrimazole (Figure 4.3), and the drug treatments did not result in measurable cell death (data not shown). This contrasts to treatment of L87-NIS cells which demonstrated statistically significant increases in radioiodide uptake after treatment with the specific VCP inhibitors CB-5083 and CB-5339 (Figure 3.2 and Figure 3.4), and suggests that VCP inhibitors may be subject to cell-type specific effects.

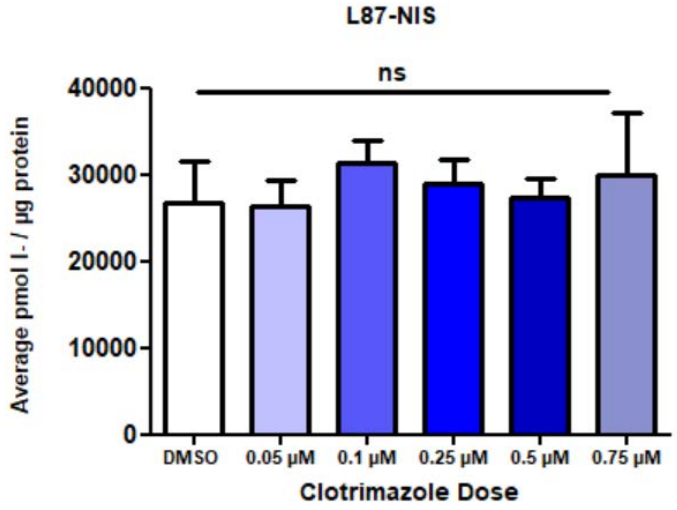


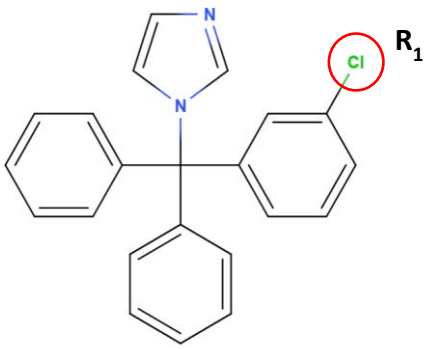
Figure 4.3 ***L87-NIS cells did not respond to increasing doses of clotrimazole after treatment for 24 hours.*** *This experiment was performed at Klinikum Großhadern, Munich and normalised to an MTT survival assay. Cell survival was not affected by increasing doses of clotrimazole (data not shown).*

4.3.2 Modifications to the Chloro-Substituted Aryl Ring of Clotrimazole Do Not Affect Iodide Uptake

Clotrimazole was shown to induce NIS-mediated iodide uptake by at least two-fold by Fletcher *et al* 2020. However, this observation did not translate to L87-NIS cells, as above. Similarly, exploratory *in vivo* experiments with clotrimazole did not modulate thyroidal iodide uptake in wild-type mice (McCabe group, unpublished data). Together, these suggest the potency of

the drug as a VCP inhibitor may limit the wider use of clotrimazole in this capacity. Consequently, an attempt was made to model, modify, and improve the interaction between clotrimazole and VCP to enhance the potency and specificity of the compound. While radioiodide uptake assays were performed 24 hours downstream of treatment in (Fletcher et al., 2020), timepoint optimisation on the cells utilised in these experiments determined that treatment for 12 hours was more consistent in eliciting an increase in radioiodide uptake.

In the first iteration of compounds, changes were made to the second phenyl ring, labelled R1, to assess its potential effect on the functionality of clotrimazole (Figure 4.4). This was to determine whether the chloride group was essential for VCP binding and whether it could be substituted with groups that theoretically improved binding to VCP or reduced the logP value of the compound. For these compounds, the logP values range from 4.07 to 4.76 (Figure 4.4), which are below the higher logP value of clotrimazole which is 5.37.



Compound Name	R1	logP
Clotrimazole	Cl	5.37
Compound-1	COOH	4.07
Compound-2	$CONH_2$	4.67
Compound-3	OH	4.69
Compound-4	$COOCH_3$	4.67
Compound-5	COC_4H_9NO	4.44
Compound-7	No R_1 group	4.76

Figure 4.4 ***Changes to the clotrimazole structure made during the first round of drug synthesis.*** *Changes were made to the chloro-substituted aryl ring labelled R1. Compound-6 provided by the lab of Dr Liam Cox was identical to the original clotrimazole compound and was removed from subsequent analysis.*

Experiments to test the novel clotrimazole derivatives included treatment combinations with the histone deacetylase SAHA with the aim of maximising NIS expression and function. The first round of screening compounds resulted in no changes to NIS-mediated iodide uptake, as compared to the original clotrimazole compound. Notably, treatment with clotrimazole as a single agent for 12 hours did not result in a statistically significant increase in iodide uptake compared to the DMSO control. Co-treatment with SAHA resulted in a more pronounced increase in radioiodide uptake than treatment with clotrimazole alone. Given the lack of change between DMSO and clotrimazole, the removal or substitution of the Cl group on R1, had significant effect on clotrimazole's capacity to enhance iodide uptake.

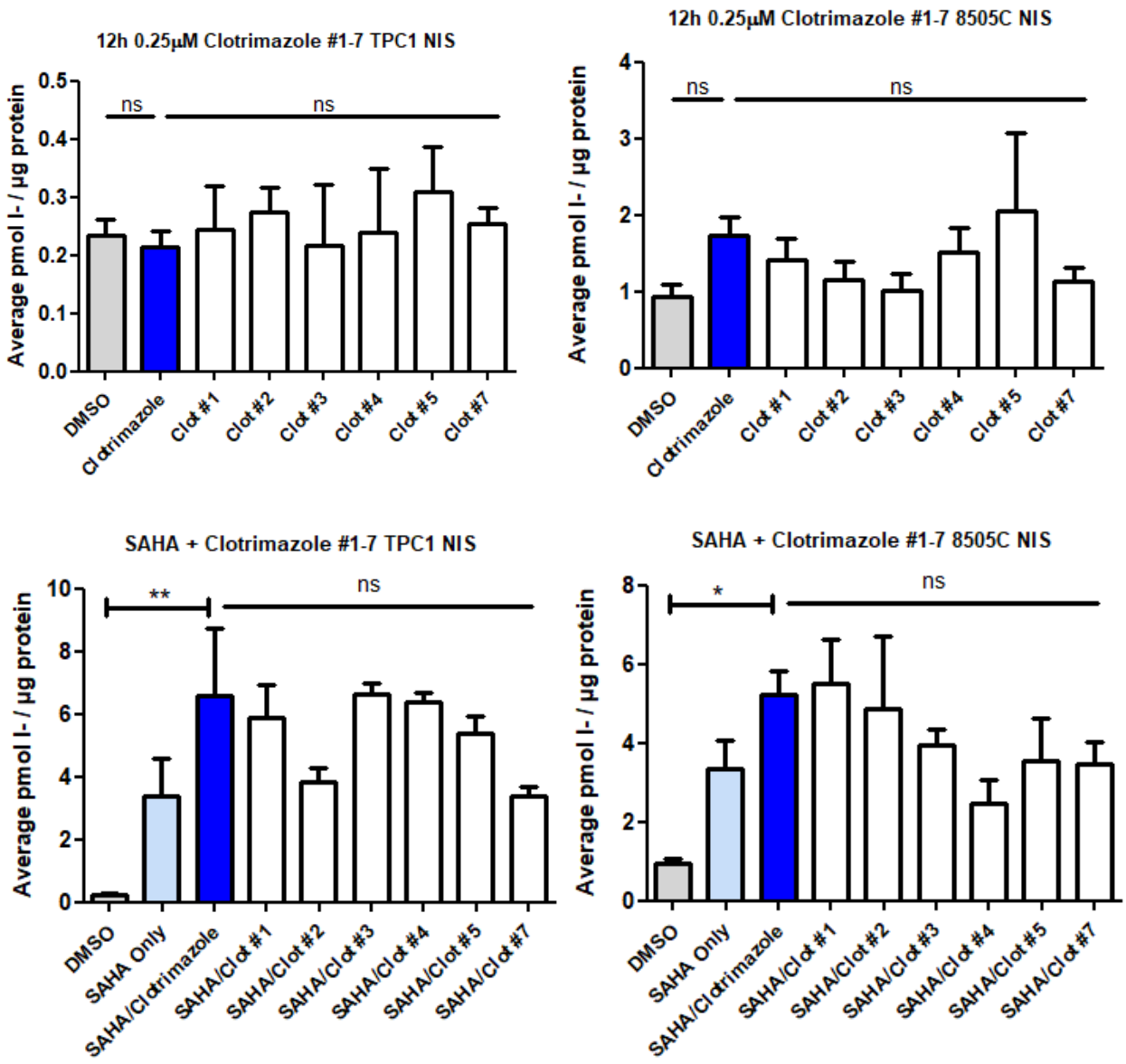
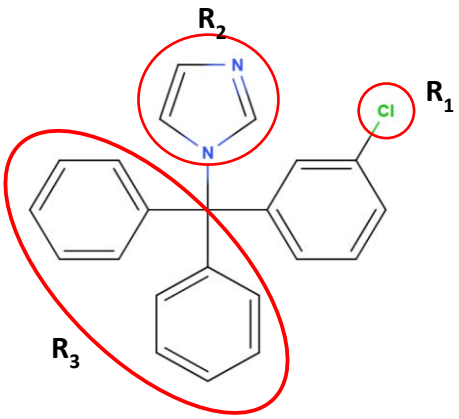


Figure 4.5 ***Removal of groups on the chloro-substituted aryl ring of clotrimazole had no effect on radioiodide uptake****. In the first round of screening clotrimazole derived compounds, cells were treated with the compounds at a dose of 0.25 µM for 12 hours. Cells were treated with clotrimazole compounds individually and alongside a 24 hour treatment with 2.5 µM SAHA deacetylase. n=3 experimental repeats.*

4.3.3 Modifications to the Imidazole Ring on Clotrimazole Can Increase Iodide Uptake

The second iteration of modifications included further modifications to R1, the addition of moieties to the imidazole ring (labelled R2), debulking of the second and third phenyl ring (labelled R3), and salt formulations to improve solubility (Figure 4.6). Loss of the two aryl rings aimed to reduce the molecular weight and logP of the compound.



Compound Name	R1	R2	R3	logP
Clotrimazole	Cl	$C_3H_4N_2$	$(C_6H_6)_2$	5.37
Compound-8	CH_2OH	$C_3H_4N_2$	$(C_6H_6)_2$	4.16
Compound-9	Cl	$C_3H_6N_2^+ + Cl^-$	$(C_6H_6)_2$	1.31
Compound-10	Cl	$C_3H_4N_2$	No R_3 group	1.91
Compound-11	Cl	$C_3H_4N_2NO_2$	$(C_6H_6)_2$	4.62
Compound-12	Cl	$C_3H_6N_2^+ + Cl^-$	No R_3 group	-2.14
Compound-13	Cl	$C_7H_6N_2$	$(C_6H_6)_2$	6.81
Compound-14	Cl	$C_2H_3N_3$	$(C_6H_6)_2$	4.78

Figure 4.6 ***Changes to the clotrimazole structure made during the second round of novel compounds.*** *Changes were made to the chloro-substituted aryl ring labelled R1, the imidazole ring labelled R2, and the two aryl substituent groups labelled R3.*

The second round of screening demonstrated a significant increase in iodide uptake after treatment with two of the clotrimazole analogues compared to treatment with the clotrimazole parent compound. Compound-11 resulted increased iodide uptake in 8505C-NIS cells when co-treated with SAHA (Figure 4.7). In TCP1-NIS cells there was an upwards trend in iodide uptake after treatment with compound-11 as a single agent, although TPC1-NIS cells did not demonstrate an increase in iodide uptake after combined treatment with SAHA and compound-11. However, it is noticeable that in 8505C-NIS cells clotrimazole did not elicit an

increase in iodide uptake when treated alongside SAHA, compared to SAHA alone, nor as a single agent treatment against the DMSO control. Compound-12 demonstrated a significant increase in iodide uptake when co-treated with SAHA in 8505C-NIS cells, and there was an upwards trend after treatment with compound-12 alone in 8505C-NIS cells. TPC1-NIS cells did not show any changes in iodide uptake after treatment with compound-12.

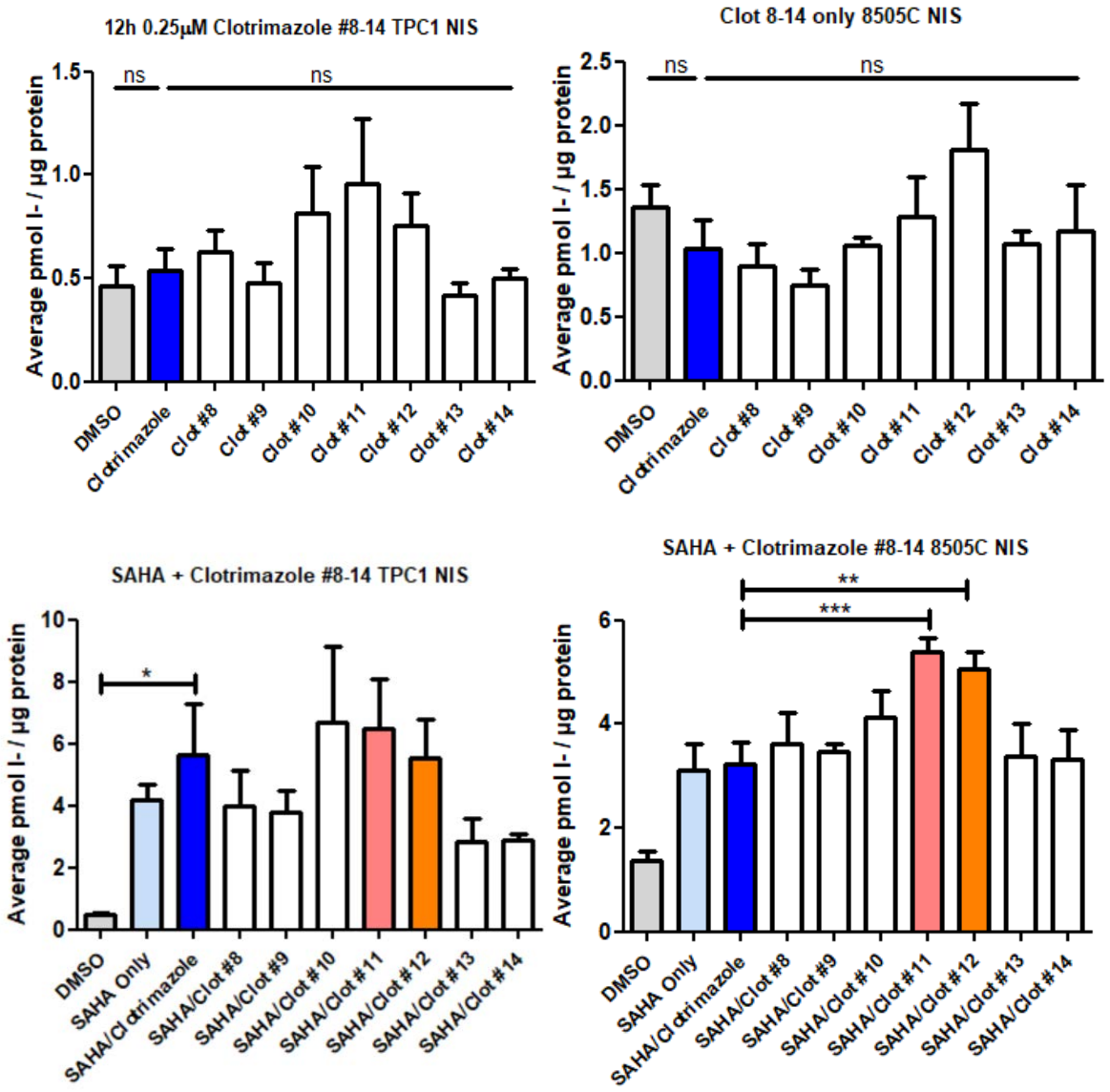


Figure 4.7 ***In the second iteration of analysing clotrimazole analogues, two compounds significantly increased iodide uptake when co-treated with SAHA in 8505C-NIS cells.*** *A significant increase in iodide uptake was observed in 8505C-NIS cells after treatment with SAHA + Compound-11 and SAHA + compound-12 as assessed by one way ANOVA. n=3 experimental repeats.*

Based on the effect of compound-11 and compound-12 on 8505C-NIS cells, its binding to VCP was modelled as described in Section 4.2.4. Compound-11 has a highly similar structure to the parent compound with the addition of a nitro functional group onto the imidazole ring. This modification may enable the structure to orient differently within the VCP binding pocket

and form a hydrogen bond interaction with Gln-494 of VCP (Figure 4.8B). During the synthesis of compound-12, the two non -substituted phenyl rings were removed, and the debulking of this compound made the structure less lipophilic, with a logP value of -2.14, compared to clotrimazole. Additionally, compound-12 was prepared as a hydrochloride salt, which can also affect the permeability of the compound. Modelling suggests that imidazole ring structure of compound-12 is now free to rotate and interact with Glu-498 of VCP via the basic nitrogen group, an interaction which is sterically excluded in clotrimazole due to the two aryl groups (Dr Giovanni Bottegoni, Personal Communication; Figure 4.8A). Hence, the increase in iodide uptake after treatment with compound-12 may be a result of either increased affinity for VCP or improved delivery across membranes by the hydrochloride salt formulation.

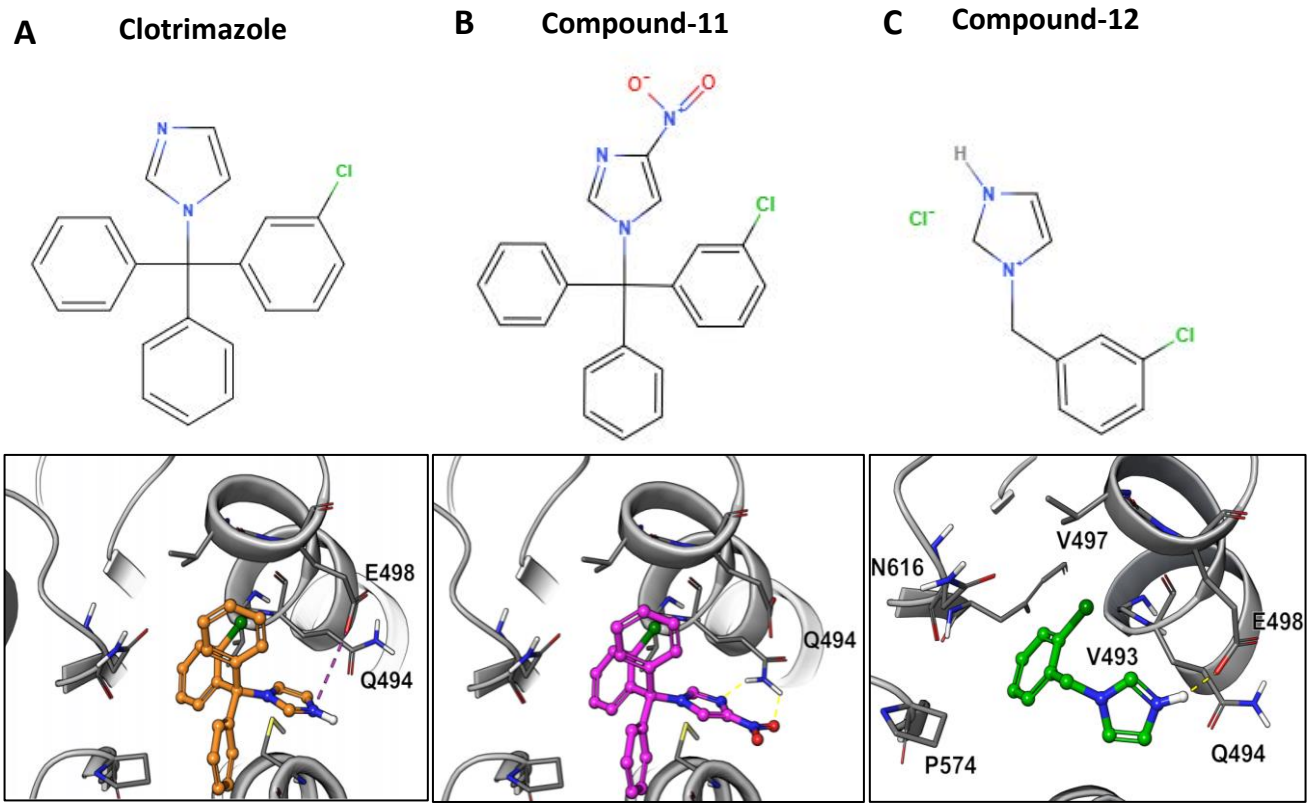
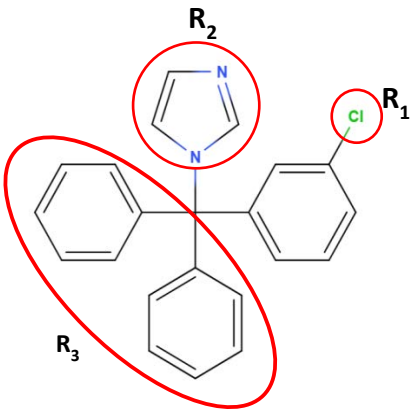


Figure 4.8 ***Modelling the binding of clotrimazole, compound-11 and compound-12 to VCP.*** *Modelling performed by Dr Giovanni Bottegoni using UCSF Chimera software. Orange = clotrimazole; purple = compound-11; green = compound-12; yellow dashed lines represent hydrogen bonds with residue in allosteric binding pocket of VCP. The long pink dashed line in (**A**) between clotrimazole and residue E498 represents the hydrogen interaction that is sterically excluded by this molecule, but that can be formed in (**C**) between compound-12 and E498 where it is represented by a shorter, yellow dashed line.*

The third iteration of compounds further built on the imidazole ringed side chains and salt formulations and included combinations of modifications tested in the second round of screening (Figure 4.9). Clotrimazole analogues in this group which did not have the second and third aryl ring structures has drastically reduced the logP values compared to clotrimazole.



Compound Name	R1	R2	R3	logP
Clotrimazole	Cl	$C_3H_4N_2$	$(C_6H_6)_2$	5.37
Compound-15	Cl	$C_4H_4N_3O$	$(C_6H_6)_2$	5.42
Compound-16	No R_1 group	$C_3H_6N_2^+ + Cl^-$	No R_3 group	-2.14
Compound-17	Cl	$C_3H_2N_3O_2$	No R_3 group	1.18
Compound-18	F	$C_3H_6N_2^+ + Cl^-$	No R_3 group	-2.64
Compound-19	F + F on $C_{2\ of}$ benzyl ring	$C_3H_6N_2^+ + Cl^-$	No R_3 group	-2.55
Compound-20	No R_1 group	$C_3H_6N_2^+ + Cl^-$	No R_3 group	-2.75
Compound-21	Cl	$C_3H_4N_2$	CO	2.31

Figure 4.9 ***Changes to the clotrimazole structure made during the third round of novel compounds****. Changes were made to the chloro-substituted aryl ring labelled R1, the imidazole ring labelled R2 and the two aryl substituent groups labelled R3. Combinations of changes tested in the first and second round of screening were also synthesised such as compound 16 which combines modifications previously tested in compounds 9 and 10.*

The final round of screening demonstrated that compound-17 was at least as effective as the parent compound in TPC1-NIS cells, and with an improved logP value of 1.18 (Figure 4.10). Despite being a structural amalgamation of compound-11 and compound-12, compound-17 was more effective in TPC1-NIS cells, compared to the stronger effect of compound-11 and compound-12 in 8505C-NIS cells. When analysed by one-way ANOVA, these compounds

approached significance in TPC1-NIS and were pursued in further cell lines for additional characterisation on drug efficacy.

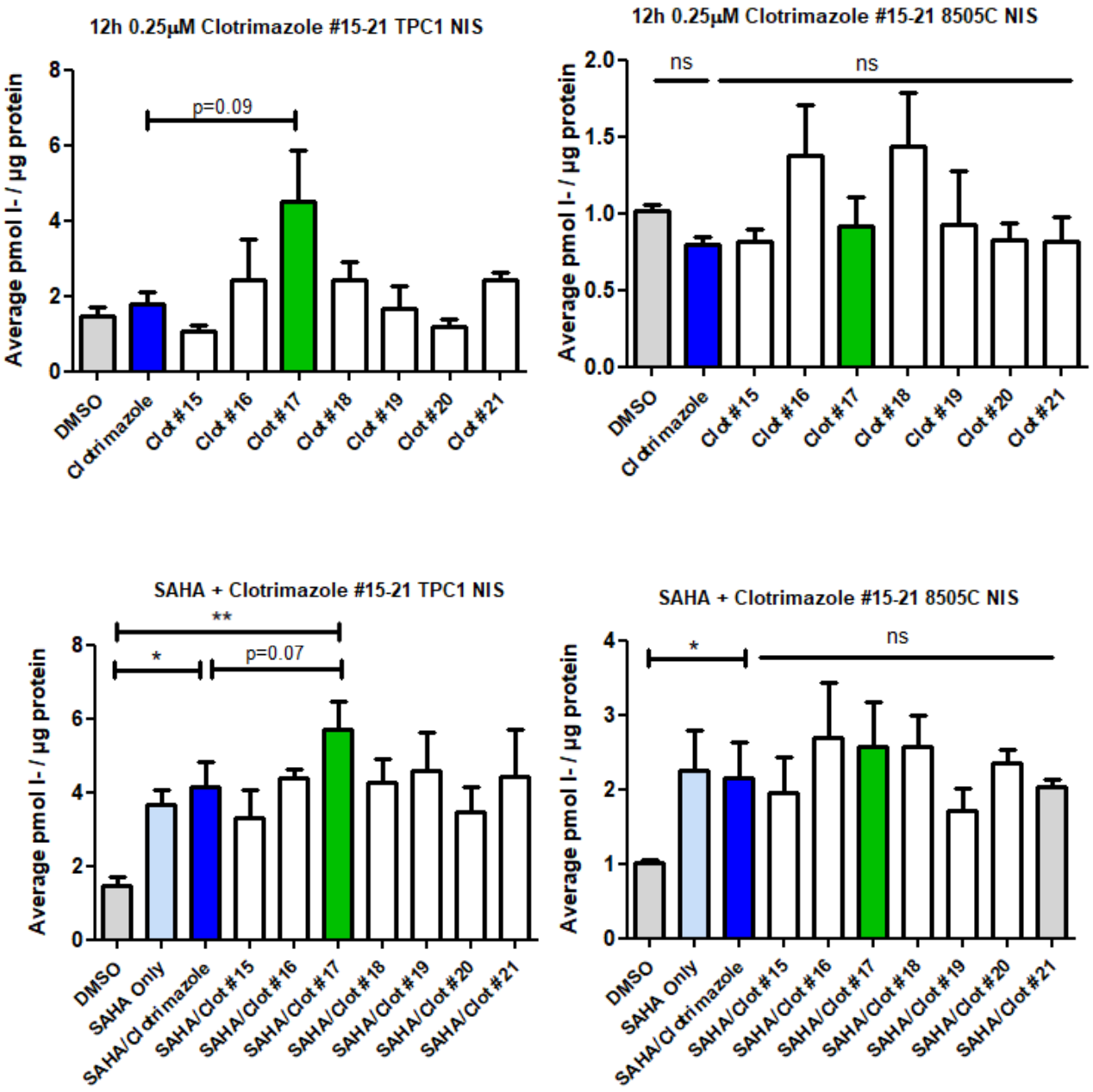


Figure 4.10 ***In the final round of screening clotrimazole analogues, TPC1-NIS cells treated with compound-17 resulted in statistically significant increases in radioiodide uptake.*** *Analysis of the effect of seven more clotrimazole-derived compounds when treated as a single agent treatment at 0.25 µM for 12 hours, and in combination with 2.5 µM SAHA for 24 hours in both TPC1-NIS and 8505C-NIS cell lines. n= 4 experimental repeats.*

Compound-17 combines the structural modifications of compound-11 and compound-12, although it was not prepared as a hydrochloride salt. This strengthened the hypothesis that removal of the second and third aryl ring and addition of a nitro-group onto the imidazole ring improved iodide uptake may enhance compound activity compared to clotrimazole alone. The predicted binding of compound-17 to the allosteric binding pocket of VCP was modelled (Figure 4.11). In this model, compound-17 interacts with Gln-494 which is consistent with the model of compound-11 binding to VCP. Although compound-12 was also predicted to rotate and bind to Glu-498, the model of compound-17 did not predict this additional interaction.

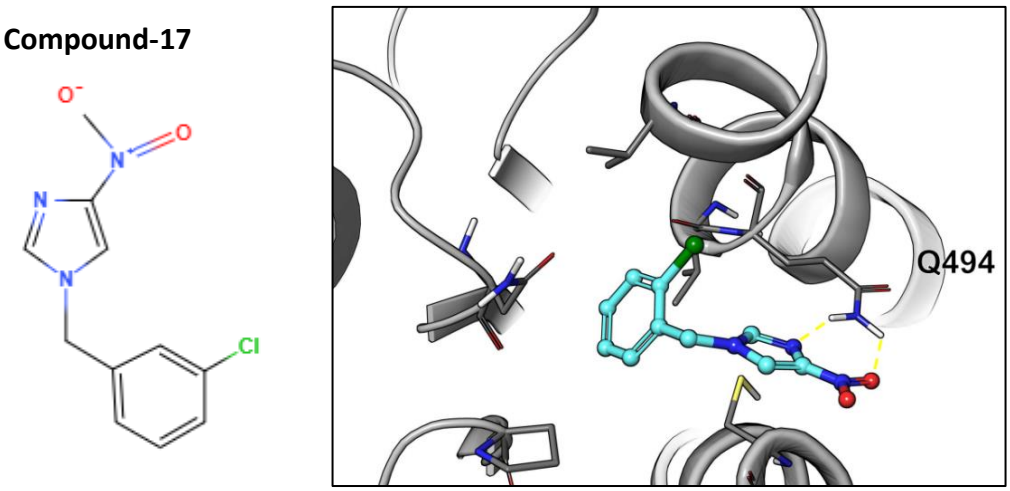


Figure 4.11 ***The binding of compound 17 to the allosteric binding pocket of VCP was modelled by Dr Giovanni Bottegoni****. It was predicated that debulking of compound-17 compared to clotrimazole may result in extended range of movement in the allosteric binding pocket which may facilitate enhanced interactions with Gln-494.*

4.3.4 Characterisation of Compound-17 in Additional Thyroid Cell Lines

To investigate whether compound-17 could increase iodide uptake in other cell models, the compound was tested on three established thyroid cancer cell lines and human primary thyrocytes (Figure 4.12). TPC1, 8505C and BCPAP cell lines have strongly repressed *SLC5A5*

expression and display minimal iodide uptake. To both stimulate NIS expression in these non-stable cell lines and recapitulate the condition which previously showed most uptake (Figure 4.10), these cells were treated with SAHA for 12 hours before the addition of compound-17 at three doses. BCPAP and 8505C cells demonstrated an upwards trend of iodide uptake with increasing doses of compound-17 (Figure 4.12B and C). In these cell lines, iodide counts were understandably lower compared to stable cell lines, rendering these changes statistically insignificant.

Given the inconsistency in the efficacy of clotrimazole treatment as a control in the NIS-stable cell lines, compound-17 was also tested in human primary thyrocytes alongside SAHA treatment. These samples were comprised of three genetically discrete human thyroid multinodular goitre samples. Compound-17 demonstrated a significant 2.59-fold increase in iodide uptake in compared to DMSO when treated alongside SAHA, and 1.89-fold change compared to SAHA treatment alone (Figure 4.12D).

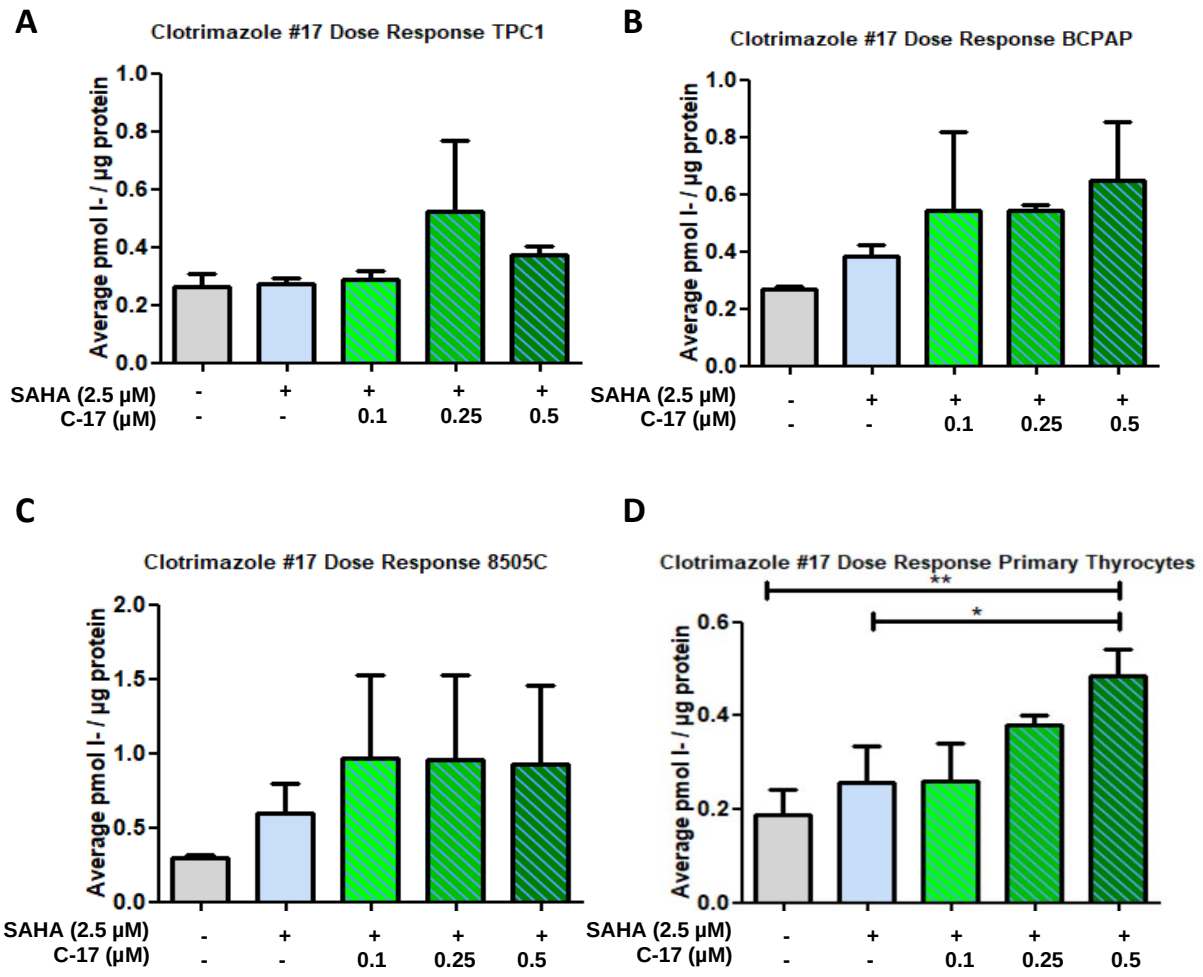


Figure 4.12 ***The effect of compound-17 on four additional cell lines was assessed.*** *An increase in iodide uptake between DMSO and SAHA treatment was observed in BCPAP and 8505C cell lines and a non-significant upwards trend with increasing dose of compound-17 co-treated with SAHA. Human primary thyrocytes derived from three different patient multinodular goitre samples demonstrated a significant increase in iodide uptake at 0.5µM compound-17. Compound-17 did not markedly affect cell survival, data not shown. C-17 = Compound-17.*

Three rounds of screening clotrimazole analogue compounds yielded two potential modifications which may subtly increase the effect of clotrimazole such that when combined, as in compound-17, resulted in an increase in NIS- mediated iodide uptake in multiple cell lines including human primary thyrocytes. In an endeavour to improve the potency of

compound-17, the structure of the drug was compared to the structure of the known VCP inhibitor UPCDC30245 and an overlapping model of these two inhibitors in the VCP binding pocket was modelled (Figure 4.13A). The UPCDC30245/compound-17 model was used to predict which additional moieties could be coupled to compound-17 to capture further drug-amino acid interactions within the VCP binding pocket that are exploited by the larger UPCDC30245 compound but not by clotrimazole (Figure 4.13B). Based on this overlapping model, it was predicted that addition of a fluoroindole group linked by a short carbon chain to the chloro-substituted aryl ring of compound-17 may project the drug into the space occupied by UPCDC30245. In the resolved cryo-EM structure of UPCDC30245 in complex with VCP, this fluoroindole moiety of UPCDC30245 putatively interacts with residues Val-497 and Asn-616, and these interactions can also be modelled by the fluoroindole conjugated to compound-17 (Figure 4.13D). This new compound, labelled GB002, was designed by Dr Giovanni Bottegoni (Figure 4.13C), it has a predicted logP value of 2.80 and is currently undergoing *in vitro* testing.

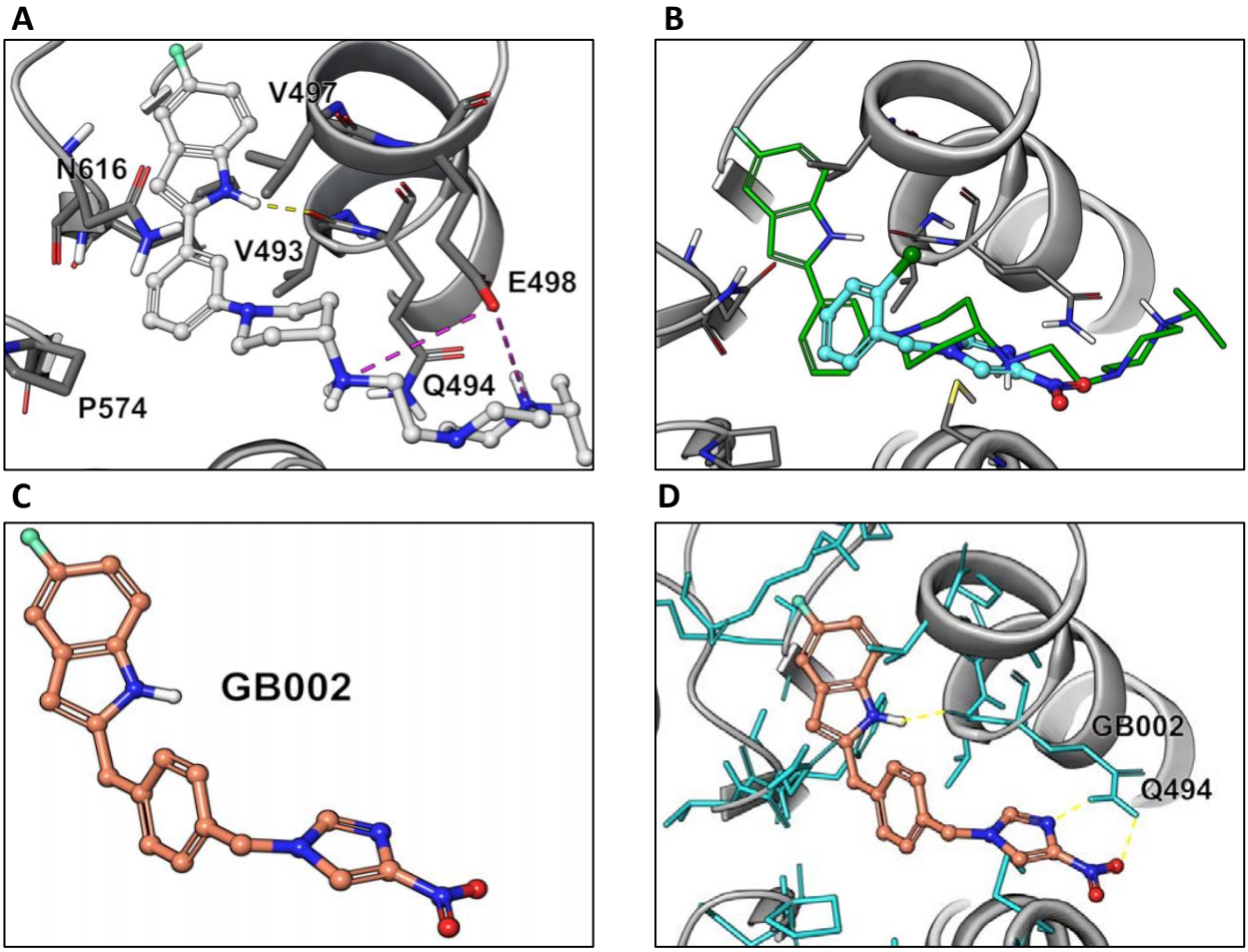


Figure 4.13 ***Compound-17 was redeveloped to GB002 based on an overlapping model with the VCP inhibitor UPCDC30245.*** *(A) UPCDC30245 modelled in the VCP allosteric binding pocket interacts with E498 via a basic nitrogen atom, based on the original cryo-EM structure identified by Banerjee et al 2016. The piperazine tail extends into the binding pocket further than the clotrimazole derived compound, compound-17, demonstrated by overlapping UPCDC30245 and compound-17 in (B). Based on this, GB002 was proposed as a modified compound-17 which mimics the piperazine tail of UPCDC30245 to capture further interactions with VCP residues forming the binding pocket. (D) GB002 modelled in the binding pocket of VCP. Modelling performed by Dr Giovanni Bottegoni at the University of Birmingham. Blue ion = Nitrogen; Red ion = Oxygen; Green ion = Fluorine; Yellow dashes = hydrogen bonds; pink dashes= hydrogen bonds predicted to form between compound-17 and VCP but which are sterically excluded between UPCDC30245 and VCP.*

4.4 Discussion

4.4.1 Structural Modifications to Clotrimazole Can Affect its Function as a VCP Inhibitor

Modified clotrimazole analogues were synthesised to achieve two primary aims: to improve potency so that the compound may be more effective, and to improve solubility after clotrimazole showed little efficacy in *in vivo* experiments. A total of twenty new compounds were assessed for efficacy in increasing radioiodide uptake. Of this pool, three compounds showed promise in being both efficacious at increasing radioiodide uptake, and having improved logP values.

The output of the investigations into the efficacy of the clotrimazole analogues was radioiodide uptake. This is an indirect measurement of the VCP inhibitor activity of these analogues that theoretically relies on disrupting the interaction between VCP and NIS which subsequently affects radioiodide uptake. However, the purpose of inhibiting VCP in thyroid cancer is to increase radioiodide uptake, and therefore this assay provides a useful output for this endpoint. In these experiments, the modelling of clotrimazole analogues to VCP is predictive of how these compounds may allosterically inhibit VCP and reduce NIS degradation, but they do not represent specific functional assays on how these analogues affect the ATPase activity of VCP.

The first round of screening new clotrimazole analogues determined that the substitution or removal of the chlorine group on the first aryl ring of clotrimazole did not significantly affect the function of the drug in modulating iodide uptake (Figure 4.5). This confirms the hypothesis that it is not the chloro-substituted aryl ring that acts as the pharmacophore of the compound

and mediates binding to VCP, but more likely the imidazole ringed structure, as predicted by the *in-silico* binding model. However, compound-7 represented the full clotrimazole structure without the single chloride group, and treatment with this compound caused a downwards trend in iodide uptake, as compared to treatment with clotrimazole or SAHA plus clotrimazole. Although this was non-significant (p= 0.13 between clotrimazole and compound-7 in 8505C-NIS cells), this repeated downwards trend was noted and the second and third round of analogue synthesis mostly retained the chloride ion in the R_1 group.

4.4.2 The Relationship Between the logP Value of Clotrimazole Analogues and Radioiodide Uptake

Of the twenty analogues that were tested, seventeen did not elicit significant changes in iodide uptake compared to the clotrimazole parent compound. Data from these compounds may be useful in determining how compounds-11, 12, and 17 may exert a positive effect on iodide uptake. For example, the structure of compound-9 was identical to clotrimazole but synthesised in a hydrochloride salt formulation, with a reduced logP value of 1.31 compared to the logP value of clotrimazole which is 5.37. This compound would be expected to possess enhanced crossing of the plasma membrane, and therefore increased iodide uptake compared to clotrimazole. However, treatment with compound-9 did not result in a measurable increase in iodide uptake either as a single agent treatment or in combination with SAHA. This implies that either the variability of clotrimazole response is not due to impeded delivery across a lipid bilayer but by the effectiveness of its interaction with VCP, or that this reduction in logP value is not enough to improve delivery of the compound across the plasma membrane.

A comparison between the effects of compound-10 and compound-12 can also directly appraise the impact of the logP value on drug efficacy. Both of these compounds have removed the second and third aryl rings which reduces the molecular weight and logP value, although compound-12 was also prepared as a hydrochloride salt. Treatment with compound-10, which has a logP value of 1.92, did not result in changes to iodide uptake compared to clotrimazole. However, compound-12, which has a logP value of -2.14, did significantly increase iodide uptake in 8505C-NIS cells when co-treated with SAHA. Hydrochloride salt preparations specifically aim to reduce logP and improve drug delivery across membranes. It is possible that the logP values of compound-9 and compound-10, which were 1.31 and 1.92 respectively, were not enough to elicit a further effect on VCP inhibition, although this could be achieved by combined removal of the two aryl groups and salt preparation in compound-12 which reduced the logP value further to -2.14. A negative logP indicates that a compound has a higher affinity for the aqueous phase over the lipid phase; the compound is more hydrophilic.

Compound-17 has a logP value of 1.18. Given that compounds with similar logP values have not demonstrated changes in iodide uptake, the relationship between logP value and drug efficacy is unclear. During *in vitro* experiments, the compounds were highly soluble in DMSO at concentrations of 10 mM. The logP value is vital when considering the efficacy of these compounds in *in vivo* settings, when DMSO is typically replaced by an alternative, safer solvent. In this case, a lower logP enables a compound to be dissolved in more commonly used solvents such as the 0.5 % methyl cellulose vehicle used in the CB-5083 *in vivo* investigations (Anderson et al., 2015).

4.4.3 Clotrimazole Analogues May Have Improved Binding to VCP

In vivo data showed that the logP value of the clotrimazole parent compound was a limiting factor for oral administration of the compound. However, modified compounds which have largely reduced logP values within what would be considered an orally bioavailable range, did not exert measurable changes in radioiodide uptake. This suggests that while logP value is a contributing factor to drug efficacy, and efforts should be made to reduce the value for improved solubility, it is not the only factor that affects how clotrimazole binds to and inhibits VCP.

This notion is also supported by the increase in iodide uptake after treatment with compound-11 which has a predicted logP value of 4.63. This indicates that modifications to the imidazole ring which facilitate interactions with additional residues in the VCP binding pocket can be sufficient to improve iodide uptake even with a relatively high logP. Compound-13, compound-14, and compound-15 also had modifications to the imidazole ring structure (Figure 4.6 and Figure 4.9), but did not induce changes in iodide uptake after treatment, as compared to clotrimazole. This suggests that it is the specific modification to the imidazole ring in compound-11, namely the addition of a nitro group, that is responsible for the 1.67-fold increase in iodide uptake that was observed when this compound was co-treated with SAHA. This is supported by the modelling of compound-11 in the allosteric binding pocket of VCP that predicts that the additional nitro group specifically facilitates formation of hydrogen bonds between the oxygen anion of the nitro group in compound-11 and Gln-494 of VCP (Figure 4.8B).

There was a degree of inconsistency in the cellular response to the original clotrimazole compound across cell lines and timepoints. The inconsistency of the effect of clotrimazole may be a result of the cell lines used to measure iodide uptake in these experiments, which differ from the TPC1-NIS cells utilised in experiments that initially demonstrated significant increases in iodide uptake after treatment with clotrimazole (Fletcher et al., 2020). The NIS-expression in TPC1 and 8505C-NIS stable cell lines is driven by the CMV promoter and maintained by culture in geneticin selection media. In contrast, the thyroid and breast cancer cell lines described in Fletcher *et al* were stable cell lines formed from lentiviral transduction with particles containing NIS, but also driven by the CMV promoter. Both cells are monoclonal populations; it is conceivable that the cellular differences from the distinct transformation protocols or differences between single clones used to populate the cell line result in the different responses to VCP inhibitors. Recently, a high-throughput assay was developed to measure iodide uptake via YFP-based luminescence (McCabe group, unpublished data). This assay was applied to a large library of compounds to measure their effects on iodide uptake in TPC1-NIS and 8505C-NIS cells. In these experiments, which utilised the same clonal TPC1-NIS and 8505C-NIS cells as used in this Chapter, clotrimazole was again identified as a compound that significantly increased iodide uptake. This observation supported the conclusions previously reported which show that treatment with clotrimazole can induce an increase in iodide uptake, and also demonstrated that this could be reproduced in the TPC1-NIS and 8505C-NIS cell lines used in these more recent experiments on clotrimazole analogues. In contrast to this, the data presented in Figure 4.5 suggest that additional treatment with SAHA is required for clotrimazole to significantly increase radioiodide uptake in these cell lines.

Despite this rationale, the distinct observations that TPC1-NIS and 8505C-NIS cells do not consistently respond to treatment with clotrimazole with a large-fold increase in radioiodide uptake questions the suitability of clotrimazole as a VCP inhibitor in the thyroid cancer setting. Additionally, when an observable increase in radioiodide uptake was observed in cell lines after treatment with 0.25µM clotrimazole, this was invariably statistically insignificant due to the small fold change difference between DMSO and clotrimazole. The translational endpoint of this work would be to offer patients a compound or compounds to improve the proportion of NIS at the plasma membrane in the short period prior to radioiodide therapy. Considering this, the fold changes observed after treatment with both the clotrimazole compound and the clotrimazole- derived compound-11, -12 and -17 are inadequate to boost uptake enough to present a clinical use. Although SAHA was used to exaggerate increases in radioiodide uptake by boosting NIS transcription, the response to SAHA may have overwhelmed small fold changes from the clotrimazole-derived compounds. The large, statistically significant increase in radioiodide uptake after treatment with SAHA indicated that SAHA itself may be sufficient to produce the large fold-changes in iodide uptake. Prior research has shown that stimulating *SLC5A5* expression does lead to increases in radioiodide uptake, and data in this chapter seek to maximise NIS protein levels by inhibiting concurrent VCP-mediated degradation of NIS. However, the data indicate that *de novo* NIS levels which have been stimulated by SAHA cannot be further augmented by clotrimazole or clotrimazole-derived compounds.

4.5 Concluding Remarks

Together, these data indicate that the VCP inhibition function of clotrimazole may be enhanced by addition of a nitro group to the imidazole ring and removal of two aryl rings which do not participate in VCP binding. The resolved cryo-EM structure of UPCDC30245 in complex with VCP has been critical in predicting which interactions may be exploited in the allosteric VCP binding pocket that these two inhibitors share. Structural modifications to clotrimazole can enable additional interactions with residues that are utilised by the now-obsolete VCP inhibitor UPCDC30245, and many of the clotrimazole analogues display enhance solubility as compared to clotrimazole. These modifications may result in formation of a compound which possesses the critical characteristics of being both a potent VCP inhibitor and orally bioavailable. The potential efficacy of the three clotrimazole-derived compounds which produced statistically significant increases in radioiodide uptake as compared to the parent compound is limited by the starkly small fold changes in iodide uptake that were observed, particularly compared to the previous findings by Fletcher *et al* that demonstrated a 2-3-fold increase in iodide uptake after treatment of TPC1 and MDA-MB-231 cells with clotrimazole. The final compound, GB002, may only represent a useful *in vitro* and *in vivo* tool for improving iodide uptake if the additional fluoroindole moiety drastically improves its VCP inhibitor function and subsequently causes larger fold-changes in radioiodide uptake. Future hypotheses should seek to determine whether these data indicate that clotrimazole and the twenty derived compounds tested in this investigation are insufficiently strong VCP inhibitors to produce an adequate change in radioiodide uptake, or whether targeting VCP itself is a flawed approach for improving radioiodide uptake.

5 Moesin and Annexin A1 Interact with NIS

5.1 Introduction

5.1.1 Moesin and Annexin A1 in Thyroid Cancer

Recent mass spectrometry experiments sought to identify interactors of the sodium iodide symporter (Fletcher, 2018). In this study, peptides of both moesin and annexin A1 were detected as binding to NIS from the plasma membrane fraction of cells. The investigation by Fletcher *et al* was the first to propose that targeting components of the NIS interactome may be a viable strategy for increasing radioiodide uptake in thyroid cancer. This research also highlighted VCP as a putative NIS interacting protein which was subsequently confirmed through multiple *in vitro* approaches (Fletcher et al., 2020). Further validation of NIS interacting proteins predicted by mass spectrometry data can elucidate additional targets that may improve iodide uptake beyond the increase provided by treatment with VCP inhibitors discussed in Chapter 3 and 4. Alternatively, targeting other NIS interactors may provide a summative approach for use alongside a VCP inhibitor to maximise iodide uptake in thyroid cancer cells.

Moesin (MSN) and annexin A1 (ANXA1) were both distinguished as biomarkers for thyroid cancer amongst a panel of diagnostic and prognostic genes that are upregulated in classical and tall cell variant papillary thyroid cancer compared to non-cancer controls (Ciregia et al., 2013; Ciregia et al., 2016; Giusti et al., 2008). Both moesin and annexin A1 protein are upregulated in both papillary and follicular thyroid cancer versus normal tissue controls (Brown et al., 2006; Martínez-Aguilar et al., 2016; Smith et al., 2019). The studies indicate that analysis of annexin A1 and moesin as specific protein markers may be useful in

discriminating between malignant and benign thyroid nodules at an earlier stage than is currently clinically used.

In this chapter, the mass spectrometry data that indicated moesin and annexin A1 can bind to NIS was challenged through protein-protein interaction studies. The dysregulation of moesin and annexin A1 in PTC tumour samples was explored using the THCA database from TCGA. Whilst these putative interacting proteins are analysed in tandem throughout these experiments, the functions underlying their interactions with NIS, as well as their particular roles in the thyroid cancer phenotype, are distinct.

5.2 Materials and Methods

5.2.1 Second-Round of Screening Putative NIS Interactors

The final list of sixty-nine peptides identified as binding to NIS in the mass spectrometry screen in (Fletcher, 2018) was surveyed for reported functions in protein trafficking. The five interactors that had been analysed previously and the *SLC5A5* gene product itself were excluded from this analysis. A comparative analysis of putative interactors involved in protein trafficking with dysregulation in thyroid cancer was performed using data from the THCA database of the cancer genome atlas. Finally, gene expression was compared in the presence of known driver mutations of differentiated thyroid cancer to ascertain whether up or downregulation of the interactors may be associated with activation or disruption of specific signalling pathways known to play a role in thyroid cancer. Data processing of the THCA database from TCGA is described in Section 2.10.

5.2.2 siRNA Transfection

TPC1-NIS and 8505C-NIS cells were treated with siRNA targeting four different sequences of the target genes and a non-targeting control as described in Section 2.3.2. Downstream analyses were performed 72 hours after transfection.

5.2.3 Plasmid Preparation

VCP, moesin and annexin A1 coding sequences were tagged at the C and N-termini with LgBiT, SmBiT and Nanoluc tags as outlined in Section 2.8.2 for protein-protein interaction assay analysis. NIS was tagged only on the C-terminus as N-terminal tagging is known to abrogate function by preventing trafficking to the plasma membrane. NIS-SmBiT^{K554A}, NIS-SmBiT^{R555A} and NIS-SmBiT$^{K554A/R555A}$ mutants were generated using Agilent Quikchange II site directed mutagenesis kit as described in Section 2.8.4

5.2.4 Co-Immunoprecipitation

TPC1-NIS cell protein lysates were incubated with the NIS antibody, which was used to pull back NIS protein and bound interactors. HA antibody pullback was used as an IgG isotype control to assess non-specific interactions between the protein extracts and IgG protein. One lysate was incubated with no primary antibody to control for the carry-over of unbound protein from the lysate after the beads have been washed. The samples were analysed by Western blot as described in Section 2.5.3 and the specific protein G-HRP conjugated secondary antibody (Bio-Rad) was used to prohibit cross reaction of secondary antibody with the IgG antibodies used in the experiment.

5.2.5 Microscopy

Imaging slides were prepared from HeLa and TPC1 cells as described in Section 2.6 and stained using HA (Biolegend, mouse), moesin (Proteintech, rabbit) and annexin A1 (Proteintech, rabbit) primary antibodies, and anti- mouse-488 and anti-rabbit-594 secondary antibodies. 24-hour after mounting, slides were imaged on a Zeiss 780 confocal microscope using the 100x objective.

5.2.6 Bioluminescence Resonance Energy Transfer (BRET)

C-terminally tagged NIS-GFP functioned as the acceptor protein for BRET assays. HeLa cells were utilised based on their high transfection efficiency. The conditions used for transfection are outlined in Table 5-1. HeLa cells were processed as described in section 2.8.5 and a single luciferase reading was measured six minutes after addition of the NanoGlo Luciferase Solution (Promega) substrate to the plate.

Plasmid 1	Plasmid 2	Control or Experimental Condition
NIS-GFP	Untagged Nanoluc	Assay specific negative control
NIS-GFP	NIS-Nanoluc	Assay specific positive control 1 (C only)
NIS-GFP	VCP-Nanoluc	Assay specific positive control 1 (C)
NIS-GFP	Nanoluc-VCP	Assay specific positive control 1 (N)
NIS-GFP	MSN-Nanoluc	Experimental
NIS-GFP	Nanoluc-MSN	Experimental
NIS-GFP	ANXA1-Nanoluc	Experimental
NIS-GFP	Nanoluc-ANXA1	Experimental

Table 5-1. ***Transfection combinations for the BRET assay****.*

5.2.7 NanoBiT

HeLa cells were prepared as outlined in Section 2.8.3. Table 5-2 outlines the transfection combinations used in the NanoBiT assay. Two technical replicates of each condition were used per experiment. Only the inner 60 wells of the plate were used to prevent edge effects or thermal gradients across the plate. Luminescence was measured at two-minute intervals for twenty cycles on a PHERAstar luminescent plate reader.

Plasmid 1	Plasmid 2	Control or Experimental Condition
Halotag-SmBiT	None	Manufacturer supplied negative control
SmBiT-PRKACA	LgBiT-PRKAR2A	Manufacturer supplied positive control
NIS-SmBiT	LgBiT-PRKAR2A	Assay specific negative control
NIS-SmBiT	NIS- LgBiT	Assay specific positive control 1 (C only)
NIS-SmBiT	VCP- LgBiT	Assay specific positive control 1 (C)
NIS-SmBiT	LgBiT- VCP	Assay specific positive control 1 (N)
NIS-SmBiT	MSN-LgBiT	Experimental
NIS-SmBiT	LgBiT-MSN	Experimental
NIS-SmBiT	ANXA1-LgBiT	Experimental
NIS-SmBiT	LgBiT-ANXA1	Experimental

Table 5-2 ***Transfection combinations for the NanoBiT assay.***

Additionally, a NanoBiT reverse assay was performed for further validation of the observed interactions. The transfection combinations for the reverse experiment are detailed in Table 5-3.

Plasmid 1	Plasmid 2	Control or Experimental Condition
Halotag-SmBiT	None	Manufacturer supplied negative control
SmBiT-PRKACA	LgBiT-PRKAR2A	Manufacturer supplied positive control
NIS-SmBiT	LgBiT-PRKAR2A	Assay specific negative control
NIS-LgBiT	VCP- SmBiT	Assay specific positive control 1 (C)
NIS-LgBiT	SmBiT- VCP	Assay specific positive control 1 (N)
NIS-LgBiT	MSN-SmBiT	Experimental
NIS-LgBiT	SmBiT-MSN	Experimental
NIS-LgBiT	ANXA1-SmBiT	Experimental
NIS-LgBiT	SmBiT-ANXA1	Experimental

Table 5-3. ***Transfection combinations for the reverse NanoBiT assay****.*

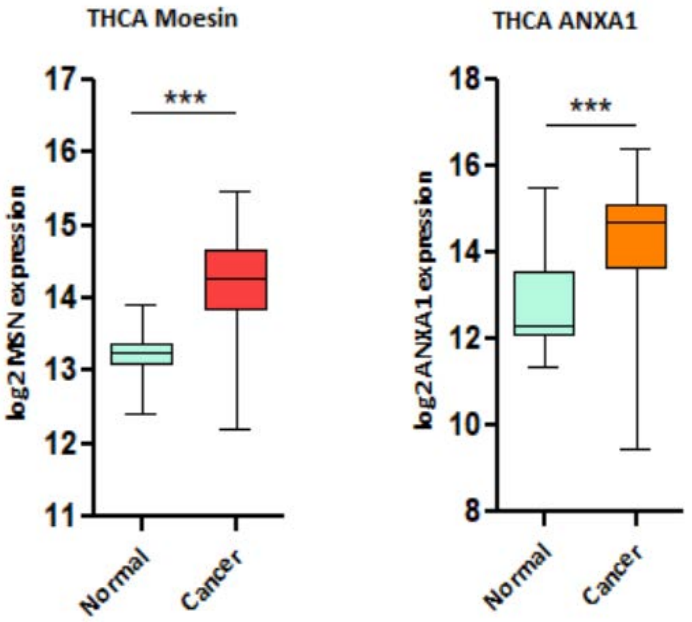
5.3 Results

5.3.1 Selection of Further Potential NIS Interactors Relevant to Protein Trafficking and Thyroid Cancer

The relevance of moesin and annexin A1 in thyroid cancer was explored by comparing gene expression levels in thyroid cancer samples against normal thyroid tissue. For this, RNAseq data were obtained from the THCA dataset of TCGA. An initial comparison showed that moesin and annexin A1 are significantly upregulated in papillary thyroid tumours compared to matched normal tissue (Figure 5.1A). Overall, papillary thyroid cancer samples exhibited a 2.07-fold and 2.77-fold increase in average moesin and annexin A1 gene expression, respectively (Figure 5.1A).

The majority of papillary thyroid cancers arise due to a small number of oncogenic drivers, most commonly the *BRAF*^{T1799A} oncogene that encodes the BRAF^{V600E} protein. *MSN* and *ANXA1* gene expression were compared between known driver mutations or fusion gene-driven subtypes (Figure 5.1B). This comparison highlighted strongly elevated expression of *MSN* and *ANXA1* in the BRAF mutant subgroup of samples, 98 % of which carry the BRAF^{V600E} mutation (Figure 5.1B). *BRAF* and *RET* fusion events also demonstrated significantly upregulated *MSN* and *ANXA1* expression compared with normal tissue. *RAS* mutated samples and *PPARG*-fusion genes did not display significantly upregulated expression of either *MSN* or *ANXA1*. Interestingly, samples with confirmed *NTRK1*/3 fusion gene tumours showed upregulated *ANXA1,* albeit in a small sample size (Figure 5.1B). *NTRK1/3* fusions result in activated tropomyosin receptor kinase oncogenes which can signal via the MAPK, PKC and PI3K-Akt-mTOR pathways (Cocco et al., 2018).

A



B

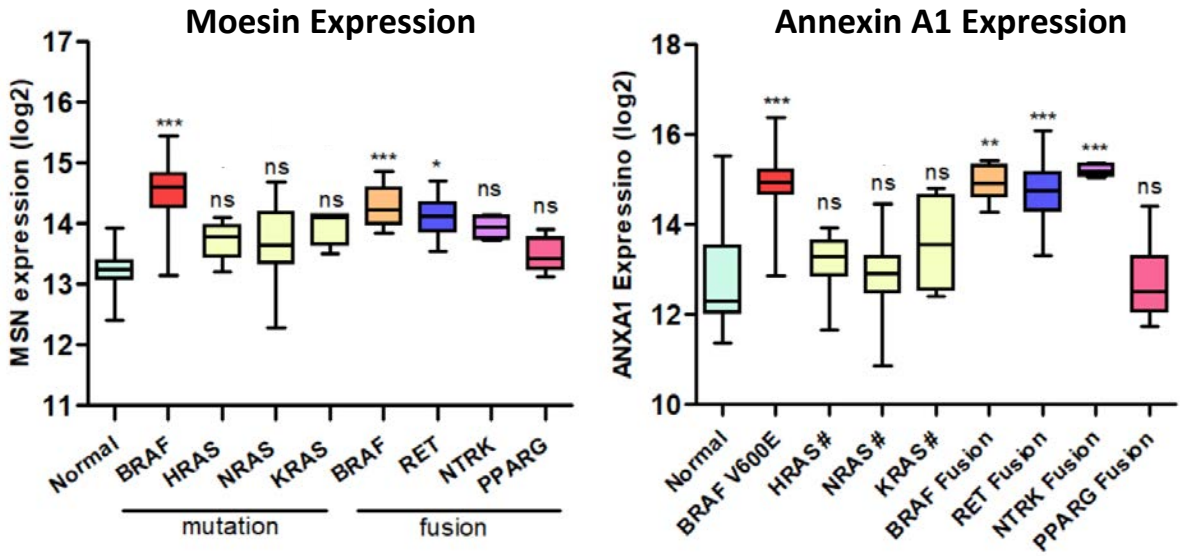


Figure 5.1 ***Comparison of Moesin (MSN) and Annexin A1 (ANXA1) expression in thyroid cancer vs normal and across multiple known driver mutations in thyroid cancer.*** *(**A**) Cancer vs matched normal tissue samples from The Cancer Genome Atlas. Statistical analysis by Mann-Whitney test. Normal n=59; cancer n=501. (**B**) Comparison of the log2 MSN and ANXA1 expression values across papillary thyroid cancer subtypes separated by common driver mutations. Analyzed by Kruskal-Wallis test against normal samples. Mutations: BRAF n=232 ; HRAS n=14; KRAS n=4; NRAS n=34; Fusions: BRAF n=7;RET n=30; NTRK n=4, PPARG n=6.*

Although tumours harbouring a *RET* fusion gene demonstrated significantly higher *MSN* and *ANXA1* expression, this group comprised only ~10 % (52/501) of the cancer samples. Therefore, the *BRAF* mutation status was compared within this group to test whether the elevated expression levels observed in *RET* fusion tumours were due to a concomitant $BRAF^{V600E}$ mutation. However, *RET* fusions with $BRAF^{WT}$ also showed significantly higher *MSN* and *ANXA1* expression than normal tissue (Figure 5.2). The combination of *RET* fusion and $BRAF^{V600E}$ did show higher expression of moesin compared to *RET* fusion with $BRAF^{WT}$, albeit with a small sample size of 13 indicating this combination is rare, making up only 2.6 % of total PTC samples tested (Figure 5.2A).

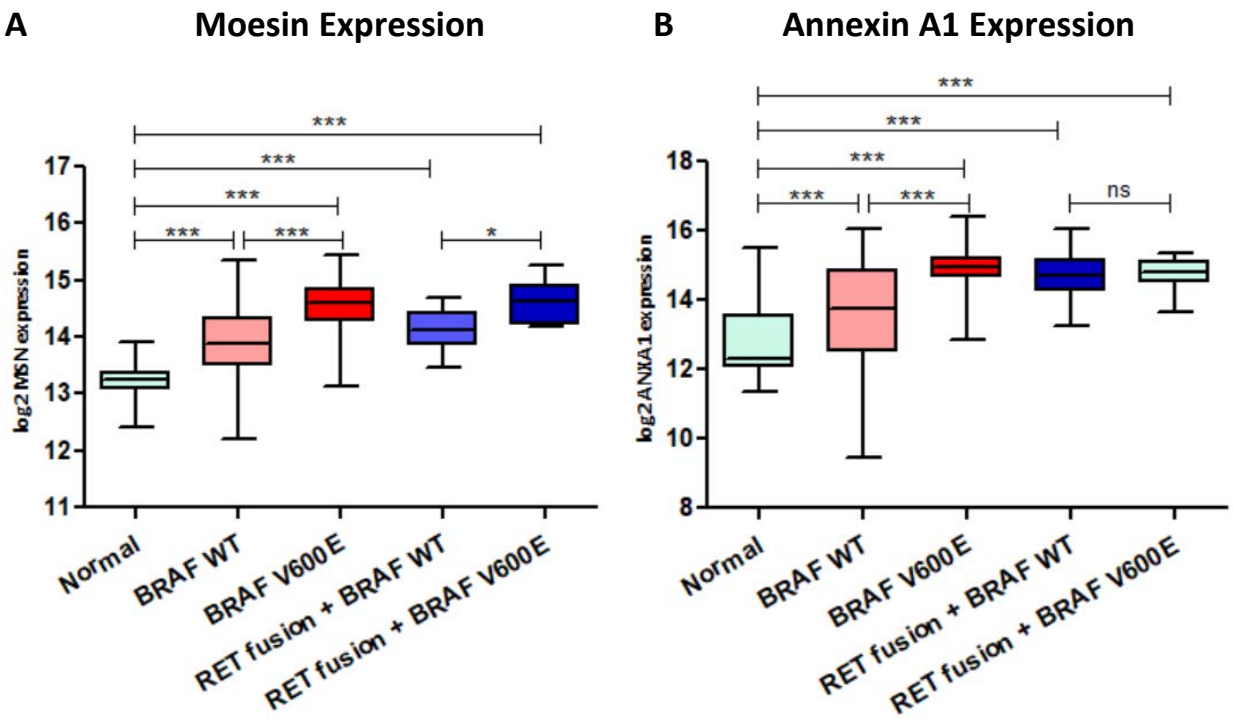


Figure 5.2 ***Breakdown of groups that have upregulated MSN and ANXA1 expression by oncogenic driver mutation, compared to normal tissue control.*** *All the groups displayed significantly higher expression of both MSN (**A**) and ANXA1 (**B**) compared to normal tissue. For moesin expression, samples with both RET fusion and the $BRAF^{V600E}$ mutation were significant compared to RET fusion and wild-type BRAF. Normal n = 59; $BRAF^{WT}$ n= 252; $BRAF^{V600E}$ n=236; RET fusion + $BRAF^{WT}$ n= 39; RET fusion + $BRAF^{V600E}$ n=13. Analysed by one way ANOVA using Tukey post-hoc test. * = p < 0.05; *** = P < 0.001; ns = non-significant.*

5.3.2 The Effect of Moesin and Annexin A1 on Radioiodide Uptake

The impact of *MSN* or *ANXA1* siRNA knockdown and gene overexpression on radioiodide uptake was assessed in TPC1-NIS and 8505C-NIS thyroid cell lines. siRNA mediated knockdown of *MSN* and *ANXA1* both resulted in statistically significant increase in NIS-mediated radioiodide uptake (Figure 5.3A). Specifically, *MSN* knockdown induced a 101 % and 73.4 % increase in TPC1-NIS and 8505C-NIS cells, respectively; annexin A1 knockdown resulted in a 157 % and 56.9 % increase in TPC1-NIS and 8505C-NIS cells, respectively (Figure 5.3A). Successful knockdown of moesin and annexin A1 at the protein level was confirmed by Western blot (Figure 5.3B). The knockdown of moesin or annexin A1 did not result in observable cell death, morphological changes (data not shown), nor in changes to NIS protein levels (Figure 5.3)

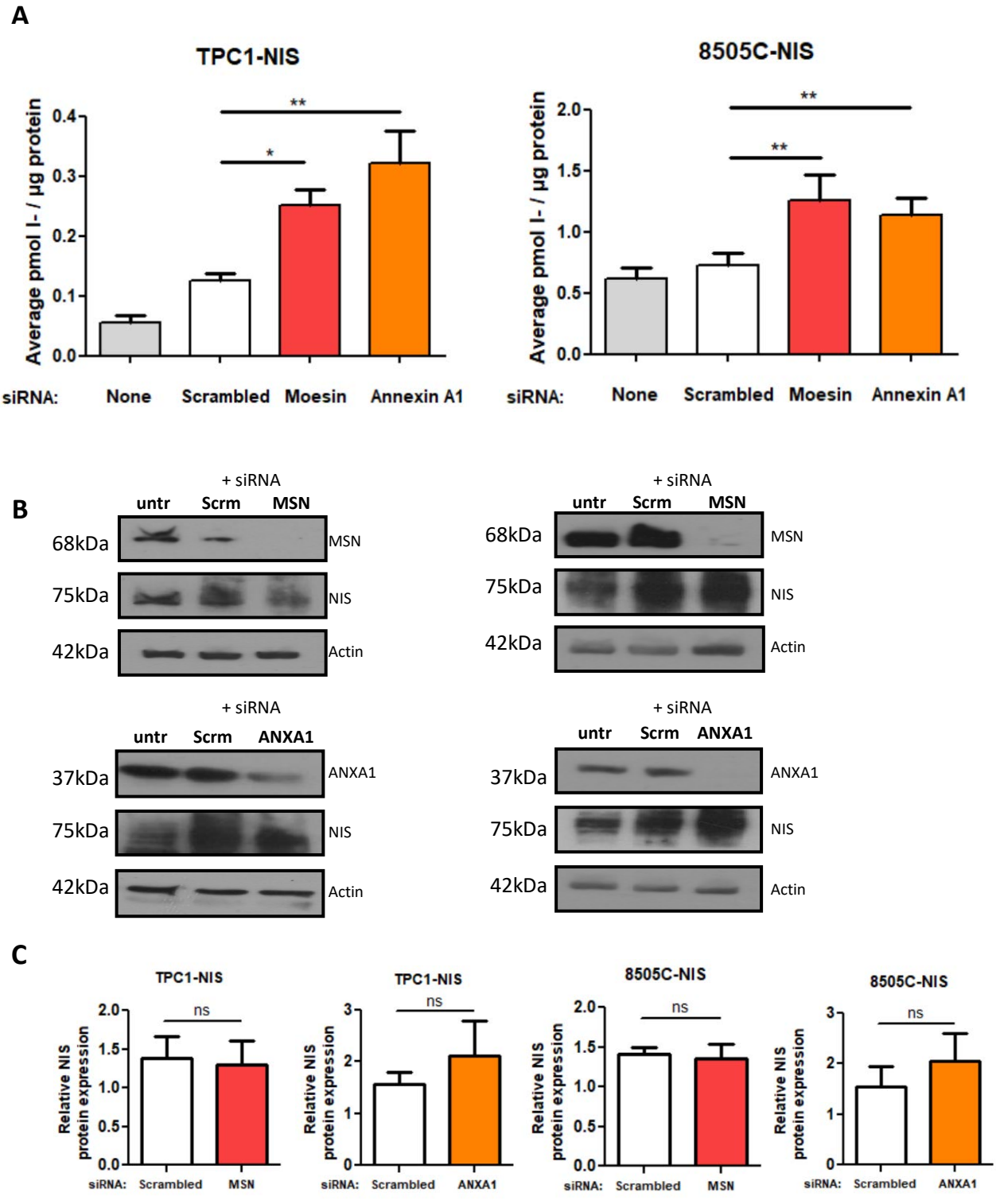


Figure 5.3 ***(A) siRNA knockdown of Moesin and Annexin A1 genes resulted in statistically significant increases in radioiodide uptake in TPC1-NIS and 8505C-NIS cells****. * p < 0.05, ** p < 0.01. (**B**) Confirmation of knockdown of moesin and annexin A1 by Western blot. Knockdown of moesin or annexin A1 did not result in changes to NIS protein level in either TPC1-NIS or 8505C-NIS cells as measured by densitometry analysis against beta-Actin in (**C**) using paired t-test; ns= non-significant.*

To assess whether overexpressing *MSN* or *ANXA1* would result in reduced iodide uptake as an inverse effect of siRNA knockdown, *MSN* and *ANXA1* genes were introduced exogenously by transfection. Overexpression did not result in changes to radioiodide uptake compared to the VO control in TPC1-NIS or 8505C-NIS cell lines (Figure 5.4A). Overexpression at the protein level was confirmed by Western blot analysis (Figure 5.4B). High levels of both proteins in the cell lysate in VO were observed, and the magnitude of overexpression was relatively small. This may underlie the lack of effect on radioiodide uptake; with high levels of these proteins at the basal level it is feasible that the protein levels in the system cannot be further increased to cause measurable changes to radioiodide uptake.

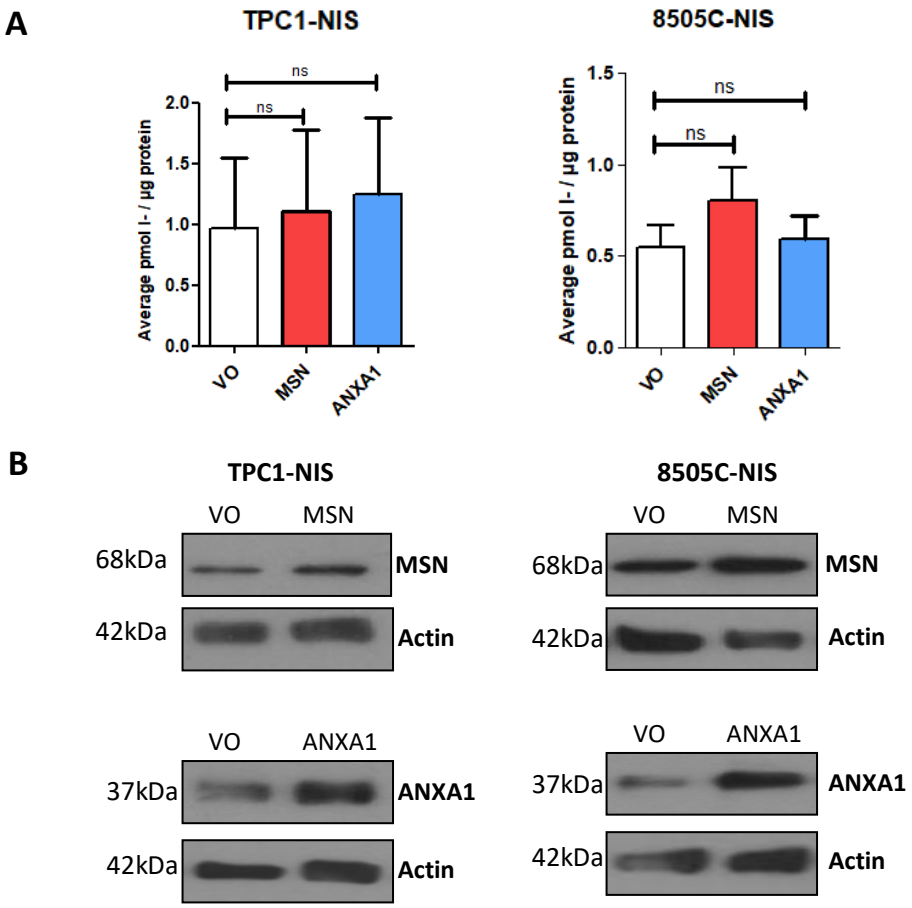
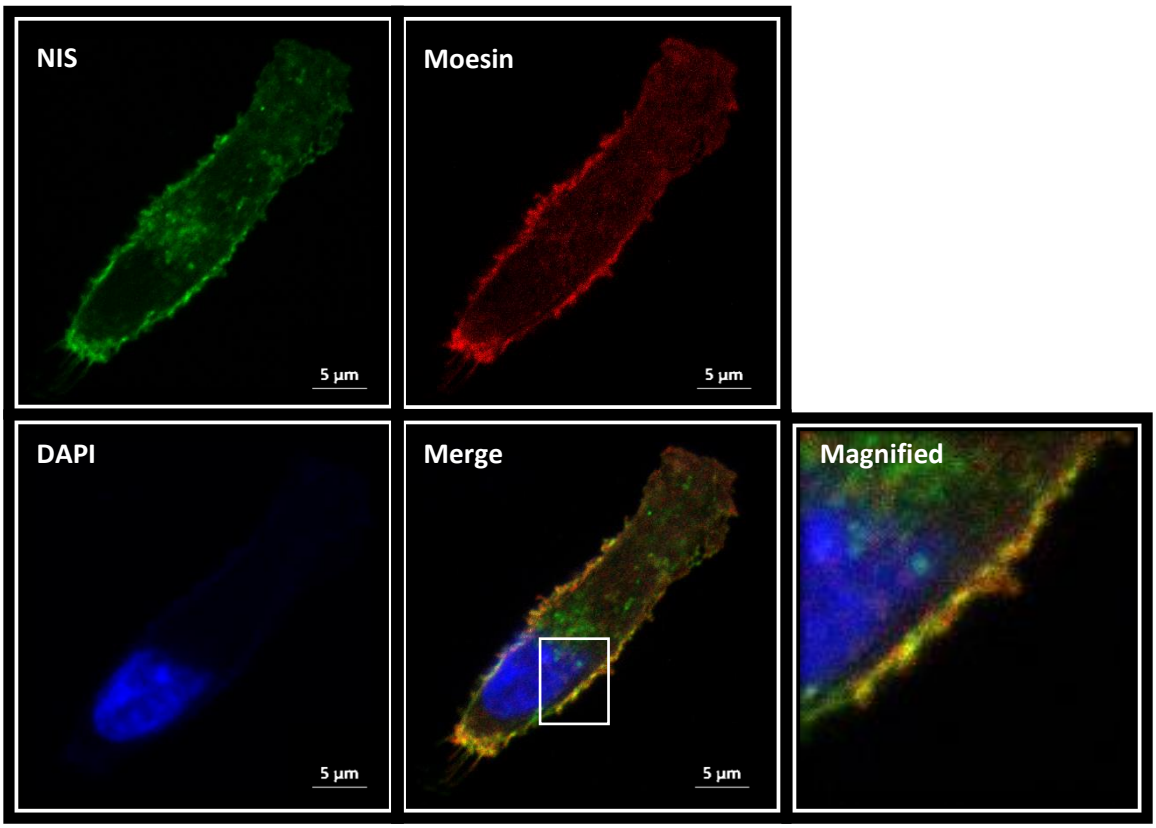


Figure 5.4 ***(A) Overexpression of moesin or annexin A1 by exogenous gene transfection did not affect radioiodide uptake on TPC1-NIS and 8505C-NIS cells****. (**B**) Confirmation of overexpression of moesin and annexin A1 in both cell lines.*

5.3.3 The Distribution of Moesin and Annexin A1 in Cells

To observe whether there are regions of colocalisation in the cell between moesin and NIS, and annexin A1 and NIS, TPC1 and HeLa cells were transfected with NIS-HA and stained for HA, and endogenous moesin or Annexin A1. Moesin is a well-characterised membrane interacting protein and was typically observed at the plasma membrane in TPC1 and HeLa cells during microscopy (Figure 5.5). NIS was observed in both the cytosol and membrane, and regions of overlapping NIS and moesin signal were apparent (Figure 5.5). Annexin A1 staining was mainly cytosolic and distributed throughout the cell; there were no overt regions of colocalisation with NIS in TPC1 or HeLa cells (Figure 5.6). Interestingly, although annexin A1 was initially identified by mass spectrometry as interacting with NIS at the plasma membrane, strong annexin A1 staining at the membrane was not observed (Figure 5.6).

A TPC1



B HeLa

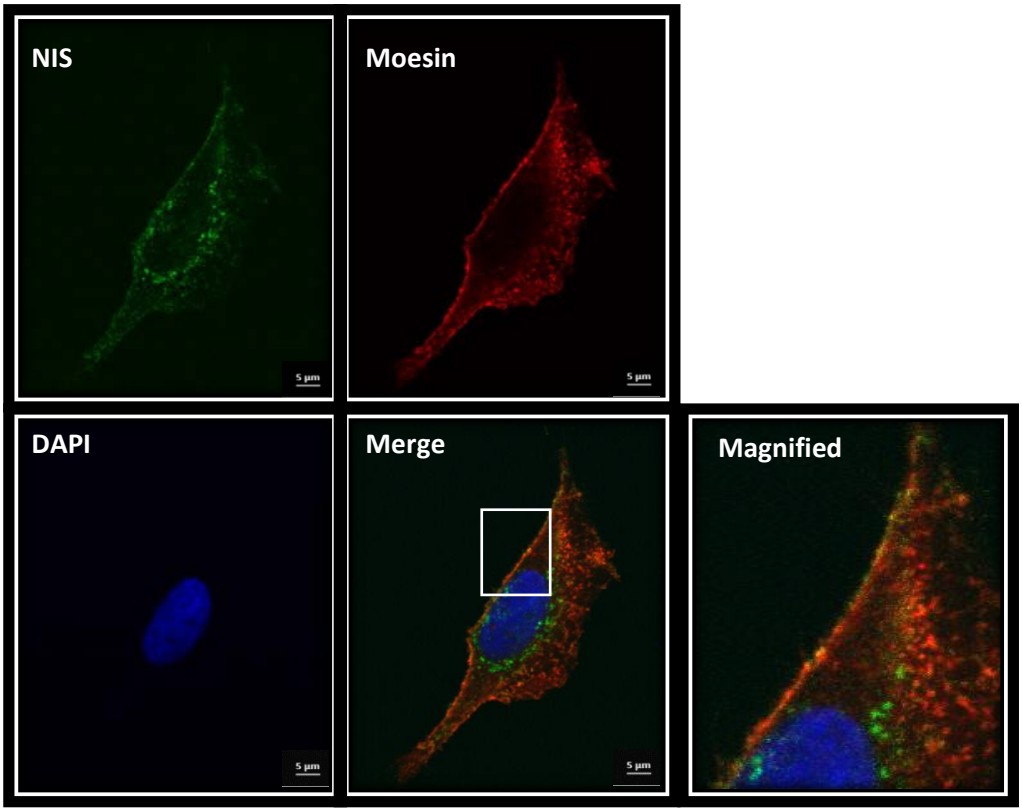
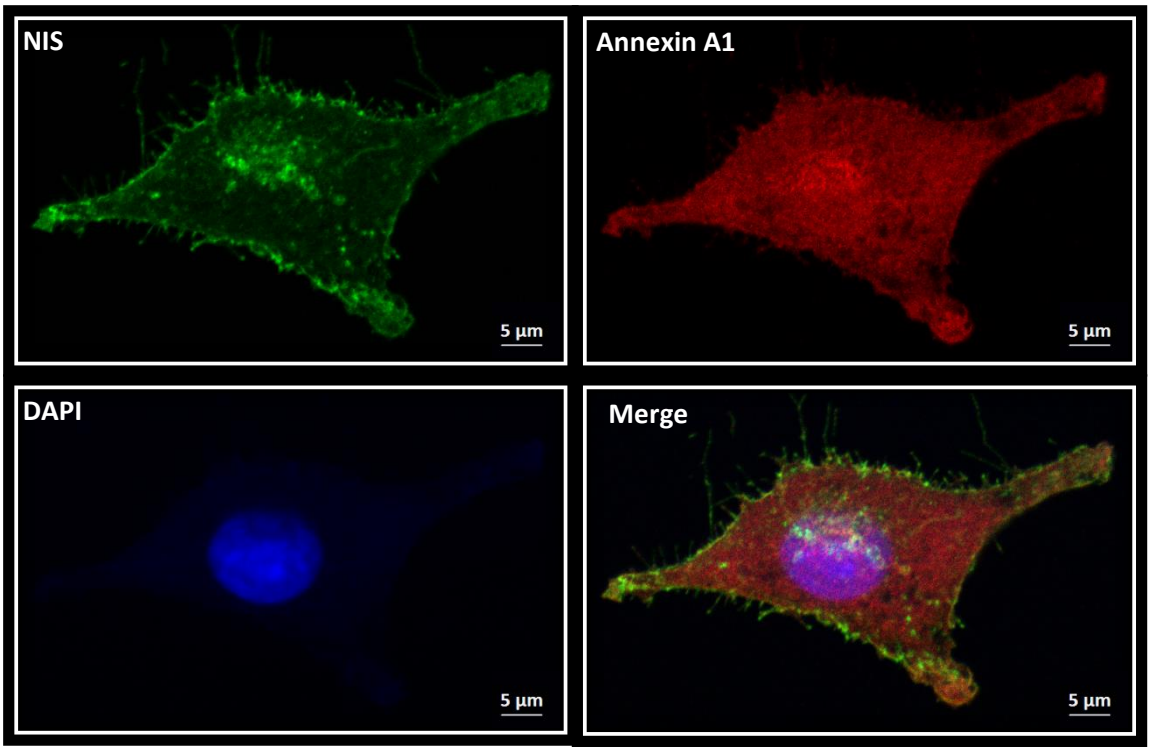


Figure 5.5 ***(A) TPC1 cells and (B) HeLa cells transfected with NIS-HA and stained with anti-HA (green), anti moesin (red) and DAPI nuclear stain****. Both moesin typically stains at the plasma membrane and NIS at both the membrane and in the cytoplasm. White box represents area in magnified image. Areas of colocalisation at the plasma membrane were outlined with a white box and shown in the magnified images on the right-hand side (4x magnification).*

A TPC1



B HeLa

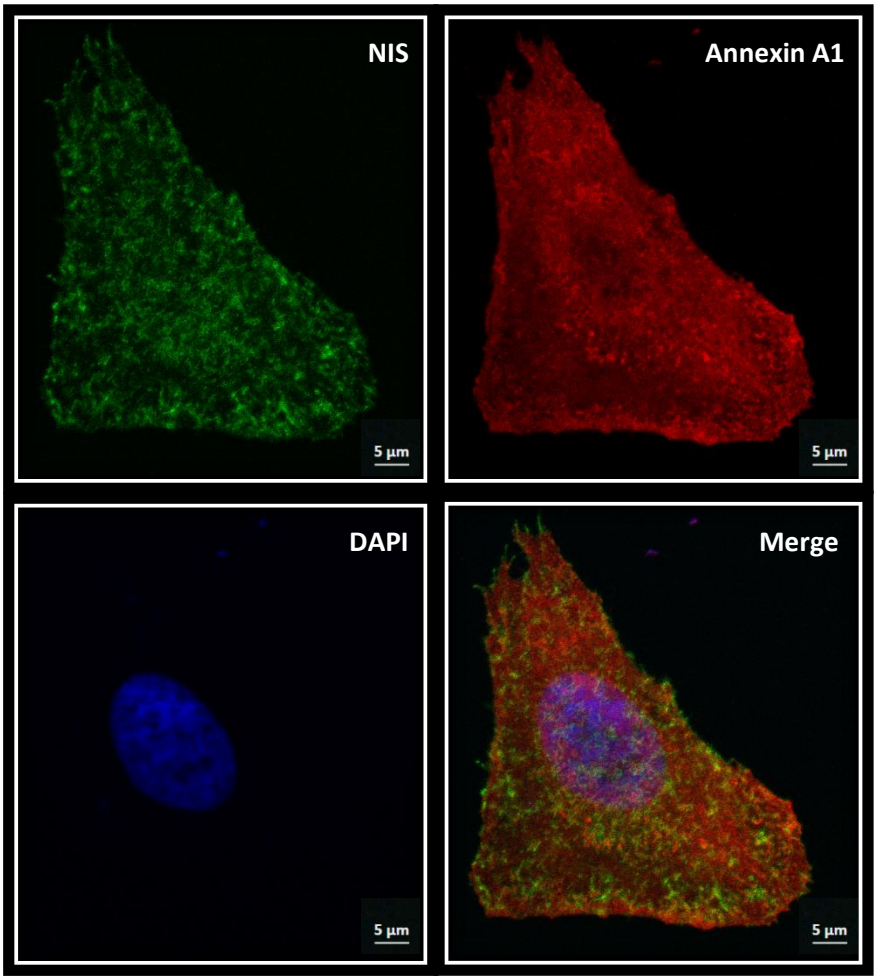


Figure 5.6 ***(A) TPC1 cells and (B) HeLa cells were transfected with NIS-HA and stained for anti-HA, anti-annexin A1 and the DAPI nuclear stain.*** *Annexin A1 protein is typically distributed throughout the cell while NIS is generally both cytoplasmic and membrane bound. There were no obvious areas of colocalisation between NIS-HA and endogenous annexin A1.*

5.3.4 Moesin and Annexin A1 Bind to NIS

5.3.4.1 Co-Immunoprecipitation

Physical interactions between NIS and moesin, and NIS and annexin A1 were examined through protein-protein interaction assays: co-IP, BRET and NanoBiT. Co-immunoprecipitation assays were performed using NIS and HA antibodies to pullback proteins, followed by probing for the proposed interactors via Western blot. The validity of these experiments was limited by presence of bands in the isotype control antibody lane (Figure 5.7). This is indicative of non-specific binding of proteins in the cell lysate to IgG protein. As a result, non-NIS binding proteins were pulled back in one or both antibody-samples resulting in bands observed in the IgG isotype control lane. Absence of moesin bands in the no antibody lane shows the contamination observed in the HA pullback lane is dependent on IgG binding rather than inadequate removal of unbound protein in the lysate during the washing steps.

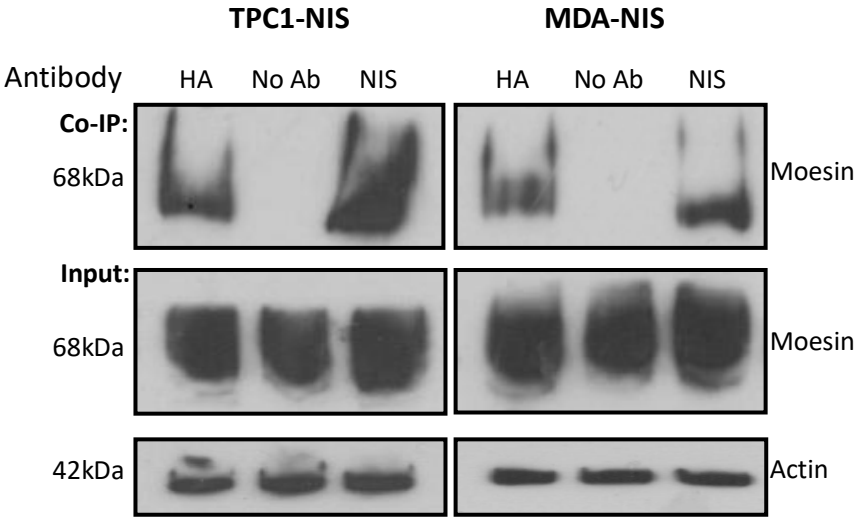


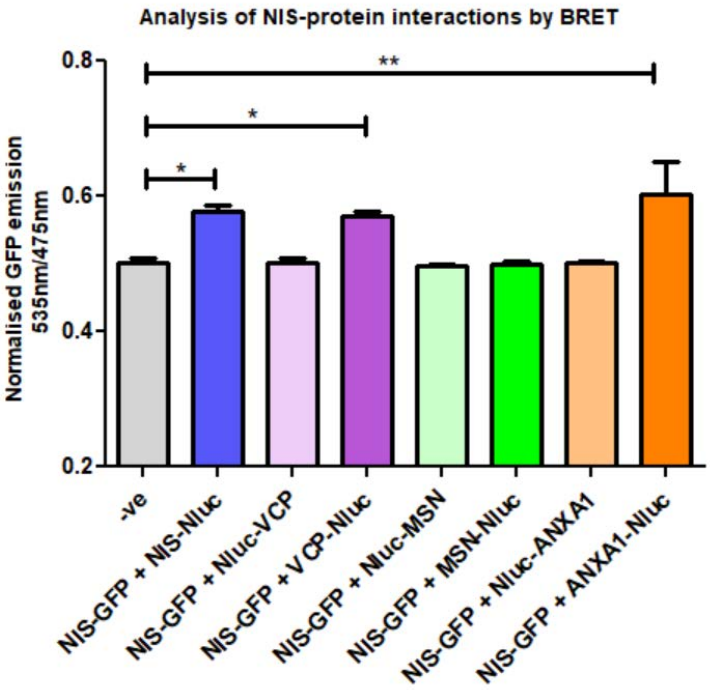
Figure 5.7 ***Co-immunoprecipitation assays in TPC1-NIS and MDA-NIS cells****. Cell lysates were incubated with anti-HA IgG, no IgG and anti-NIS IgG.Moesin bands were identified in lanes from samples incubated with anti-HA. Input represents samples taken from the protein lysate prior to incubating with respective antibodies, and confirms presence of moesin in all lysates prior to incubating with NIS/HA antibodies or no antibody control.*

5.3.4.2 Bioluminescence Resonance Energy Transfer

Given the issues with validity of the co-IP assay, alternative experimental approaches were employed to appraise interactions between NIS and moesin, and between NIS and annexin A1. The bioluminescence resonance energy transfer (BRET) assay relies on the excitation of luciferase inducing a transfer of energy to GFP fluorophores in the immediate vicinity. The assay output is the ratio of donor luciferase stimulation over acceptor GFP emission: an increase in this ratio compared to a negative control is indicative of proximity between the two proteins of interest that may reflect a physical interaction (Figure 2.3).

Transfecting the combination of NIS-GFP and NIS-nanoluc was used to measure NIS dimerisation and displayed enhanced GFP emission and GFP: luminescence ratio, which was significant against the negative control (Figure 5.8A). NIS-GFP/VCP-Nanoluc and NIS-GFP/ANXA1-Nanoluc were the only experimental lanes which demonstrated significant changes in BRET ratio. However, when comparing the average luminescence in these wells (Figure 5.8B), notably lower measurements of both donor luminescence emission and subsequent acceptor GFP excitation were measured. The cause of this anomaly is not obvious given that all the plasmids were sequenced prior to transfection. No other transfected combinations demonstrated unequivocal and reliable changes in the BRET ratio and therefore assessment of functional interactions with NIS could not be ascertained using BRET analysis.

A



B

Condition	Average Luminescence emitted at 535 nm (n=3)	Average NIS-GFP emission at 485nm (n=3)
NIS-GFP + Nanoluc (-ve ctrl)	600657	300408.7
NIS-GFP + NIS-Nluc	2489434	1479325
NIS-GFP + Nluc-VCP	602191	300710.3
NIS-GFP + VCP-Nluc	**1473**	**829.6667**
NIS-GFP + Nluc-MSN	839101	413977
NIS-GFP + MSN-Nluc	533708	264318.3
NIS-GFP + Nluc-ANXA1	1254036	618860.7
NIS-GFP + ANXA1-Nluc	**680**	**389**

Figure 5.8 ***BRET ratio of fluorescence signal divided by luminescence background.*** *(**A**) NIS-GFP and NIS-luciferase show elevated signal to background ratio indicative of protein protein interaction. Although NIS-GFP and VCP-luciferase and NIS-GFP-AnnexinA1-Luciferase also had elevated signal to background ratio but the overall fluorescence signal in these conditions was markedly lower (**B-** see emboldened values), suggesting potentially anomalous results.*

5.3.4.3 NanoBiT

NanoBiT represents the third technique used to appraise the potential interactions identified by the mass spectrometry data. This assay relies on two fragments of the luciferase enzyme, the 18 kDa LgBiT and the 1.3 kDa SmBiT, which are attached to proteins-of-interest. In the event of an interaction between these proteins of interest, the SmBiT and LgBiT tags form a full luciferase enzyme which catalyses the oxidation of luciferin substrate and produces a measurable luminescent signal. The positive control supplied by the manufacturer was the LgBiT-PRKAR2A and SmBiT-PRKACA positive control pair which encode two subunits of a cAMP-dependent protein kinase that interact in cells without requiring stimulation. The assay

uses a Halotag-SmBiT negative control which is a modified haloalkane dehydrogenase designed to only bind to synthetic ligands, and this was transfected individually as a negative control in the assay. To provide a second, more assay-specific negative control, NIS-SmBiT and LgBiT-PRKAR2A were also co-transfected. Figure 5.9A demonstrates a strong luciferase emission over twenty cycles in the positive control wells, and minimal emission over time in both the Halo-SmBiT negative control and assay specific NIS-SmBiT and LgBiT-PRKAR2A negative control. Two assay-specific positive controls were also used as we have previously demonstrated that NIS dimerises, and that NIS can interact with VCP. These positive controls utilised NIS-SmBiT and NIS-LgBiT monomers, and NIS-SmBiT and VCP-LgBiT (Table 5-2). NIS dimerisation demonstrated much higher luciferase values than the standard positive control (Figure 5.9B). Interestingly, the NIS-VCP interaction was measurable only when VCP was tagged on the N-terminus (Figure 5.9C). The luciferase signal increased over approximately ten cycles in all measurements, consistent with movement of the luciferase substrate from the media across the cell membranes to equilibrium. Subsequently, the luciferase reading at cycle ten was carried over for paired statistical analysis. The half-life of the luminescent reagent is 120 minutes and the decrease in luminescent signal after ten cycles can be explained by partial degradation of the signal.

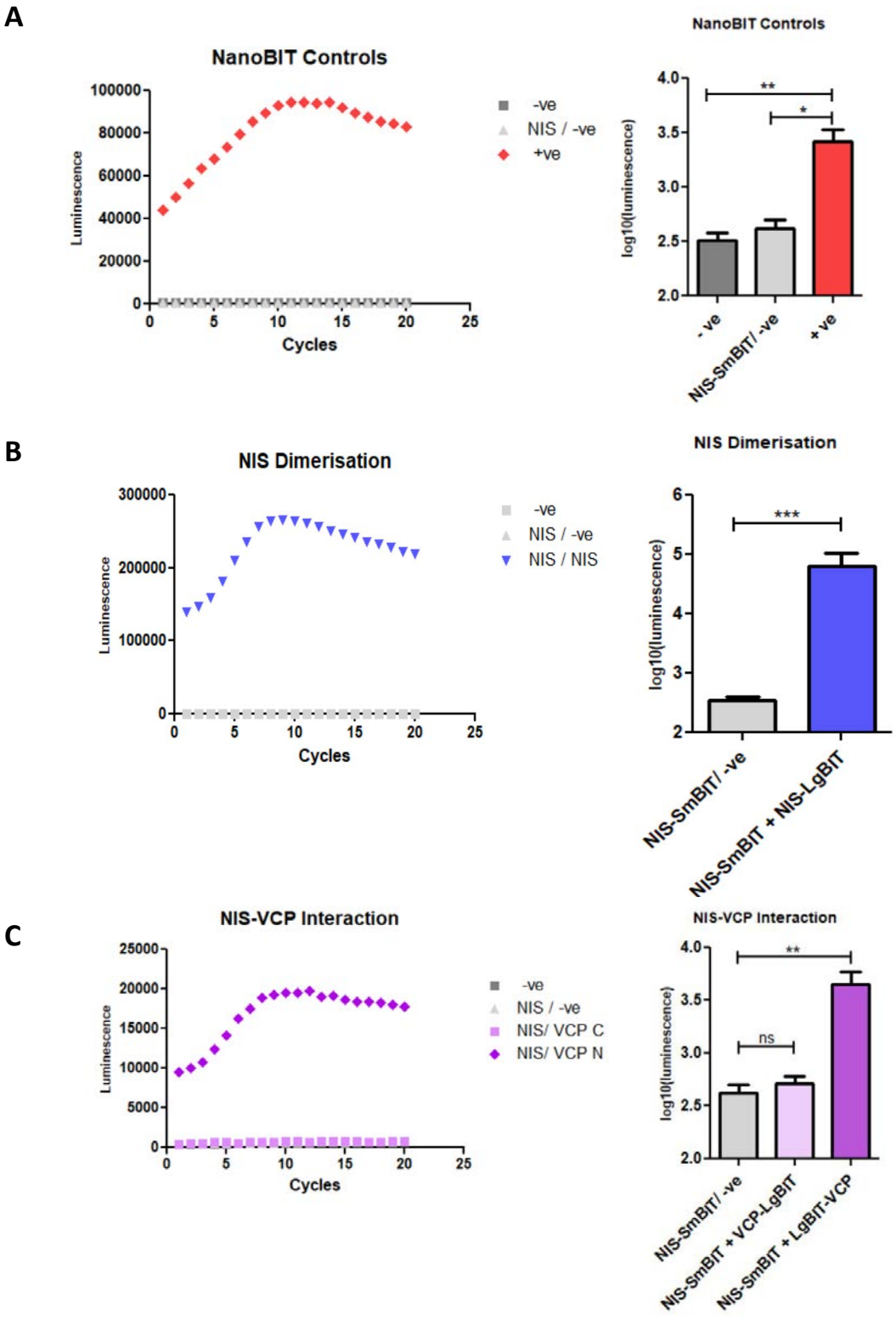


Figure 5.9 ***Three NanoBiT assay positive controls show significant increases in luminescence against assay specific negative control****. The NanoBiT assay positive control LgBiT-PRKAR2A and SmBiT-PRKACA positive control vectors (**A**) and additional NIS specific experimental controls NIS-NIS dimer interaction(**B**) and the NIS-VCP interaction (**C**) were used to validate the NanoBiT protein-protein interaction assay. Statistical analysis was performed by paired, two-tailed t-tests against the NIS-SmBiT + LgBiT-PRKAR2A negative control. * = P < 0.05; ** = P < 0.01; *** = p < 0.001; ns = non-significant.*

Having confirmed the NanoBIT assay was sensitive by multiple positive and negative controls, the interactions between NIS and moesin, and NIS and annexin A1 were tested. The NanoBiT data confirmed an interaction between NIS and moesin as significantly higher luciferase than the two negative controls were apparent (Figure 5.10A). The physical interaction between NIS and annexin A1 was also significantly higher than either negative control confirming an interaction between these proteins. The binding of NIS-SmBiT and LgBiT-ANXA1 (N-terminal tag) was consistent over multiple experimental repeats. The interaction between NIS-SmBiT and ANXA1-LgBiT (C-terminal tag) demonstrated higher variation in luciferase activity but was consistently above the NIS-SmBiT/LgBiT-PRKAR2A negative control.

In some cases, these interactions were influenced by which end of the interacting protein was tagged with LgBiT. Measurements of both NIS and moesin, and NIS and annexin A1 resulted in a higher emission when the interacting partner of NIS was tagged on the N-terminus. Despite this, the luminescent signal of all interactions between NIS and moesin or annexin A1 remained more than 10-fold higher than the negative control.

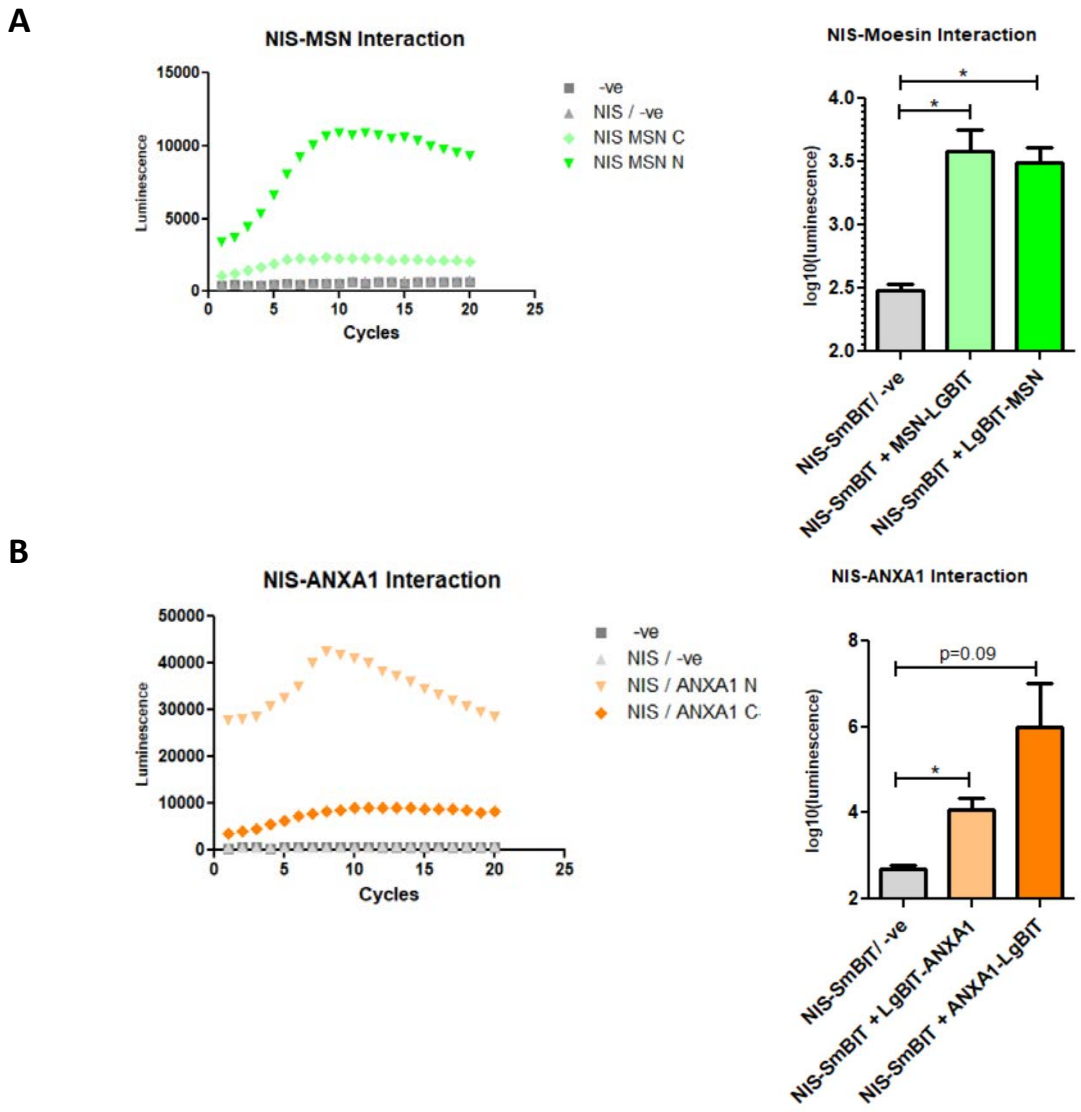


Figure 5.10 ***The NanoBiT assay to assess the interaction between (A) NIS and Moesin and (B) NIS and Annexin A1.*** *Right hand plots show luminescence detected over twenty cycles as average of two technical replicates and are representative of n = 3 experiments. Left hand bar charts are collated data from n = 3 biological replicates and statistical significance was assessed by paired, two-tailed t-test against assay specific negative control. * = p < 0.05.*

For further validation, the reverse NanoBiT assay was completed using LgBiT tagged NIS and SmBiT tagged protein-of-interest (Figure 5.11). This experiment confirmed the interactions between NIS and N-terminally tagged VCP, NIS and moesin, and NIS and annexin A1.

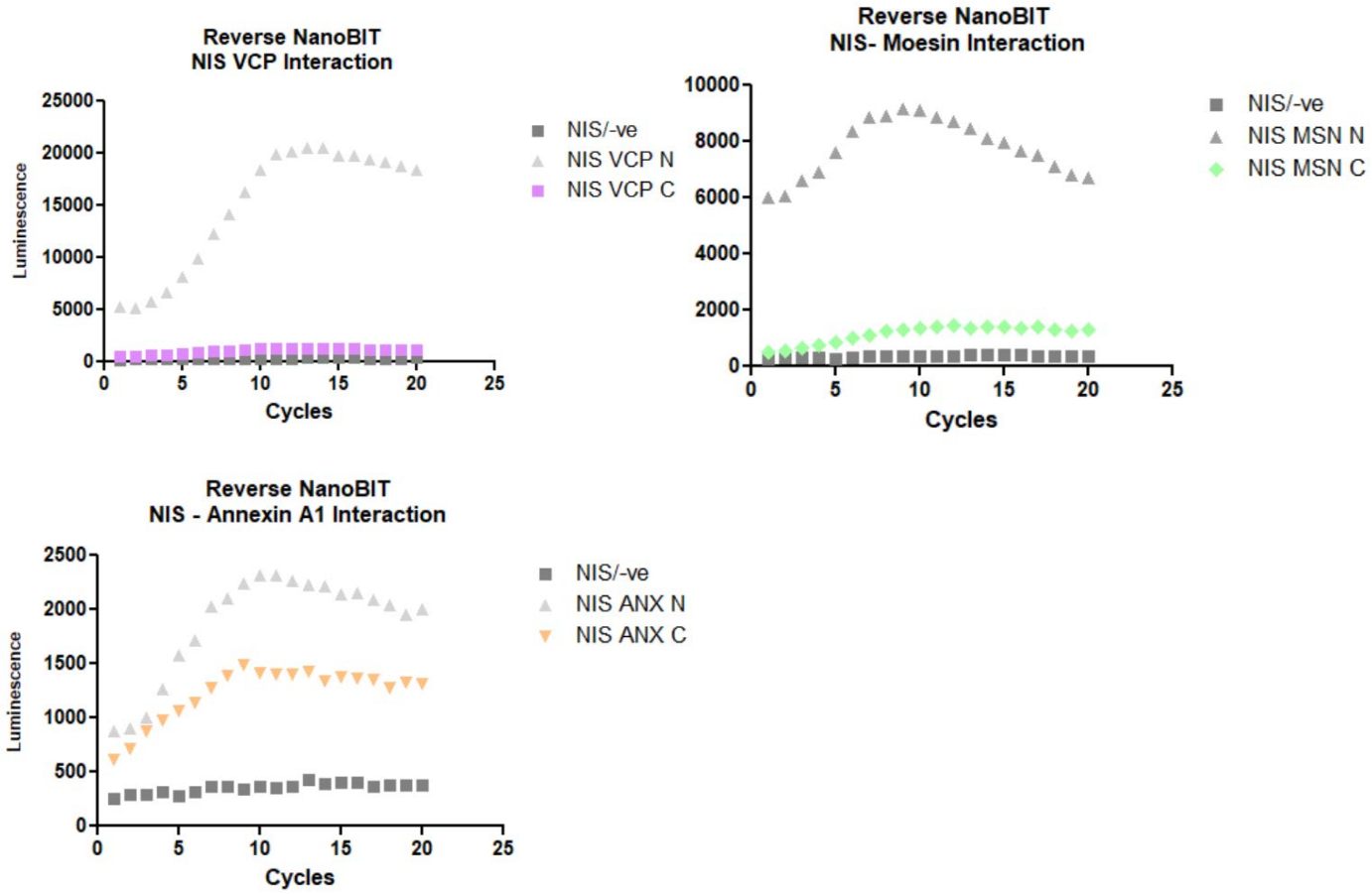


Figure 5.11 ***The Reverse NanoBiT assay using LgBiT tagged NIS and SmBiT tagged protein of interest.*** *Replicate observations measured by SmBiT tagged NIS and LgBiT tagged protein of interest. n=1.*

5.3.5 The Putative NIS Binding Site for Moesin

Moesin has been shown to interact with multiple proteins through a single or double positively charged arginine or lysine residue in a cytosolic region of the protein close to the plasma membrane (Ivetic and Ridley, 2004; Yonemura et al., 1998). In the juxta-membrane region of the C-terminal tail on NIS there are residues K554 and R555 which fit this profile (Figure 5.12).

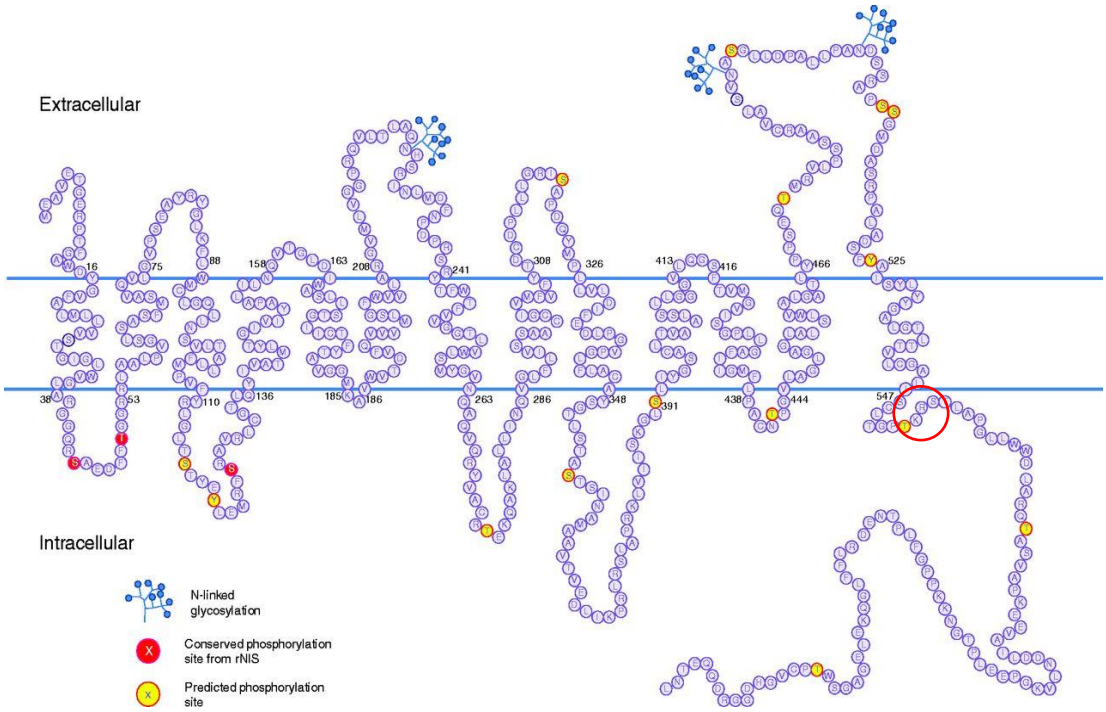


Figure 5.12 ***The amino acid structure of NIS in the plasma membrane reveals a KR motif, in the juxta membrane region of the cytoplasmic C-terminus.*** *This motif of K554 and R555, circled in red, compares to moesin binding motifs in other reported ERM-binding proteins. Adapted from Poole et al 2015.*

These residues were mutated to neutral alanines, both individually and in tandem, to assess the effect on the NIS and moesin interaction. First, the effect of these mutations on radioiodide uptake was measured (Figure 5.13). This demonstrated that neither individual mutation nor the double mutant significantly affected the iodide uptake function of NIS.

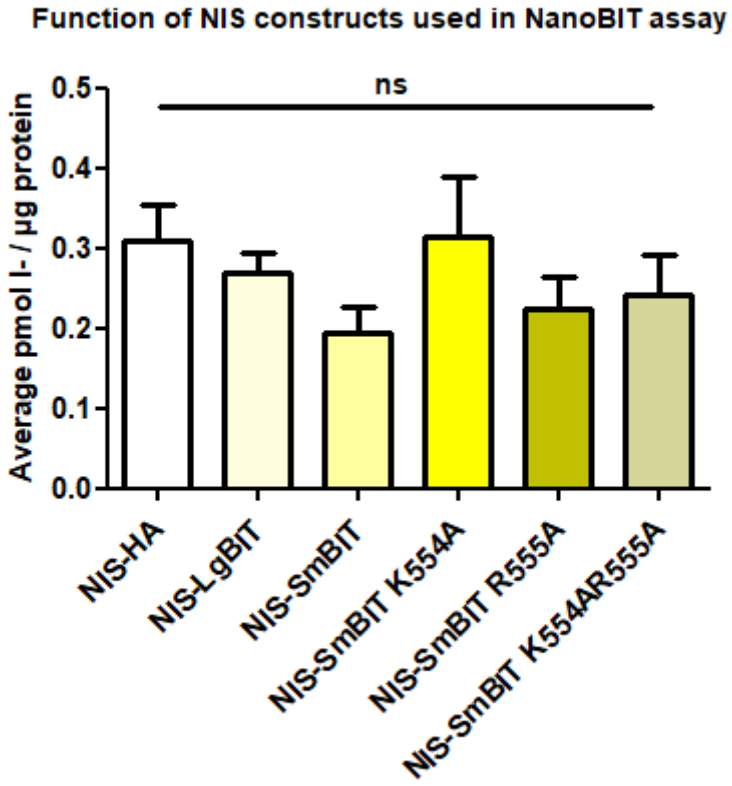


Figure 5.13 ***Comparison of the iodide uptake functionality of the NIS vectors used in NanoBiT analysis in HeLa cells.*** *All constructs contain c-terminal tags to enable NIS trafficking to the plasma membrane and were introduced by transfection to HeLa cells for 48 hours. LgBiT and SmBiT tags, and c-terminal mutations in NIS did not significantly affect iodide uptake function. n=3 replicates. Analysed by one-way ANOVA. ns = non-significant.*

Next, the effect of these C-terminal mutations on the interaction between NIS and moesin was assessed (Figure 5.14). NIS^{K554A}-SmBiT was capable of binding moesin in a similar capacity to NIS^{WT}-SmBiT. NIS^{R555A}-SmBiT had a diminished but non-significant effect on moesin binding. However, the double mutant had significantly lower capacity for moesin binding. Notably, the interaction between $NIS^{K554A/R555A}$-SmBiT and LgBiT-MSN was still significantly higher than the NIS-SmBiT + LgBiT-PRKAR2A assay specific negative control demonstrating that the mutations did not prohibit binding completely and instead reduced the NIS-moesin interaction by 56 %.

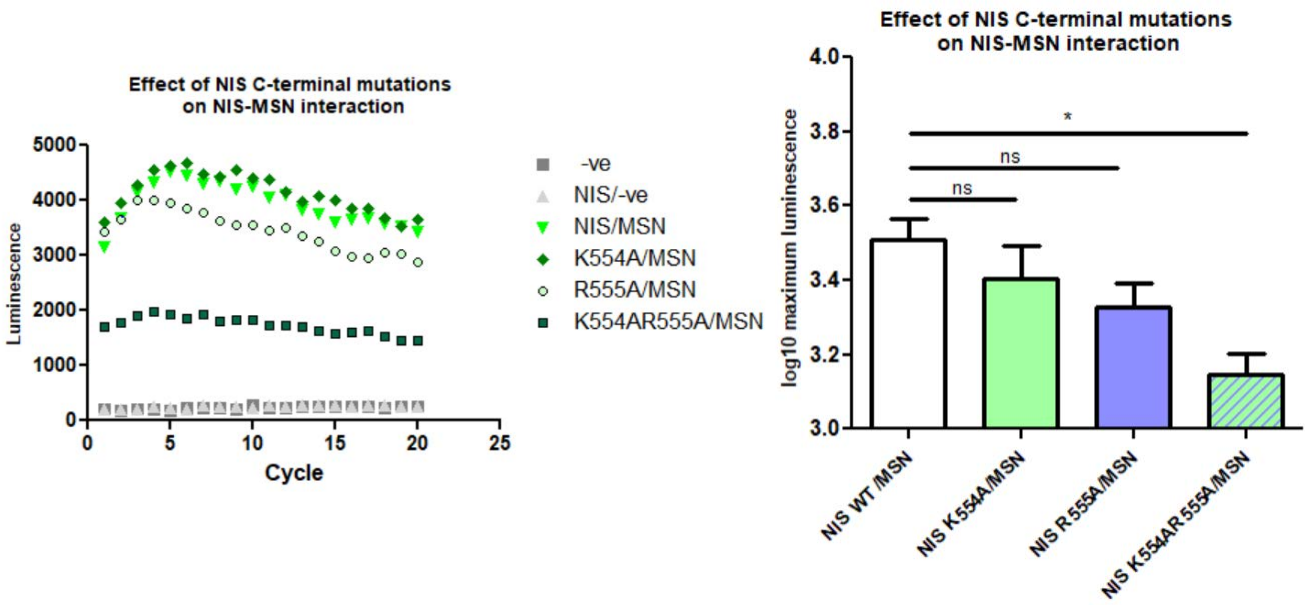


Figure 5.14. ***The influence of NIS C-terminal mutations on the binding of NIS-SmBiT and LgBiT-MSN.*** *Whilst the NIS^{K554A} and NIS^{R555A}-SmBiT mutations individually showed a non-significant reduction in the interaction between NIS and moesin, the double mutation NIS$^{K554A/R555A}$-SmBiT was associated with a statistically significant decrease in NIS-MSN interaction. Statistically analysed by one way ANOVA, * = p < 0.05; ns = non-significant.*

5.4 Discussion

5.4.1 Moesin and Annexin A1 are Upregulated in Thyroid Cancer

Moesin and annexin A1 are both significantly upregulated in thyroid cancer compared to normal tissue, and even more so in BRAF^{V600E} driven thyroid cancer (Figure 5.1B). The exact functional implication of this upregulation is not known. Moesin and annexin A1 were also identified as highly expressed in *RET* fusion papillary thyroid cancers. *RET* chromosomal rearrangements are relatively rare in papillary thyroid cancer (52/501 samples) and of these, only 25 % (13/52) had a concomitant BRAF^{V600E} mutation. When these samples were separated into *RET* fusion + BRAF^{WT} and *RET* fusion + BRAF^{V600E} (Figure 5.2), expression of moesin and annexin A1 remained significantly higher than normal tissue in both groups. This indicates that both BRAF^{V600E} and *RET* fusion are sufficient singular events to drive up

expression of moesin and annexin A1, but may act summatively in the small number of patients displaying both mutations.

5.4.2 Moesin and Annexin A1 Modulate Iodide Uptake

Knockdown of both *MSN* and *ANXA1* resulted in a significant increase in radioiodide uptake in two thyroid cancer derived cell lines but did not resulted in significant changes to NIS protein level (Figure 5.3B). siRNA knockdown of *ANXA1* resulted in an upwards trend in NIS protein and despite this being non-significant, further analysis across more cell lines may be warranted. The non-significant changes in NIS protein in Figure 5.3 imply that moesin or annexin A1 do not act on radioiodide uptake by stimulating *de novo* expression of *SLC5A5* or by modulating protein degradation, and instead may act to modulate post-translational processing of NIS or its movement around the cell.

Overexpression of moesin or annexin A1 did not modulate iodide uptake in cells (Figure 5.4). It is feasible that the capacity for moesin or annexin A1 to affect NIS function is already high enough to prohibit any additional effect when exogenous protein is transfected, but that reduction in already abundant protein levels by siRNA knockdown may produce a measurable effect. To address this possibility, overexpression of moesin and annexin A1 in human primary thyroid cells, would examine their roles in a more physiological context.

From the siRNA knockdown data (Figure 5.3), it can be inferred that elevated tumoural expression of *MSN* or *ANXA1* may negatively affect iodide uptake. The upregulation of both *MSN* and *ANXA1* is biased towards $BRAF^{V600E}$ tumours, and activated MAPK signalling is also associated with a loss of *SLC5A5* expression and reduced iodide uptake. The extent to which

reduced iodide uptake is a result of elevated *MSN* and *ANXA1* expression versus the co-occurring $BRAF^{V600E}$ will be complicated to dissect. However, some $BRAF^{WT}$ papillary thyroid carcinomas do exhibit significantly higher average moesin and annexin A1 compared to matched normal tissue, indicating *MSN* and *ANXA1* are not solely upregulated in tumours with high MAPK signalling. To address this, the regulation of moesin and annexin A1 by the MAPK pathway is further explored in Chapter 6.

5.4.3 NIS Interacts with Moesin and Annexin A1

Confocal microscopy supported the hypothesis that NIS and moesin interact at the plasma membrane, but did not equivocally indicate a physical interaction, rendering Figure 5.5 supportive but circumstantial data. Although initial mass spectrometry data measured NIS and annexin A1 as interacting in the plasma membrane fraction of cells, distribution of annexin A1 in TPC1 and HeLa cells did not reveal strong staining at the plasma membrane nor areas of staining overlap. A lack of colocalisation of NIS and annexin A1 in immunofluorescence does not undermine on the validity of the interaction measured by NanoBIT. Indeed, fluorescent imaging of NIS and VCP did not reveal obvious areas of colocalisation despite VCP having been shown to bind to NIS via multiple methods (Fletcher et al., 2020). It is possible that interactions between NIS and VCP, and NIS and annexin A1 are transient and rapid and therefore immunofluorescent techniques are not optimised to detect these interactions. More sensitive methodologies that can be performed on live cells are necessary and hence these interactions were measurable by NanoBiT technology.

To challenge the preliminary conclusions based on mass spectrometry data that NIS functionally interacts with Moesin and Annexin A1, three technologies were employed: co-immunoprecipitation, BRET and NanoBIT. Of these three methods, only the data derived from NanoBIT experiments supported a conclusion that Moesin and AnnexinA1 represent novel NIS interacting proteins. Whilst overall this may appear to weaken the hypothesis, the co-immunoprecipitation experiments failed at the technical level when moesin was detected in the IgG antibody control lane. The BRET assay showed a significant difference between the negative control (NIS-GFP and untagged NanoLuc) and one positive control only (NIS-GFP and NIS-Nanoluc); however, the second positive control (NIS-GFP and VCP-Nanoluc) did not show any difference in BRET ratio when VCP was N-terminally tagged despite this interaction having been demonstrated to occur through multiple experimental techniques previously (Fletcher et al., 2020). Considering the incongruities of the BRET positive controls, the reliability of the assay for identifying novel NIS interacting proteins was questioned. Limitations of the BRET assay includes the lytic nature of the NanoGlo buffer which results in a single timepoint snapshot of the protein-protein interactions in the cell at the point of addition, which may not be sufficient to capture highly transient interactions in live cells, as also reflected in the lack of observable NIS-moesin or NIS-annexin interactions in the fixed immunofluorescent imaging. In contrast, NanoBiT was employed with both manufacturer-provided and assay-specific controls to assess whether the assay reproduced previous findings, with Figure 5.9 demonstrating that the multiple controls could determine that the NanoBiT assay provides valid data regarding both intracellular PRKACA subunit interactions and previously validated NIS interactions. Whilst a second, non- luciferase based assay would be valuable to further validate the findings in Figure 5.10, the data derived from the highly controlled NanoBIT assay should be considered valid and reliable evidence of a protein-protein interaction.

The plasmids transfected for the NanoBiT assay contained the gene-of-interest driven by the CMV promoter. CMV promoters are utilised to drive high levels of construct expression, therefore it should be considered whether an overload of the system resulted in non-specific interactions between NIS-SmBiT and LgBiT-tagged proteins. In this case the NIS-SmBiT and LgBiT-PRKAR2A negative control is valuable in appraising the occurrence of non-specific interaction, and indicated that the observed interactions between NIS and either VCP, moesin, and annexin A1 are valid. Additionally, abrogation of measurable luminescence when VCP was tagged on the C-terminus further indicates that high expression levels do not result in non-specific binding. Interactions between the two tags are dependent on a favourable conformation of the interacting proteins-of-interest which enables formation of the SmBiT/LgBiT active complex. Confirmation of NIS- interactor binding by reverse NanoBiT assay (Figure 5.11) further validates findings that measurements were not due to non-specifically favourable tag dynamics.

NanoBiT demonstrated a robust interaction between NIS and moesin and NIS and annexin A1 using multiple controls (Figure 5.10 and Figure 5.11). The interaction between NIS and moesin was stronger when the LgBiT luciferase tag was attached to the N-terminus of moesin. The amino terminal of ERM proteins has been shown to bind other membrane proteins, hence tagging this region of moesin may present a more favourable interaction between the luciferase tags on the interacting proteins.

Notably, the luminescence emitted by the NIS-NIS interaction was orders of magnitude higher than that of the NanoBiT positive control or NIS-VCP interaction. The oxidation of the luciferin

substrate by luciferase to produce a luminescence output is limited by the entry of the luciferin substrate into the cell, hence there is a measurable increase in luminescence for approximately the first ten cycles. The NanoBiT assay does not signal the specific location of these interactions in the cell. However, as the NIS-NIS interaction begins at a much higher luciferase emission than other wells, it is possible that NIS dimer exists primarily at the membrane, and hence oxidation of the substrate occurs quickly after addition. Mass spectrometry data (Fletcher *et al* 2020; Table 1-2), and immunofluorescence colocalisation (Figure 5.5), implies that NIS and moesin interact at the plasma membrane. If the higher luminescence observed in the NIS dimer condition was based on immediate oxidation of luciferin after entry into the cell, this hypothesis should follow for the NIS and moesin interaction. However, although NIS and moesin exhibited significantly higher luminescence that the negative controls, the average luminescence was notably lower than the NIS dimerisation measurement. An alternative rationale for the higher luminescence observed in NIS dimerisation was that the conformation of NIS monomers in the dimer result in more favourable interaction between SmBiT and LgBiT which interact to form active luciferase. In this instance, luminescence would be higher than other protein-protein interactions which may form active luciferase in a less favourable, and hence less kinetic, conformation. This is supported by the homology model of NIS structure based on the crystal structure of the vSGLT transporter which positions a small dimerisation interface between the C-termini of NIS monomers (Thompson et al., 2019). This would position the C-terminal SmBiT and LgBiT tags in close proximity and may enable a high-affinity interaction which results in higher enzymatic activity compared to other interactors of NIS. The hypothesis that NIS dimers form a favourable conformation for interactions between two C-terminal tags is also supported by

the significant increase in the BRET ratio of the NIS-GFP and NIS-Nanoluc combination, compared to the BRET assay negative control (Figure 5.8A).

The $NIS^{K554A/R555A}$ mutant and moesin emitted much lower luminescence, suggesting reduced binding between NIS and moesin (Figure 5.14). Given that these NIS mutants do not show reduced iodide uptake capacity (Figure 5.13), it can be inferred that the mutants correctly traffic to the plasma membrane. If the KR motif in the C-terminal region of NIS is indeed required for moesin to bind to NIS, it may have been expected that emission of luminescence would be entirely abrogated, and non-significant when compared to the negative control. As the measured luminescence had only a 56 % decrease from NIS^{WT}, and remained significantly higher than the negative control, it may be that this motif aids in moesin binding, but some form of interaction can still take place after its mutation, perhaps via interacting with nearby amino acids that were not mutated in this study.

5.4.4 Hypothesis for the Interaction Between NIS and Moesin

Moesin has been implicated in the clathrin-dependent endocytosis of G-protein coupled receptors and in the trafficking of nascent clathrin-coated vesicles (Barroso-González et al., 2009; Nomachi et al., 2013). As a link between integral membrane proteins and the cell cytoskeleton, moesin is well positioned to facilitate the membrane-cytoskeleton rearrangements that are required for endocytosis. The hypothesis that moesin binds to NIS at the plasma membrane and facilitates its internalisation would account for the observed increase in NIS-mediated iodide uptake when moesin is knocked down, without affecting NIS protein level.

5.4.5 Hypothesis for the Interaction Between NIS and Annexin A1

Many reported cytoplasmic functions of annexin A1 focus on the post-endocytosis pathway, especially in the inward formation of vesicles in multivesicular bodies and in trafficking EGFR to lysosomes (Eden et al., 2016; Raulf et al., 2018; White et al., 2006). Whether annexin A1 functions at membranes of endosomal or lysosomal compartments to facilitate NIS degradation warrants further exploration. If annexin A1 facilitates NIS degradation, this accounts for the increase in radioiodide uptake analysis observed after *ANXA1* knockdown (Figure 5.3).

5.5 Concluding remarks

Investigating the post-translational processing of NIS is a developing area in thyroid cancer research. Adding new interactions along this pathway will build a holistic picture of post-translational NIS processing and highlight interactions which may be more vulnerable to pharmacological disruption to increase iodide uptake. In this chapter, two further protein are shown to interact with NIS in thyroid cells, and to be dysregulated in thyroid cancer at both the gene and protein level.

In many cancers, moesin and annexin A1 have been reported to be markers of aggressive characteristics such as invasion and migration. How these two proteins act at a subcellular level to contribute to the malignant phenotype has not been well described but both proteins have previously identified roles in protein trafficking, specifically in protein internalisation and trafficking. Moesin and annexin A1 showed greater upregulation of gene expression in $BRAF^{V600E}$ driven carcinomas, positioning *MSN* and *ANXA1* genes as possible downstream

targets of the MAPK pathway. The effect of inducing and inhibiting the MAPK pathway on moesin and annexin A1 protein levels and further investigation into the regulation of these proteins in thyroid cancer will be explored in Chapter 6.

6 Exploring the Regulation of Moesin and Annexin A1 in Thyroid Cancer Cells

6.1 Introduction

Chapter 5 demonstrated that moesin and annexin A1 both bind to NIS *in vitro* and modulate radioiodide uptake into thyroid cells, and that expression of the genes encoding these proteins are dysregulated in samples of PTC. It may now be useful to determine the potential for modulating these proteins *in vitro*. To explore the regulation and function of moesin and annexin A1 in thyroid cancer, data from TGCA were analysed to identify genes that were co-enriched in tumours that express high levels of *MSN* and *ANXA1*. Furthermore, the regulation of moesin and annexin A1 by signalling pathways that are hyperactive in thyroid cancer were explored. Finally, the regulation of moesin protein levels by retinoic acid, which has been reported previously in breast cancer, was investigated in thyroid cancer cells.

6.1.1 Downstream Targets of the MAPK Pathway in Thyroid Cancer

BRAF-activating mutations are the most common genetic alteration of papillary thyroid cancer. Many genes that are downstream targets of the MAPK pathway have well-characterised roles in thyroid cancer including proteins that mediate NIS internalisation, cell invasion and migration, and extrathyroidal invasion (Hu et al., 2006; Li et al., 2020; Read et al., 2017). For instance, PTTG- binding factor (PBF) has been demonstrated to bind to NIS and facilitate its internalisation (Smith et al., 2009). PBF is a downstream target of MAPK signalling and was downregulated after treatment of cells with 200 nM selumetinib (Read et al., 2017; Smith et al., 2009); Figure 6.1).

Thus, identifying proteins which function downstream of the MAPK pathway may provide more specific targets for modulating the thyroid cancer phenotype than broad-spectrum

MAPK inhibitors. Moesin and annexin A1 are overexpressed in thyroid cancer generally but display a stronger overexpression in $BRAF^{V600E}$ tumours (Figure 5.1). The principle that MAPK targeted genes may be upregulation by the activation of MAPK signalling or downregulated by treatment with MAPK inhibitors was used to challenge the hypothesis that overexpression of moesin and annexin A1 arise due to hyperactive MAPK signalling.

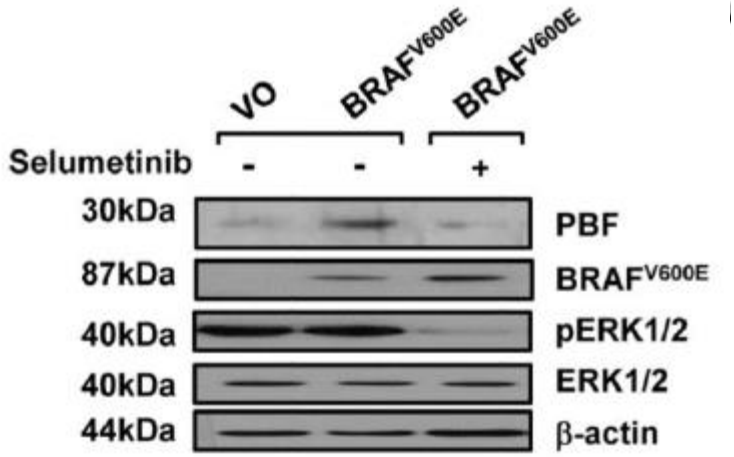


Figure 6.1 ***Proteins which are downstream effectors of the MAPK pathway and contribute to thyroid cancer phenotypes can be downregulated in thyroid cells by treatment with MAPK inhibitors****. PBF protein is upregulated by expression of* $BRAF^{V600E}$*, and this effect can be reversed by treatment with 200nM selumetinib. Adapted from Read et al 2016.*

6.1.2 PIK3CA Genomic Alterations in Endocrine Cancers

Mutations in *RAS* and *PIK3CA* both lead to hyperactivity of the PI3K-Akt-mTOR signalling pathway in cancers. *PIK3CA* encodes p110α, the catalytic subunit of PI3K. *PIK3CA* is a well characterised oncogene in breast cancer whereby heterozygous mutations are observed in 35.7 % of patient samples (Martínez-Sáez et al., 2020). Alpelisib is a potent, small molecular inhibitor specific to p110α. Alpelisib has been tested in large-scale clinical trials and is approved for use in metastatic breast cancer by the FDA and MHRA. In combination with

fulvestrant, alpelisib was shown to improve progression-free survival from 5.7 months to 11 months in patients with *PIK3CA*-mutated breast cancer (André et al., 2021).

In thyroid cancer, PI3KCA mutations are more commonly observed in PDTC and ATC which carry the $BRAF^{V600E}$ mutation (Landa et al., 2016). A combination of *BRAF* and *PIK3CA* mutations induce a faster, more aggressive phenotype associated with anaplastic thyroid cancer in mouse models, compared to either mutation individually (Charles et al., 2014). Although activating *PIK3CA* mutations are rare in PTC, one study reported that *PI3KCA* was amplified in 265 of 499 PTC samples, suggesting that over 50 % of PTC tumours may have elevated PI3K-Akt-mTOR signalling via the amplified gene expression of key components of this pathway (Abubaker et al., 2008). In this Chapter, treatment with Alpelisib was used to challenge the hypothesis that moesin overexpression is potentially driven by induction of *PIK3CA* gene expression in thyroid cancer.

6.1.3 Moesin May be Targeted by Retinoic Acid

MAPK or PI3K pathway inhibitors alter the expression of many genes simultaneously. For the specific aim of increasing radioiodide uptake, it may be more efficient to target moesin or annexin A1 more directly. The scientific literature was screened for drugs which were associated with a reduction in moesin or annexin A1 protein levels. Retinoic acid (RA) has previously been shown to decrease moesin expression at a concentration of 1 µM for 72 hours in MCF7 and T47D breast cancer cell lines (Flamini et al., 2014). In a later study, a shorter incubation period of ten to twenty minutes with RA increased the phosphorylation and activation of moesin via a pathway mediated by the kinase c-Src (Sanchez et al., 2016).

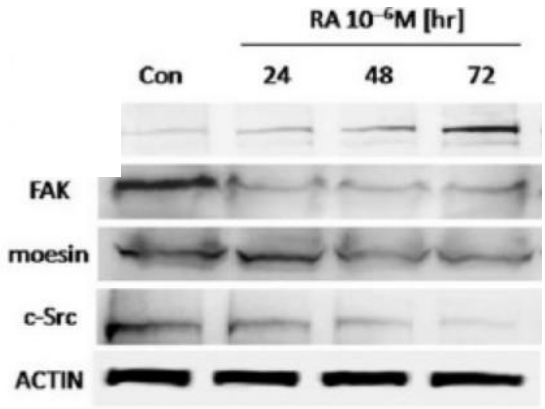


Figure 6.2 ***Treatment with retinoic acid decreases moesin protein level in MCF7 cells****. Adapted from Flamini et al, 2014.*

Retinoids have been investigated as a therapeutic redifferentiation factor for patients with radioiodide-refractory thyroid cancer (RRTC) for many years. Multiple small- scale studies have examined the effect of all-*trans*-retinoic acid or 13-*cis*-retinoic acid on groups ranging in size from eleven to fifty-three patients with RRTC (Coelho et al., 2011; Damle et al., 2011; Fernández et al., 2009; Handkiewicz-Junak et al., 2009; Simon et al., 2002). These studies reported variable levels of efficacy of RA in the inhibition of tumour growth and a low frequency of adverse side-effects. However, each study also reported a subgroup of patients who demonstrated increased iodide avidity compared to baseline iodide uptake although this response was often not accompanied by a clinical tumour response. Furthermore, 33 % of patients who had previously shown no iodide uptake reported a positive iodide uptake scan after treatment with 13-*cis*-RA (Fernández et al., 2009). Retinoid treatment induced a partial response in tumour size in three out of sixteen patients, although the response was not correlated with the number of cycles of RA treatment. This suggests that the determining factors for a positive response after treatment with RA response may lie in the underlying pathology of the tumour rather than cumulative dose of RA (Coelho et al., 2011). Overall, evidence is lacking to support indiscriminate treatment with retinoic acid in patients with

advanced, radioiodide-refractory thyroid cancer. In this Chapter, the hypothesis that treatment with RA may modulate radioiodide uptake *in vitro* via downregulation of moesin was examined.

6.2 Materials and Methods

6.2.1 TCGA Gene Expression Analysis in Tumours with Upregulated Moesin and Annexin A1

Data from the cancer genome atlas were accessed via cbioportal (Cerami et al., 2012; Gao et al., 2013). 510 papillary thyroid cancer samples were analysed from the cell 2014 database of RNAseq data.

RNAseq data for all patients were downloaded into Microsoft Excel and samples from tumour metastases were identified and removed. 51 matched normal control samples were separated, and the remaining cancer samples were split into $BRAF^{WT}$ and $BRAF^{V600E}$. Thirteen patient samples with *BRAF* fusion events were excluded from the analysis due to these fusion proteins having unconfirmed functionalities and effects on MAPK signalling. For the remaining 488 samples, the RNAseq data for moesin were extracted and the log2 transformed values were calculated to bring the data towards a normal distribution for subsequent comparison and statistical analysis. Patients in the $BRAF^{WT}$ and $BRAF^{V600E}$ cohorts were ranked according to their log2 expression of moesin. According to the log2(*MSN*) values, the cohorts were split into four quartiles, and the upper and lower quartiles of the $BRAF^{WT}$ and $BRAF^{V600E}$ cohorts were compared for genes which were significantly upregulated in the upper quartiles compared to the lower quartile. The resulting two lists of significantly upregulated genes were cross matched between the $BRAF^{WT}$ and $BRAF^{V600E}$ samples. The final list represented genes that were co-enriched alongside moesin in both $BRAF^{WT}$ and $BRAF^{V600E}$ tumour samples. The

functions of the genes in this list were assessed by conversion to ENTREZ ID and inputting into the DAVID functional clustering tool (https://david.ncifcrf.gov/) with KEGG pathway analysis. A schematic of the gene expression data extraction process is recapitulated in Figure 6.3. A likewise list, generated using the same cross matching but for upregulated *proteins* was also extracted. Secondly, this process was repeated for assessing the genes and proteins that were co-enriched in tumour samples that express high levels of *ANXA1.*

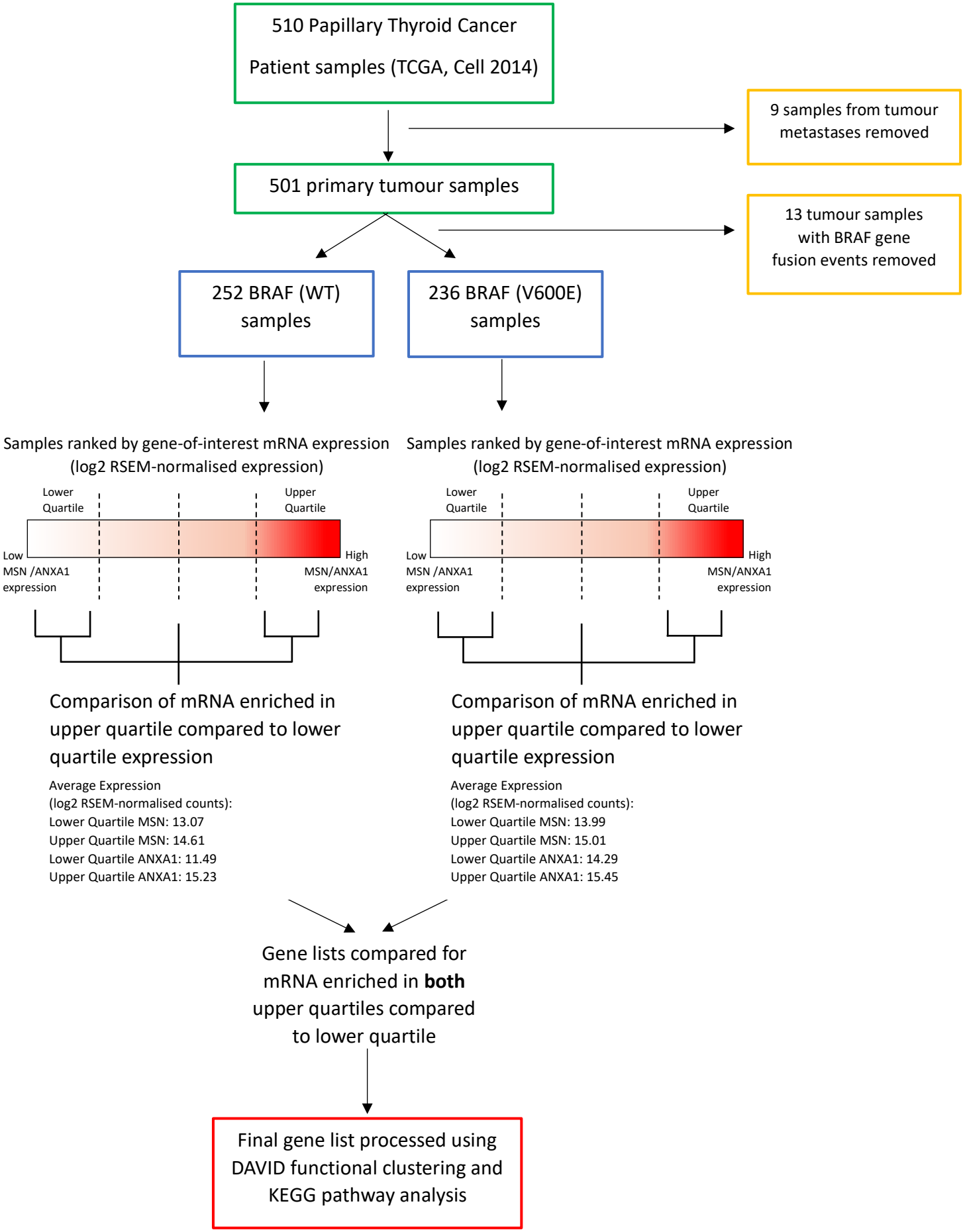


Figure 6.3 ***A flow diagram of RNAseq data obtained from THCA database of the Cancer Genome Atlas.*** *This process was used to analyse the expression of MSN and ANXA1 in BRAF^{WT} and BRAF^{V600E} driven tumours.*

6.2.2 $BRAF^{WT}$ and $BRAF^{V600E}$ Inducible Cell Systems

The generation of specific plasmids for the Invitrogen Flp-In™ T-Rex™ system containing $BRAF^{WT}$ and $BRAF^{T1799A}$ is described in Section 2.9. These plasmids were transfected into HeLa and U2OS cells which already contained a single FRT recombination sites stably integrated into the genome. Transformants were selected by combination of 5 µg/ml blasticidin and 400 µg/ml hygromycin B. Expression of the *BRAF* construct was induced by addition of 1 µg/ml tetracycline to the cell culture medium and protein was harvested after 24 hours to assess effect of MAPK stimulation on moesin and annexin A1 protein by Western blot, as outlined in Section 2.5.3.

6.2.3 MAPK and PI3K Pathway Inhibitor Treatments

Selumetinib, vemurafenib, and alpelisib were all purchased from Selleck Chemicals Scientific (S1008, S1267 and S2814, respectively) and were prepared as 10 mM stock solutions in DMSO then stored at -20°C. 24 hours after seeding, the cells were treated with the following increasing doses of inhibitors (Table 6-1).

Inhibitor	Protein Target	Doses
Selumetinib	MEK1/2	DMSO only, 200 nM, 500 nM, 750 nM and 1 µM
Vemurafenib	$BRAF^{V600E}$	DMSO only, 1 µM, 2 µM, 5 µM and 8 µM.
Alpelisib	PI3K subunit p110α	DMSO only, 10 µM, 15 µM, 20 µM and 40 µM

Table 6-1 ***The doses of MAPK and PI3K inhibitors that were used to assess the effect on moesin and annexin A1 protein level****.*

The duration of the drug treatments was 24 hours before protein was harvested in a combination of RIPA lysis buffer, protease inhibitors and phosphatase inhibitors and prepared

for Western blot analysis. MAPK and Akt pathway inhibition were evaluated by probing for phosphorylated ERK after treatment with selumetinib and vemurafenib, and phosphorylated Akt after treatment with alpelisib.

6.2.4 Retinoic Acid Treatment

Retinoic Acid was purchased from Sigma-Aldrich (R2625) and resuspended in DMSO to 100 mM stock solutions that were stored at -80^{o}C. On the day of treatment, the stock solution was diluted in DMSO to a 10 mM working solution and TPC1 and 8505C cells were treated with 1 µM. Protein was harvested at 24, 48 and 72 hour timepoints and analysed by Western blot, see Section 2.5.3.

6.3 Results

6.3.1 mRNA Expression of Moesin and Annexin A1 in Differentiated Thyroid Cancer

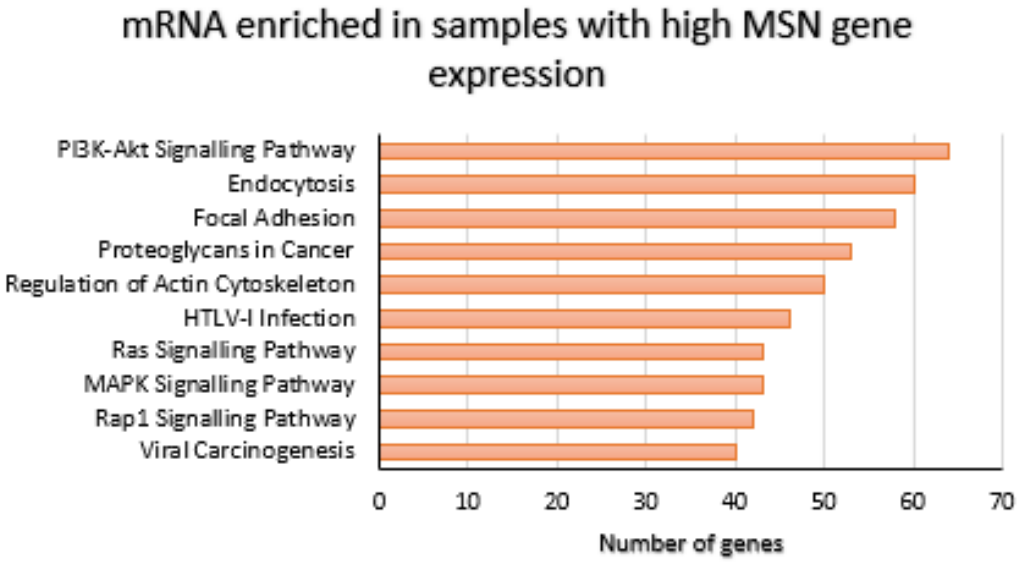
To explore the broader transcriptome in tumours with elevated *MSN* or *ANXA1* expression, genes and proteins which were co-enriched alongside either moesin or annexin A1 in both $BRAF^{WT}$ and $BRAF^{V600E}$ tumours were cross-matched. As both *MSN* and *ANXA1* are overexpressed more in $BRAF^{V600E}$ tumours than $BRAF^{WT}$ tumours, transcriptomic analysis of the tumours in the top quartile of *MSN* or *ANXA1* expression in the whole THCA dataset resulted in all upper quartile samples harbouring the $BRAF^{V600E}$ mutation. Therefore, it was not possible to dissect changes in the transcriptome that might have been related to *MSN* overexpression as opposed to the $BRAF^{V600E}$ driver mutation. Cross-matching these genes with the subgroup of $BRAF^{WT}$ tumours that also expressed high *MSN* and *ANXA1* aimed to

highlight changes which may be related to *MSN* or *ANXA1* overexpression rather than to the $BRAF^{V600E}$ mutation alone.

The list of genes that are co-enriched in high-moesin expressing tumours contained groups of genes associated with multiple signalling pathways as well as endocytosis, and cytoskeleton regulation (Figure 6.4A). There were 43 genes associated with MAPK signalling, which was consistent with the observation that $BRAF^{V600E}$ tumours typically express the highest levels of *MSN.* There were 64 enriched genes associated with the PI3K-Akt-mTOR pathway including *PIK3CA*, *AKT3, JAK* 1 and *JAK2, MEK, FN1* and *ITGA3*. 60 genes in the list mapped to endocytosis pathways including *ARF6, AP2A1* and *AP2B1* adaptors and multiple guanine-nucleotide exchange factors. Cross referencing of the proteins enriched in $BRAF^{WT}$ and $BRAF^{V600E}$ tumours which highly expressed moesin yielded only one match: *PIC3KA/*p110α. It should be noted that the range of proteomic analysis performed on TCGA samples is limited to the 219 protein markers in the reverse-phase protein array.

In the list of genes enriched in high annexin A1 expressing tumours, genes related to focal adhesion were most commonly upregulated alongside annexin A1 including the *ELK1*, *ITGA3*, *CAV2* and *MET* (Figure 6.4B). Notably, genes related to lysosome function were upregulated, including *LAPTM4A*, *CD63* and *CTSH*. Cross referencing of the proteins enriched in $BRAF^{WT}$ and $BRAF^{V600E}$ tumours which highly expressed annexin A1 yielded no matches from the markers assess by the reverse phase protein array.

A



B

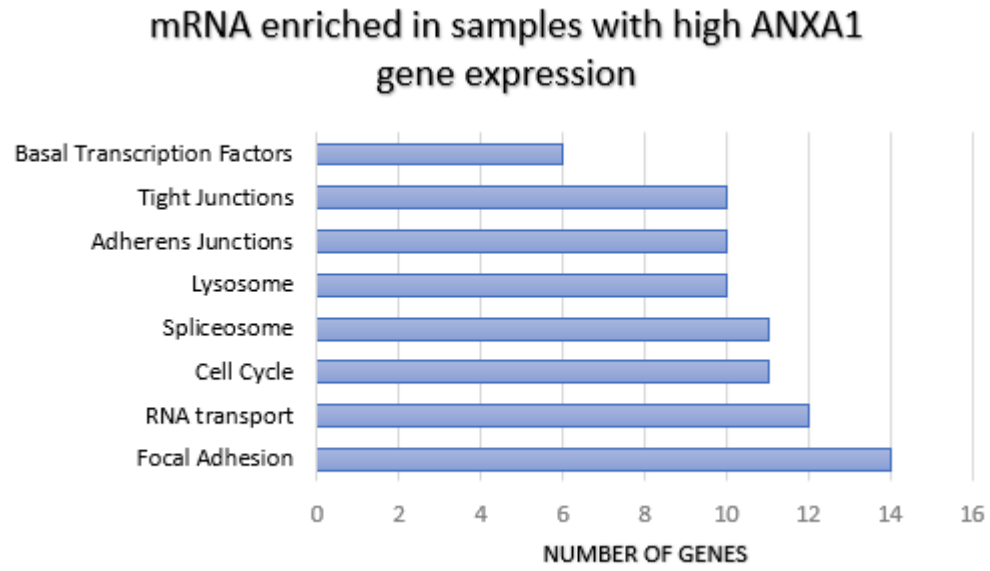


Figure 6.4 ***A comparison of the genes which display enriched expression in samples which also express high levels of (A) Moesin and (B) Annexin A1, in both BRAF^{WT} and BRAF^{V600E} tumour samples.*** *Analysis was completed using DAVID functional clustering and KEGG Pathway analysis.*

6.3.2 Moesin and Annexin A1 are Not Modulated by Induction of the MAPK Pathway

Inducible $BRAF^{WT}$ and $BRAF^{V600E}$ systems were generated in HeLa and U2OS cell lines by employing the Invitrogen T-Rex™ system. It was hypothesised that if moesin or annexin A1 were induced downstream of MAPK pathway activation, a larger increase in protein level would be measured after induction of $BRAF^{V600E}$ than $BRAF^{WT}$, given the constitutive activation of the MAPK pathway conferred by the V600E mutation. Induction of the *BRAF* gene was apparent 4 hours after addition of tetracycline (Figure 6.5A); cells therefore had at least 20 hours of BRAF overexpression for an effect on moesin or annexin A1 protein level to occur. Induction of $BRAF^{WT}$ and $BRAF^{V600E}$ was shown to be entirely dependent on tetracycline addition, confirming that there was no "leaky" expression detected in non-tetracycline-induced samples (Figure 6.5B). Moesin and Annexin A1 protein levels were uniform across both cell lines after induction of both $BRAF^{WT}$ and $BRAF^{V600E}$ for 24 hours (Figure 6.5B).

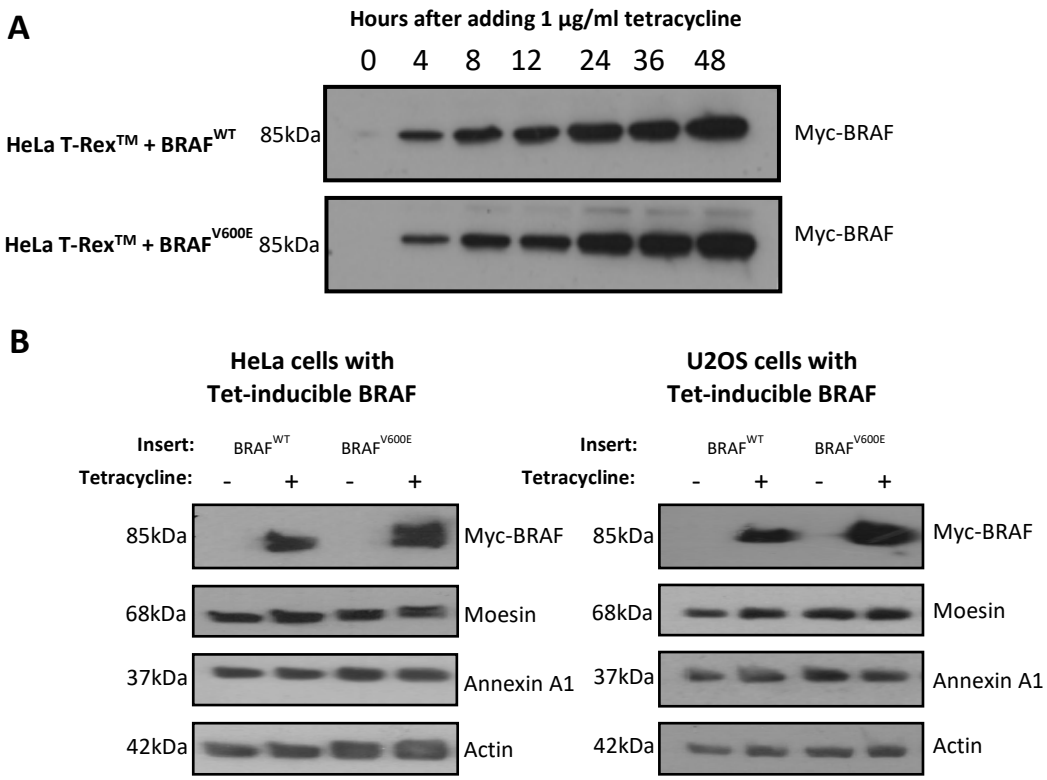


Figure 6.5 ***Moesin and Annexin A1 protein levels are not induced upon MAPK stimulation by induction of BRAF^{WT} or BRAF^{V600E}*** *(**A**) BRAF induction occurs within 4 hours of the addition of tetracycline to cell culture media in T-Rex^{TM} cells. (**B**) HeLa and U2OS cells with induced BRAF^{WT} and BRAF^{V600E} did not demonstrate altered levels of moesin or annexin A1 protein.*

6.3.3 Moesin and Annexin A1 Is Not Modulated by Inhibition of the MAPK Pathway

Activation of MAPK signalling did not result in the stimulation of *MSN* or *ANXA1* gene expression in the HeLa or U2OS BRAF-inducible system (Figure 6.5B). To challenge these data, MAPK inhibitors were employed in TPC1 and 8505C thyroid cell lines to discern the effect of disrupting MAPK signalling on moesin and annexin A1 protein levels. Selumetinib reduced the amount of phosphorylated ERK protein in both TPC1 and 8505C cell lines while total ERK protein remained constant (Figure 6.6), confirming the functional inhibition of the MAPK pathway. Vemurafenib is a selective inhibitor for the BRAF^{V600E} monomer and reduced phosphorylated ERK only in the 8505C cell line which harbours this mutation (Figure 6.7).

Despite a reduction in MAPK signalling, there was no significant change in moesin or annexin A1 protein levels (Figure 6.6 and Figure 6.7).

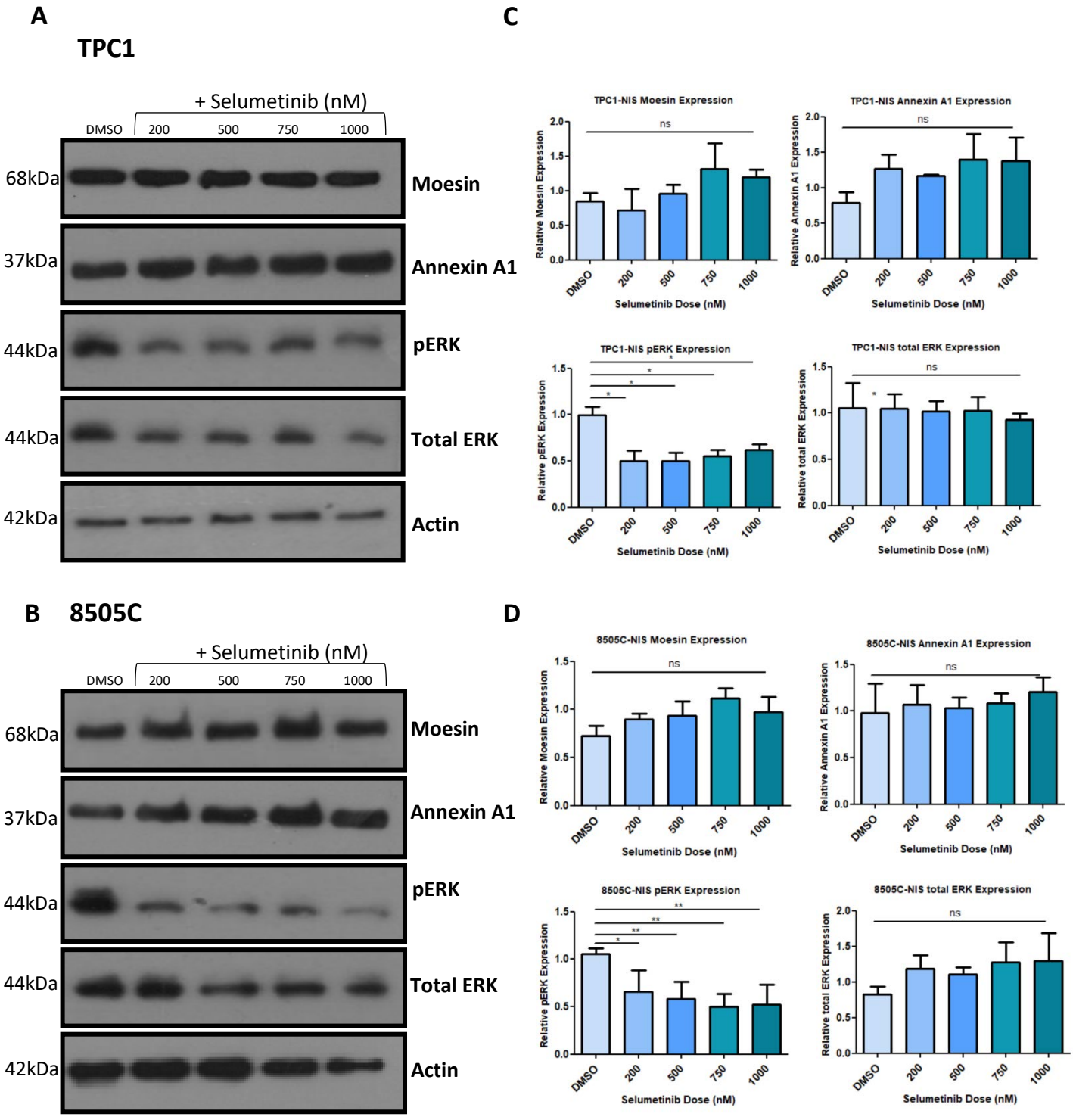


Figure 6.6 ***Treatment of TPC1-NIS (A) and 8505C-NIS cells (B) with increasing doses of selumetinib does not affect protein level of either moesin or annexin A1,*** *but does decrease the proportion of phosphorylated ERK1/2 compared to total ERK1/2 protein. Densitometry analysis in (**C**) and (**D**) normalised to the expression of β-actin. Significance assessed by one way ANOVA. * = p < 0.05; ** = p < 0.01; ns = non-significant.*

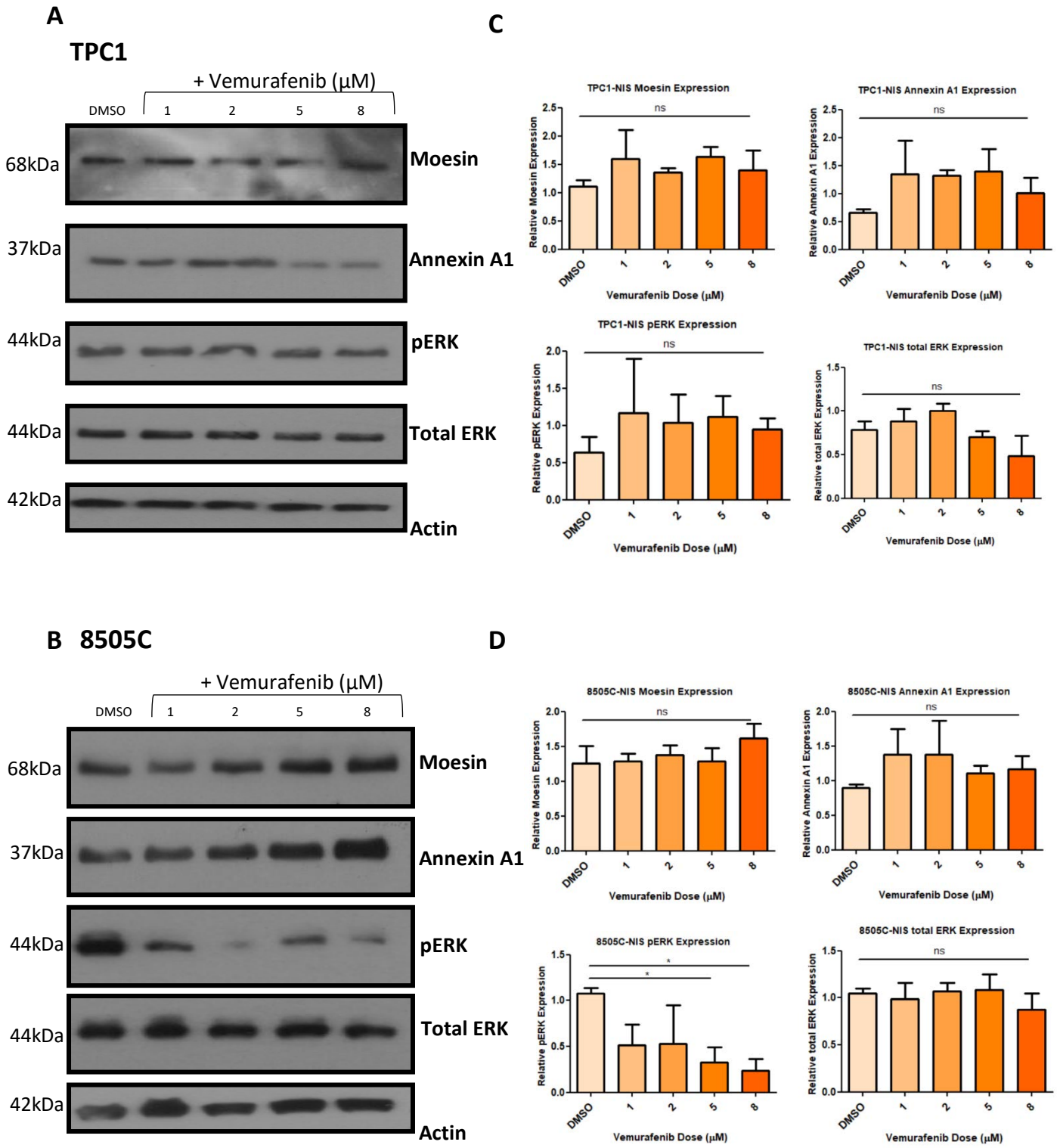


Figure 6.7 ***Treatment of TPC1-NIS (A) and 8505C-NIS cells (B) with increasing doses of vemurafenib from 1 to 8μM does not affect protein level of either moesin or annexin A1****, but does decrease the proportion of phosphorylated ERK1/2 compared to total ERK1/2 protein which is unaffected in 8505C-NIS which harbour BRAF^{V600E} mutation (**D**); the drug has no significant effect on phosphorylated ERK in TPC1-NIS cells which are homozygous BRAF^{WT} (**C**). Densitometry analysis in (**C**) and (**D**) normalised to expression of beta-actin. N=3 experimental repeats Significance assessed by one way ANOVA. * = p < 0.05; ** = p < 0.01; ns = non-significant.*

.

The effect of selumetinib and vemurafenib on radioiodide uptake was assessed; it was observed that inhibition of the MAPK pathway resulted in increased iodide uptake (Figure 6.8).

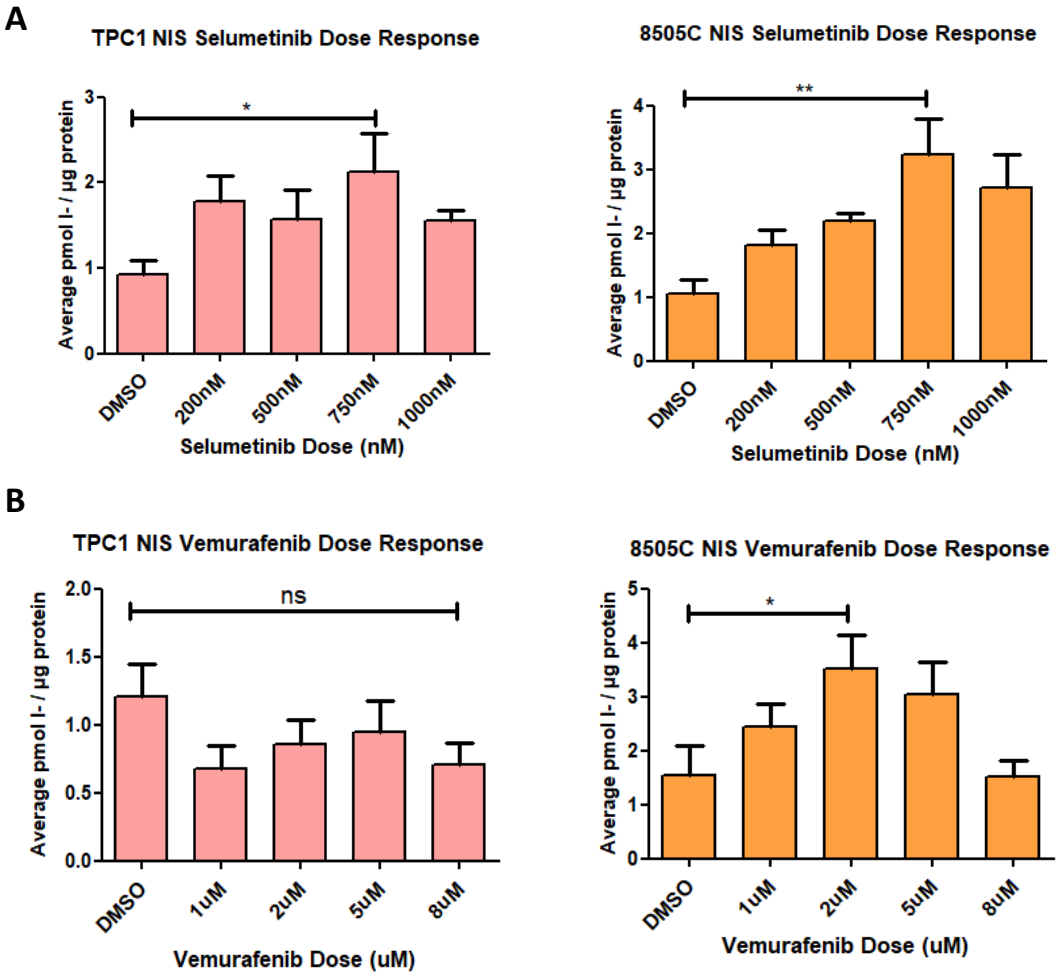


Figure 6.8 ***Effect of MAPK inhibition on radioiodide uptake in TPC1-NIS and 8505C-NIS cells.*** *(**A**) Selumetinib treatment significantly increased NIS-mediated radioiodide uptake in TPC1-NIS and 8505C-NIS cells after treatment with 750 nM for 24 hours. (**B**) Vemurafenib significantly increased radioiodide uptake after treatment with 2µM in 8505C-NIS cells that harbour the $BRAF^{V600E}$ mutation that is targeted specifically by the drug. Vemurafenib had no significant effect on radioiodide uptake in TPC1-NIS cells which are homozygous for $BRAF^{WT}$. Significance was assessed by ANOVA, * = $p < 0.05$; ** = $p < 0.01$. n=3*

6.3.4 Moesin is Not Downregulated by Inhibition of the PI3K-Akt-mTOR Pathway

*PIK3CA/*p110α was shown to be enriched at both the mRNA and protein level in samples with high levels of *MSN* expression, and multiple other genes involved in PI3K signalling were also co-enriched in these samples (Figure 6.4A). Therefore, the effect of p110α inhibition by the specific inhibitor alpelisib was used to measure the effect of inhibiting PI3K signalling on moesin protein levels. Treatment with alpelisib showed unmeasurable levels of phospho-AKT at all doses of alpelisib, indicating inhibition of the PI3K pathway from treatment with 10 μM upwards (Figure 6.9A and B). However, this did not translate to any significant changes in moesin protein expression. As analysis of TCGA data did not indicate annexin A1 was regulated by PI3K signalling, the effect of alpelisib on annexin A1 protein was not studied.

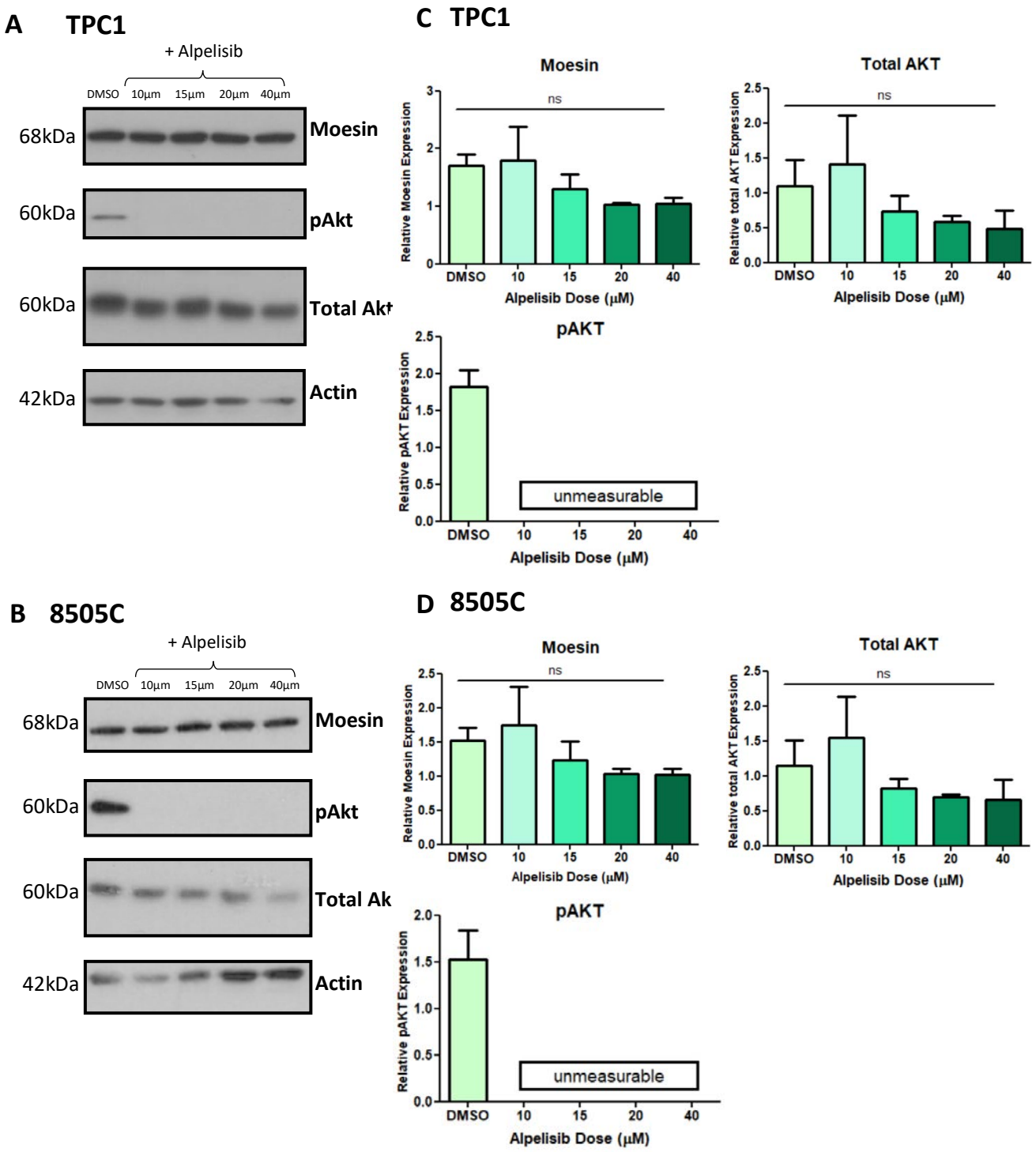


Figure 6.9 ***The PI3K-Akt-mTOR inhibitor alpelisib has no effect on moesin protein levels after treatment with doses between 10 and 40 µM in TPC1-NIS (A) and 8505C-NIS (B) cells.*** *Phosphorylated AKT was unmeasurable at 10 µM and above. Densitometry analysis on protein levels in (**C**) and (**D**) was performed after normalising to beta-actin protein expression. Alpelisib had no significant change on the total AKT protein level. n=3, analysed by one way ANOVA. ns = non-significant.*

The effect of inhibiting PI3K signalling on NIS-mediated iodide uptake was assessed; treatment with alpelisib did not result in any changes in uptake (Figure 6.10).

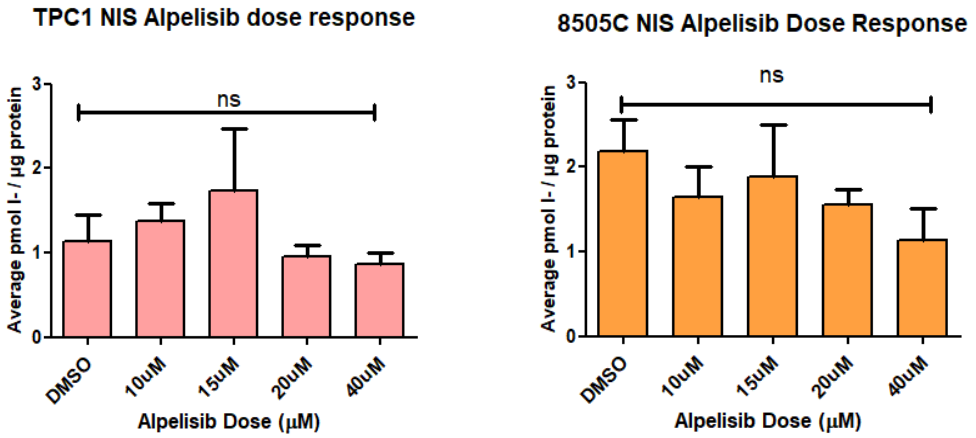


Figure 6.10 ***The PI3K-Akt-mTOR pathway inhibitor alpelisib has no effect on radioiodide uptake in TPC1-NIS and 8505C-NIS cells after treatment for 24 hours at multiple doses.***

6.3.5 Moesin is Not Regulated by Retinoic Acid in Thyroid Cancer Cell Lines

Flamini *et al* first reported that moesin protein was downregulated after treatment of breast cancer cells with 1 µM retinoic acid (Flamini et al., 2014). Despite some discordant clinical trials data on the effectiveness of RA in thyroid cancer, further analysis of how this link may be relevant in thyroid cancer would be useful to determine whether RA may reduce moesin protein levels and affect radioiodide uptake. Protein analysis after treatment with 1 µM retinoic acid for 24, 48 and 72 hours did not show a change in moesin protein level as described in breast cancer cells (Flamini *et al* 2014; Figure 6.11). Treatment with retinoic acid did not result in observable cell death or morphological changes (data not shown).

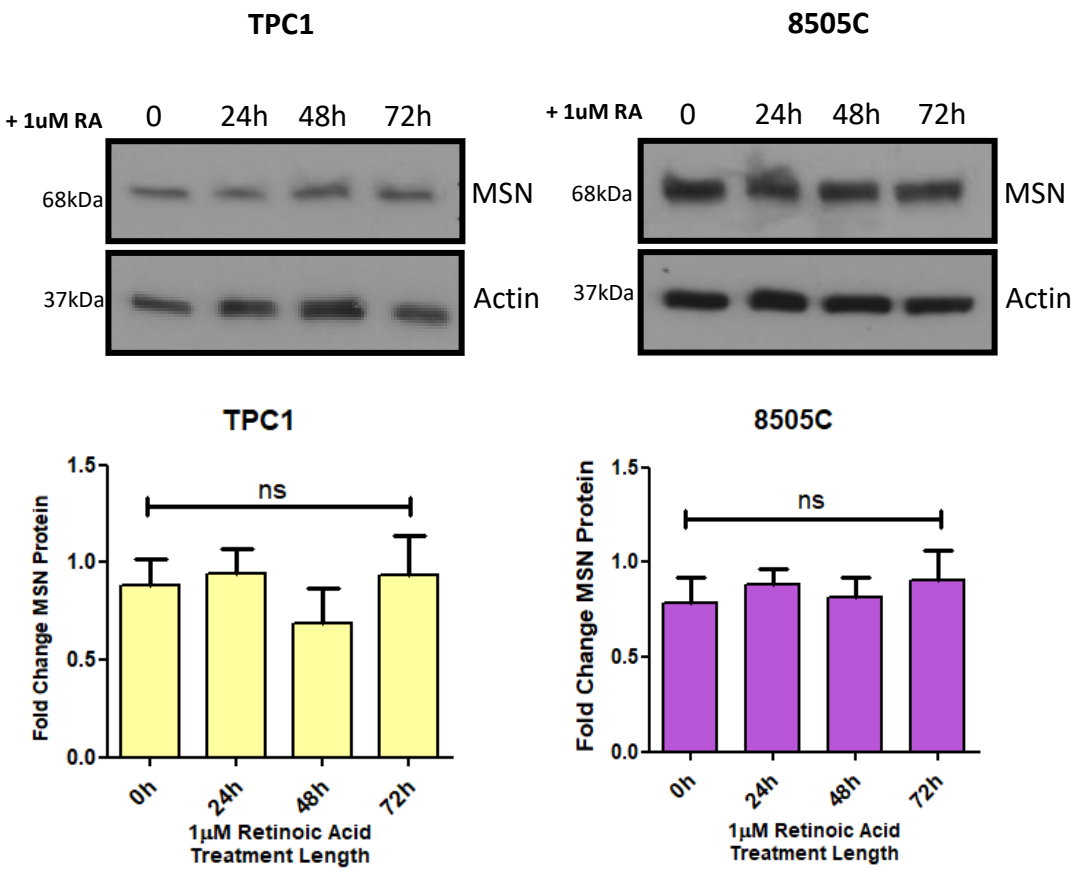


Figure 6.11 ***Treatment with 1 μM retinoic acid over 72 hours does not affect moesin protein level in TPC1 and 8505C cell lines.***

6.4 Discussion

6.4.1 Transcriptomic Analysis of Tumour Samples which Express High Levels of *MSN* or *ANXA1*

Figure 6.4A demonstrates that tumours that express the highest levels of *MSN* also overexpress genes associated with MAPK and PI3K signalling pathways. This led to the hypothesis that these signalling pathways may be driving the overexpression of moesin; however, this was not equivocally confirmed by inhibition of the pathways.

The transcriptome analysis of tumours which most highly express *ANXA1* had a smaller list of cross-matched genes between the $BRAF^{WT}$ and $BRAF^{V600E}$ tumours (Figure 6.4B). In this list,

were many genes related to cell junctions and movement, which is consistent with the reported pro-metastatic role of annexin A1 in some cancers. Additionally, the tumours that highly expressed *ANXA1* were also enriched for expression of genes related to lysosomal function, which tentatively supports the working hypothesis that annexin A1 has a role in lysosomal degradation in thyroid cancer, including potentially the degradation of NIS.

6.4.2 The Regulation of Moesin and Annexin A1 by the MAPK Pathway

Neither induction nor inhibition of MAPK signalling modulate the protein levels of moesin or annexin A1, controverting the hypothesis that *MSN* and *ANXA1* are downstream targets of the MAPK pathway.

HeLa and U2OS cells do not harbour mutations that are known to upregulate moesin and annexin A1 compared to non-cancerous cells, such as *BRAF*, *RET* fusions or *NTRK1/3* fusion genes. As a result, these cells may have a lower baseline level of these proteins and provide a more appropriate system for assessing the upregulation of moesin and annexin A1. Conversely, TPC1 and 8505C cells harbour RET fusion and $BRAF^{V600E}$ drivers, respectively. As these mutations are associated with higher moesin and annexin A1 gene expression, these two cell lines may be better placed to measure a decrease in moesin and annexin A1 protein levels, in this case after treatment with MAPK inhibitors.

Tetracycline-induced BRAF did not result in changes to the protein levels of moesin or annexin A1 in T-Rex™ cells (Figure 6.5). This implies that induction of the MAPK pathway does not stimulate expression of *MSN* or *ANXA1* genes. Additionally, moesin and annexin A1 protein levels remained constant during MAPK inhibition by selumetinib or vemurafenib. Therefore,

the increased iodide uptake observed by siRNA knockdown of *MSN* and *ANXA1* (Figure 5.3) cannot be reproduced by targeting the MAPK pathway to downregulate these proteins. It is possible that transcriptional activation of these proteins arises after a longer duration of MAPK signalling, and that induction for only 24 hours was not sufficient to produce a measurable change in protein level. BRAF induction using the T-Rex^{TM} system could be extended to 72 hours for further validation. The 24 hour timeframe for MAPK inhibitor experiments was adopted based on findings that ERM proteins and annexin A1 undergo rapid turnover in cells (Fritzsche et al., 2014; Shimoji et al., 2009). However, if the half-life of moesin or annexin A1 is longer than 24 hours, a decrease in protein level may not be observed until prolonged inhibition of MAPK signalling. Despite the relevance of activated MAPK signalling in thyroid cancer, many cellular processes are regulated outside of this critical pathway. Consequently, it now must be considered whether moesin and annexin A1 are regulated outside of the MAPK pathway. TCGA data of PTC samples demonstrated that moesin is upregulated in some cancers which are not driven by BRAF^{V600E} (Figure 5.1). Considering the data indicating that moesin and annexin A1 proteins are not affected by short-term manipulation of the MAPK pathway, it reasons that moesin and annexin A1 may be regulated by proteins which are frequently dysregulated in BRAF^{V600E} tumours, and this dysregulation may also arise in BRAF^{WT} tumours to elicit the same increase in moesin and annexin A1 protein level. For example, the BRAF^{V600E} mutation is associated with epigenetic dysregulation in thyroid cancer cells, which can cause in broad changes to the genetic profile of a tumour cell (Guo et al., 2015; Hou et al., 2011). It is possible that the upregulation of *MSN* and *ANXA1* expression are driven by the loss of DNA methylation sites in the promoter regions of these genes. Indeed, some of these DNA methylation changes are highly stable and may not be

instigated immediately after MAPK activation, nor reversed by treatment with MAPK inhibitors.

Despite a positive increase in radioiodide uptake being conferred by MAPK inhibitors at 24 hours this is not a result of changes to moesin or annexin A1 protein. Therefore, these proteins remain therapeutic targets aside from MAPK inhibition and which may yield a summative effect on iodide uptake when targeted in combination. This may be achieved by the development of specific inhibitors to moesin or annexin A1, or by determining the mechanism underlying their interaction with NIS in thyroid cancer which may reveal alternative druggable targets.

6.4.3 The Regulation of Moesin by PI3K Signalling

Analysis of the RNA profiles for patients with elevated moesin RNA from the cancer genome atlas suggested that higher *MSN* expression co-occurred with elevated *PIK3CA* expression and p110α protein level in patients with both $BRAF^{WT}$ and $BRAF^{V600E}$ tumours. Moreover, tumours from both $BRAF^{WT}$ and $BRAF^{V600E}$ tumours with high levels of *MSN* expression also displayed enriched expression of genes related to PI3K signalling (Figure 6.4). *PI3KCA* mutations are observed in fewer than 2 % of all PTC cases, therefore this oncogenic mutation was not considered in the comparison of moesin and annexin A1 by driver mutations (Figure 5.1B). However, frequent *RAS* mutations in PTC tumours which signals via the PI3K pathway, and data demonstrating that 53.7 % of PTC tumour samples exhibited *PIK3CA* amplification, make the PI3K pathway an important regulatory pathway in papillary thyroid cancer (Abubaker et al., 2008). It would have been predicted that *MSN* expression

was upregulated in *RAS*-driven PTC if the gene were a downstream target of PI3K signalling, however this was not observed during TCGA tumour sample analyses (Figure 5.1B).

Alpelisib is a specific p110α inhibitor shown to downregulate phospho-Akt in many cell lines at doses above 10 µM. In this investigation, this range of doses showed complete inhibition of Akt phosphorylation downstream of PI3K, but elicited no change in moesin protein level (Figure 6.9). Similarly, alpelisib had no overt effect on radioiodide uptake in TCP1 or 8505C cells. These data indicate moesin is unlikely to be a downstream target of PI3K signalling.

6.4.4 The Regulation of Moesin By Retinoic Acid in Thyroid Cancer Cells

Retinoic acid remains the only published drug reported to result in a downregulation of moesin protein levels. Following an identical protocol as in (Flamini et al., 2014), treatment with 1 µM RA over 72 hours did not alter moesin protein levels (Figure 6.11). When compared to thyroid carcinomas, breast cancers have separate and overlapping regulatory mechanisms and varied drug responses are common between cancers of different cell origins. Although the restoration of radioiodide avidity was observed in a minority of patients in thyroid cancer trials that utilised retinoic acid, it is unlikely these changes were mediated by modulating moesin protein levels.

6.5 Concluding Remarks

In its present form, although the function of Moesin and Annexin A1 as NIS interactors has shown to be relevant to radioiodide uptake in thyroid cancer cell lines, these proteins do not currently represent promising therapeutic targets for improving uptake in DTC patients. This is primarily due to the lack of effect of direct or specific inhibitors that target either of these

proteins. As the regulation of these two new NIS-interacting proteins remains unchanged by the inhibition of canonical signalling pathways in papillary thyroid cancer, targeting these proteins in order to increase radioiodide uptake now relies on dissecting the processes that underpin the interactions of these proteins with NIS. It is possible that future research may yield direct moesin or annexin A1 inhibitors and in this case these proteins may provide a useful tool for manipulating the protein trafficking of NIS to temporarily optimise radioiodide uptake. In the absence of specific inhibitors, further investigations into the role of moesin and annexin A1 in thyroid cancer should focus on challenging the role of moesin in the endocytosis of NIS, and annexin A1 in the lysosomal degradation of NIS, and how these interactions may be disrupted to maximise cellular iodide uptake.

7 Concluding Thoughts and Future Directions

7.1 The Challenge of Radioiodide-Refractory Thyroid Cancer

The high survival rate of papillary thyroid cancer is attributed to successful first line therapy of surgical resection and post-surgical radioiodide ablation. However, up to 15 % of localised PTCs are refractory to radioiodide therapy, arising as a result of dysregulated expression or trafficking of the sodium/iodide symporter (Choi et al., 2014; Fletcher et al., 2020; Lazar et al., 1999). Patients who do not respond to radioiodide therapy require additional treatment with targeted tyrosine kinase inhibitors which have moderate to severe side effects and these patients remain at risk of progressive disease and recurrence. Incompletely treated PTC can acquire mutations in multiple oncogenic signalling pathways and progress to aggressive poorly differentiated or anaplastic thyroid carcinomas. Accordingly, treatment to resensitise cells to radioiodide therapy may offer a clinical benefit for PTC patients. The mainstay of iodide uptake is high expression of *SLC5A5* and efficient NIS trafficking to the plasma membrane. This investigation sought to add further detail to the NIS interactome which regulates the post-translational processing of NIS, and to explore how these interactions may be targeted to improve radioiodide uptake.

7.2 Investigating the Interaction Between NIS and VCP

7.2.1 Targeting the interaction between NIS and VCP with CB-5083 and CB-5339

The development of CB-5083 and CB-5339 provided an approach to specifically inhibit VCP activity and was validated by a wealth of *in vitro* and *in vivo* data (Anderson et al., 2015; Zhou et al., 2015). The positive effect of CB-5083 on radioiodide uptake in TPC1-NIS and L87-NIS cells added to the growing data that indicate VCP is a valuable therapeutic target for

optimising radioiodide uptake. CB-5339 was presented as the stronger VCP inhibitor than CB-5083 in NanoBIT protein interaction studies. However, this conflicted with the iodide uptake assays in TPC1-NIS cells which crucially did not reproduce the increase in I^{125} uptake that was observed after treatment with CB-5083. Despite CB-5083 producing a stronger iodide response across multiple cell lines, this compound is not approved by any regulatory bodies nor is it currently being investigated in randomised controlled trials, having been effectively superseded by CB-5339. CB-5339, which is currently under investigation in two clinical trials, may therefore be a more opportune compound to investigate *in vivo* in order to measure changes in iodide uptake after treatment. The conflicting data between CB-5083 and CB-5339 in TPC1-NIS cells should be resolved as a matter of high importance before pursuing *in vivo* studies on either of these compounds. This requires analysis of CB-5339 on further TPC1-NIS clonal populations aside from those utilised in Chapter 3, and alternative cell lines of papillary thyroid cancer origin.

If CB-5339 is to be selected as the more favourable of the two specific VCP inhibitors, additional characterisation of this drug in cell models is imperative to ensure it elicits a response of a comparable magnitude to that of CB-5083. CB-5339 showed limited efficacy in modulating radioiodide uptake in 8505C-NIS cells, despite a paradoxical increase in NIS protein level at higher doses. It should be investigated whether the 24 hour timeframe is adequate to induce measurable changes in iodide uptake in 8505C-NIS cells. In future studies, the timeframe for measuring the effect of CB-5339 should be extended to 48 hours to determine whether, in 8505C-NIS cells, elevated NIS protein may take longer to reach the plasma membrane where it can be functional. If an extended time frame does not elicit a change in iodide uptake, the mechanism by which an increase in NIS protein did not translate

to increased iodide uptake could be further investigated. This would begin with comparison to other clonal populations of 8505C-NIS cells to rule out this discrepancy being artefactual within this specific monoclonal population and human primary thyroid cells should also undergo treatment with CB-5339.

7.2.2 Targeting the Interaction Between NIS and VCP Using Clotrimazole-Derived Compounds

From the multiple screening rounds of clotrimazole analogues, compound-17 emerged as the leading compound and has been tested in a variety of cell lines. Compound-17 was modelled *in-silico* and predicted to have additional interaction with the residue Gln-494 in the allosteric binding pocket of VCP. The majority of cell lines that were treated with compound-17 demonstrated a subtle increase in iodide uptake compared to the clotrimazole parent compound. Crucially, compound-17 induced a significant increase in iodide uptake in human primary thyroid cells.

The data presented in Chapter 4 provided an indirect measurement of VCP inhibition by the clotrimazole analogues through radioiodide uptake. To strengthen the hypothesis that compound-17 shows an increased level of VCP inhibition than the parent compound, an *in vitro* VCP ATPase assay using recombinant VCP protein and individual VCP mutants with deficiencies in ATPase activity of the D1 and D2 domains, respectively, should be applied (Anderson et al., 2015; Segura-Cabrera et al., 2017). This can test whether these novel compounds do indeed directly inhibit facets of VCP activity, as was shown for clotrimazole and CB-5083, but also can be used to determine the IC_{50} which may be useful when comparing the efficacy of different VCP inhibitors.

Based on these positive data, compound-17 was developed into GB002 which is now the foremost clotrimazole-derived compound to undergo additional testing. It is possible that the additional moiety in GB002, designed by comparison to UPCDC30245, may provide additional interactions with the VCP binding pocket and raise the capacity for VCP inhibition compared to the clotrimazole-derived compounds. However, the investigations into GB002 should stringently determine whether this compound presents enough VCP inhibitory capacity to translate to an *in vivo* increase in radioiodide uptake. For GB002 to be a useful tool in optimising radioiodide uptake, the fold changes in radioiodide uptake elicited by the compound compared to a DMSO control must be considerably higher than the relatively small fold changes observed after treatment with compound-17. The *in vitro* testing of GB002 should encompass multiple NIS-expressing and NIS-stimulated cell lines as well as human thyrocytes. The effect of GB002 should also be tested in time course and dose response assays, for an effect on both radioiodide uptake and NIS protein levels, to determine whether the structural changes may modulate iodide uptake at alternative time points or doses to the treatment with 0.25 μM for 12 hours that was applied during the initial rounds of screening in Chapter 4.

7.2.3 Determining the Optimal VCP Inhibitor

Studies to combine the inhibition of VCP by siRNA and treatment with CB-5083 to completely deplete the intracellular pool of VCP resulted in extensive cell death and iodide uptake could not be measured. This suggests that targeting VCP by multiple approaches may be too toxic to produce a summative effect on iodide uptake. Equally, given the proximity of the binding

of CB-5339 and compound-17 compounds within the allosteric binding site of VCP, it may be that binding is mutually exclusive and that combined treatment with CB-5339 and the clotrimazole analogue may not elicit a summative effect. To progress with the strategy of targeting VCP in thyroid cancer, it is likely that a single candidate VCP inhibitor may have to be selected. Assays which seek to investigate the role of compound-17, and the role of GB002 if it is demonstrated to produce an increase in radioiodide uptake, should be directly compared to the specific inhibitor CB-5339 to determine the optimal VCP inhibitor. Considering the data presented in Figure 3.5 that demonstrates the VCP inhibitors CB-5083 and CB-5339 can disrupt the NIS-VCP interaction, this approach may also be applied to compound-17 and GB002 to challenge the modelling data. If these drugs disrupt the interaction between NIS and VCP, this will support the hypothesis that they functionally inhibit VCP. Furthermore, this assay may also allow direct comparison to the specific VCP inhibitor CB-5339 which currently produces the highest percentage decrease in the NIS and VCP interaction of 58.1 %.

7.2.4 Determining the Efficacy of VCP Inhibitors Against Thyroid Cancer in vivo

To advance with the hypothesis that targeting VCP in thyroid cancer can improve radioiodide uptake, is it imperative that these *in vitro* experiments are advanced to *in vivo* experiments in mice. The subsequent discussion for testing VCP inhibitors *in vivo* excludes the compound GB002, as the progression of this compound is contingent on GB002 having a positive effect on iodide uptake in *in vitro* experiments.

CB-5083 has been demonstrated to be orally bioavailable, and produces a measurable reduction in tumour growth after only five days treatment in mouse xenograft models (Anderson et al., 2015). CB-5339 is also orally bioavailable based on its use in phase I clinical trials. CB-5339 could be first tested in wild-type mouse models to determine whether it induces an increase in thyroidal iodide uptake after systemic treatment. This could be developed to include thyroid cancer mouse models which can test the efficacy of these compounds specifically in the cancer setting. For these experiments, an identical treatment schedule to that employed by Anderson *et al* to administer CB-5083 could be utilised, as this schedule was well-tolerated in mice and resulted in a measurable therapeutic effect (Anderson et al., 2015). Multiple tracers could be used to study thyroidal iodide uptake including Tc^{99}, I^{123}, I^{124} and I^{131} which can be measured by scintigraphy or PET-CT. The tracer uptake before and after treatment with CB-5339 would best be compared by normalising thyroidal uptake to that in the stomach to account for variations in the administration of the tracer, as was performed when surveying the effect of clotrimazole in wild-type mice (unpublished data, McCabe group, 2019).

Orthotopic models provide additional insight regarding delivery of the compound specifically to tumours in the thyroid gland. These data cannot be obtained from xenograft models in which tumours are typically sub-cutaneous. There are multiple orthotopic models of PTC which may be useful in assessing the capacity of VCP inhibitors to resensitise PTC to radioiodide therapy. As papillary thyroid cancer has a much lower mutational burden than anaplastic thyroid cancers, mouse models of PTC can usually be generated by a single gene mutation, commonly $BRAF^{V600E}$, which can achieve thyroid specific induction by coupling to the promoters of Tg or TPO, or by generating tamoxifen-inducible transgenes (Chakravarty et

al., 2011; Charles et al., 2011; Knauf et al., 2005). However, the development of papillary thyroid cancers results in dedifferentiation and loss of normal Tg expression and the Tg-driven transgene. Comparatively, individual mutations in *RAS* or *RET/PTC* rearrangements have not consistently led to the development of PTC in mouse models (Charles et al., 2011; Knostman et al., 2007). The tamoxifen- inducible $BRAF^{V600E}$ model demonstrated that NIS expression at the plasma membrane could be restored by treatment with small molecular MAPK inhibitors and I^{124} uptake was analysed in these models (Chakravarty et al., 2011). The Chakravarty *et al* mouse model has been characterised extensively, has established protocols for quantifying iodide uptake and is driven by the $BRAF^{V600E}$ oncogene which is observed in over half of patients with PTC, and is associated with a loss of iodide avidity. Therefore, this model may be the most appropriate PTC model in which to assess how VCP inhibitors can affect tumoral iodide uptake.

Treatment of non-thyroidal tumours with radioiodide therapy is currently being explored by scientists in the Spitzweg group (Ludwig-Maximilians University, Germany). This system involves three sequential injections of L87-NIS cells in a PBS suspension into the tail vein of mice; the L87 mesenchymal stem cells home in on the tumour site and accumulate in the tumour stroma (Schug et al., 2018; Schug et al., 2019). The reintroduction of NIS to the tumour environment permits the subsequent ablation of the tumour by treatment with 131-I. The positive data for improving iodide uptake in L87-NIS cells after treatment with CB-5339 in Chapter 3 provides the impetus for this compound to be tested in this system by administering alongside the L87-NIS injections, prior to injecting 131-I. This may validate whether systemic treatment with these VCP inhibitors can improve tumoural iodide uptake *in vivo*. The discussion on inhibiting VCP in thyroid cancer largely focusses on increasing iodide

uptake in patients with low avidity but in patients who uptake adequate levels of radioiodide for tumour ablation, treatment with these inhibitors may enable a reduction in the cumulative dose of 131-I. Therefore, treatment with CB-5339 in the Spitzweg models may be useful to investigate whether mice may require a lower dose of 131-I to achieve the same inhibition of tumour growth which is consistent with non-CB-5339 treated mice that received the standard dose of 55.5 MBq (Schug et al., 2019).

7.3 Investigating the Interaction Between NIS and Moesin

Data presented in Chapter 5 sought to test the preliminary mass spectrometry findings indicating that NIS and moesin interact. The silencing of moesin by siRNA demonstrated a significant increase in radioiodide uptake in thyroid cancer cell lines. Via NanoBiT technology, NIS and moesin were shown to physically interact *in vitro* and this could be reduced by mutating the residues K554 and R555 in NIS. *MSN* is significantly upregulated in papillary thyroid cancer samples, with an overt bias towards $BRAF^{V600E}$ tumours. However, the protein levels of moesin were not affected by inhibition of either the MAPK pathway or the PI3K-Akt-mTOR pathways, which often drive thyroid tumourigenesis by constitutive activation. While it seems plausible that MAPK signalling may drive the upregulation of moesin in thyroid cancer, modulating moesin protein levels to improve NIS-mediated iodide uptake may be achievable only by a specific moesin inhibitor. Moesin has reported roles in facilitating the cytoskeletal rearrangements necessary for endocytosis. Consistent with this, tumours which highly express the *MSN* gene also display elevated genes related to the endocytosis of membrane proteins.

7.3.1 Future Directions

Future studies on the interaction between NIS and moesin should seek to challenge the hypothesis that moesin facilitates the internalisation of NIS by clathrin-mediated endocytosis, and that targeting moesin protein may enhance the proportion of NIS at the plasma membrane and increase radioiodide uptake. Whether moesin regulates NIS internalisation could be further investigated through cell-surface biotinylation assays in conjunction with moesin knockdown. If this hypothesis is correct, moesin knockdown would significantly increase the proportion of NIS at the plasma membrane due to the disruption in internalisation, and would result in the increased iodide uptake that was observed in both TPC1-NIS and 8505C-NIS cell lines (Figure 5.3).

Clathrin-mediated endocytosis of proteins requires the co-operation between multiple protein complexes to select integral membrane proteins for vesicle cargo, induce membrane curvature and facilitate scission of the vesicle neck to separate the vesicle into the cytoplasm (McMahon and Boucrot, 2011). In the hypothesis that moesin facilitates the internalisation of NIS into vesicles, it is likely that many other proteins also aid this process. The protein PBF has been specifically linked to NIS internalisation in clathrin-coated vesicles (Smith et al., 2009). If the role of moesin in NIS internalisation is established, studies into the internalisation of NIS should also consider the role of PBF in the interaction between NIS and moesin. If moesin is demonstrated to facilitate NIS internalisation, whether it acts cooperatively with PBF to internalise NIS together, or by two discrete internalisation mechanisms, should also be studied. Potential crosstalk between PBF and moesin in NIS internalisation could be clarified by the simultaneous siRNA knockdown of both genes whereby a summative effect may indicate these proteins function by discrete mechanisms. Alternatively, if PBF and moesin

function cooperatively, this may involve a functional interaction between these proteins that can be measured by NanoBiT.

The NIS$^{K554A/R555A}$ mutant which had significantly reduced moesin binding provides another valuable tool for investigating the mechanism by which moesin modulates NIS and iodide uptake. If moesin regulates the internalisation of NIS, then NIS$^{K554A/R555A}$ may be retained in the plasma membrane which could be imaged using immunofluorescent staining and confocal imaging. In this instance, this mutant would likely display elevated iodide uptake compared to wild-type NIS, and while this was not measured in HeLa cells (Figure 5.14), this should be confirmed by transfection into additional non-NIS stable thyroid cell lines.

Furthermore, in the NIS dimerisation homology model, K554 and R555 were identified as the only amino acids in the C-terminal dimerisation interface that were within 0.3 nm from the opposite monomer, and hence were hypothesised as facilitating the dimeric interaction (Thompson et al., 2019). However, the effect of mutation of these two residues on NIS dimerisation was not explored. Given that these residues have previously been implicated in NIS dimerisation, the NIS$^{K554A/R555A}$ should be assessed for dimerisation capacity. Indeed, if these mutations result in NIS that is unable to dimerise, this may suggest that moesin preferentially binds dimeric NIS. Dimerisation of NIS has been linked to trafficking to the membrane, and it may be that moesin is in fact capable of binding to NIS$^{K554A/R555A}$ and instead the reduction in luminescence emitted is a result of mislocalisation of the NIS mutant which reduces the opportunity of interacting with moesin. To determine whether moesin preferentially binds monomeric or dimeric NIS, other mutants which are incapable of dimerisation such as Y242, T243, and Q471 could be generated and analysed for their

interaction with moesin by NanoBiT. As the functional implication of NIS dimerisation is not fully known, more information on the cellular locations where NIS exists as a dimer is useful in determining how important NIS dimerisation may be for optimal iodide uptake.

Investigating the role of moesin in thyroid cancer has been limited by the lack of a specific moesin inhibitor. Recently, a BRET-based biosensor has been developed to faithfully monitor the real-time activation of ERM proteins (Leguay et al., 2021). The researchers utilised luciferase tagged ERM proteins and plasma membrane localised GFP, and observed an elevated BRET ratio when ERM proteins are activated and recruited to the plasma membrane. This assay was validated by demonstrating that the BRET signal was measurably decreased by the protein kinase inhibitor Staurosporine which promotes the non-specific dephosphorylation and deactivation of ERM proteins. These data may offer the necessary innovation for developing a high-throughput assay to measure large libraries of compounds for their ability to deactivate ERM proteins; it is possible that the development of a specific moesin inhibitor is on the horizon. Determining the broader regulation of moesin in thyroid cancer through manipulating key signalling pathways, as was endeavoured in Chapter 6, could have provided insight into how moesin is dysregulated in thyroid cancer more generally. However, considering the aim to targeting specific NIS interacting proteins to temporarily optimise radioiodide uptake, a direct inhibitor would be valuable and prevent the broader scale genomic changes that accompany treatment with MAPK and PI3K inhibitors. Therefore, a breakthrough in the development of small molecular moesin inhibitors may allow for potential optimisation of radioiodide uptake and could also provide further knowledge on the regulation of moesin in cells by observing changes to a cells' transcriptome after moesin inhibition, which could not be concluded from the data presented in Chapter 6.

7.4 Investigating the Interaction Between NIS and Annexin A1

Chapter 5 demonstrated an interaction between NIS and annexin A1 *in vitro,* and showed that knockdown of *ANXA1* translated to a significant increase in NIS-mediated iodide uptake. Clinical evidence has proposed annexin A1 as a biomarker of thyroid cancer and strong upregulation of the protein is observed in papillary thyroid cancer, predominantly in $BRAF^{V600E}$ driven tumours. Annexin A1 protein levels were unaffected by MAPK inhibition and therefore the regulation of annexin A1 remains unclear. Annexin A1 has been reported to facilitate the formation of internal vesicles in multivesicular bodies (MVBs) and tether MVBs and endosomes to sites on the ER membrane (Diakonova et al., 1997; Eden et al., 2016; White et al., 2006). This was supported by data in Chapter 6 highlighting the concomitant upregulation in genes that are related to lysosomal function in tumours which express high levels of the *ANXA1* gene. Inhibiting the lysosomal degradation of NIS as a strategy of increasing radioiodide uptake has not been explored in thyroid cancer thus far. Therefore, understanding the role of annexin A1 in thyroid cancer may yet still provide an additional druggable target for improving NIS-mediated iodide uptake.

7.4.1 Future Directions

Aside from the canonical function of externalised Annexin A1 in mediating an anti-inflammatory signalling cascade, cytoplasmic annexin A1 has been shown to localise to membranes of the lysosome and multivesicular bodies which facilitate protein degradation. However, initial mass spectrometry data suggested that NIS and annexin A1 interact at the plasma membrane as the interaction was only detected in the membrane fraction of the cell lysate (Fletcher, 2018). Annexin A1 is described to interact at the plasma membrane with its

cognate receptor FPR2. Investigating the hypothesis that the interaction between annexin A1 and NIS may include FPR2 could be assessed through the use of FPR2 agonists which may disrupt the interaction (Stenfeldt et al., 2007). This may provide a method of reducing the NIS-annexin A1 interaction without specifically inhibiting annexin A1 activity. Additionally, if treatment with FPR2 agonists has no effect on NIS-mediated iodide uptake, this may exclude the role of annexin A1 as an anti-inflammatory in the thyroid cancer setting and instead favour the hypothesis that annexin A1 interacts with NIS intracellularly.

Annexin A1 forms a heterodimer with S100A11 at membrane contact sites between ER and lysosomal or endosomal membranes (Poeter et al., 2013). If the interaction between NIS and annexin A1 occurs at these membranes as part of NIS recycling or turnover, then knockdown of S100A11 may result in similar increases in iodide uptake as annexin A1 knockdown. Equally, if S100A11 is required for the interaction between NIS and Annexin A1, then knockdown of this protein may also result in a measurable disruption of this interaction by NanoBiT. This hypothesis could be further validated by measuring the effect of lysosomal inhibitors on the NIS and annexin A1 interaction by NanoBiT, as was performed with the VCP inhibitors CB-5083 and CB-5339 in Chapter 3.

The primary caveat to the hypothesis that annexin A1 and NIS interact during recycling of NIS from the plasma membrane is that knockdown of annexin A1 would have been expected to result in a concomitant increase in NIS protein. Although there was an upwards trend in NIS protein in Figure 5.3, this was statistically insignificant. Further protein analysis by Western blot over multiple thyroid cancer cell lines could be performed to confirm the effect of siRNA knockdown on NIS protein level.

If annexin A1 facilitates lysosomal degradation of NIS, this provides a second approach by which NIS degradation may be targeted, alongside VCP-mediated ER-associated degradation. Interestingly, annexin A2 was also identified as a potential NIS interactor by co-IP and mass spectrometry (Fletcher, 2018). Annexin A2 has been implicated in both clathrin-mediated endocytosis and the formation of multi-vesicular bodies (Futter and White, 2007). If an interaction between NIS and annexin A2 is also verified, the annexin family may contribute to a broader model of processing NIS that has been internalised from the plasma membrane.

7.5 Concluding Remarks

This investigation has expanded the model of the NIS interactome and addressed the importance of post-translational processing of NIS in regulating cellular iodide uptake (Figure 7.1). Currently, the NIS interacting protein VCP can be targeted through the use of inhibitors to optimise radioiodide uptake in some cell lines. Progression to *in vivo* studies with these inhibitors is an exciting strategy to improve tumoral iodide uptake and if successful, would supersede the discrepancies in the *in vitro* data between thyroid cancer cell lines. The two additional interactors identified in this thesis are grossly dysregulated in thyroid cancer and may contribute to a radioiodide refractory phenotype. Figure 7.1 demonstrates how moesin and annexin A1 may fit into the working model of the intracellular processing of NIS. Future experiments which seek to target moesin and annexin A1 may be combined with the inhibition of VCP to summatively increase iodide uptake, without compromising cell viability. This investigation has taken a small step further towards developing the strategy of

administering a cocktail of compounds to temporarily maximise NIS-mediated iodide uptake in differentiated thyroid tumours prior to treatment with 131-I.

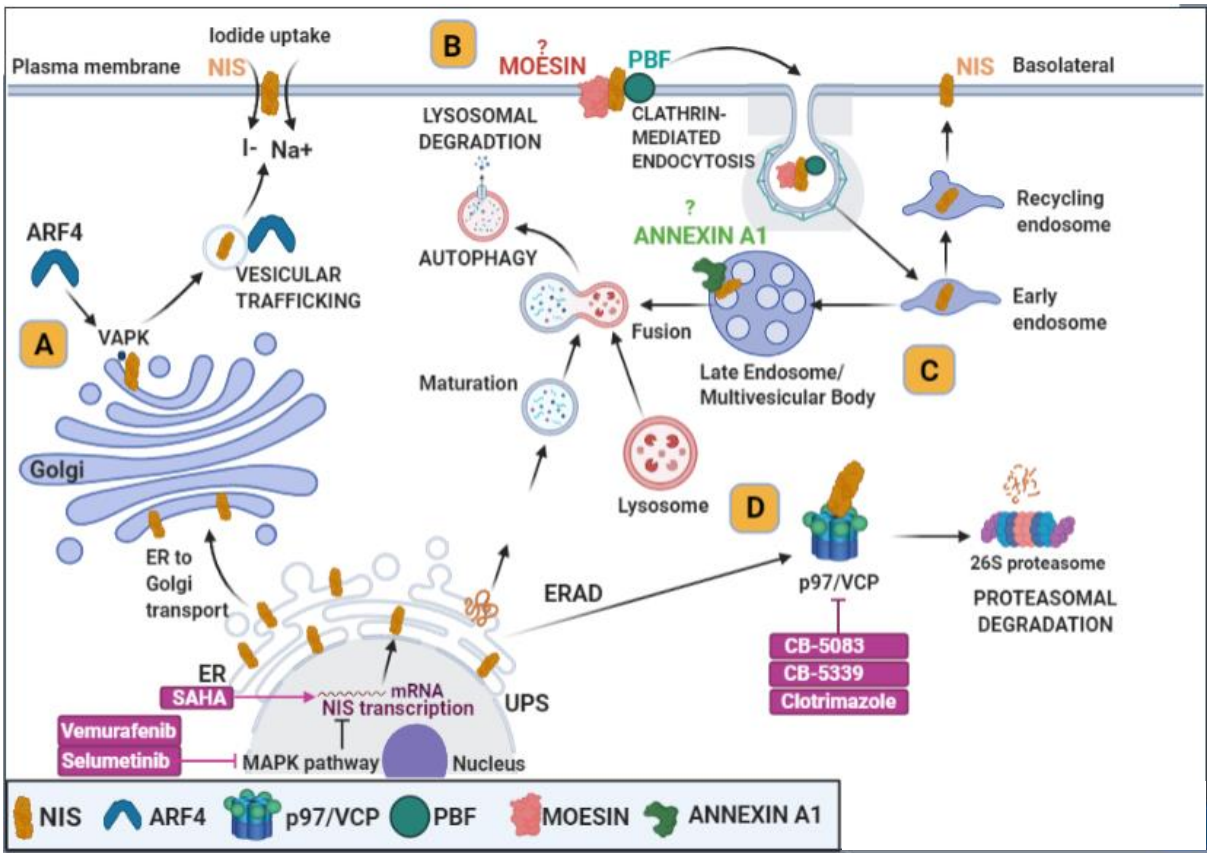


Figure 7.1 ***The working model of post-translational processing of NIS.*** *(**A**) NIS binds to ARF4 via a VAPK motif in the C-terminal tail of NIS; ARF4 facilitates forwards trafficking of NIS to the plasma membrane. (**B**) Moesin putatively binds to NIS at the plasma membrane to facilitate internalisation of NIS into clathrin coated vesicles. During this process PBF interacts with NIS to facilitate its internalisation. (**C**) Annexin A1 putatively binds to NIS in multivesicular bodies to promote its lysosomal degradation. (**D**) VCP extracts NIS from the ER and diverts it towards proteasomal degradation, this can be disrupted by the VCP inhibitors CB-5083, CB-5339 and clotrimazole. Figure adapted with input from Kate Brookes and Dr Martin Read.*

8 Appendix

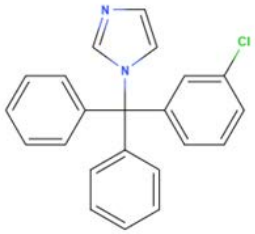
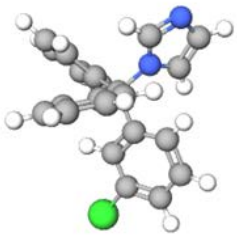
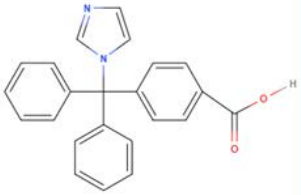
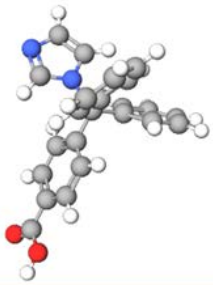
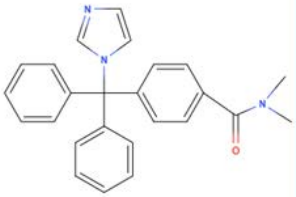
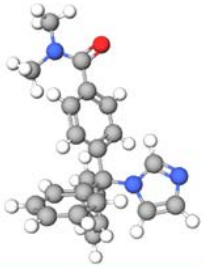
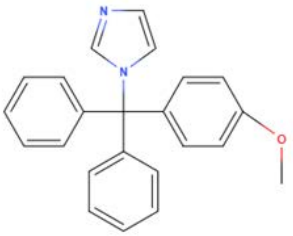
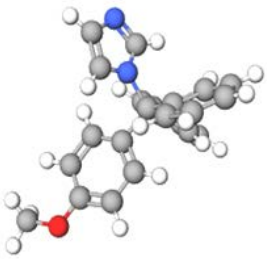
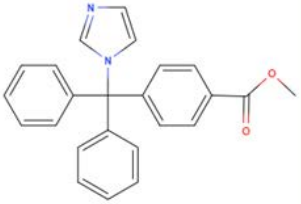
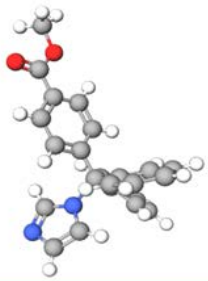
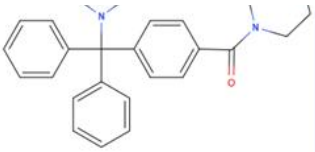
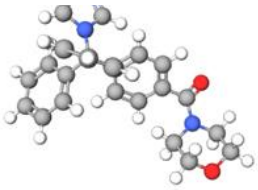
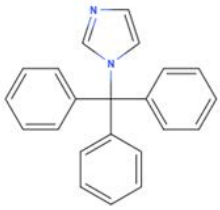
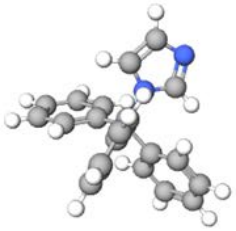
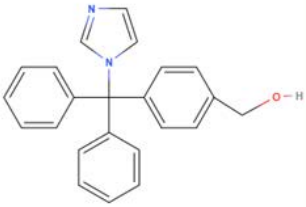
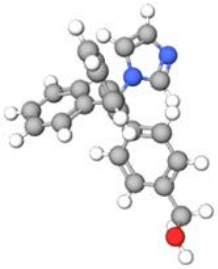
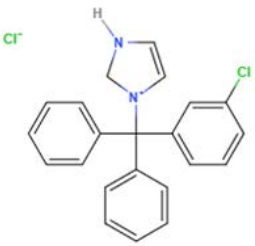
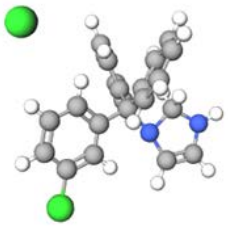
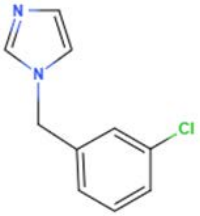
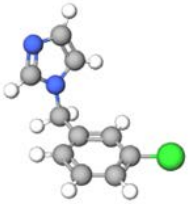
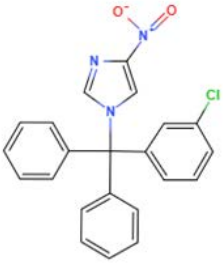
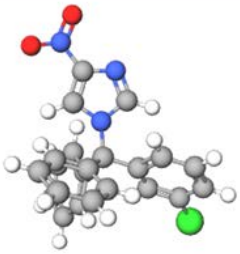
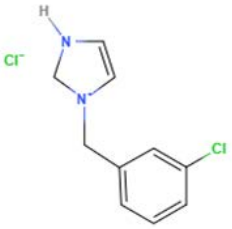
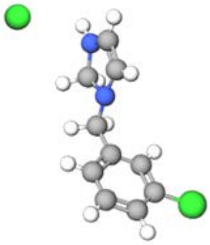
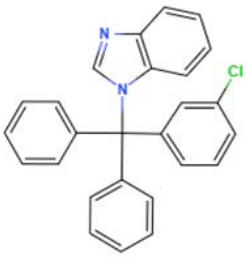
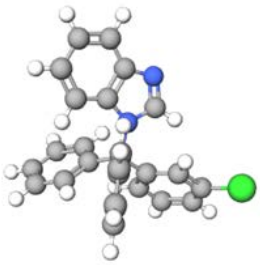
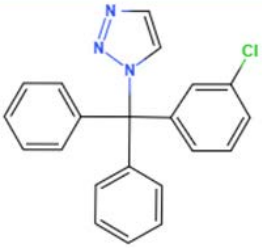
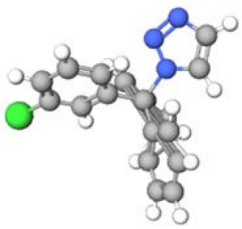
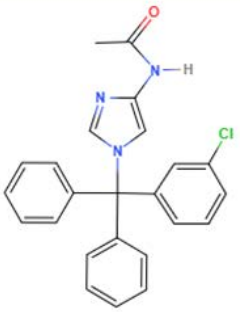
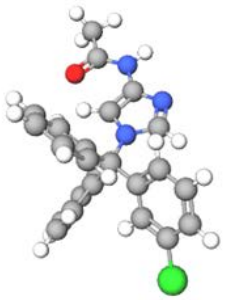
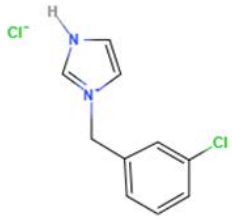
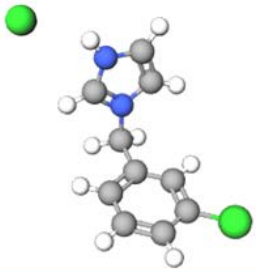
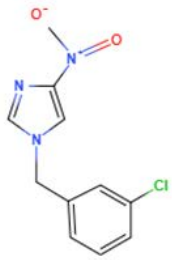
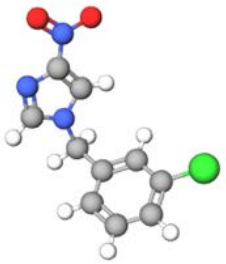
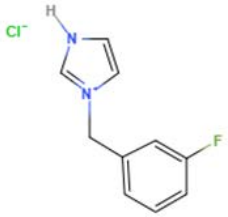
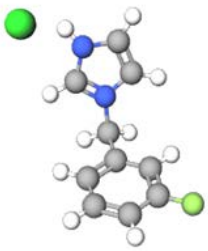
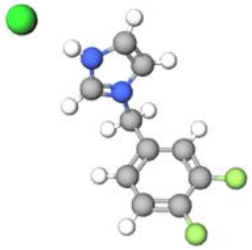
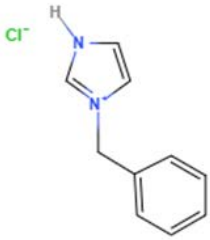
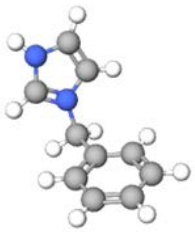
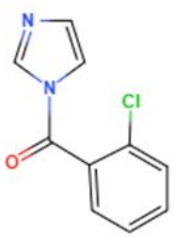
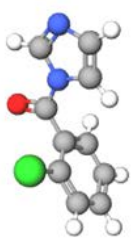
Compound Number	2D Structure	3D Structure	Formula	MW	logP	Rotational bonds
Clotrimazole (original)			$C_{22}H_{17}ClN_2$	344.842	5.3668	4
Compound-1			$C_{23}H_{18}N_2O_2$	354.409	4.07	5
Compound-2			$C_{25}H_{23}N_3O$	381.479	4.4661	5
Compound-3			$C_{23}H_{20}N_2O$	340.426	4.6908	5
Compound-4			$C_{24}H_{20}N_2O_2$	368.436	4.6738	6

Table 8-1 ***Full summary of clotrimazole-derived compounds: compound name, 2-D structure, 3-D structure, chemical formula, molecular weight, logP value as indicator of lipophilicity and number of rotational bonds which may form interactions in allosteric VCP binding pocket.*** *Compounds 5-21 continued overleaf.*

Compound Number	2D Structure	3D Structure	Formula	MW	logP	Rotational bonds
Compound-5			$C_{27}H_{25}N_3O_2$	423.516	4.4351	5
Compound-7			$C_{22}H_{18}N_2$	310.4	4.7608	4
Compound-8			$C_{23}H_{20}N_2O$	340.426	4.1635	5
Compound-9			$C_{22}H_{18}Cl_2N_2$	381.3	1.31	5
Compound-10			$C_{10}H_9ClN_2$	192.646	1.9161	2

Compound Number	2D Structure	3D Structure	Formula	MW	logP	Rotational bonds
Compound-11			$C_{22}H_{16}ClN_3O_2$	389.839	4.6262	5
Compound-12			$C_{10}H_{10}Cl_2N_2$	229.104	-2.1403	2
Compound-13			$C_{26}H_{19}ClN_2$	394.902	6.8062	4
Compound-14			$C_{21}H_{16}ClN_3$	345.83	4.7817	4
Compound-15			$C_{24}H_{20}ClN_3O$	401.894	5.4219	5

Compound Number	2D Structure	3D Structure	Formula	MW	logP	Rotational bonds
Compound-16			$C_{10}H_{10}Cl_2N_3O_2$	229.104	-2.1403	2
Compound-17			$C_{10}H_8ClN_3O_2$	237.643	1.1755	3
Compound-18			$C_{10}H_{10}ClFN_2$	212.652	-2.6455	2
Compound-19			$C_{10}H_9ClF_2N_2$	230.643	-2.5477	2
Compound-20			$C_{10}H_{11}ClN_2$	194.662	-2.7463	2
Compound-21			$C_{10}H_7ClN_2O$	206.629	2.3125	2

9 References

A, T., S. F, P. G, and B. M, 2011, Genetic alterations in medullary thyroid cancer: diagnostic and prognostic markers: Curr Genomics, v. 12, p. 618-25.

Abdullah, M. I., S. M. Junit, K. L. Ng, J. J. Jayapalan, B. Karikalan, and O. H. Hashim, 2019, Papillary Thyroid Cancer: Genetic Alterations and Molecular Biomarker Investigations: Int J Med Sci, v. 16, p. 450-460.

Abubaker, J., Z. Jehan, P. Bavi, M. Sultana, S. Al-Harbi, M. Ibrahim, A. Al-Nuaim, M. Ahmed, T. Amin, M. Al-Fehaily, O. Al-Sanea, F. Al-Dayel, S. Uddin, and K. S. Al-Kuraya, 2008, Clinicopathological analysis of papillary thyroid cancer with PIK3CA alterations in a Middle Eastern population: J Clin Endocrinol Metab, v. 93, p. 611-8.

Alam, F., F. Mezhal, H. El Hasasna, V. A. Nair, S. R. Aravind, M. Saber Ayad, A. El-Serafi, and W. M. Abdel-Rahman, 2017, The role of p53-microRNA 200-Moesin axis in invasion and drug resistance of breast cancer cells: Tumour Biol, v. 39, p. 1010428317714634.

Alverez, C., M. R. Arkin, S. L. Bulfer, R. Colombo, M. Kovaliov, M. G. LaPorte, C. Lim, M. Liang, W. J. Moore, R. J. Neitz, Y. Yan, Z. Yue, D. M. Huryn, and P. Wipf, 2015, Structure-Activity Study of Bioisosteric Trifluoromethyl and Pentafluorosulfanyl Indole Inhibitors of the AAA ATPase p97: ACS Med Chem Lett, v. 6, p. 1225-30.

Amino, N., T. Yamada, T. Mitsuma, T. Nogimori, O. Tanizawa, M. Kawashima, K. Kurachi, and K. Miyai, 1981, Increase in plasma thyrotropin-releasing hormone in normal human pregnancy: J Clin Endocrinol Metab, v. 53, p. 1288-90.

Anderson, D. J., R. Le Moigne, S. Djakovic, B. Kumar, J. Rice, S. Wong, J. Wang, B. Yao, E. Valle, S. Kiss von Soly, A. Madriaga, F. Soriano, M. K. Menon, Z. Y. Wu, M. Kampmann, Y. Chen, J. S. Weissman, B. T. Aftab, F. M. Yakes, L. Shawver, H. J. Zhou, D. Wustrow, and M. Rolfe, 2015, Targeting the AAA ATPase p97 as an Approach to Treat Cancer through Disruption of Protein Homeostasis: Cancer Cell, v. 28, p. 653-665.

André, F., E. M. Ciruelos, D. Juric, S. Loibl, M. Campone, I. A. Mayer, G. Rubovszky, T. Yamashita, B. Kaufman, Y. S. Lu, K. Inoue, Z. Pápai, M. Takahashi, F. Ghaznawi, D. Mills, M. Kaper, M. Miller, P. F. Conte, H. Iwata, and H. S. Rugo, 2021, Alpelisib plus fulvestrant for PIK3CA-mutated, hormone receptor-positive, human epidermal growth factor receptor-2-negative advanced breast cancer: final overall survival results from SOLAR-1: Ann Oncol, v. 32, p. 208-217.

Ang, E. Z., H. T. Nguyen, H. L. Sim, T. C. Putti, and L. H. Lim, 2009, Annexin-1 regulates growth arrest induced by high levels of estrogen in MCF-7 breast cancer cells: Mol Cancer Res, v. 7, p. 266-74.

Artandi, S. E., S. Alson, M. K. Tietze, N. E. Sharpless, S. Ye, R. A. Greenberg, D. H. Castrillon, J. W. Horner, S. R. Weiler, R. D. Carrasco, and R. A. DePinho, 2002, Constitutive telomerase expression promotes mammary carcinomas in aging mice: Proc Natl Acad Sci U S A, v. 99, p. 8191-6.

Bahn, R. S., 2010, Graves' ophthalmopathy: N Engl J Med, v. 362, p. 726-38.

Bai, X. F., X. G. Ni, P. Zhao, S. M. Liu, H. X. Wang, B. Guo, L. P. Zhou, F. Liu, J. S. Zhang, K. Wang, Y. Q. Xie, Y. F. Shao, and X. H. Zhao, 2004, Overexpression of annexin 1 in

pancreatic cancer and its clinical significance: World J Gastroenterol, v. 10, p. 1466-70.

Banerjee, S., A. Bartesaghi, A. Merk, P. Rao, S. L. Bulfer, Y. Yan, N. Green, B. Mroczkowski, R. J. Neitz, P. Wipf, V. Falconieri, R. J. Deshaies, J. L. Milne, D. Huryn, M. Arkin, and S. Subramaniam, 2016, 2.3 A resolution cryo-EM structure of human p97 and mechanism of allosteric inhibition: Science, v. 351, p. 871-5.

Bardia, A., M. Gounder, J. Rodon, F. Janku, M. P. Lolkema, J. J. Stephenson, P. L. Bedard, M. Schuler, C. Sessa, P. LoRusso, M. Thomas, H. Maacke, H. Evans, Y. Sun, and D. S. W. Tan, 2020, Phase Ib Study of Combination Therapy with MEK Inhibitor Binimetinib and Phosphatidylinositol 3-Kinase Inhibitor Buparlisib in Patients with Advanced Solid Tumors with RAS/RAF Alterations: Oncologist, v. 25, p. e160-e169.

Barroso-González, J., J. D. Machado, L. García-Expósito, and A. Valenzuela-Fernández, 2009, Moesin regulates the trafficking of nascent clathrin-coated vesicles: J Biol Chem, v. 284, p. 2419-34.

Bastola, P., F. Wang, M. A. Schaich, T. Gan, B. D. Freudenthal, T. F. Chou, and J. Chien, 2017, Specific mutations in the D1-D2 linker region of VCP/p97 enhance ATPase activity and confer resistance to VCP inhibitors: Cell Death Discov, v. 3, p. 17065.

Bebeacua, C., A. Förster, C. McKeown, H. H. Meyer, X. Zhang, and P. S. Freemont, 2012, Distinct conformations of the protein complex p97-Ufd1-Npl4 revealed by electron cryomicroscopy: Proc Natl Acad Sci U S A, v. 109, p. 1098-103.

Bell, R. J., H. T. Rube, A. Kreig, A. Mancini, S. D. Fouse, R. P. Nagarajan, S. Choi, C. Hong, D. He, M. Pekmezci, J. K. Wiencke, M. R. Wrensch, S. M. Chang, K. M. Walsh, S. Myong, J. S. Song, and J. F. Costello, 2015, Cancer. The transcription factor GABP selectively binds and activates the mutant TERT promoter in cancer: Science, v. 348, p. 1036-9.

Berontiene, R., E. Jasinskiene, R. Kiudeliene, G. Kuprionis, J. Makstiene, R. Macaityte, D. Marciulionyte, L. Poskiene, A. Semetaite, V. Sidlauskas, R. Valickas, R. Zalinkevicius, and R. Verkauskiene, 2017, Thirty-Five Years of Thyroid Cancer Experience in a Paediatric Population: Incidence Trends in Lithuania between 1980 and 2014: Eur Thyroid J, v. 6, p. 40-46.

Bianco, A. C., D. Salvatore, B. Gereben, M. J. Berry, and P. R. Larsen, 2002, Biochemistry, cellular and molecular biology, and physiological roles of the iodothyronine selenodeiodinases: Endocr Rev, v. 23, p. 38-89.

Bist, P., S. C. Leow, Q. H. Phua, S. Shu, Q. Zhuang, W. T. Loh, T. H. Nguyen, J. B. Zhou, S. C. Hooi, and L. H. Lim, 2011, Annexin-1 interacts with NEMO and RIP1 to constitutively activate IKK complex and NF-κB: implication in breast cancer metastasis: Oncogene, v. 30, p. 3174-85.

Blythe, E. E., K. C. Olson, V. Chau, and R. J. Deshaies, 2017, Ubiquitin- and ATP-dependent unfoldase activity of P97/VCP*NPLOC4*UFD1L is enhanced by a mutation that causes multisystem proteinopathy: Proc Natl Acad Sci U S A, v. 114, p. E4380-E4388.

Bodnar, N., and T. Rapoport, 2017a, Toward an understanding of the Cdc48/p97 ATPase: F1000Res, v. 6, p. 1318.

Bodnar, N. O., and T. A. Rapoport, 2017b, Molecular Mechanism of Substrate Processing by the Cdc48 ATPase Complex: Cell, v. 169, p. 722-735 e9.

Boelaert, K., V. E. Smith, A. L. Stratford, T. Kogai, L. A. Tannahill, J. C. Watkinson, M. C. Eggo, J. A. Franklyn, and C. J. McCabe, 2007, PTTG and PBF repress the human sodium iodide symporter: Oncogene, v. 26, p. 4344-56.

Boye, T. L., K. Maeda, W. Pezeshkian, S. L. Sønder, S. C. Haeger, V. Gerke, A. C. Simonsen, and J. Nylandsted, 2017, Annexin A4 and A6 induce membrane curvature and constriction during cell membrane repair: Nat Commun, v. 8, p. 1623.

Brand, M. D., D. Steverding, B. Kadenbach, P. M. Stevenson, and R. P. Hafner, 1992, The mechanism of the increase in mitochondrial proton permeability induced by thyroid hormones: Eur J Biochem, v. 206, p. 775-81.

Brose, M. S., M. E. Cabanillas, E. E. Cohen, L. J. Wirth, T. Riehl, H. Yue, S. I. Sherman, and E. J. Sherman, 2016, Vemurafenib in patients with BRAF(V600E)-positive metastatic or unresectable papillary thyroid cancer refractory to radioactive iodine: a non-randomised, multicentre, open-label, phase 2 trial: Lancet Oncol, v. 17, p. 1272-82.

Brose, M. S., C. M. Nutting, B. Jarzab, R. Elisei, S. Siena, L. Bastholt, C. de la Fouchardiere, F. Pacini, R. Paschke, Y. K. Shong, S. I. Sherman, J. W. Smit, J. Chung, C. Kappeler, C. Pena, I. Molnar, M. J. Schlumberger, and D. investigators, 2014, Sorafenib in radioactive iodine-refractory, locally advanced or metastatic differentiated thyroid cancer: a randomised, double-blind, phase 3 trial: Lancet, v. 384, p. 319-28.

Brown, L. M., S. M. Helmke, S. W. Hunsucker, R. T. Netea-Maier, S. A. Chiang, D. E. Heinz, K. R. Shroyer, M. W. Duncan, and B. R. Haugen, 2006, Quantitative and qualitative differences in protein expression between papillary thyroid carcinoma and normal thyroid tissue: Mol Carcinog, v. 45, p. 613-26.

Brunet, A., D. Roux, P. Lenormand, S. Dowd, S. Keyse, and J. Pouyssegur, 1999, Nuclear translocation of p42/p44 mitogen-activated protein kinase is required for growth factor-induced gene expression and cell cycle entry: EMBO J, v. 18, p. 664-74.

Cao, H. J., H. Y. Lin, M. K. Luidens, F. B. Davis, and P. J. Davis, 2009, Cytoplasm-to-nucleus shuttling of thyroid hormone receptor-beta1 (Trbeta1) is directed from a plasma membrane integrin receptor by thyroid hormone: Endocr Res, v. 34, p. 31-42.

Carrasco, N., 1993, Iodide transport in the thyroid gland: Biochim Biophys Acta, v. 1154, p. 65-82.

Carvalho, D. P., and C. Dupuy, 2017, Thyroid hormone biosynthesis and release: Mol Cell Endocrinol, v. 458, p. 6-15.

Carvalho, P., A. M. Stanley, and T. A. Rapoport, 2010, Retrotranslocation of a misfolded luminal ER protein by the ubiquitin-ligase Hrd1p: Cell, v. 143, p. 579-91.

Cerami, E., J. Gao, U. Dogrusoz, B. E. Gross, S. O. Sumer, B. A. Aksoy, A. Jacobsen, C. J. Byrne, M. L. Heuer, E. Larsson, Y. Antipin, B. Reva, A. P. Goldberg, C. Sander, and N. Schultz, 2012, The cBio cancer genomics portal: an open platform for exploring multidimensional cancer genomics data: Cancer Discov, v. 2, p. 401-4.

Chakravarty, D., E. Santos, M. Ryder, J. A. Knauf, X. H. Liao, B. L. West, G. Bollag, R. Kolesnick, T. H. Thin, N. Rosen, P. Zanzonico, S. M. Larson, S. Refetoff, R. Ghossein, and J. A. Fagin, 2011, Small-molecule MAPK inhibitors restore radioiodine incorporation in mouse thyroid cancers with conditional BRAF activation: J Clin Invest, v. 121, p. 4700-11.

Chandra, V., P. Huang, Y. Hamuro, S. Raghuram, Y. Wang, T. P. Burris, and F. Rastinejad, 2008, Structure of the intact PPAR-gamma-RXR- nuclear receptor complex on DNA: Nature, v. 456, p. 350-6.

Chapman, E. M., and R. D. Evans, 1946, The treatment of hyperthyroidism with radioactive iodine: J Am Med Assoc, v. 131, p. 86-91.

Charles, R. P., G. Iezza, E. Amendola, D. Dankort, and M. McMahon, 2011, Mutationally activated BRAF(V600E) elicits papillary thyroid cancer in the adult mouse: Cancer Res, v. 71, p. 3863-71.

Charles, R. P., J. Silva, G. Iezza, W. A. Phillips, and M. McMahon, 2014, Activating BRAF and PIK3CA mutations cooperate to promote anaplastic thyroid carcinogenesis: Mol Cancer Res, v. 12, p. 979-86.

Chekhun, V. F., A. V. Andriiv, and N. Y. Lukianova, 2017, Significance of iodine symporter for prognosis of the disease course and efficacy of neoadjuvant chemotherapy in patients with breast cancer of luminal and basal subtypes: Exp Oncol, v. 39, p. 65-68.

Chen, Y., Y. Zhang, and X. Guo, 2017, Proteasome dysregulation in human cancer: implications for clinical therapies: Cancer Metastasis Rev, v. 36, p. 703-716.

Chia, W. S., D. X. Chia, F. Rao, S. Bar Nun, and S. Geifman Shochat, 2012, ATP binding to p97/VCP D1 domain regulates selective recruitment of adaptors to its proximal N-domain: PLoS One, v. 7, p. e50490.

Chng, C. L., A. Y. Lim, H. C. Tan, J. P. Kovalik, K. W. Tham, Y. M. Bee, W. Lim, S. Acharyya, O. F. Lai, M. F. Chong, and P. M. Yen, 2016, Physiological and Metabolic Changes During the Transition from Hyperthyroidism to Euthyroidism in Graves' Disease: Thyroid, v. 26, p. 1422-1430.

Choi, Y. W., H. J. Kim, Y. H. Kim, S. H. Park, Y. J. Chwae, J. Lee, E. Y. Soh, J. H. Kim, and T. J. Park, 2014, B-RafV600E inhibits sodium iodide symporter expression via regulation of DNA methyltransferase 1: Exp Mol Med, v. 46, p. e120.

Chou, T. F., S. J. Brown, D. Minond, B. E. Nordin, K. Li, A. C. Jones, P. Chase, P. R. Porubsky, B. M. Stoltz, F. J. Schoenen, M. P. Patricelli, P. Hodder, H. Rosen, and R. J. Deshaies, 2011, Reversible inhibitor of p97, DBeQ, impairs both ubiquitin-dependent and autophagic protein clearance pathways: Proc Natl Acad Sci U S A, v. 108, p. 4834-9.

Christmas, P., J. Callaway, J. Fallon, J. Jones, and H. T. Haigler, 1991, Selective secretion of annexin 1, a protein without a signal sequence, by the human prostate gland: J Biol Chem, v. 266, p. 2499-507.

Ciregia, F., L. Giusti, A. Molinaro, F. Niccolai, P. Agretti, T. Rago, G. Di Coscio, P. Vitti, F. Basolo, P. Iacconi, M. Tonacchera, and A. Lucacchini, 2013, Presence in the pre-surgical fine-needle aspiration of potential thyroid biomarkers previously identified in the post-surgical one: PLoS One, v. 8, p. e72911.

Ciregia, F., L. Giusti, A. Molinaro, F. Niccolai, M. R. Mazzoni, T. Rago, M. Tonacchera, P. Vitti, G. Giannaccini, and A. Lucacchini, 2016, Proteomic analysis of fine-needle aspiration in differential diagnosis of thyroid nodules: Transl Res, v. 176, p. 81-94.

Cocco, E., M. Scaltriti, and A. Drilon, 2018, NTRK fusion-positive cancers and TRK inhibitor therapy: Nat Rev Clin Oncol, v. 15, p. 731-747.

Coelho, S. M., F. Vaisman, A. Buescu, R. C. Mello, D. P. Carvalho, and M. Vaisman, 2011, Follow-up of patients treated with retinoic acid for the control of radioiodine non-responsive advanced thyroid carcinoma: Braz J Med Biol Res, v. 44, p. 73-7.

Collu, R., J. Tang, J. Castagne, G. Lagace, N. Masson, C. Huot, C. Deal, E. Delvin, E. Faccenda, K. A. Eidne, and G. Van Vliet, 1997, A novel mechanism for isolated central hypothyroidism: inactivating mutations in the thyrotropin-releasing hormone receptor gene: J Clin Endocrinol Metab, v. 82, p. 1561-5.

Cristofanilli, M., Y. Yamamura, S. W. Kau, T. Bevers, S. Strom, M. Patangan, L. Hsu, S. Krishnamurthy, R. L. Theriault, and G. N. Hortobagyi, 2005, Thyroid hormone and

breast carcinoma. Primary hypothyroidism is associated with a reduced incidence of primary breast carcinoma: Cancer, v. 103, p. 1122-8.

Crowley, P. D., and H. C. Gallagher, 2014, Clotrimazole as a pharmaceutical: past, present and future: J Appl Microbiol, v. 117, p. 611-7.

Cyster, J. G., and S. R. Schwab, 2012, Sphingosine-1-phosphate and lymphocyte egress from lymphoid organs: Annu Rev Immunol, v. 30, p. 69-94.

D'Acunto, C. W., H. Gbelcova, M. Festa, and T. Ruml, 2014, The complex understanding of Annexin A1 phosphorylation: Cell Signal, v. 26, p. 173-8.

Dai, G., O. Levy, and N. Carrasco, 1996, Cloning and characterization of the thyroid iodide transporter: Nature, v. 379, p. 458-60.

Damle, N., M. Patnecha, P. Kumar, S. Maharjan, and C. Bal, 2011, Retinoic acid therapy in patients with radioiodine negative differentiated thyroid cancer and clinical or biochemical evidence of disease: An initial experience: Indian J Nucl Med, v. 26, p. 144-8.

de Coupade, C., R. Gillet, M. Bennoun, P. Briand, F. Russo-Marie, and E. Solito, 2000, Annexin 1 expression and phosphorylation are upregulated during liver regeneration and transformation in antithrombin III SV40 T large antigen transgenic mice: Hepatology, v. 31, p. 371-80.

de Groot, J. W., T. P. Links, J. T. Plukker, C. J. Lips, and R. M. Hofstra, 2006, RET as a diagnostic and therapeutic target in sporadic and hereditary endocrine tumors: Endocr Rev, v. 27, p. 535-60.

Di Palma, T., A. Conti, T. de Cristofaro, S. Scala, L. Nitsch, and M. Zannini, 2011, Identification of novel Pax8 targets in FRTL-5 thyroid cells by gene silencing and expression microarray analysis: PLoS One, v. 6, p. e25162.

Di Palma, T., R. Nitsch, A. Mascia, L. Nitsch, R. Di Lauro, and M. Zannini, 2003, The paired domain-containing factor Pax8 and the homeodomain-containing factor TTF-1 directly interact and synergistically activate transcription: J Biol Chem, v. 278, p. 3395-402.

Diakonova, M., V. Gerke, J. Ernst, J. P. Liautard, G. van der Vusse, and G. Griffiths, 1997, Localization of five annexins in J774 macrophages and on isolated phagosomes: J Cell Sci, v. 110 (Pt 10), p. 1199-213.

Dohan, O., C. Portulano, C. Basquin, A. Reyna-Neyra, L. M. Amzel, and N. Carrasco, 2007, The Na+/I symporter (NIS) mediates electroneutral active transport of the environmental pollutant perchlorate: Proc Natl Acad Sci U S A, v. 104, p. 20250-5.

Drozdovitch, V., O. Zhukova, M. Germenchuk, A. Khrutchinsky, T. Kukhta, N. Luckyanov, V. Minenko, M. Podgaiskaya, M. Savkin, S. Vakulovsky, P. Voilleque, and A. Bouville, 2013, Database of meteorological and radiation measurements made in Belarus during the first three months following the Chernobyl accident: J Environ Radioact, v. 116, p. 84-92.

Drücker, P., M. Pejic, H. J. Galla, and V. Gerke, 2013, Lipid segregation and membrane budding induced by the peripheral membrane binding protein annexin A2: J Biol Chem, v. 288, p. 24764-76.

Duan, H., X. Liu, X. Ren, H. Zhang, H. Wu, and Z. Liang, 2019, Mutation profiles of follicular thyroid tumors by targeted sequencing: Diagn Pathol, v. 14, p. 39.

Duncan, R., B. Carpenter, L. C. Main, C. Telfer, and G. I. Murray, 2008, Characterisation and protein expression profiling of annexins in colorectal cancer: Br J Cancer, v. 98, p. 426-33.

Durante, C., E. Puxeddu, E. Ferretti, R. Morisi, S. Moretti, R. Bruno, F. Barbi, N. Avenia, A. Scipioni, A. Verrienti, E. Tosi, A. Cavaliere, A. Gulino, S. Filetti, and D. Russo, 2007, BRAF mutations in papillary thyroid carcinomas inhibit genes involved in iodine metabolism: J Clin Endocrinol Metab, v. 92, p. 2840-3.

Díez, J. J., P. Sánchez, and P. Iglesias, 2011, Prevalence of thyroid dysfunction in patients with type 2 diabetes: Exp Clin Endocrinol Diabetes, v. 119, p. 201-7.

Eden, E. R., E. Sanchez-Heras, A. Tsapara, A. Sobota, T. P. Levine, and C. E. Futter, 2016, Annexin A1 Tethers Membrane Contact Sites that Mediate ER to Endosome Cholesterol Transport: Dev Cell, v. 37, p. 473-83.

Eggo, M. C., W. J. King, E. G. Black, and M. C. Sheppard, 1996, Functional human thyroid cells and their insulin-like growth factor-binding proteins: regulation by thyrotropin, cyclic 3',5' adenosine monophosphate, and growth factors: J Clin Endocrinol Metab, v. 81, p. 3056-62.

El-Shafie, K. T., 2003, Clinical presentation of hypothyroidism: J Family Community Med, v. 10, p. 55-8.

ElMokh, O., D. Ruffieux-Daidié, M. A. Roelli, A. Stooss, W. A. Phillips, J. Gertsch, M. S. Dettmer, and R. P. Charles, 2017, Combined MEK and Pi3'-kinase inhibition reveals synergy in targeting thyroid cancer in vitro and in vivo: Oncotarget, v. 8, p. 24604-24620.

Eskandari, S., D. D. Loo, G. Dai, O. Levy, E. M. Wright, and N. Carrasco, 1997, Thyroid Na+/I- symporter. Mechanism, stoichiometry, and specificity: J Biol Chem, v. 272, p. 27230-8.

Feng, F., L. Yehia, Y. Ni, Y. S. Chang, S. M. Jhiang, and C. Eng, 2018, A Nonpump Function of Sodium Iodide Symporter in Thyroid Cancer via Cross-talk with PTEN Signaling: Cancer Res, v. 78, p. 6121-6133.

Feng, X., Y. Jiang, P. Meltzer, and P. M. Yen, 2000, Thyroid hormone regulation of hepatic genes in vivo detected by complementary DNA microarray: Mol Endocrinol, v. 14, p. 947-55.

Fernández, C. A., M. Puig-Domingo, F. Lomeña, M. Estorch, V. Camacho Martí, A. L. Bittini, M. Marazuela, J. Santamaría, J. Castro, P. Martínez de Icaya, I. Moraga, T. Martín, A. Megía, M. Porta, D. Mauricio, and I. Halperin, 2009, Effectiveness of retinoic acid treatment for redifferentiation of thyroid cancer in relation to recovery of radioiodine uptake: J Endocrinol Invest, v. 32, p. 228-33.

Ferris, S. P., V. K. Kodali, and R. J. Kaufman, 2014, Glycoprotein folding and quality-control mechanisms in protein-folding diseases: Dis Model Mech, v. 7, p. 331-41.

Flamini, M. I., G. V. Gauna, M. L. Sottile, B. S. Nadin, A. M. Sanchez, and L. M. Vargas-Roig, 2014, Retinoic acid reduces migration of human breast cancer cells: role of retinoic acid receptor beta: J Cell Mol Med, v. 18, p. 1113-23.

Fletcher, A., 2018, IDENTIFICATION OF NOVEL SODIUM IODIDE SYMPORTER INTERACTORS WHICH MODULATE RADIOIODINE UPTAKE, University of Birmingham, 341 p.

Fletcher, A., M. L. Read, C. E. M. Thornton, D. P. Larner, V. L. Poole, K. Brookes, H. R. Nieto, M. Alshahrani, R. J. Thompson, G. G. Lavery, I. Landa, J. A. Fagin, M. J. Campbell, K. Boelaert, A. S. Turnell, V. E. Smith, and C. J. McCabe, 2020, Targeting Novel Sodium Iodide Symporter Interactors ADP-Ribosylation Factor 4 and Valosin-Containing Protein Enhances Radioiodine Uptake: Cancer Res, v. 80, p. 102-115.

French, C. A., E. K. Alexander, E. S. Cibas, V. Nose, J. Laguette, W. Faquin, J. Garber, F. Moore, J. A. Fletcher, P. R. Larsen, and T. G. Kroll, 2003, Genetic and biological subgroups of low-stage follicular thyroid cancer: Am J Pathol, v. 162, p. 1053-60.

Friesema, E. C., S. Ganguly, A. Abdalla, J. E. Manning Fox, A. P. Halestrap, and T. J. Visser, 2003, Identification of monocarboxylate transporter 8 as a specific thyroid hormone transporter: J Biol Chem, v. 278, p. 40128-35.

Fritzsche, M., R. Thorogate, and G. Charras, 2014, Quantitative analysis of ezrin turnover dynamics in the actin cortex: Biophys J, v. 106, p. 343-53.

Fugazzola, L., S. Pilotti, A. Pinchera, T. V. Vorontsova, P. Mondellini, I. Bongarzone, A. Greco, L. Astakhova, M. G. Butti, E. P. Demidchik, and et al., 1995, Oncogenic rearrangements of the RET proto-oncogene in papillary thyroid carcinomas from children exposed to the Chernobyl nuclear accident: Cancer Res, v. 55, p. 5617-20.

Futter, C. E., and I. J. White, 2007, Annexins and endocytosis: Traffic, v. 8, p. 951-8.

Galo, M. G., L. E. Uñates, and R. N. Farías, 1981, Effect of membrane fatty acid composition on the action of thyroid hormones on (Ca2+ + Mg2+)-adenosine triphosphatase from rat erythrocyte: J Biol Chem, v. 256, p. 7113-4.

Gao, J., B. A. Aksoy, U. Dogrusoz, G. Dresdner, B. Gross, S. O. Sumer, Y. Sun, A. Jacobsen, R. Sinha, E. Larsson, E. Cerami, C. Sander, and N. Schultz, 2013, Integrative analysis of complex cancer genomics and clinical profiles using the cBioPortal: Sci Signal, v. 6, p. pl1.

Gardner, R. G., G. M. Swarbrick, N. W. Bays, S. R. Cronin, S. Wilhovsky, L. Seelig, C. Kim, and R. Y. Hampton, 2000, Endoplasmic reticulum degradation requires lumen to cytosol signaling. Transmembrane control of Hrd1p by Hrd3p: J Cell Biol, v. 151, p. 69-82.

Gavins, F. N., and M. J. Hickey, 2012, Annexin A1 and the regulation of innate and adaptive immunity: Front Immunol, v. 3, p. 354.

Giusti, L., P. Iacconi, F. Ciregia, G. Giannaccini, G. L. Donatini, F. Basolo, P. Miccoli, A. Pinchera, and A. Lucacchini, 2008, Fine-needle aspiration of thyroid nodules: proteomic analysis to identify cancer biomarkers: J Proteome Res, v. 7, p. 4079-88.

Gopinath, B., J. J. Wang, A. Kifley, J. R. Wall, S. R. Leeder, and P. Mitchell, 2008, Type 2 diabetes does not predict incident thyroid dysfunction in the elderly: Diabetes Res Clin Pract, v. 82, p. e11-3.

Goy, A., A. Younes, P. McLaughlin, B. Pro, J. E. Romaguera, F. Hagemeister, L. Fayad, N. H. Dang, F. Samaniego, M. Wang, K. Broglio, B. Samuels, F. Gilles, A. H. Sarris, S. Hart, E. Trehu, D. Schenkein, F. Cabanillas, and A. M. Rodriguez, 2005, Phase II study of proteasome inhibitor bortezomib in relapsed or refractory B-cell non-Hodgkin's lymphoma: J Clin Oncol, v. 23, p. 667-75.

Gregory Powell, J., X. Wang, B. L. Allard, M. Sahin, X. L. Wang, I. D. Hay, H. J. Hiddinga, S. S. Deshpande, T. G. Kroll, S. K. Grebe, N. L. Eberhardt, and B. McIver, 2004, The PAX8/PPARgamma fusion oncoprotein transforms immortalized human thyrocytes through a mechanism probably involving wild-type PPARgamma inhibition: Oncogene, v. 23, p. 3634-41.

Guo, X., Y. Xu, and Z. Zhao, 2015, In-depth genomic data analyses revealed complex transcriptional and epigenetic dysregulations of BRAFV600E in melanoma: Mol Cancer, v. 14, p. 60.

Guo, Z., H. Hardin, and R. V. Lloyd, 2014, Cancer stem-like cells and thyroid cancer: Endocr Relat Cancer, v. 21, p. T285-300.

Gupta, N., A. K. Dasyam, S. E. Carty, M. N. Nikiforova, N. P. Ohori, M. Armstrong, L. Yip, S. O. LeBeau, K. L. McCoy, C. Coyne, M. T. Stang, J. Johnson, R. L. Ferris, R. Seethala, Y. E. Nikiforov, and S. P. Hodak, 2013, RAS mutations in thyroid FNA specimens are highly predictive of predominantly low-risk follicular-pattern cancers: J Clin Endocrinol Metab, v. 98, p. E914-22.

Haluzik, M., J. Nedvidkova, V. Bartak, I. Dostalova, P. Vlcek, P. Racek, M. Taus, S. Svacina, S. Alesci, and K. Pacak, 2003, Effects of hypo- and hyperthyroidism on noradrenergic activity and glycerol concentrations in human subcutaneous abdominal adipose tissue assessed with microdialysis: J Clin Endocrinol Metab, v. 88, p. 5605-8.

Handkiewicz-Junak, D., J. Roskosz, K. Hasse-Lazar, S. Szpak-Ulczok, Z. Puch, A. Kukulska, T. Olczyk, A. Piela, E. Paliczka-Cieslik, and B. Jarzab, 2009, 13-cis-retinoic acid re-differentiation therapy and recombinant human thyrotropin-aided radioiodine treatment of non-Functional metastatic thyroid cancer: a single-center, 53-patient phase 2 study: Thyroid Res, v. 2, p. 8.

Hannon, R., J. D. Croxtall, S. J. Getting, F. Roviezzo, S. Yona, M. J. Paul-Clark, F. N. Gavins, M. Perretti, J. F. Morris, J. C. Buckingham, and R. J. Flower, 2003, Aberrant inflammation and resistance to glucocorticoids in annexin 1-/- mouse: FASEB J, v. 17, p. 253-5.

Harris, A. R., D. Christianson, M. S. Smith, S. L. Fang, L. E. Braverman, and A. G. Vagenakis, 1978, The physiological role of thyrotropin-releasing hormone in the regulation of thyroid-stimulating hormone and prolactin secretion in the rat: J Clin Invest, v. 61, p. 441-8.

He, H., W. Li, P. Yan, R. Bundschuh, J. A. Killian, J. Labanowska, P. Brock, R. Shen, N. A. Heerema, and A. de la Chapelle, 2018, Identification of a Recurrent LMO7-BRAF Fusion in Papillary Thyroid Carcinoma: Thyroid, v. 28, p. 748-754.

Hellström, L., H. Wahrenberg, S. Reynisdottir, and P. Arner, 1997, Catecholamine-induced adipocyte lipolysis in human hyperthyroidism: J Clin Endocrinol Metab, v. 82, p. 159-66.

Hertz, S., and A. Roberts, 1946, Radioactive iodine in the study of thyroid physiology; the use of radioactive iodine therapy in hyperthyroidism: J Am Med Assoc, v. 131, p. 81-6.

Hingorani, M., C. Spitzweg, G. Vassaux, K. Newbold, A. Melcher, H. Pandha, R. Vile, and K. Harrington, 2010, The biology of the sodium iodide symporter and its potential for targeted gene delivery: Curr Cancer Drug Targets, v. 10, p. 242-67.

Ho, A. L., R. K. Grewal, R. Leboeuf, E. J. Sherman, D. G. Pfister, D. Deandreis, K. S. Pentlow, P. B. Zanzonico, S. Haque, S. Gavane, R. A. Ghossein, J. C. Ricarte-Filho, J. M. Dominguez, R. Shen, R. M. Tuttle, S. M. Larson, and J. A. Fagin, 2013, Selumetinib-enhanced radioiodine uptake in advanced thyroid cancer: N Engl J Med, v. 368, p. 623-32.

Hou, P., D. Liu, and M. Xing, 2011, Genome-wide alterations in gene methylation by the BRAF V600E mutation in papillary thyroid cancer cells: Endocr Relat Cancer, v. 18, p. 687-97.

Hsiao, S. J., and Y. E. Nikiforov, 2014, Molecular approaches to thyroid cancer diagnosis: Endocr Relat Cancer, v. 21, p. T301-13.

Hu, S., D. Liu, R. P. Tufano, K. A. Carson, E. Rosenbaum, Y. Cohen, E. H. Holt, K. Kiseljak-Vassiliades, K. J. Rhoden, S. Tolaney, S. Condouris, G. Tallini, W. H. Westra, C. B. Umbricht, M. A. Zeiger, J. A. Califano, V. Vasko, and M. Xing, 2006, Association of aberrant methylation of tumor suppressor genes with tumor aggressiveness and BRAF mutation in papillary thyroid cancer: Int J Cancer, v. 119, p. 2322-9.

Huang, L., T. Y. Wong, R. C. Lin, and H. Furthmayr, 1999, Replacement of threonine 558, a critical site of phosphorylation of moesin in vivo, with aspartate activates F-actin binding of moesin. Regulation by conformational change: J Biol Chem, v. 274, p. 12803-10.

Huang, Z., Y. Wu, X. Zhou, J. Xu, W. Zhu, Y. Shu, and P. Liu, 2014, Efficacy of therapy with bortezomib in solid tumors: a review based on 32 clinical trials: Future Oncol, v. 10, p. 1795-807.

Huc-Brandt, S., D. Marcellin, F. Graslin, O. Averseng, L. Bellanger, P. Hivin, E. Quemeneur, C. Basquin, V. Navarro, T. Pourcher, and E. Darrouzet, 2011, Characterisation of the purified human sodium/iodide symporter reveals that the protein is mainly present in a dimeric form and permits the detailed study of a native C-terminal fragment: Biochim Biophys Acta, v. 1808, p. 65-77.

Hyman, D. M., I. Puzanov, V. Subbiah, J. E. Faris, I. Chau, J. Y. Blay, J. Wolf, N. S. Raje, E. L. Diamond, A. Hollebecque, R. Gervais, M. E. Elez-Fernandez, A. Italiano, R. D. Hofheinz, M. Hidalgo, E. Chan, M. Schuler, S. F. Lasserre, M. Makrutzki, F. Sirzen, M. L. Veronese, J. Tabernero, and J. Baselga, 2015, Vemurafenib in Multiple Nonmelanoma Cancers with BRAF V600 Mutations: N Engl J Med, v. 373, p. 726-36.

Hänzelmann, P., and H. Schindelin, 2011, The structural and functional basis of the p97/valosin-containing protein (VCP)-interacting motif (VIM): mutually exclusive binding of cofactors to the N-terminal domain of p97: J Biol Chem, v. 286, p. 38679-90.

Hébert, M., S. Potin, M. Sebbagh, J. Bertoglio, J. Bréard, and J. Hamelin, 2008, Rho-ROCK-dependent ezrin-radixin-moesin phosphorylation regulates Fas-mediated apoptosis in Jurkat cells: J Immunol, v. 181, p. 5963-73.

Ito, Y., A. Miyauchi, M. Kihara, M. Fukushima, T. Higashiyama, and A. Miya, 2018, Overall Survival of Papillary Thyroid Carcinoma Patients: A Single-Institution Long-Term Follow-Up of 5897 Patients: World J Surg, v. 42, p. 615-622.

Ivetic, A., and A. J. Ridley, 2004, The telling tail of L-selectin: Biochem Soc Trans, v. 32, p. 1118-21.

James, B. C., J. M. Mitchell, H. D. Jeon, N. Vasilottos, R. H. Grogan, and B. Aschebrook-Kilfoy, 2018, An update in international trends in incidence rates of thyroid cancer, 1973-2007: Cancer Causes Control, v. 29, p. 465-473.

Ju, J. S., R. A. Fuentealba, S. E. Miller, E. Jackson, D. Piwnica-Worms, R. H. Baloh, and C. C. Weihl, 2009, Valosin-containing protein (VCP) is required for autophagy and is disrupted in VCP disease: J Cell Biol, v. 187, p. 875-88.

Kalderon, B., O. Hermesh, and J. Bar-Tana, 1995, Mitochondrial permeability transition is induced by in vivo thyroid hormone treatment: Endocrinology, v. 136, p. 3552-6.

Kalderon, B., R. Hertz, and J. Bar-Tana, 1992, Effect of thyroid hormone treatment on redox and phosphate potentials in rat liver: Endocrinology, v. 131, p. 400-7.

Kang, J. H., M. Li, X. Chen, and X. M. Yin, 2011, Proteomics analysis of starved cells revealed Annexin A1 as an important regulator of autophagic degradation: Biochem Biophys Res Commun, v. 407, p. 581-6.

Keston, A. S., R. P. Ball, V. K. Frantz, and W. W. Palmer, 1942, Storage of Radioactive Iodine in a Metastasis from Thyroid Carcinoma: Science, v. 95, p. 362-3.

Kilfoy, B. A., S. S. Devesa, M. H. Ward, Y. Zhang, P. S. Rosenberg, T. R. Holford, and W. F. Anderson, 2009, Gender is an age-specific effect modifier for papillary cancers of the thyroid gland: Cancer Epidemiol Biomarkers Prev, v. 18, p. 1092-100.

Kim, D. S., J. A. Franklyn, K. Boelaert, M. C. Eggo, J. C. Watkinson, and C. J. McCabe, 2006, Pituitary tumor transforming gene (PTTG) stimulates thyroid cell proliferation via a vascular endothelial growth factor/kinase insert domain receptor/inhibitor of DNA binding-3 autocrine pathway: J Clin Endocrinol Metab, v. 91, p. 4603-11.

Kim, H. I., and Y. H. Ahn, 2004, Role of peroxisome proliferator-activated receptor-gamma in the glucose-sensing apparatus of liver and beta-cells: Diabetes, v. 53 Suppl 1, p. S60-5.

Kim, K. M., D. K. Kim, Y. M. Park, C. K. Kim, and D. S. Na, 1994, Annexin-I inhibits phospholipase A2 by specific interaction, not by substrate depletion: FEBS Lett, v. 343, p. 251-5.

Kim, S. H., H. S. Park, K. H. Kim, H. Yoo, B. J. Chae, J. S. Bae, S. S. Jung, and B. J. Song, 2015, Correlation between obesity and clinicopathological factors in patients with papillary thyroid cancer: Surg Today, v. 45, p. 723-9.

Kim, S. J., J. Cho, E. J. Song, H. M. Kim, K. E. Lee, S. W. Suh, and E. E. Kim, 2014, Structural basis for ovarian tumor domain-containing protein 1 (OTU1) binding to p97/valosin-containing protein (VCP): J Biol Chem, v. 289, p. 12264-74.

Klugbauer, S., E. Lengfelder, E. P. Demidchik, and H. M. Rabes, 1995, High prevalence of RET rearrangement in thyroid tumors of children from Belarus after the Chernobyl reactor accident: Oncogene, v. 11, p. 2459-67.

Knauf, J. A., H. Kuroda, S. Basu, and J. A. Fagin, 2003, RET/PTC-induced dedifferentiation of thyroid cells is mediated through Y1062 signaling through SHC-RAS-MAP kinase: Oncogene, v. 22, p. 4406-12.

Knauf, J. A., X. Ma, E. P. Smith, L. Zhang, N. Mitsutake, X. H. Liao, S. Refetoff, Y. E. Nikiforov, and J. A. Fagin, 2005, Targeted expression of BRAFV600E in thyroid cells of transgenic mice results in papillary thyroid cancers that undergo dedifferentiation: Cancer Res, v. 65, p. 4238-45.

Knoop, K., N. Schwenk, P. Dolp, M. J. Willhauck, C. Zischek, C. Zach, M. Hacker, B. Göke, E. Wagner, P. J. Nelson, and C. Spitzweg, 2013, Stromal targeting of sodium iodide symporter using mesenchymal stem cells allows enhanced imaging and therapy of hepatocellular carcinoma: Hum Gene Ther, v. 24, p. 306-16.

Knostman, K. A., A. Venkateswaran, B. Zimmerman, C. C. Capen, and S. M. Jhiang, 2007, Creation and characterization of a doxycycline-inducible mouse model of thyroid-targeted RET/PTC1 oncogene and luciferase reporter gene coexpression: Thyroid, v. 17, p. 1181-8.

Kogai, T., T. Endo, T. Saito, A. Miyazaki, A. Kawaguchi, and T. Onaya, 1997, Regulation by thyroid-stimulating hormone of sodium/iodide symporter gene expression and protein levels in FRTL-5 cells: Endocrinology, v. 138, p. 2227-32.

Kogai, T., S. Sajid-Crockett, L. S. Newmarch, Y. Y. Liu, and G. A. Brent, 2008, Phosphoinositide-3-kinase inhibition induces sodium/iodide symporter expression in rat thyroid cells and human papillary thyroid cancer cells: J Endocrinol, v. 199, p. 243-52.

Kosugi, S., S. Inoue, A. Matsuda, and S. M. Jhiang, 1998, Novel, missense and loss-of-function mutations in the sodium/iodide symporter gene causing iodide transport defect in three Japanese patients: J Clin Endocrinol Metab, v. 83, p. 3373-6.

Koumarianou, P., A. De la Vieja, and P. Santisteban, 2014, NIS is basolateraly sorted by AP-1A and AP-1B Clathrin adaptors in MDCK cells, European Thyroid Journal 3 (Supplement 1) 188.

Kraiem, Z., O. Sadeh, D. L. Blithe, and B. C. Nisula, 1994, Human chorionic gonadotropin stimulates thyroid hormone secretion, iodide uptake, organification, and adenosine 3',5'-monophosphate formation in cultured human thyrocytes: J Clin Endocrinol Metab, v. 79, p. 595-9.

Kvetny, J., L. Wilms, P. L. Pedersen, and J. Larsen, 2010, Subclinical hypothyroidism affects mitochondrial function: Horm Metab Res, v. 42, p. 324-7.

Lakshmanan, A., A. Wojcicka, M. Kotlarek, X. Zhang, K. Jazdzewski, and S. M. Jhiang, 2015, microRNA-339-5p modulates Na+/I- symporter-mediated radioiodide uptake: Endocr Relat Cancer, v. 22, p. 11-21.

Landa, I., T. Ibrahimpasic, L. Boucai, R. Sinha, J. A. Knauf, R. H. Shah, S. Dogan, J. C. Ricarte-Filho, G. P. Krishnamoorthy, B. Xu, N. Schultz, M. F. Berger, C. Sander, B. S. Taylor, R. Ghossein, I. Ganly, and J. A. Fagin, 2016, Genomic and transcriptomic hallmarks of poorly differentiated and anaplastic thyroid cancers: J Clin Invest, v. 126, p. 1052-66.

Landa, I., N. Pozdeyev, C. Korch, L. A. Marlow, R. C. Smallridge, J. A. Copland, Y. C. Henderson, S. Y. Lai, G. L. Clayman, N. Onoda, A. C. Tan, M. E. R. Garcia-Rendueles, J. A. Knauf, B. R. Haugen, J. A. Fagin, and R. E. Schweppe, 2019, Comprehensive Genetic Characterization of Human Thyroid Cancer Cell Lines: A Validated Panel for Preclinical Studies: Clin Cancer Res, v. 25, p. 3141-3151.

Lazar, V., J. M. Bidart, B. Caillou, C. Mahe, L. Lacroix, S. Filetti, and M. Schlumberger, 1999, Expression of the Na+/I- symporter gene in human thyroid tumors: a comparison study with other thyroid-specific genes: J Clin Endocrinol Metab, v. 84, p. 3228-34.

Lecona, E., J. I. Barrasa, N. Olmo, B. Llorente, J. Turnay, and M. A. Lizarbe, 2008, Upregulation of annexin A1 expression by butyrate in human colon adenocarcinoma cells: role of p53, NF-Y, and p38 mitogen-activated protein kinase: Mol Cell Biol, v. 28, p. 4665-74.

Lee, J. H., E. S. Lee, and Y. S. Kim, 2007, Clinicopathologic significance of BRAF V600E mutation in papillary carcinomas of the thyroid: a meta-analysis: Cancer, v. 110, p. 38-46.

Leguay, K., B. Decelle, Y. Y. He, A. Pagniez, M. Hogue, H. Kobayashi, C. Le Gouill, M. Bouvier, and S. Carréno, 2021, Development of conformational BRET biosensors that monitor ezrin, radixin and moesin activation in real-time: J Cell Sci.

Lei, J., S. Nowbar, C. N. Mariash, and D. H. Ingbar, 2003, Thyroid hormone stimulates Na-K-ATPase activity and its plasma membrane insertion in rat alveolar epithelial cells: Am J Physiol Lung Cell Mol Physiol, v. 285, p. L762-72.

Lemoine, N. R., E. S. Mayall, F. S. Wyllie, E. D. Williams, M. Goyns, B. Stringer, and D. Wynford-Thomas, 1989, High frequency of ras oncogene activation in all stages of human thyroid tumorigenesis: Oncogene, v. 4, p. 159-64.

Lengana, T., I. O. Lawal, K. Mokoala, M. Vorster, and M. M. Sathekge, 2019, 68Ga-PSMA: a One-stop Shop in Radioactive Iodine Refractory Thyroid Cancer?: Nucl Med Mol Imaging, v. 53, p. 442-445.

Levy, O., A. De la Vieja, C. S. Ginter, C. Riedel, G. Dai, and N. Carrasco, 1998, N-linked glycosylation of the thyroid Na+/I- symporter (NIS). Implications for its secondary structure model: J Biol Chem, v. 273, p. 22657-63.

Li, Y., X. Su, C. Feng, S. Liu, H. Guan, Y. Sun, N. He, M. Ji, and P. Hou, 2020, CYP2S1 is a synthetic lethal target in BRAF: Signal Transduct Target Ther, v. 5, p. 191.

Liaw, D., D. J. Marsh, J. Li, P. L. Dahia, S. I. Wang, Z. Zheng, S. Bose, K. M. Call, H. C. Tsou, M. Peacocke, C. Eng, and R. Parsons, 1997, Germline mutations of the PTEN gene in

Cowden disease, an inherited breast and thyroid cancer syndrome: Nat Genet, v. 16, p. 64-7.

Lim, H., S. S. Devesa, J. A. Sosa, D. Check, and C. M. Kitahara, 2017, Trends in Thyroid Cancer Incidence and Mortality in the United States, 1974-2013: JAMA, v. 317, p. 1338-1348.

Lin, H. C., T. C. Südhof, and R. G. Anderson, 1992, Annexin VI is required for budding of clathrin-coated pits: Cell, v. 70, p. 283-91.

Lin, H. Y., M. Sun, H. Y. Tang, C. Lin, M. K. Luidens, S. A. Mousa, S. Incerpi, G. L. Drusano, F. B. Davis, and P. J. Davis, 2009, L-Thyroxine vs. 3,5,3'-triiodo-L-thyronine and cell proliferation: activation of mitogen-activated protein kinase and phosphatidylinositol 3-kinase: Am J Physiol Cell Physiol, v. 296, p. C980-91.

Liu, X., N. Zheng, Y. N. Shi, J. Yuan, and L. Li, 2014, Thyroid hormone induced angiogenesis through the integrin alphavbeta3/protein kinase D/histone deacetylase 5 signaling pathway: J Mol Endocrinol, v. 52, p. 245-54.

Liu, Y. F., P. F. Zhang, M. Y. Li, Q. Q. Li, and Z. C. Chen, 2011, Identification of annexin A1 as a proinvasive and prognostic factor for lung adenocarcinoma: Clin Exp Metastasis, v. 28, p. 413-25.

Liu, Y. Y., X. Zhang, M. D. Ringel, and S. M. Jhiang, 2012, Modulation of sodium iodide symporter expression and function by LY294002, Akti-1/2 and Rapamycin in thyroid cells: Endocr Relat Cancer, v. 19, p. 291-304.

Lui, W. O., L. Zeng, V. Rehrmann, S. Deshpande, M. Tretiakova, E. L. Kaplan, I. Leibiger, B. Leibiger, U. Enberg, A. Höög, C. Larsson, and T. G. Kroll, 2008, CREB3L2-PPARgamma fusion mutation identifies a thyroid signaling pathway regulated by intramembrane proteolysis: Cancer Res, v. 68, p. 7156-64.

Lukianova, N. Y., A. V. Andriiv, and V. F. Chekhun, 2016, Correlation of iodine symporter expression in highly and low malignant cell lines of human breast cancer differed in their sensitivity to doxorubicin: Exp Oncol, v. 38, p. 169-71.

Lupi, C., R. Giannini, C. Ugolini, A. Proietti, P. Berti, M. Minuto, G. Materazzi, R. Elisei, M. Santoro, P. Miccoli, and F. Basolo, 2007, Association of BRAF V600E mutation with poor clinicopathological outcomes in 500 consecutive cases of papillary thyroid carcinoma: J Clin Endocrinol Metab, v. 92, p. 4085-90.

Ma, R., S. Bonnefond, S. A. Morshed, R. Latif, and T. F. Davies, 2014, Stemness is Derived from Thyroid Cancer Cells: Front Endocrinol (Lausanne), v. 5, p. 114.

Mady, L. J., M. C. Grimes, N. I. Khan, R. H. Rao, S. I. Chiosea, L. Yip, R. L. Ferris, Y. E. Nikiforov, S. E. Carty, and U. Duvvuri, 2020, Molecular Profile of Locally Aggressive Well Differentiated Thyroid Cancers: Sci Rep, v. 10, p. 8031.

Magnaghi, P., R. D'Alessio, B. Valsasina, N. Avanzi, S. Rizzi, D. Asa, F. Gasparri, L. Cozzi, U. Cucchi, C. Orrenius, P. Polucci, D. Ballinari, C. Perrera, A. Leone, G. Cervi, E. Casale, Y. Xiao, C. Wong, D. J. Anderson, A. Galvani, D. Donati, T. O'Brien, P. K. Jackson, and A. Isacchi, 2013, Covalent and allosteric inhibitors of the ATPase VCP/p97 induce cancer cell death: Nat Chem Biol, v. 9, p. 548-56.

Mansouri, A., K. Chowdhury, and P. Gruss, 1998, Follicular cells of the thyroid gland require Pax8 gene function: Nat Genet, v. 19, p. 87-90.

Marcello, M. A., L. L. Cunha, F. A. Batista, and L. S. Ward, 2014, Obesity and thyroid cancer: Endocr Relat Cancer, v. 21, p. T255-71.

Marotta, P., E. Amendola, M. Scarfò, P. De Luca, P. Zoppoli, A. Amoresano, M. De Felice, and R. Di Lauro, 2014, The paired box transcription factor Pax8 is essential for function and survival of adult thyroid cells: Mol Cell Endocrinol, v. 396, p. 26-36.

Martin, M., C. P. Modenutti, V. Peyret, R. C. Geysels, E. Darrouzet, T. Pourcher, A. M. Masini-Repiso, M. A. Marti, N. Carrasco, and J. P. Nicola, 2019, A Carboxy-Terminal Monoleucine-Based Motif Participates in the Basolateral Targeting of the Na+/I- Symporter: Endocrinology, v. 160, p. 156-168.

Martínez-Aguilar, J., R. Clifton-Bligh, and M. P. Molloy, 2016, Proteomics of thyroid tumours provides new insights into their molecular composition and changes associated with malignancy: Sci Rep, v. 6, p. 23660.

Martínez-Sáez, O., N. Chic, T. Pascual, B. Adamo, M. Vidal, B. González-Farré, E. Sanfeliu, F. Schettini, B. Conte, F. Brasó-Maristany, A. Rodríguez, D. Martínez, P. Galván, A. B. Rodríguez, A. Martinez, M. Muñoz, and A. Prat, 2020, Frequency and spectrum of PIK3CA somatic mutations in breast cancer: Breast Cancer Res, v. 22, p. 45.

Matsuda, A., and S. Kosugi, 1997, A homozygous missense mutation of the sodium/iodide symporter gene causing iodide transport defect: J Clin Endocrinol Metab, v. 82, p. 3966-71.

Matsui, J., Y. Yamamoto, Y. Funahashi, A. Tsuruoka, T. Watanabe, T. Wakabayashi, T. Uenaka, and M. Asada, 2008, E7080, a novel inhibitor that targets multiple kinases, has potent antitumor activities against stem cell factor producing human small cell lung cancer H146, based on angiogenesis inhibition: Int J Cancer, v. 122, p. 664-71.

McKelvey, B. A., M. A. Zeiger, and C. B. Umbricht, 2020, Characterization of TERT and BRAF copy number variation in papillary thyroid carcinoma: An analysis of the cancer genome atlas study: Genes Chromosomes Cancer.

McMahon, H. T., and E. Boucrot, 2011, Molecular mechanism and physiological functions of clathrin-mediated endocytosis: Nat Rev Mol Cell Biol, v. 12, p. 517-33.

Michie, K. A., A. Bermeister, N. O. Robertson, S. C. Goodchild, and P. M. G. Curmi, 2019, Two Sides of the Coin: Ezrin/Radixin/Moesin and Merlin Control Membrane Structure and Contact Inhibition: Int J Mol Sci, v. 20.

Miele, L., E. Cordella-Miele, A. Facchiano, and A. B. Mukherjee, 1988, Novel anti-inflammatory peptides from the region of highest similarity between uteroglobin and lipocortin I: Nature, v. 335, p. 726-30.

Milano, A. F., 2018, Thyroid Cancer: 20-Year Comparative Mortality and Survival Analysis of Six Thyroid Cancer Histologic Subtypes by Age, Sex, Race, Stage, Cohort Entry Time-Period and Disease Duration (SEER*Stat 8.3.2) A Systematic Review of 145,457 Cases for Diagnosis Years 1993-2013: J Insur Med, v. 47, p. 143-158.

Montero-Conde, C., S. Ruiz-Llorente, J. M. Dominguez, J. A. Knauf, A. Viale, E. J. Sherman, M. Ryder, R. A. Ghossein, N. Rosen, and J. A. Fagin, 2013, Relief of feedback inhibition of HER3 transcription by RAF and MEK inhibitors attenuates their antitumor effects in BRAF-mutant thyroid carcinomas: Cancer Discov, v. 3, p. 520-33.

Mortoglou, A., and H. Candiloros, 2004, The serum triiodothyronine to thyroxine (T3/T4) ratio in various thyroid disorders and after Levothyroxine replacement therapy: Hormones (Athens), v. 3, p. 120-6.

Mousa, S. A., G. V. Glinsky, H. Y. Lin, O. Ashur-Fabian, A. Hercbergs, K. A. Keating, and P. J. Davis, 2018, Contributions of Thyroid Hormone to Cancer Metastasis: Biomedicines, v. 6.

Muriel, O., A. Tomas, C. C. Scott, and J. Gruenberg, 2016, Moesin and cortactin control actin-dependent multivesicular endosome biogenesis: Mol Biol Cell, v. 27, p. 3305-3316.

Nakamura, F., M. R. Amieva, C. Hirota, Y. Mizuno, and H. Furthmayr, 1996, Phosphorylation of 558T of moesin detected by site-specific antibodies in RAW264.7 macrophages: Biochem Biophys Res Commun, v. 226, p. 650-6.

Nakayama, H., A. Yoshida, Y. Nakamura, H. Hayashi, Y. Miyagi, N. Wada, Y. Rino, M. Masuda, and T. Imada, 2007, Clinical significance of BRAF (V600E) mutation and Ki-67 labeling index in papillary thyroid carcinomas: Anticancer Res, v. 27, p. 3645-9.

Nelen, M. R., W. C. van Staveren, E. A. Peeters, M. B. Hassel, R. J. Gorlin, H. Hamm, C. F. Lindboe, J. P. Fryns, R. H. Sijmons, D. G. Woods, E. C. Mariman, G. W. Padberg, and H. Kremer, 1997, Germline mutations in the PTEN/MMAC1 gene in patients with Cowden disease: Hum Mol Genet, v. 6, p. 1383-7.

Nelson, M., A. Hercbergs, L. Rybicki, and M. Strome, 2006, Association between development of hypothyroidism and improved survival in patients with head and neck cancer: Arch Otolaryngol Head Neck Surg, v. 132, p. 1041-6.

Network, C. G. A. R., 2014, Integrated genomic characterization of papillary thyroid carcinoma: Cell, v. 159, p. 676-90.

Nicola, J. P., C. Basquin, C. Portulano, A. Reyna-Neyra, M. Paroder, and N. Carrasco, 2009, The Na+/I- symporter mediates active iodide uptake in the intestine: Am J Physiol Cell Physiol, v. 296, p. C654-62.

Nie, M., A. Aslanian, J. Prudden, J. Heideker, A. A. Vashisht, J. A. Wohlschlegel, J. R. Yates, 3rd, and M. N. Boddy, 2012, Dual recruitment of Cdc48 (p97)-Ufd1-Npl4 ubiquitin-selective segregase by small ubiquitin-like modifier protein (SUMO) and ubiquitin in SUMO-targeted ubiquitin ligase-mediated genome stability functions: J Biol Chem, v. 287, p. 29610-9.

Nikiforov, Y. E., 2002, RET/PTC rearrangement in thyroid tumors: Endocr Pathol, v. 13, p. 3-16.

Nikiforova, M. N., R. A. Lynch, P. W. Biddinger, E. K. Alexander, G. W. Dorn, G. Tallini, T. G. Kroll, and Y. E. Nikiforov, 2003, RAS point mutations and PAX8-PPAR gamma rearrangement in thyroid tumors: evidence for distinct molecular pathways in thyroid follicular carcinoma: J Clin Endocrinol Metab, v. 88, p. 2318-26.

Nomachi, A., M. Yoshinaga, J. Liu, P. Kanchanawong, K. Tohyama, D. Thumkeo, T. Watanabe, S. Narumiya, and T. Hirata, 2013, Moesin controls clathrin-mediated S1PR1 internalization in T cells: PLoS One, v. 8, p. e82590.

Ohno, M., M. Zannini, O. Levy, N. Carrasco, and R. di Lauro, 1999, The paired-domain transcription factor Pax8 binds to the upstream enhancer of the rat sodium/iodide symporter gene and participates in both thyroid-specific and cyclic-AMP-dependent transcription: Mol Cell Biol, v. 19, p. 2051-60.

Okuda, T., C. Osawa, H. Yamada, K. Hayashi, S. Nishikawa, T. Ushio, Y. Kubo, M. Satou, H. Ogawa, and T. Haga, 2012, Transmembrane topology and oligomeric structure of the high-affinity choline transporter: J Biol Chem, v. 287, p. 42826-34.

Ortega, J., C. Sala, B. Flor, and S. Lledo, 2004, Efficacy and cost-effectiveness of the UltraCision harmonic scalpel in thyroid surgery: an analysis of 200 cases in a randomized trial: J Laparoendosc Adv Surg Tech A, v. 14, p. 9-12.

Osaki, M., M. Oshimura, and H. Ito, 2004, PI3K-Akt pathway: its functions and alterations in human cancer: Apoptosis, v. 9, p. 667-76.

Oshiro, N., Y. Fukata, and K. Kaibuchi, 1998, Phosphorylation of moesin by rho-associated kinase (Rho-kinase) plays a crucial role in the formation of microvilli-like structures: J Biol Chem, v. 273, p. 34663-6.

Paroder-Belenitsky, M., M. J. Maestas, O. Dohan, J. P. Nicola, A. Reyna-Neyra, A. Follenzi, E. Dadachova, S. Eskandari, L. M. Amzel, and N. Carrasco, 2011, Mechanism of anion selectivity and stoichiometry of the Na+/I- symporter (NIS): Proc Natl Acad Sci U S A, v. 108, p. 17933-8.

Pettersen, E. F., T. D. Goddard, C. C. Huang, G. S. Couch, D. M. Greenblatt, E. C. Meng, and T. E. Ferrin, 2004, UCSF Chimera--a visualization system for exploratory research and analysis: J Comput Chem, v. 25, p. 1605-12.

Pierotti, M. A., M. Santoro, R. B. Jenkins, G. Sozzi, I. Bongarzone, M. Grieco, N. Monzini, M. Miozzo, M. A. Herrmann, A. Fusco, and et al., 1992, Characterization of an inversion on the long arm of chromosome 10 juxtaposing D10S170 and RET and creating the oncogenic sequence RET/PTC: Proc Natl Acad Sci U S A, v. 89, p. 1616-20.

Poeter, M., S. Radke, M. Koese, F. Hessner, A. Hegemann, A. Musiol, V. Gerke, T. Grewal, and U. Rescher, 2013, Disruption of the annexin A1/S100A11 complex increases the migration and clonogenic growth by dysregulating epithelial growth factor (EGF) signaling: Biochim Biophys Acta, v. 1833, p. 1700-11.

Pomerance, M., H. B. Abdullah, S. Kamerji, C. Correze, and J. P. Blondeau, 2000, Thyroid-stimulating hormone and cyclic AMP activate p38 mitogen-activated protein kinase cascade. Involvement of protein kinase A, rac1, and reactive oxygen species: J Biol Chem, v. 275, p. 40539-46.

Qi, J., and Z. A. Ronai, 2015, Dysregulation of ubiquitin ligases in cancer: Drug Resist Updat, v. 23, p. 1-11.

Rahbari, R., L. Zhang, and E. Kebebew, 2010, Thyroid cancer gender disparity: Future Oncol, v. 6, p. 1771-9.

Raman, P., and R. J. Koenig, 2014, Pax-8-PPAR-γ fusion protein in thyroid carcinoma: Nat Rev Endocrinol, v. 10, p. 616-23.

Ramanathan, R. K., D. D. Von Hoff, F. Eskens, G. Blumenschein, D. Richards, I. Genvresse, S. Reschke, C. Granvil, A. Skubala, C. Peña, and K. Mross, 2020, Phase Ib Trial of the PI3K Inhibitor Copanlisib Combined with the Allosteric MEK Inhibitor Refametinib in Patients with Advanced Cancer: Target Oncol, v. 15, p. 163-174.

Raulf, N., P. Lucarelli, S. Thavaraj, S. Brown, J. M. Vicencio, T. Sauter, and M. Tavassoli, 2018, Annexin A1 regulates EGFR activity and alters EGFR-containing tumour-derived exosomes in head and neck cancers: Eur J Cancer, v. 102, p. 52-68.

Read, M. L., J. C. Fong, B. Modasia, A. Fletcher, W. Imruetaicharoenchoke, R. J. Thompson, H. Nieto, J. J. Reynolds, A. Bacon, U. Mallick, A. Hackshaw, J. C. Watkinson, K. Boelaert, A. S. Turnell, V. E. Smith, and C. J. McCabe, 2017, Elevated PTTG and PBF predicts poor patient outcome and modulates DNA damage response genes in thyroid cancer: Oncogene, v. 36, p. 5296-5308.

Reddi, H. V., P. Madde, L. A. Marlow, J. A. Copland, B. McIver, S. K. Grebe, and N. L. Eberhardt, 2010, Expression of the PAX8/PPARγ Fusion Protein Is Associated with Decreased Neovascularization In Vivo: Impact on Tumorigenesis and Disease Prognosis: Genes Cancer, v. 1, p. 480-492.

Renier, C., H. Vogel, O. Offor, C. Yao, and I. Wapnir, 2010, Breast cancer brain metastases express the sodium iodide symporter: J Neurooncol, v. 96, p. 331-6.

Rentero, C., P. Blanco-Muñoz, E. Meneses-Salas, T. Grewal, and C. Enrich, 2018, Annexins-Coordinators of Cholesterol Homeostasis in Endocytic Pathways: Int J Mol Sci, v. 19.

Richardson, P. G., B. Barlogie, J. Berenson, S. Singhal, S. Jagannath, D. Irwin, S. V. Rajkumar, G. Srkalovic, M. Alsina, R. Alexanian, D. Siegel, R. Z. Orlowski, D. Kuter, S. A. Limentani, S. Lee, T. Hideshima, D. L. Esseltine, M. Kauffman, J. Adams, D. P. Schenkein, and K. C. Anderson, 2003, A phase 2 study of bortezomib in relapsed, refractory myeloma: N Engl J Med, v. 348, p. 2609-17.

Riesco-Eizaguirre, G., L. Wert-Lamas, J. Perales-Paton, A. Sastre-Perona, L. P. Fernandez, and P. Santisteban, 2015, The miR-146b-3p/PAX8/NIS Regulatory Circuit Modulates the Differentiation Phenotype and Function of Thyroid Cells during Carcinogenesis: Cancer Res, v. 75, p. 4119-30.

Rondepierre, F., B. Bouchon, J. Papon, M. Bonnet-Duquennoy, R. Kintossou, N. Moins, J. Maublant, J. C. Madelmont, M. D'Incan, and F. Degoul, 2009, Proteomic studies of B16 lines: involvement of annexin A1 in melanoma dissemination: Biochim Biophys Acta, v. 1794, p. 61-9.

Rosen, E. D., P. Sarraf, A. E. Troy, G. Bradwin, K. Moore, D. S. Milstone, B. M. Spiegelman, and R. M. Mortensen, 1999, PPAR gamma is required for the differentiation of adipose tissue in vivo and in vitro: Mol Cell, v. 4, p. 611-7.

Rothenberg, S. M., D. G. McFadden, E. L. Palmer, G. H. Daniels, and L. J. Wirth, 2015, Redifferentiation of iodine-refractory BRAF V600E-mutant metastatic papillary thyroid cancer with dabrafenib: Clin Cancer Res, v. 21, p. 1028-35.

Royaux, I. E., K. Suzuki, A. Mori, R. Katoh, L. A. Everett, L. D. Kohn, and E. D. Green, 2000, Pendrin, the protein encoded by the Pendred syndrome gene (PDS), is an apical porter of iodide in the thyroid and is regulated by thyroglobulin in FRTL-5 cells: Endocrinology, v. 141, p. 839-45.

Rugge, J. B., C. Bougatsos, and R. Chou, 2015, Screening and treatment of thyroid dysfunction: an evidence review for the U.S. Preventive Services Task Force: Ann Intern Med, v. 162, p. 35-45.

Ruiz-Llorente, S., E. Carrillo Santa de Pau, A. Sastre-Perona, C. Montero-Conde, G. Gómez-López, J. A. Fagin, A. Valencia, D. G. Pisano, and P. Santisteban, 2012, Genome-wide analysis of Pax8 binding provides new insights into thyroid functions: BMC Genomics, v. 13, p. 147.

Rumpf, S., S. B. Lee, L. Y. Jan, and Y. N. Jan, 2011, Neuronal remodeling and apoptosis require VCP-dependent degradation of the apoptosis inhibitor DIAP1: Development, v. 138, p. 1153-60.

Rusinek, D., M. Swierniak, E. Chmielik, M. Kowal, M. Kowalska, R. Cyplinska, A. Czarniecka, W. Piglowski, J. Korfanty, M. Chekan, J. Krajewska, S. Szpak-Ulczok, M. Jarzab, W. Widlak, and B. Jarzab, 2015, BRAFV600E-Associated Gene Expression Profile: Early Changes in the Transcriptome, Based on a Transgenic Mouse Model of Papillary Thyroid Carcinoma: PLoS One, v. 10, p. e0143688.

Sanchez, A. M., J. E. Shortrede, L. M. Vargas-Roig, and M. I. Flamini, 2016, Retinoic acid induces nuclear FAK translocation and reduces breast cancer cell adhesion through Moesin, FAK, and Paxillin: Mol Cell Endocrinol, v. 430, p. 1-11.

Santoro, M., and F. Carlomagno, 2013, Central role of RET in thyroid cancer: Cold Spring Harb Perspect Biol, v. 5, p. a009233.

Santoro, M., R. M. Melillo, M. Grieco, M. T. Berlingieri, G. Vecchio, and A. Fusco, 1993, The TRK and RET tyrosine kinase oncogenes cooperate with ras in the neoplastic transformation of a rat thyroid epithelial cell line: Cell Growth Differ, v. 4, p. 77-84.

Sasseville, L. J., M. Morin, M. J. Coady, R. Blunck, and J. Y. Lapointe, 2016, The Human Sodium-Glucose Cotransporter (hSGLT1) Is a Disulfide-Bridged Homodimer with a Re-Entrant C-Terminal Loop: PLoS One, v. 11, p. e0154589.

Sawin, C. T., and D. V. Becker, 1997, Radioiodine and the treatment of hyperthyroidism: the early history: Thyroid, v. 7, p. 163-76.

Schindelin, J., I. Arganda-Carreras, E. Frise, V. Kaynig, M. Longair, T. Pietzsch, S. Preibisch, C. Rueden, S. Saalfeld, B. Schmid, J. Y. Tinevez, D. J. White, V. Hartenstein, K. Eliceiri, P. Tomancak, and A. Cardona, 2012, Fiji: an open-source platform for biological-image analysis: Nat Methods, v. 9, p. 676-82.

Schlumberger, M., M. Tahara, L. J. Wirth, B. Robinson, M. S. Brose, R. Elisei, M. A. Habra, K. Newbold, M. H. Shah, A. O. Hoff, A. G. Gianoukakis, N. Kiyota, M. H. Taylor, S. B. Kim, M. K. Krzyzanowska, C. E. Dutcus, B. de las Heras, J. Zhu, and S. I. Sherman, 2015, Lenvatinib versus placebo in radioiodine-refractory thyroid cancer: N Engl J Med, v. 372, p. 621-30.

Schmohl, K. A., A. M. Mueller, M. Dohmann, R. Spellerberg, S. Urnauer, N. Schwenk, S. I. Ziegler, P. Bartenstein, P. J. Nelson, and C. Spitzweg, 2019, Integrin αvβ3-Mediated Effects of Thyroid Hormones on Mesenchymal Stem Cells in Tumor Angiogenesis: Thyroid, v. 29, p. 1843-1857.

Schram, A. M., L. Gandhi, M. M. Mita, L. Damstrup, F. Campana, M. Hidalgo, E. Grande, D. M. Hyman, and R. S. Heist, 2018, A phase Ib dose-escalation and expansion study of the oral MEK inhibitor pimasertib and PI3K/MTOR inhibitor voxtalisib in patients with advanced solid tumours: Br J Cancer, v. 119, p. 1471-1476.

Schug, C., W. Sievert, S. Urnauer, A. M. Müller, K. A. Schmohl, A. Wechselberger, N. Schwenk, K. Lauber, M. Schwaiger, G. Multhoff, E. Wagner, P. J. Nelson, and C. Spitzweg, 2018, External Beam Radiation Therapy Enhances Mesenchymal Stem Cell-Mediated Sodium-Iodide Symporter Gene Delivery: Hum Gene Ther, v. 29, p. 1287-1300.

Schug, C., S. Urnauer, C. Jaeckel, K. A. Schmohl, M. Tutter, K. Steiger, N. Schwenk, M. Schwaiger, E. Wagner, P. J. Nelson, and C. Spitzweg, 2019, TGFB1-driven mesenchymal stem cell-mediated NIS gene transfer: Endocr Relat Cancer, v. 26, p. 89-101.

Sciuto, R., L. Romano, S. Rea, F. Marandino, I. Sperduti, and C. L. Maini, 2009, Natural history and clinical outcome of differentiated thyroid carcinoma: a retrospective analysis of 1503 patients treated at a single institution: Ann Oncol, v. 20, p. 1728-35.

Scott, D. A., R. Wang, T. M. Kreman, V. C. Sheffield, and L. P. Karniski, 1999, The Pendred syndrome gene encodes a chloride-iodide transport protein: Nat Genet, v. 21, p. 440-3.

Segura-Cabrera, A., R. Tripathi, X. Zhang, L. Gui, T. F. Chou, and K. Komurov, 2017, A structure- and chemical genomics-based approach for repositioning of drugs against VCP/p97 ATPase: Sci Rep, v. 7, p. 44912.

Seidlin, S. M., E. Oshry, and A. A. Yalow, 1948, Spontaneous and experimentally induced uptake of radioactive iodine in metastases from thyroid carcinoma; a preliminary report: J Clin Endocrinol Metab, v. 8, p. 423-32.

Shapiro, G. I., P. LoRusso, E. Kwak, S. Pandya, C. M. Rudin, C. Kurkjian, J. M. Cleary, M. J. Pilat, S. Jones, A. de Crespigny, J. Fredrickson, L. Musib, Y. Yan, M. Wongchenko, H. J. Hsieh, M. R. Gates, I. T. Chan, and J. Bendell, 2020, Phase Ib study of the MEK inhibitor cobimetinib (GDC-0973) in combination with the PI3K inhibitor pictilisib (GDC-0941) in patients with advanced solid tumors: Invest New Drugs, v. 38, p. 419-432.

Shimamura, M., N. Shibusawa, T. Kurashige, Z. Mussazhanova, H. Matsuzaki, M. Nakashima, M. Yamada, and Y. Nagayama, 2018, Mouse models of sporadic thyroid cancer derived from BRAFV600E alone or in combination with PTEN haploinsufficiency under physiologic TSH levels: PLoS One, v. 13, p. e0201365.

Shimoji, T., K. Murakami, Y. Sugiyama, M. Matsuda, S. Inubushi, J. Nasu, M. Shirakura, T. Suzuki, T. Wakita, T. Kishino, H. Hotta, T. Miyamura, and I. Shoji, 2009, Identification of annexin A1 as a novel substrate for E6AP-mediated ubiquitylation: J Cell Biochem, v. 106, p. 1123-35.

Simon, D., C. Körber, M. Krausch, J. Segering, P. Groth, R. Görges, F. Grünwald, H. W. Müller-Gärtner, C. Schmutzler, J. Köhrle, H. D. Röher, and C. Reiners, 2002, Clinical impact of retinoids in redifferentiation therapy of advanced thyroid cancer: final results of a pilot study: Eur J Nucl Med Mol Imaging, v. 29, p. 775-82.

Sitte, H. H., H. Farhan, and J. A. Javitch, 2004, Sodium-dependent neurotransmitter transporters: oligomerization as a determinant of transporter function and trafficking: Mol Interv, v. 4, p. 38-47.

Smith, A., M. Galli, I. Piga, V. Denti, M. Stella, C. Chinello, N. Fusco, D. Leni, M. Manzoni, G. Roversi, M. Garancini, A. I. Pincelli, V. Cimino, G. Capitoli, F. Magni, and F. Pagni, 2019, Molecular signatures of medullary thyroid carcinoma by matrix-assisted laser desorption/ionisation mass spectrometry imaging: J Proteomics, v. 191, p. 114-123.

Smith, V. E., M. L. Read, A. S. Turnell, N. Sharma, G. D. Lewy, J. C. Fong, R. I. Seed, P. Kwan, G. Ryan, H. Mehanna, S. Y. Chan, V. M. Darras, K. Boelaert, J. A. Franklyn, and C. J. McCabe, 2012, PTTG-binding factor (PBF) is a novel regulator of the thyroid hormone transporter MCT8: Endocrinology, v. 153, p. 3526-36.

Smith, V. E., M. L. Read, A. S. Turnell, R. J. Watkins, J. C. Watkinson, G. D. Lewy, J. C. Fong, S. R. James, M. C. Eggo, K. Boelaert, J. A. Franklyn, and C. J. McCabe, 2009, A novel mechanism of sodium iodide symporter repression in differentiated thyroid cancer: J Cell Sci, v. 122, p. 3393-402.

Solito, E., C. Raguenes-Nicol, C. de Coupade, A. Bisagni-Faure, and F. Russo-Marie, 1998, U937 cells deprived of endogenous annexin 1 demonstrate an increased PLA2 activity: Br J Pharmacol, v. 124, p. 1675-83.

Song, C., Q. Wang, and C. C. Li, 2003, ATPase activity of p97-valosin-containing protein (VCP). D2 mediates the major enzyme activity, and D1 contributes to the heat-induced activity: J Biol Chem, v. 278, p. 3648-55.

Stenfeldt, A. L., J. Karlsson, C. Wennerås, J. Bylund, H. Fu, and C. Dahlgren, 2007, Cyclosporin H, Boc-MLF and Boc-FLFLF are antagonists that preferentially inhibit activity triggered through the formyl peptide receptor: Inflammation, v. 30, p. 224-9.

Stratford, A. L., K. Boelaert, L. A. Tannahill, D. S. Kim, A. Warfield, M. C. Eggo, N. J. Gittoes, L. S. Young, J. A. Franklyn, and C. J. McCabe, 2005, Pituitary tumor transforming gene binding factor: a novel transforming gene in thyroid tumorigenesis: J Clin Endocrinol Metab, v. 90, p. 4341-9.

Subbiah, V., R. J. Kreitman, Z. A. Wainberg, J. Y. Cho, J. H. M. Schellens, J. C. Soria, P. Y. Wen, C. Zielinski, M. E. Cabanillas, G. Urbanowitz, B. Mookerjee, D. Wang, F. Rangwala, and B. Keam, 2018, Dabrafenib and Trametinib Treatment in Patients With Locally Advanced or Metastatic BRAF V600-Mutant Anaplastic Thyroid Cancer: J Clin Oncol, v. 36, p. 7-13.

Suh, J. M., J. H. Song, D. W. Kim, H. Kim, H. K. Chung, J. H. Hwang, J. M. Kim, E. S. Hwang, J. Chung, J. H. Han, B. Y. Cho, H. K. Ro, and M. Shong, 2003, Regulation of the phosphatidylinositol 3-kinase, Akt/protein kinase B, FRAP/mammalian target of rapamycin, and ribosomal S6 kinase 1 signaling pathways by thyroid-stimulating hormone (TSH) and stimulating type TSH receptor antibodies in the thyroid gland: J Biol Chem, v. 278, p. 21960-71.

Tazebay, U. H., I. L. Wapnir, O. Levy, O. Dohan, L. S. Zuckier, Q. H. Zhao, H. F. Deng, P. S. Amenta, S. Fineberg, R. G. Pestell, and N. Carrasco, 2000, The mammary gland iodide transporter is expressed during lactation and in breast cancer: Nat Med, v. 6, p. 871-8.

Thompson, R. J., A. Fletcher, K. Brookes, H. Nieto, M. M. Alshahrani, J. W. Mueller, N. H. F. Fine, D. J. Hodson, K. Boelaert, M. L. Read, V. E. Smith, and C. J. McCabe, 2019, Dimerization of the Sodium/Iodide Symporter: Thyroid, v. 29, p. 1485-1498.

Totsuka, Y., M. S. Ferdows, T. B. Nielsen, and J. B. Field, 1983, Effects of forskolin on adenylate cyclase, cyclic AMP, protein kinase and intermediary metabolism of the thyroid gland: Biochim Biophys Acta, v. 756, p. 319-27.

Tutter, M., C. Schug, K. A. Schmohl, S. Urnauer, C. Kitzberger, N. Schwenk, M. Petrini, C. Zach, S. Ziegler, P. Bartenstein, W. A. Weber, G. Multhoff, E. Wagner, L. H. Lindner, P. J. Nelson, and C. Spitzweg, 2020, Regional Hyperthermia Enhances Mesenchymal Stem Cell Recruitment to Tumor Stroma: Implications for Mesenchymal Stem Cell-Based Tumor Therapy: Mol Ther.

Tzeng, H. T., and Y. C. Wang, 2016, Rab-mediated vesicle trafficking in cancer: J Biomed Sci, v. 23, p. 70.

Urnauer, S., K. A. Schmohl, M. Tutter, C. Schug, N. Schwenk, S. Morys, S. Ziegler, P. Bartenstein, D. A. Clevert, E. Wagner, and C. Spitzweg, 2019, Dual-targeted NIS polyplexes-a theranostic strategy toward tumors with heterogeneous receptor expression: Gene Ther, v. 26, p. 93-108.

Vadysirisack, D. D., E. S. Chen, Z. Zhang, M. D. Tsai, G. D. Chang, and S. M. Jhiang, 2007a, Identification of in vivo phosphorylation sites and their functional significance in the sodium iodide symporter: J Biol Chem, v. 282, p. 36820-8.

Vadysirisack, D. D., A. Venkateswaran, Z. Zhang, and S. M. Jhiang, 2007b, MEK signaling modulates sodium iodide symporter at multiple levels and in a paradoxical manner: Endocr Relat Cancer, v. 14, p. 421-32.

Wang, J., J. A. Knauf, S. Basu, E. Puxeddu, H. Kuroda, M. Santoro, A. Fusco, and J. A. Fagin, 2003, Conditional expression of RET/PTC induces a weak oncogenic drive in thyroid PCCL3 cells and inhibits thyrotropin action at multiple levels: Mol Endocrinol, v. 17, p. 1425-36.

Wang, Q., L. Li, and Y. Ye, 2008, Inhibition of p97-dependent protein degradation by Eeyarestatin I: J Biol Chem, v. 283, p. 7445-54.

Wang, Q., X. Lu, S. Zhao, M. Pang, X. Wu, H. Wu, R. M. Hoffman, Z. Yang, and Y. Zhang, 2017, Moesin Expression Is Associated with Glioblastoma Cell Proliferation and Invasion: Anticancer Res, v. 37, p. 2211-2218.

Wang, Q., C. Song, and C. C. Li, 2004, Molecular perspectives on p97-VCP: progress in understanding its structure and diverse biological functions: J Struct Biol, v. 146, p. 44-57.

Wang, Y. J., G. Y. Zhang, Z. Q. Xiao, H. M. Wang, and Z. C. Chen, 2006, Preliminary proteomic analysis of indomethacin's effect on tumor transplanted with colorectal cancer cell in nude mice: J Biochem Mol Biol, v. 39, p. 171-7.

Wapnir, I. L., M. van de Rijn, K. Nowels, P. S. Amenta, K. Walton, K. Montgomery, R. S. Greco, O. Dohan, and N. Carrasco, 2003, Immunohistochemical profile of the sodium/iodide symporter in thyroid, breast, and other carcinomas using high density tissue microarrays and conventional sections: J Clin Endocrinol Metab, v. 88, p. 1880-8.

White, I. J., L. M. Bailey, M. R. Aghakhani, S. E. Moss, and C. E. Futter, 2006, EGF stimulates annexin 1-dependent inward vesiculation in a multivesicular endosome subpopulation: EMBO J, v. 25, p. 1-12.

Wilhelm, S. M., L. Adnane, P. Newell, A. Villanueva, J. M. Llovet, and M. Lynch, 2008, Preclinical overview of sorafenib, a multikinase inhibitor that targets both Raf and VEGF and PDGF receptor tyrosine kinase signaling: Mol Cancer Ther, v. 7, p. 3129-40.

Wong, P. F., W. F. Cheong, M. H. Shu, C. H. Teh, K. L. Chan, and S. AbuBakar, 2012, Eurycomanone suppresses expression of lung cancer cell tumor markers, prohibitin, annexin 1 and endoplasmic reticulum protein 28: Phytomedicine, v. 19, p. 138-44.

Worden, F., 2014, Treatment strategies for radioactive iodine-refractory differentiated thyroid cancer: Ther Adv Med Oncol, v. 6, p. 267-79.

Woyach, J. A., R. T. Kloos, M. D. Ringel, D. Arbogast, M. Collamore, J. A. Zwiebel, M. Grever, M. Villalona-Calero, and M. H. Shah, 2009, Lack of therapeutic effect of the histone deacetylase inhibitor vorinostat in patients with metastatic radioiodine-refractory thyroid carcinoma: J Clin Endocrinol Metab, v. 94, p. 164-70.

Wu, X., and T. A. Rapoport, 2018, Mechanistic insights into ER-associated protein degradation: Curr Opin Cell Biol, v. 53, p. 22-28.

Wächter, S., A. I. Damanakis, M. Elxnat, S. Roth, A. Wunderlich, F. A. Verburg, S. A. Fellinger, D. K. Bartsch, and P. Di Fazio, 2018, Epigenetic Modifications in Thyroid Cancer Cells Restore NIS and Radio-Iodine Uptake and Promote Cell Death: J Clin Med, v. 7.

Xing, M., B. R. Haugen, and M. Schlumberger, 2013, Progress in molecular-based management of differentiated thyroid cancer: Lancet, v. 381, p. 1058-69.

Xing, M., R. Liu, X. Liu, A. K. Murugan, G. Zhu, M. A. Zeiger, S. Pai, and J. Bishop, 2014, BRAF V600E and TERT promoter mutations cooperatively identify the most aggressive papillary thyroid cancer with highest recurrence: J Clin Oncol, v. 32, p. 2718-26.

Xing, M., W. F. Ooi, J. Tan, A. Qamra, P. H. Lee, Z. Li, C. Xu, N. Padmanabhan, J. Q. Lim, Y. A. Guo, X. Yao, M. Amit, L. M. Ng, T. Sheng, J. Wang, K. K. Huang, C. G. Anene-Nzelu, S. W. T. Ho, M. Ray, L. Ma, G. Fazzi, K. J. Lim, G. C. Wijaya, S. Zhang, T. Nandi, T. Yan, M. M. Chang, K. Das, Z. F. A. Isa, J. Wu, P. S. Y. Poon, Y. N. Lam, J. S. Lin, S. T. Tay, M. H. Lee, A. L. K. Tan, X. Ong, K. White, S. G. Rozen, M. Beer, R. S. Y. Foo, H. I. Grabsch, A. J. Skanderup, S. Li, B. T. Teh, and P. Tan, 2020, Genomic and epigenomic EBF1 alterations modulate TERT expression in gastric cancer: J Clin Invest.

Xu, B., T. Fuchs, S. Dogan, I. Landa, N. Katabi, J. A. Fagin, R. M. Tuttle, E. Sherman, A. J. Gill, and R. Ghossein, 2020, Dissecting Anaplastic Thyroid Carcinoma: A Comprehensive Clinical, Histologic, Immunophenotypic, and Molecular Study of 360 Cases: Thyroid.

Xu, X., R. M. Quiros, P. Gattuso, K. B. Ain, and R. A. Prinz, 2003, High prevalence of BRAF gene mutation in papillary thyroid carcinomas and thyroid tumor cell lines: Cancer Res, v. 63, p. 4561-7.

Yamada, M., Y. Saga, N. Shibusawa, J. Hirato, M. Murakami, T. Iwasaki, K. Hashimoto, T. Satoh, K. Wakabayashi, M. M. Taketo, and M. Mori, 1997, Tertiary hypothyroidism and hyperglycemia in mice with targeted disruption of the thyrotropin-releasing hormone gene: Proc Natl Acad Sci U S A, v. 94, p. 10862-7.

Yao, Z., N. M. Torres, A. Tao, Y. Gao, L. Luo, Q. Li, E. de Stanchina, O. Abdel-Wahab, D. B. Solit, P. I. Poulikakos, and N. Rosen, 2015, BRAF Mutants Evade ERK-Dependent Feedback by Different Mechanisms that Determine Their Sensitivity to Pharmacologic Inhibition: Cancer Cell, v. 28, p. 370-83.

Yarwood, R., J. Hellicar, P. G. Woodman, and M. Lowe, 2020, Membrane trafficking in health and disease: Dis Model Mech, v. 13.

Yi, M., and J. E. Schnitzer, 2009, Impaired tumor growth, metastasis, angiogenesis and wound healing in annexin A1-null mice: Proc Natl Acad Sci U S A, v. 106, p. 17886-91.

Yonemura, S., M. Hirao, Y. Doi, N. Takahashi, T. Kondo, and S. Tsukita, 1998, Ezrin/radixin/moesin (ERM) proteins bind to a positively charged amino acid cluster in the juxta-membrane cytoplasmic domain of CD44, CD43, and ICAM-2: J Cell Biol, v. 140, p. 885-95.

Yoshimura, M., and J. M. Hershman, 1995, Thyrotropic action of human chorionic gonadotropin: Thyroid, v. 5, p. 425-34.

Yuan, X., C. Larsson, and D. Xu, 2019, Mechanisms underlying the activation of TERT transcription and telomerase activity in human cancer: old actors and new players: Oncogene, v. 38, p. 6172-6183.

Zannini, M., H. Francis-Lang, D. Plachov, and R. Di Lauro, 1992, Pax-8, a paired domain-containing protein, binds to a sequence overlapping the recognition site of a homeodomain and activates transcription from two thyroid-specific promoters: Mol Cell Biol, v. 12, p. 4230-41.

Zhang, J., and M. A. Lazar, 2000, The mechanism of action of thyroid hormones: Annu Rev Physiol, v. 62, p. 439-66.

Zhang, Z., D. Liu, A. K. Murugan, Z. Liu, and M. Xing, 2014, Histone deacetylation of NIS promoter underlies BRAF V600E-promoted NIS silencing in thyroid cancer: Endocr Relat Cancer, v. 21, p. 161-73.

Zhao, Z. G., X. G. Guo, C. X. Ba, W. Wang, Y. Y. Yang, J. Wang, and H. Y. Cao, 2012, Overweight, obesity and thyroid cancer risk: a meta-analysis of cohort studies: J Int Med Res, v. 40, p. 2041-50.

Zhou, H. J., J. Wang, B. Yao, S. Wong, S. Djakovic, B. Kumar, J. Rice, E. Valle, F. Soriano, M. K. Menon, A. Madriaga, S. Kiss von Soly, A. Kumar, F. Parlati, F. M. Yakes, L. Shawver, R. Le Moigne, D. J. Anderson, M. Rolfe, and D. Wustrow, 2015, Discovery of a First-in-Class, Potent, Selective, and Orally Bioavailable Inhibitor of the p97 AAA ATPase (CB-5083): J Med Chem, v. 58, p. 9480-97.

Zhu, X., F. C. Morales, N. K. Agarwal, T. Dogruluk, M. Gagea, and M. M. Georgescu, 2013, Moesin is a glioma progression marker that induces proliferation and Wnt/β-catenin pathway activation via interaction with CD44: Cancer Res, v. 73, p. 1142-55.